PLANETARY SURFACE EVOLUTION FROM IMPACT CRATERING:
A VIEW FROM APPLIED GEOSPATIAL METHODS

Dissertation

Submission for the Academic Title

Doctor of Natural Sciences

(Dr. rer. nat.)

Submitted by

Christian Riedel

Submitted to the Department of Earth Sciences

Freie Universität Berlin

Berlin, March 2021

Supervisor:	Prof. Dr. Kai Wünnemann Museum für Naturkunde Leibniz Institute for Evolution and Biodiversity Science and Freie Universität Berlin Institute of Geological Sciences
Second examiner:	Prof. Dr. Harald Hiesinger University of Münster Institut für Planetologie
Date of defense:	09 July 2021

Hiermit versichere ich, die vorliegende Arbeit selbstständig angefertigt und keine anderen als die angeführten Quellen und Hilfsmittel benutzt zu haben.

Berlin, 2021

ACKNOWLEDGMENTS

To begin with, I want to thank everyone who supported me in putting this work together. A huge thank you goes to Dr. Greg Michael (Freie Universität Berlin) for his continuous advice and support. I also thank Prof. Dr. Kai Wünnemann (Natural History Museum Berlin & Freie Universität Berlin) and Prof. Dr. Harald Hiesinger (University of Münster) for the supervision, support, and inspiring discussions over the past years. I would especially like to thank Dr. Thomas Christiansen (Namibia University of Science and Technology), who encouraged me to embark on a science career.

Furthermore, I am very thankful to everyone who supported and contributed to the collaborative research center TRR-170. TRR-170 provided the research framework to conduct the research presented in this thesis. My gratitude goes to Prof. Dr. Harry Becker (Freie Universität Berlin) for the continuous financial support and the organization of TRR-170 and Elfrun Lehmann (Freie Universität Berlin) for taking care of the project's coordination.

I also want to thank all the scientists who supported me professionally in compiling this thesis. I would particularly like to thank Prof. Dr. David Minton, who made it possible to do a research stay at Purdue University and gave me generous support with his specialist knowledge. I also thank Trent Hare for the encouraging discussions and the opportunity to visit the USGS Astrogeology Science Center in Flagstaff and Dr. Jackie Clark and Dr. Hannes Bernhardt for inviting me to Arizona State University. Furthermore, I would like to thank Dr. Caleb Fassett (NASA Marshall Space Flight Center), Dr. Carolyn van der Bogert (University of Münster), Dr. Frank Sohl (German Aerospace Center), and Prof. Dr. Vikram Unnithan (Jacobs University Bremen) for the numerous exciting and motivating discussions.

I am also very grateful for the discussions and shared experiences with the doctoral students from the University of Münster, Purdue University, and the TRR-170. A special salute goes to Wajiha Iqbal (University of Münster) for the continuous discussions and Dr. Csilla Orgel (ESA ESTEC), with who I shared a tiny office at Freie University Berlin for the past years. This work was also broadly supported by my colleagues from the Planetary Sciences and Remote Sensing group at Freie Universität Berlin. I want to thank Prof. Dr. Frank Postberg, Alicia Neesemann, Sebastian Walter, Wilhelm Zuschneid, Dr. Tiantian Liu (Natural History Museum Berlin), Dr. Jingyan Hao, and Dr. Thomas Kneissl for the motivating discussions.

Finally, I want to thank my friends and family for the continuous moral support while working on this thesis. This work would not have been possible without you.

ABSTRACT

The collision of cosmic projectiles with a terrestrial planet's surface forms topographic depressions, known as impact craters. Since planetary surfaces are continuously bombarded, these features can be observed on nearly all solid bodies in the Solar System. On airless bodies with limited endogenic geologic activity, such as the Moon, impact cratering is the primary geologic process. Therefore, the lunar surface hosts a substantial impact crater record that is often used as a reference to study impact cratering, planetary surface evolution, impactor populations, and the timing of geologic events in the inner Solar System. The work presented in this thesis introduces novel methods to modify and analyze geospatial data under the consideration of a planet's curvature. The developed techniques are applied to planetary spatial data to investigate the cratered surface evolution of planetary bodies in the inner Solar System.

The main emphasis in developing geospatial methods involves considering planetary curvature when analyzing and modifying planetary spatial data. This is achieved by implementing geodesic measurements, developing approaches for geodesic polygon modifications, and considering map projection properties. The developed techniques can be used to solve specific tasks in planetary data analyses. These tasks include quantifying the spatial randomness of a planet's impact crater record and considering geometric crater obliteration in crater size-frequency distribution measurements.

The studies presented in this thesis apply the developed geospatial techniques to provide new insights on (1) surface evolution scenarios on Mercury, Venus, and the Moon, (2) the influence of cratering-induced crater degradation on the observable crater record, and (3) the impact of geometric crater obliteration on interpretations about planetary impactor populations. It is confirmed that the non-random spatial distribution of craters on Mercury and the Moon indicates the presence of extended resurfacing processes that formed major geologic units on the respective surfaces. Craters on Venus are mostly randomly distributed due to its young surface and the absence of extended volcanic events in its recent geologic history. This absence suggests that a global decline in volcanic activity affected the recent surface evolution of Venus. The presented studies also indicate that the cratering-induced degradation of pre-existing lunar craters leads to two distinct scenarios in which measured crater size-frequency distributions do not reflect the impactor population. The two scenarios include crater equilibrium, which affects small, simple lunar craters, and non-sparse cratering, affecting larger lunar craters. Crater equilibrium is mainly caused by the cumulative effects of high-velocity ejecta, contributing to the downslope diffusion of surface material, whereas non-sparseness is caused by the cumulative effects of geometric crater obliteration. It is shown that small lunar craters are more destructive to the pre-existing terrain relative to their size because of a higher relative contribution to topographic diffusion from distal ejecta. Therefore, large lunar craters mainly contribute to crater degradation by geometric crater obliteration. In this obliteration scenario, the difference between the visible crater record and the impactor population can be corrected when measuring crater size-frequency distributions. If such correction is applied, the crater size-frequency distribution on ancient lunar terrains reflects an impacting population that is well approximated by a continuous size-frequency distribution.

ZUSAMMENFASSUNG

Kollidiert ein kosmisches Projektil mit der Oberfläche eines planetaren Körpers, so entstehen topografische Vertiefungen – sogenannte Impaktkrater. Da die Himmelskörper des Sonnensystems seit ihrer Entstehung kontinuierlich bombardiert werden, können diese Strukturen auf nahezu allen festen Körpern im Sonnensystem beobachtet werden. Auf Himmelskörpern, die weder eine Atmosphäre, noch ausgeprägte geologische Aktivität besitzen, wie es beispielsweise auf dem Mond der Fall ist, ist die Bildung von Impaktkratern der primäre geologische Prozess, der zu Veränderungen der Oberfläche führt. Aus diesem Grund besitzt die Mondoberfläche eine umfangreiche Aufzeichnung über die Impakthistorie des inneren Sonnensystems, die häufig als Referenz für die Untersuchung von Kraterbildungsprozessen, die Evolution planetarer Oberflächen, Impaktorpopulationen und die Datierung geologischer Prozesse im inneren Sonnensystem verwendet wird. In dieser Arbeit werden neuartige Methoden zur Modifizierung und Analyse räumlicher Daten unter Berücksichtigung der Planetenkrümmung vorgestellt. Die entwickelten Techniken werden auf planetare Geodaten angewendet, um die Entwicklungsgeschichte planetarer Oberflächen im inneren Sonnensystems anhand von Impaktkratern zu untersuchen.

Wesentlich bei der Entwicklung der technischen Methoden ist die Berücksichtigung der Planetenkrümmung bei der Analyse und Modifikation von Geodaten. Dies wird über die Implementierung geodätischer Messungen und der Entwicklung von Prozessen zur Modifizierung von Polygonen auf gekrümmten Oberflächen und unter Berücksichtigung von Kartenprojektionen erarbeitet. Die entwickelten Methoden werden angewendet, um individuelle Fragestellungen bei der Analyse planetarer Daten zu bearbeiten. Diese umfassen die räumliche Verteilung von Impaktkratern und die Berücksichtigung von Kraterüberlagerungseffekten bei Messungen der Kratergrößen-Häufigkeitsverteilung.

Bei den in dieser Arbeit vorgestellten Studien werden die entwickelten Methoden zur Auswertung planetarer Geodaten angewendet, um neue Erkenntnisse über (1) die Entwicklungsgeschichte der Merkur-, Venus- und Mondoberfläche, (2) den Einfluss neuer Impakte auf die Degradation bestehender Krater und (3) den Einfluss geometrischer Kraterüberlagerung auf Interpretationen zur Impaktorpopulation zu gewinnen. Es wird gezeigt, dass Krater auf dem Mond und Merkur durch ausgedehnte Oberflächenerneuerungsprozesse in der frühen geologischen Entwicklung beider Körper nicht zufällig verteilt sind. Auf der Venus wiederum sind Krater meist zufällig verteilt, was auf die junge Oberfläche und die Abwesenheit ausgedehnter vulkanischer zurückzuführen ist. Dieses Szenario deutet darauf hin, dass eine globale Abnahme der vulkanischen Aktivität die jüngste geologische Entwicklung der Venusoberfläche bestimmt hat. Die vorgestellten Studien zeigen außerdem, dass die durch neue Impakte verursachte Degradation bestehender Mondkrater zu zwei unterschiedlichen Szenarien führt, in denen die gemessene Kratergrößen-Häufigkeitsverteilung nicht die Impaktorpopulation widerspiegelt. Dies umfasst das „crater equilibrium“, welches kleine Krater auf dem Mond betrifft und das „non-sparse cratereing“, welches größere Mondkrater betrifft. Das „crater equilibrium“ wird hauptsächlich durch den Einfluss von Hochgeschwindigkeitsejekta verursacht, durch dessen Einfluss

Oberflächenmaterial gelockert und in topografischen Senken abgelagert wird („downslope diffusion"). Demgegenüber wird „non-sparse cratering" durch geometrische Kraterüberlagerung verursacht. Es wird gezeigt, dass kleine Mondkrater deutlich mehr zur „downslope diffusion" beitragen und daher der relative Einfluss kleiner Mondkrater auf die Degradation der Mondtopographie größer ist, als der größerer Krater. Größere Mondkrater tragen hautsächlich durch geometrische Kraterüberlagerung zur Degradation bestehender Impaktkrater bei. In einem Umfeld, bei dem die geometrische Kraterüberlagerung der dominierende Degradationsprozess ist, kann die Differenz zwischen den sichtbaren Kratern und der Impaktorpopulation bei der Messung von Kratergrößen-Häufigkeitsverteilungen korrigiert werden. Wenn eine solche Korrektur angewendet wird, entspricht die Kratergrößen-Häufigkeitsverteilung der ältesten geologischen Einheiten des Mondes einer Impaktorpopulation, die durch eine kontinuierliche Produktionsfunktion approximiert werden kann.

CONTENTS

LIST OF FIGURES

LIST OF TABLES

LIST OF ABBREVIATIONS

BCC	Buffered Crater Counting
BNSC	Buffered Non-Sparseness Correction
CF	Chronology Function
CSFD	Crater Size-Frequency Distribution
CTEM	Cratered Terrain Evolution Model
DFG	Deutsche Forschungsgemeinschaft
DLR	German Aerospace Center
DTM	Digital Terrain Models
GDAL	Geospatial Data Abstraction Library
GIS	Geographic Information System
GUI	Graphical User Interface
ISIS	Software for Imagers and Spectrometers
LAEA	Lambert Azimuthal Equal Area
LHB	Late Heavy Bombardment
LROC	Lunar Reconnaissance Orbiter Camera
M2CND	Mean Second Closest Neighbor Distance
NAC	Narrow Angle Camera
NSC	Non-Sparseness Correction
PF	Production Function
PKT	Procellarum KREEP Terrane
SDAA	Standard Deviation of Adjacent Area
SFD	Size-Frequency Distribution
SPA	South Pole-Aitken Basin
TCC	Traditional Crater Counting
TRR	Collaborative Research Center
WAC	Wide Angle Camera

CHAPTER 1

INTRODUCTION

The impact crater record on planetary surfaces has long been used to study the evolution of planetary bodies in the inner Solar System. The research field involves multiple disciplines and experienced a substantial advance ever since the first lunar missions returned material from the Moon's surface. For example, interpretations of geospatial data together with the radiometric analysis of lunar rock samples provide a fundamental basis for investigations on the bombardment history and planetary surface evolution on bodies in the inner Solar System. However, our knowledge about the respective topics is far from complete and various open questions are investigated by the research community. This work focuses on novel approaches in geospatial data analysis to study the evolution of cratered landscapes, the bombardment history in the inner Solar System, and the influence of crater degradation on the observable crater record.

1.1. Research Framework

The research that resulted in this Ph.D. thesis was done in the framework of the collaborative research center TRR-170 "Late Accretion onto Terrestrial Planets," funded by Deutsche Forschungsgemeinschaft (DFG). The overall goal of TRR-170 is to study the late accretion history of planetary bodies in the inner Solar System. To that end, the collaborative research center uses multidisciplinary approaches that involve planetary remote sensing, cosmochemistry, and geodynamic modeling. Three project areas, "A," "B," and "C," with assigned subprojects, outline the individual research projects that contribute to the research goals of TRR-170. Projects in area "A" study the impactor flux in the inner Solar System until about 3.5 billion years ago (3.5 Ga) based on the lunar impact history. Project area "B" investigates the chemical composition of building blocks that accreted onto the Earth-Moon system after the Moon-forming impact event. Projects in area "C" examine the effects of late-accreted material on the geodynamic evolution of the terrestrial planets.

The subproject A3, "Ancient bombardment of the inner Solar System – Reinvestigation of the 'fingerprints' of different impactor populations," is of particular importance for the research presented in this thesis. In subproject A3, the overall research goal is to investigate the population of impactors that struck the lunar surface. To that end, the lunar cratering record is taken as a reference. Previous studies on Mercury, Mars, and the Moon suggest that the size-frequency distribution of impact craters on ancient surfaces differs from crater populations found on younger surface units (e.g., Strom et al., 2005; Strom et al., 2015). Therefore, the suggested change in crater populations may indicate a possible change in impactor populations that struck bodies in the inner Solar System before 3.5 Ga (e.g., Fassett et al.,2012; Marchi et al. 2012). However, the presence of multiple impactor populations is highly debated in the scientific community and it has been suggested that the investigated change in crater populations may not be related to differences in projectiles but geologic effects (e.g., Neukum & Ivanov, 1994; Kneissl et al., 2016). The goal of subproject A3 is to re-investigate the hypothesis of a time-dependent lunar impactor population by measuring the crater size-frequency distribution (CSFD) on ancient lunar surface units. Therefore, detailed geologic mapping and innovative techniques to measure CSFDs and identify biases from insignificant reference areas and impact craters are required.

1.2. Scientific Objectives

The overall goal of this thesis is to improve the understanding of planetary surface evolution from impact cratering. To that end, cratering-induced processes, which contaminate the visible crater record, are investigated. Here, contamination is defined as a process in which the size-frequency distribution of visible impact craters does not correspond to impactors' size-frequency distribution. It is examined how such biases affect interpretations on planetary surface evolution, including a suggested change in the impactor population before 3.5 Ga. This includes the subjects of crater removal by subsequent impact events, the addition of craters through secondary impacts, and the spatial distribution of impact craters. Since planetary surface investigations often rely on geospatial data, this work focuses on developing geospatial techniques and software tools to investigate the influence of cratering-induced contamination on the observable cratering record. The majority of the required geospatial techniques are not implemented in existing Geographic Information System (GIS) software tools and require individual solutions to modify geometries on curved planetary surfaces. Thus, due to the complexity of the available data sets, reference bodies, and map projections, the research presented in this thesis includes a wide range of technical topics regarding the analytical modification and handling of geospatial data. Some general research questions that will be discussed are:

1. **How do surface processes affect the global spatial distribution of impact craters?**

2. **How do fresh impacts contribute to the degradation of the pre-existing cratered landscape?**

3. **How does the cratering-induced degradation of impact craters affect planetary surface evolution interpretations?**

4. **Does the change in the CSFD on ancient lunar surface units reflect a change in the impactor population?**

The necessary steps to address these questions are:

1. **Develop approaches to modify and analyze geospatial data while accounting for a planet’s curvature**
    - Implement geodesic methods to modify and analyze geospatial data
    - Find solutions to geometric issues when modifying geospatial vector data
    - Consider the influence of map projections on geospatial data modification and analysis
    - Implement multicore functionality to increase the computation efficiency compared to existing proprietary GIS methods

2. Analyze the influence of geometric crater obliteration on lunar terrains

- Develop a software tool to consider the effect of geometric crater obliteration while measuring CSFDs

3. Analyze the contribution of fresh impacts to the degradation of pre-existing craters

- Simulate the evolution of a cratered landscape from a known impactor population
- Quantify differences between the produced and observable impact crater record using different CSFD measurement techniques
- Analyze the per-crater contribution to the degradation of the pre-existing landscape

1.3. Organization of the Thesis

This cumulative dissertation thesis consists of five major parts. Sections I and IV outline the general scientific framework and summarize the overall conclusions. These parts were specially written for this thesis and encompass the central scientific studies. These studies include four published, peer-reviewed publications presented in sections II and III. Therefore, these parts contain individual introduction and conclusion chapters.

Part I covers the scientific and technical background of this thesis. The section contains two chapters, which introduce the scientific and geospatial framework that constitute the overall research topic. The first chapter in this section (Chapter 2) covers the scientific background. Here, impact crater formation is described and methods to derive information from the planetary impact crater record are discussed. The described methods involve the chronostratigraphic analysis of planetary surfaces and implications on the inner Solar System's bombardment history obtained from planetary crater records. Chapter 2 also covers the given techniques' current limitations and mentions cratering-related processes that contaminate the visible crater record on planetary surfaces.

The second chapter of part I (Chapter 3) covers the technical background of this thesis. Since studies on planetary surfaces typically rely on geospatial data, the analysis and modification of raster and vector data play an essential role in scientific investigations on planetary surface evolution. Therefore, Chapter 3 contains an overview of geospatial data, map projections, and GIS-based software tools provided by the scientific community.

Chapters within parts II and III contain published scientific work. Part II contains two peer-reviewed publications that address the development of geospatial methods to study planetary crater records. Chapter 4 on "Studying the global spatial randomness of impact craters on Mercury, Venus, and the Moon with geodesic neighborhood relationships" was accepted for publication in the Earth and Space Science journal (Riedel et al., 2021). The paper describes improved methods to quantify the spatial randomness of impact craters based on geodesic measurements and geospatial data modification on curved planetary reference bodies. The developed approaches are applied to global crater datasets of Mercury, Venus, and the Moon to investigate crater population variations and surface evolution scenarios on the respective planetary bodies. The author of this thesis was responsible for developing the improved geospatial methods, data analysis, and manuscript writing. All co-authors provided contributions by giving technical and scientific advice and assisting in the manuscript preparation.

Chapter 5 on “A New Tool to Account for Crater Obliteration Effects in Crater Size-Frequency Distribution Measurements” was published in the Earth and Space Science journal (Riedel et al., 2018). The paper focuses on the GIS-based implementation of a technique to consider geometric crater obliteration effects in CSFDs measurements. Chapter 5 describes the analysis and modification of geospatial vector data with respect to a curved planetary surface and the development of a software tool. The author of this thesis carried out the software programming, conducted case studies, and prepared the manuscript. All co-authors contributed to discussions and manuscript improvement.

Part III of this thesis contains two peer-reviewed publications in which the presented method of Chapter 5 is applied to lunar crater data and the crater record of a simulated surface unit. The study in Chapter 6, “Ancient Bombardment of the Inner Solar System: Reinvestigation of the “Fingerprints” of Different Impactor Populations on the Lunar Surface,” was published in the Journal of Geophysical Research: Planets (Orgel et al. (including Riedel), 2018). Here, the software tool presented in Chapter 5 was applied to study the influence of geometric crater obliteration on the lunar crater record. The author of this thesis contributed to the publication by providing software analysis and preparing figures.

Chapter 7 on “Degradation of Small Simple and Large Complex Lunar Craters: Not a Simple Scale Dependence“ was published in the Journal of Geophysical Research: Planets (Riedel et al., 2020). The study focuses on cratering-induced crater degradation on the lunar surface. To that end, an existing cratered surface evolution model was used to simulate a lunar-like cratered terrain. The methods presented in Chapter 5 were applied to the crater records of modeled surface units to analyze the contribution of fresh lunar impacts to the degradation of pre-existing craters. To that end, the study results presented in Chapter 6 were used as a reference. The author of this thesis developed software to conduct CSFD measurements on the modeled surface units, analyzed crater statistics, and composed the manuscript. Co-author Prof. Dr. David A. Minton provided the tool to model a cratered surface evolution, assisted in interpreting the results and the writing of the manuscript. All other co-authors contributed through scientific discussions and manuscript improvement.

All chapters of parts II and III contain individual sections that summarize the respective studies' conclusions. These conclusions are summarized in part IV and related to the general research questions of this thesis, presented in Chapter 1.1.

PART I

SCIENTIFIC AND TECHNICAL BACKGROUND

CHAPTER 2

SCIENTIFIC BACKGROUND

Our Solar System hosts objects of various sizes. These range from tiny particles, such as dust, to larger objects like asteroids and planetary bodies. Throughout the evolution of the Solar System, various mechanisms caused these objects to collide with each other. These collisions are a part of multiple processes that range from the accretion of planetesimals in the early history of the Solar System (e.g., Weidenschilling, 2000) to the disruption of planetary bodies (e.g., Martelli et al., 1994) and the formation of surface features. Such surface features are known as impact craters and form when a hypervelocity impactor strikes the surface of a planetary body (e.g., Melosh, 1989). Since this process occurs continuously throughout the Solar System, impact craters are a commonly observed landform on most planetary bodies that range from sizes below the resolution limit of remote sensing sensors to structures that make up a significant fraction of a planetary body's radius.

2.1. Impact Cratering on Planetary Surfaces

Although it is assumed that the impactor populations that hit targets in the inner Solar System are similar (e.g., Neukum & Ivanov, 1994), variations in planetary conditions lead to differently cratered landscapes. On some bodies, impact craters are the dominant landform. This is particularly observable on airless bodies with limited geologic activity, such as the Moon, where a substantial crater record could accumulate since there is no atmospheric filtering and a lack of post-impact modification by endogenic processes. As a consequence, post-impact modification on the Moon is primarily controlled by impact cratering itself, which makes the Moon a perfect place to study a wide range of cratering-related topics, for example, crater morphology (e.g., Melosh, 1989), cratered surface evolution (e.g., Wood et al., 1977), and the nature of impactor populations (e.g., Fassett, 2016). In contrast, only a few impact craters are preserved on Earth since geologic processes such as volcanism, erosion, sedimentation, and plate tectonics, as well as biological weathering, contribute to the rapid degradation of a crater's topographic features (e.g., Spudis, 1993).

2.1.1. Crater Formation

Impact craters form when a cosmic projectile strikes a planetary body's surface at high velocity. This impact velocity depends on various factors, such as the velocity of the projectile, the escape velocity of the planetary body, and gravity. Since gravity is influenced by the mass of nearby objects, the impact velocity in the inner Solar System typically increases with decreasing distance to the sun. For example, in the Earth-Moon system, the average impact velocity for asteroidal impactors is 18 km/s (Melosh, 2012), while the average impact velocity for such projectiles on Mercury is 30 km/s (Marchi et al., 2005). When a projectile is large enough to maintain most of its kinetic energy while passing through a planet's atmosphere, it releases a large amount of energy as it hits the surface. The projectile's initial kinetic energy is transformed

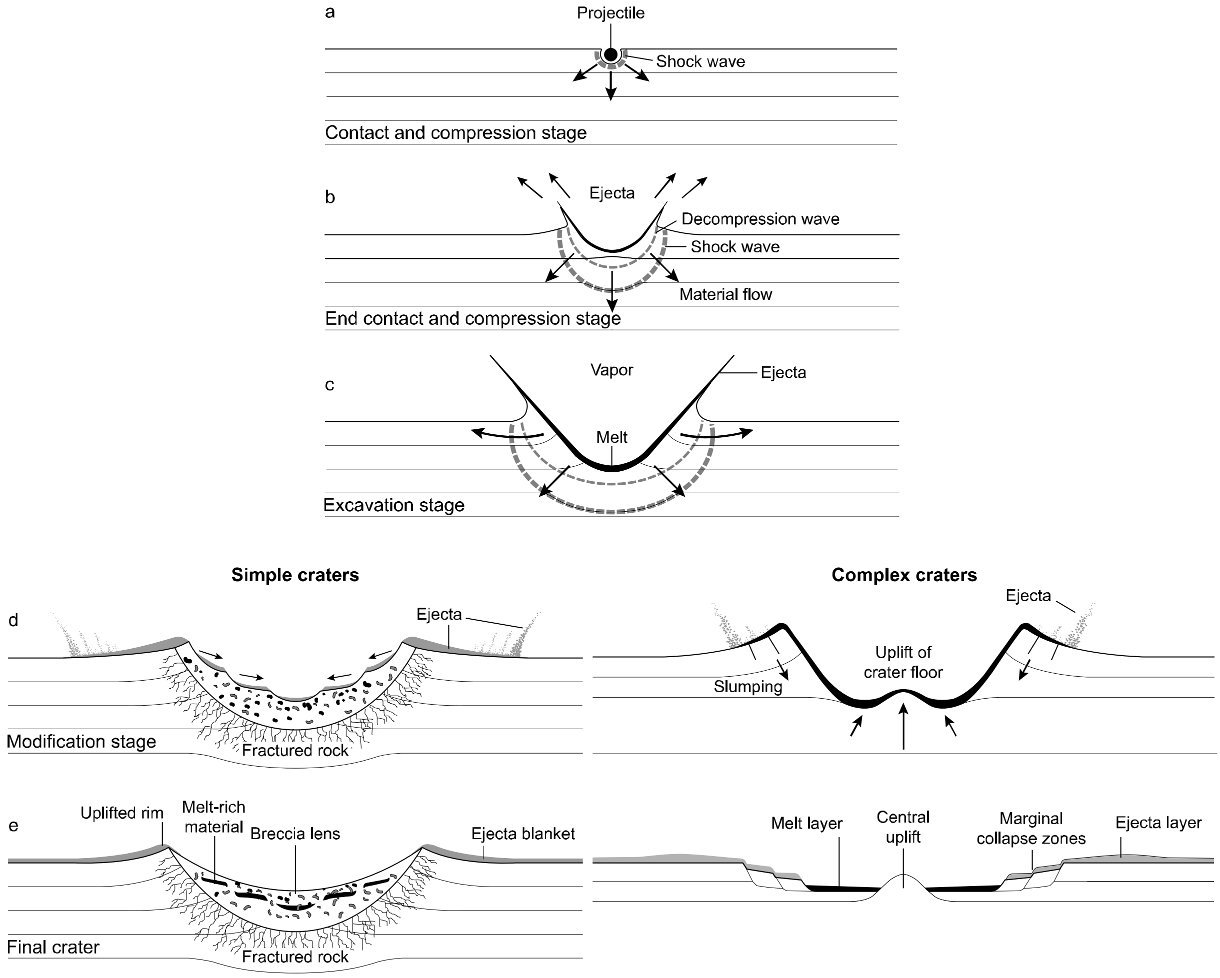

Figure 2.1: *Illustration of crater formation stages from a hypervelocity impactor (modified from French, 1998). During contact and compression (a, b), a projectile penetrates the surface of a planetary body. Due to the release of its initial kinetic energy, shock waves and decompression waves initiate the transient cavity's opening. The transient cavity reaches its maximum dimensions at the end of the excavation stage (c), while the target material is displaced and ejected. During the modification stage (d), the transient cavity is modified. Target materials rise to compensate for the excavated mass and rims may collapse under the influence of gravity. The intensity to which the transient cavity is modified depends on its size, the target lithology, and the planetary body's gravity. The modification leads to simple and complex crater morphologies in the final crater (e).*

into compression of the target, which eventually leads to an impact crater formation. Although an impact crater's formation is a continuous process, it is often divided into three stages: contact and compression, excavation, and modification (e.g., Gault et al., 1968; Melosh, 1989).

The contact and compression stage (Fig. 2.1a and 2.1b) is the first and briefest phase of impact crater formation. It is initiated when a hypervelocity projectile contacts the surface of a planetary body. While the projectile descends into the target, its initial kinetic energy is shared between the projectile and the target material, generating strong shock waves, which propagate into both objects (e.g., Melosh, 2012). During this process, the projectile typically penetrates the target material to a depth of one or two projectile diameters (e.g., French, 1998) as it is slowed and strongly compressed. Upon decompression, the produced heat may cause large parts of the projectile to melt or vaporize (e.g., Osinski &

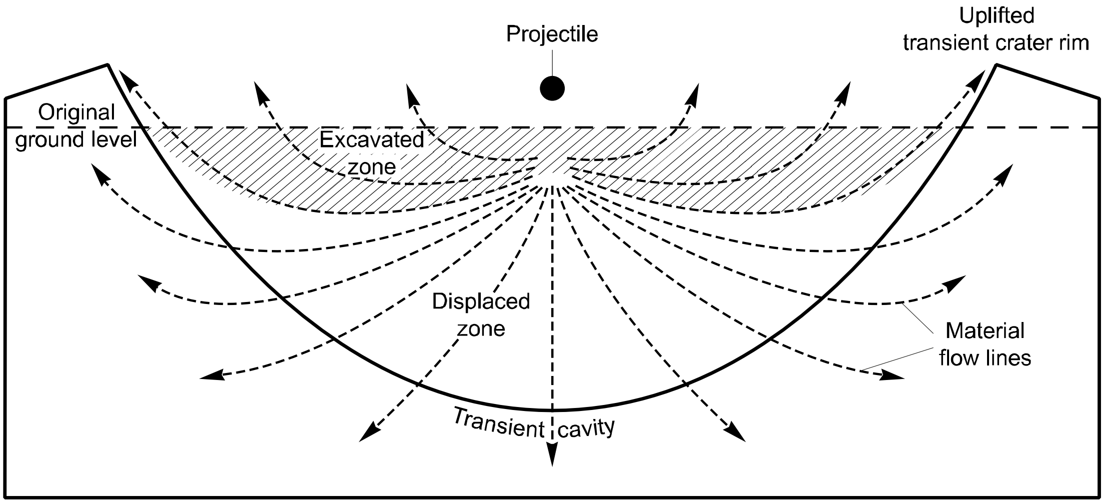

Figure 2.2: Cross-section of a transient crater cavity showing the material flow lines during a hypervelocity impact (modified from French, 1998). Shock and decompression waves produce an excavation flow that opens up the transient cavity. The surface material is transported in a downward and outward direction. This leads to a displaced zone in the lower section of the transient cavity, where target material is modified but remains within the crater, and an excavated zone in the upper part of the transient cavity, where target material is ejected beyond its rim.

Pierazzo, 2012). Impact projectiles may be molten or vaporized to the point that no physical evidence of the projectile remains on the surface (e.g., Osinski et al., 2012). Unmelted impactor material may be found mainly in small craters and more rarely in larger impacts. Depending on the projectile's size, composition, and velocity, the contact and compression stage lasts from a fraction of a second to a few seconds for large impactors (e,g, Hamann, 2018).

Melting and vaporization also occur to some fraction of the planetary surface material. When the energy and momentum from the impacting projectile are released, shock waves followed by decompression waves propagate further into the target, causing the target material to compress, heat, and accelerate downward and outward (e.g., Melosh, 2012). This marks the start of the excavation stage (Fig. 2.1c), where shock waves and decompression waves produce an excavation flow-field and generate an initial bowl-shaped transient crater cavity. The surface material within the excavation flow field is in motion and follows spiral paths away from the center (e.g., Spudis, 1993). This leads material beneath the impact point to be moved in a downward direction and material slightly away from this point to be driven downward and outward. Accordingly, the excavation flow-field trajectories cause surface material below a critical line to be displaced, while the material above this critical line is excavated ballistically beyond the transient cavity to form a crater's ejecta deposits (Fig. 2.2). The ejected material closest to the cavity center is excavated at high velocities and deposited at great distances from the impact crater.

In contrast, the surface material is excavated at lower velocities as the distance from the impact point increases. The slowly ejected material is deposited closest to the transient cavity rim and therefore forms large parts of a crater's proximal ejecta blanket (e.g., Spudis, 1993; Osinski et al., 2012). The displaced surface material that remains within the transient cavity as well as the target material below the transient crater experience various degrees of modification by shock waves. The material closest to the impact point experiences the highest degree of modification, resulting in complete melting or vaporization. With increasing distance from the point of impact, target rocks undergo less shock metamorphism as the shock wave's intensity decreases radially away from the impact location. These modifications range from partial melting to fracturing and brecciation of the target material (e.g., Spudis, 1993; Osinski et al., 2012). The excavation stage ends when the transient cavity reaches its maximum dimension. Depending on the target properties, crater size, and a planet's gravity, this process may last for seconds to several minutes (e.g., French, 1998).

During the following modification stage (Fig. 2.1d), target materials rise to compensate for the excavated mass, and the transient cavity collapses under the influence of a planet's gravity. This modification may last from several minutes to millions of years and depends on the gravity of the planetary body (e.g., Melosh, 1989), the properties of the target rock, and the size of the transient crater (e.g., Melosh & Ivanov, 1999). Compared to the contact and compression and excavation stages, the crater modification stage is less well understood, particularly for very large craters, where variations from simple bowl-shaped crater morphologies and other long-term effects occur (e.g., Melosh, 1989). In small craters, there is only minor modification by the uplift of target material and the slumping of material from the crater walls (e.g., Osinski & Pierazzo, 2012). Therefore, the dimensions of small craters approximately equal those of their transient cavities. Above a certain threshold, however, the transient cavity becomes more and more unstable, leading to a substantial modification of the cavity rim and a significant uplift of target material (e.g., Osinski & Pierazzo, 2012). The morphology of large craters, therefore, differs significantly from their transient cavities. Accordingly, the processes that induce an alteration of the transient cavity during the modification stage lead to the manifestation of simple and complex crater morphologies that change with increasing crater size (Fig.2.1e). The modification stage ends when significant motions of the target due to the impact event have ceased.

2.1.2. Crater Morphology

The crater formation characteristics lead to size-dependent crater morphologies with small simple and larger complex impact craters that can be observed on all terrestrial planets in the Solar System (e.g., Kenkmann et al., 2012). Since the initial formation of crater morphologies strongly depends on gravity (e.g., Melosh, 1989), the transition diameter between simple and complex impact craters varies among the planetary bodies in the Solar System. On Earth, for example (Fig. 2.3), the transition between simple and complex craters occurs at diameters between two and four kilometers, depending on the target material (e.g., Melosh, 1989; Osinski & Pierazzo, 2012). On Mercury, where gravity is about 1/3rd of the Earth's gravity, the transition occurs at about seven kilometers. On the Moon, where gravity is about 1/6th of Earth's gravity, the transition occurs between 10 and 20 km (e.g., Melosh, 1989). Because post-impact modification of impact craters is generally minimal on the Moon, the transition between simple and complex craters can be illustrated particularly well using lunar craters (Fig. 2.4.).

2.1.2.1. Simple Craters

Fresh simple craters have a bowl-shaped appearance with steep crater walls and an uplifted crater rim (e.g., Osinski & Pierazzo, 2012) (Fig. 2.4a). The uplift of the crater rim results from the outward and upward movements of the target

Figure 2.3: Barringer crater in Arizona is a well-preserved simple impact crater on Earth that is roughly 1.2 km in diameter and formed around 50000 years ago by an iron meteorite (Melosh, 1989). It is the first recognized impact crater on Earth (Chao et al., 1960) and with its steep walls and blocky rim, the morphology of Barringer crater is very similar to fresh simple craters on the Moon.

material during crater formation (Fig. 2.2). Although the extent of fresh simple craters is similar to their transient cavity, gravity-driven mass movements along the steep crater walls lead to a slightly shallower shape with depth to diameter (d/D) ratios of 1:4 to 1:7 (e.g., Melosh, 1989), compared to d/D ratio of transient cavities of 1:3 (e.g., Kenkmann et al., 2012). Bowl-shaped simple craters are a typical feature of a high-velocity impact. They have no lower size limit as such impact structures are also apparent in high-velocity micrometeorite impacts (e.g., Melosh, 1989). Slower projectiles, such as most secondary impactors, lead to different crater morphologies that are typically shallower and show less well-defined crater rims (e.g., Melosh, 1989).

2.1.2.2. Complex Craters

When a crater's size increases, the morphology of impact craters changes significantly, leading to complex craters. Complex craters show terraced crater walls, a flat interior floor, a shallower shape than simple craters with d/D ratios of 1:10 to 1:20 (e.g., Melosh, 1989), and a central uplift containing shocked and heavily deformed rocks (e.g., Kenkmann et al., 2012). As the morphology of the central uplift changes with increasing crater size, complex craters are typically classified into central peak and peak ring craters and multi-ring basins.

Essentially, when surface material is excavated during an impact event, it generates a negative mass that triggers an upwards movement of target material to compensate for the loss. In simple craters, the target material itself is strong enough to prevent this upward movement from significantly changing the transient cavity's morphology. However, when the transient cavity's size exceeds a critical point, the transient cavity collapses due to gravitational adjustment. This results in a substantial uplift of subsurface material, causing the uplifted rocks to reach the surface and push the cavity floor upward. This movement, where material from the depth

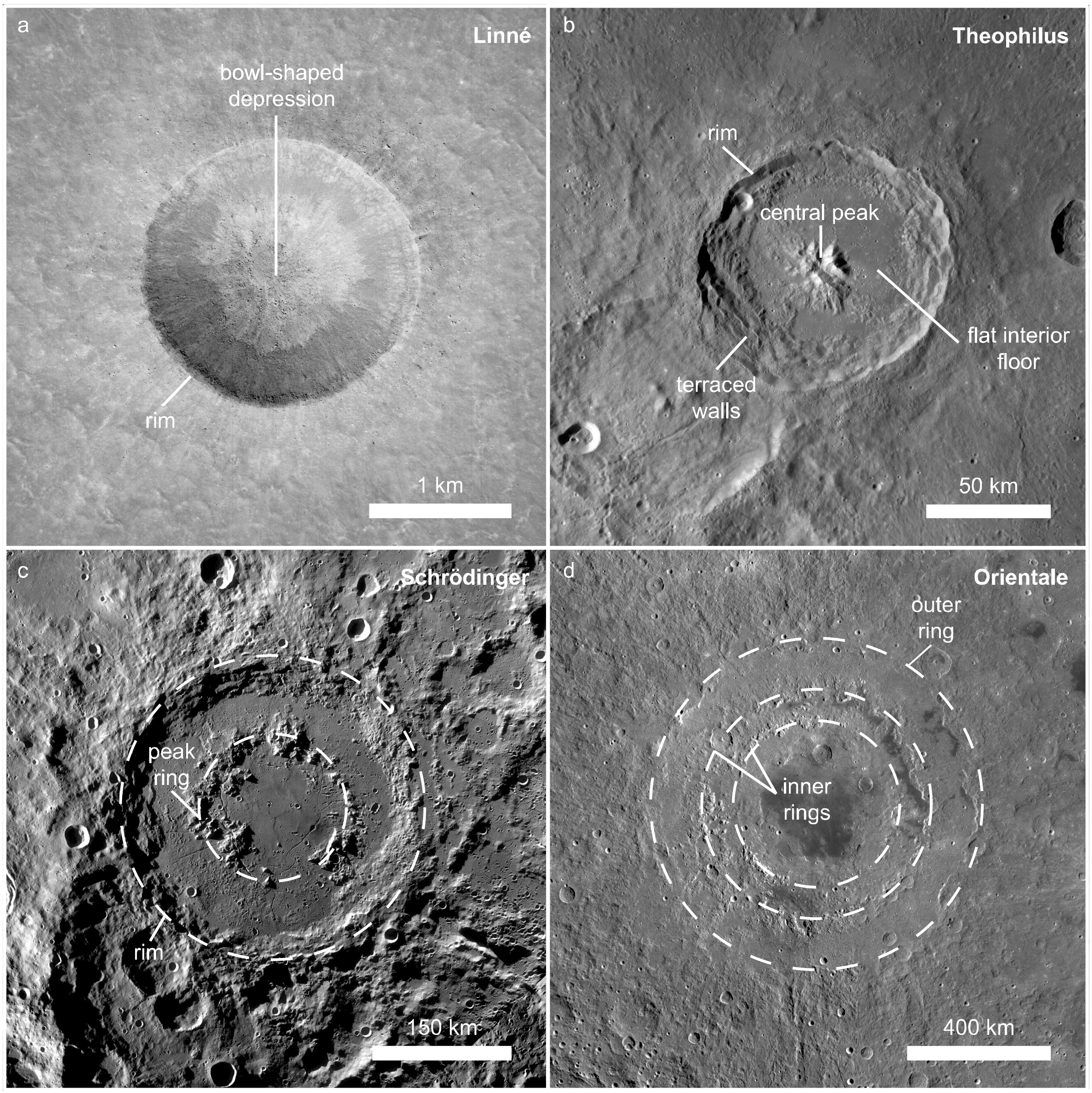

Figure 2.4: *Representation of size-dependent crater morphologies based on lunar craters. Since post-impact crater modification is minimal on the Moon, the progression from simple (a) and central peak craters (b) to peak ring (c) and multi-ring basins (d) can be well observed on the lunar surface.*

reaches the crater floor's surface, marks a complex crater's onset. At the same time, the rim of the transient cavity is stressed by the inward and upward movement of subsurface material below the central areas of the cavity and collapses, which leads to the formation of terraced crater walls (e.g., Osinski & Pierazzo, 2012 & Kenkmann et al., 2012) (Fig. 2.1d & e).

On the Moon, the transition between simple and complex craters occurs at diameters between 10 and 20 km (e.g., Melosh, 1989). The smallest complex craters show a single uplift or a cluster of uplifts in the center of the crater and are thus summarized as central peak craters (e.g., Osinski & Pierazzo, 2012) (Fig. 2.4b). With increasing crater size, the amount of uplifted subsurface material can become so large that it collapses under its weight, leading to an even more substantial modification of the transient cavity and the formation of ring-shaped uplifts that surround the crater center (e.g., Kenkmann et al., 2012). Such structures are called peak ring craters and occur on all terrestrial bodies as part of a gravity-induced change in crater morphology (e.g., Melosh, 1989). On the Moon, the transition from central peak to peak ring craters occurs at diameters around 140 km (Melosh, 1989).

As the size increases, impact structures are typically called impact basins. Traditionally, lunar craters larger than 300 km in diameter are referred to as basins (e.g., Wilhelms, 1987). Some large lunar basins and some large impact structures on other planetary bodies may exhibit a morphology that includes multiple rings, which are located inside and outside the final basin. Such structures are termed multi-ring basins (e.g., Spudis, 1993). Multi-ring basins contain either a few inward-facing scarps with smooth outward-facing slopes (e.g., Orientale basin on the Moon) or numerous closely spaced scarps (e.g., Valhalla crater on Callisto) (e.g., Osinski & Pierazzo, 2012). The formation of multi-ring basins is less well understood since not all large basins on terrestrial planets show multiple rings. Also, the transition from peak ring to multi-ring basins appears to be independent of gravitational acceleration (Melosh, 1989). Prominent multi-ring basins have been observed on the Moon and some of Jupiter's and Saturn's Moons, and several mechanisms have been proposed to describe their formation (e.g., Melosh, 1989). However, there is currently no scientific consensus about their formation (e.g., Potter, 2015). One of the reasons for this is that it is not clear whether the creation of large basins automatically initiates the formation of multiple rings. Furthermore, the determination of the basin diameter from topographic features may be ambiguous as rings may not be circular and knowledge about the basin rim's erosion may be missing (Melosh, 1989).

2.1.3. Ejected Material

Impact craters on all terrestrial bodies are typically surrounded by a layer of debris ejected from the upper third of the transient cavity during the impact event (Fig. 2.5a) (Stöffler et al., 1975). When the surface material is excavated, it follows a near parabolic trajectory and falls back at the same velocity that it was ejected (e.g., Melosh, 1989). Although the ejection velocity increases with increasing crater diameter, most of the excavated material in the inner Solar System typically remains on the planetary body (e.g., Melosh, 1989) to form a crater's ejecta. The ejecta contains broken rock fragments of all sizes. Due to a lower ejection velocity, the amount of large fragments generally decreases with increasing distance from the crater rim (Melosh, 1989). Therefore, blocks of large rocks are a common feature around fresh craters' rims (Fig. 2.3 & 2.4a).

The ejected material commonly forms a continuous deposit around the crater rim, termed proximal ejecta blanket (Fig. 2.5b). It is evident around fresh craters, thickest at the rim, and continuously thins with increasing distance from the crater (McGetchin et al. 1973; Fassett et al. 2011a). The proximal ejecta's emplacement causes a near-complete blanketing of the pre-existing topography, particularly in areas where the deposits are thickest. However, the range at which proximal ejecta blankets significantly affect the burial of the pre-existing landscape is challenging to identify. For example, the effects of proximal ejecta blanketing can be investigated at distances ranging from one crater radius beyond the rim, where about 50 % of the ejected material is deposited, to five crater radii beyond the rim, where about 90 % of the ejected material is

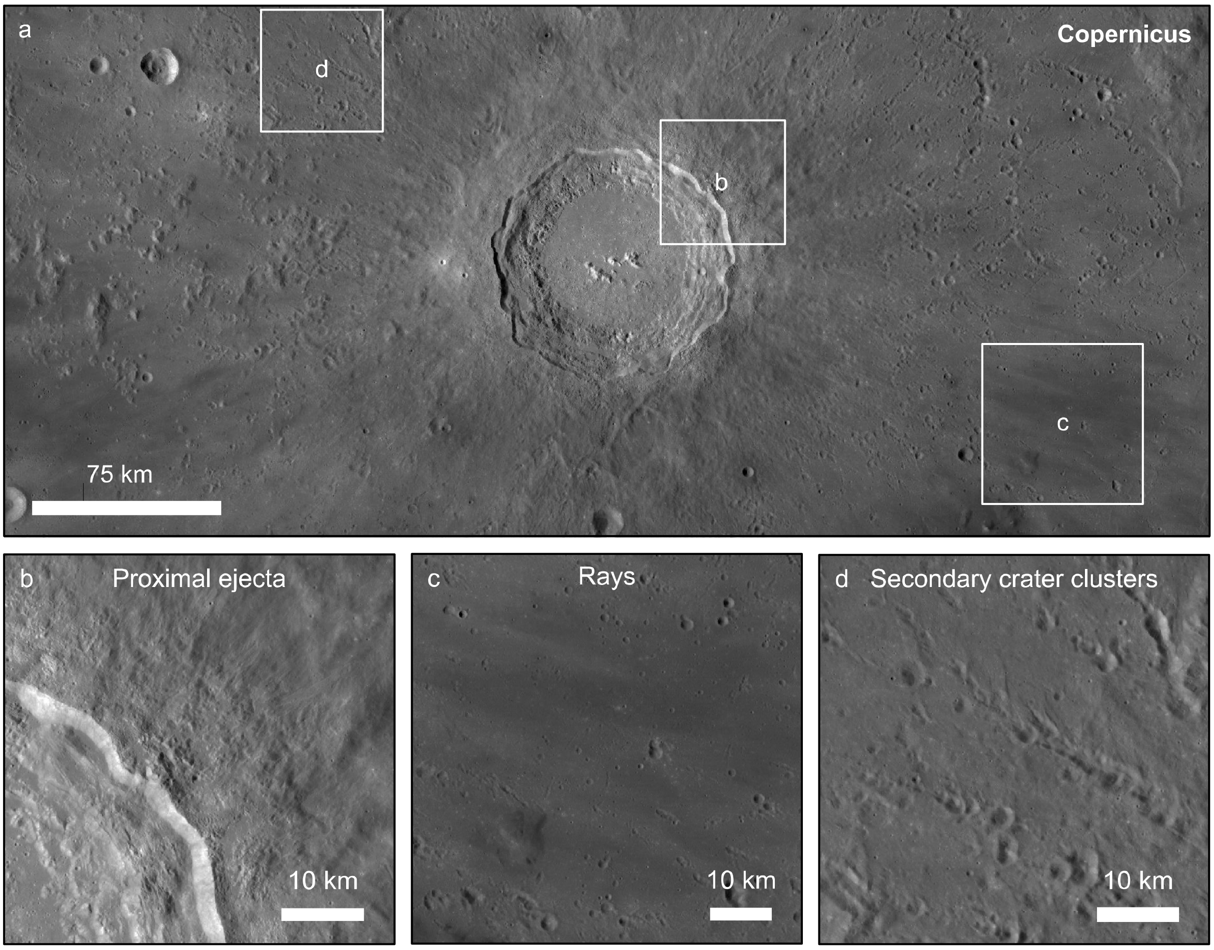

Figure 2.5: *Features formed by ejected material in the vicinity of lunar Copernicus crater (a). Features such as proximal ejecta (b), secondary crater clusters (c), and rays (d) are easily recognizable due to minor post-impact modification of the terrain.*

deposited (Melosh, 1989). However, the proximal ejecta is often referred to as the area in which a continuous ejecta blanket can clearly be identified. Such continuous blankets often have an extent of roughly one crater radius (Pierazzo & Melosh, 2012). In complex craters, proximal ejecta blankets may also be found on terraced walls due to the slumping of the cavity rim after the ejecta was emplaced (Osinski & Pierazzo, 2012).

Further away from a crater's rim, the ejected material is deposited in discontinuous, thin layers that form irregular patches or rays (e.g., Elliott et al., 2018) of highly shocked fine-grained material and larger pieces of rock (e.g., French, 1998; Pierazzo & Melosh, 2012). Such distal ejecta deposits can be found at great distances from the actual impact crater since the deposited material is excavated at high ejection velocities from the impact site (e.g., Melosh, 1989). The deposition of distal ejecta also modifies a planetary body's topography by ballistic sedimentation (Chapter 7) and secondary cratering (Fig. 2.5c) (e.g., Minton et al., 2019). Secondary cratering occurs when excavated rocks from a cosmic impact are large and fast enough to produce impact craters themselves. Such projectiles typically travel with distal ejecta deposits and commonly form clusters or linear chains of secondary craters (Fig. 2.5d). Therefore, secondary craters are often distinguished by their shallower depth and their occurrence in crater clusters (e.g., Melosh, 1989). However, some secondary projectiles may generate bowl-shaped impact craters that do not necessarily appear in crater clusters, particularly those exceeding an absolute excavation velocity (e.g., Melosh, 1989). Therefore, it may not be easy to unambiguously distinguish between primary and secondary impacts on a planetary surface.

2.2. Crater Populations

By analyzing crater populations on planetary surfaces, it is possible to interpret the bombardment history and the geologic evolution of planetary bodies in the Solar System. On bodies with no atmosphere and limited geologic activity, such as the Moon, the surface evolution is primarily controlled by impact cratering. Accordingly, extended areas of high crater density shape the lunar landscape. In regions where volcanic activity erased large numbers of lunar craters, the number of impact craters is correspondingly lower. On other planetary bodies, geologic processes such as tectonics or erosion contribute to differently cratered landscapes. On Earth, for example, the surface modification occurs at a much faster rate, and compared to other bodies in the inner Solar System, the number of impact craters is relatively low. Therefore, the analysis of crater populations on planetary surfaces can reveal information about their geologic history.

2.2.1. Representations

The analysis of crater populations requires some form of quantification to make observations comparable. Since craters occur in various sizes, the primary information about a crater population is the density of impact craters (often termed as the frequency of impact craters) as a function of crater diameter. For a particular size-range, these frequencies can be described by

$$n[D_{\min}, D_{\max}] = \frac{c}{A},$$

where c is the number of craters in a diameter range from $D_{\min}$ to $D_{\max}$ within area A. The estimated error is given by

$$\pm\sigma = \pm\sqrt{c}\,.$$

There are three standard techniques to display this information in the form of crater size-frequency distribution (CSFD) plots: differential, incremental, cumulative, and relative plots (R-plots). Each plot is a log-log representation of crater diameters on the x-axis and a crater density measure on the y-axis. The techniques differ in terms of the density metric and come with individual advantages and disadvantages (for details, see e.g. Crater Analysis Techniques Working Group, 1979; Melosh, 1989; Stöffler, 2006; Michael, 2013; Fassett, 2016).

The basic principle of the differential technique is to plot the number of craters per unit area within a series of chosen diameter ranges (bins) between $D_{\min}$ and $D_{\max}$. Here, the differential frequency at the mean bin center D_c is given by

$$N_{\mathrm{Diff}}(D_c) = \frac{n[D_{\min}, D_{\max}]}{(D_{\max} - D_{\min})}$$

and the error is estimated from

$$\pm\sigma = N_{\mathrm{Diff}} \pm \frac{N_{\mathrm{Diff}}}{\sqrt{c}}.$$

With the differential approach, the points plotted are independent of each other. This indicates that certain events that depend on the crater size (e.g., resurfacing) are easy to identify. A disadvantage of this technique is that the representation of the crater population strongly depends on the chosen bin interval between $D_{\min}$ and $D_{\max}$. Often, researchers choose a size-dependent approach, such as root-two binning, where $D_{\max} = \sqrt{2}D_{\min}$. However, since there is no optimal binning strategy, the differential technique is prone to biases.

The incremental plotting technique is closely related to the differential approach. It uses a root-two binning to normalize the interval between craters and excludes the diameter range division when calculating crater frequencies. The incremental frequency for a population with $D_c = \sqrt[4]{2}D_{\min}$ is determined by

$$N_{\mathrm{Incr}}(D_c) = n\left[D_{\min}, \sqrt{2}D_{\min}\right].$$

Although the incremental technique removes biases from the differential approach by applying a prescribed binning, it uses a subjective starting diameter. Therefore, the method remains prone to biases due to the selected binning procedure.

The cumulative plot, on the other hand, is independent of bin size. It shows the density of craters ≥ D as a function of crater diameter:

$$N_{\mathrm{Cum}}(D_{i_c}) = \sum_{K=1}^{i} n_K\left[D_{i_{\min}}, D_{i_{\max}}\right],$$

where the error is estimated by

$$\pm\sigma = \frac{\sum_{K=1}^{i} c_K \pm \sqrt{\sum_{K=1}^{i} c_K}}{A}.$$

With the cumulative representation, it is possible to display the data unbinned ($D_{\min} = D_{\max}$) and plot a point for each crater. Therefore, there is no loss of information through the applied binning technique. However, although the representation is independent of bin size, the crater frequencies are not independent of each other. Small craters receive a pronounced emphasis as they inherit weight from all larger impact craters. This makes it more challenging to recognize diameter-dependent processes from the plotted data.

R-Plots, in turn, emphasize variations in crater populations. This technique transforms differential frequencies by removing the power-law trend from the data. Here, the differential frequencies are divided by D_c^{-3}:

$$N_{\mathrm{R}}(D_c) = \frac{n[D_{\min}, D_{\max}]}{((D_{\max} - D_{\min})D_c^{-3}}.$$

The Error is given by

$$\pm\sigma = N_{\mathrm{R}} \pm \frac{N_{\mathrm{R}}}{\sqrt{c}}.$$

The R-plot shows differential slopes of -3 (cumulative -2) in the CSFD as a horizontal line, whereas slopes of -2 (cumulative -1) are rotated 45° to the left. This makes it easy to identify size-dependent variations in the crater populations based on frequently occurring changes in the CSFD slope. However, the same binning biases as in the differential plotting technique apply to the R representation.

Figure 2.6 demonstrates how a crater population is represented in differential, cumulative, and R form. The population is located on the remnants of the lunar Nectaris basin and was identified by Fassett et al. (2012) and Orgel et al. (2018) (Fig. 2.6a). Crater frequencies were obtained using traditional crater counting (Chapter 5) and are displayed in root-two-spaced bins (Fig. 2.6b). The differential and cumulative representations show the obtained CSFD as a steeply sloped distribution. In the differential plot, the CSFD appears less steep than the cumulative representation. R-values for larger craters are moderately sloped in the relative representation but decrease significantly for smaller craters. This decrease appears to deviate from the rest of the CSFD. Such differences often indicate a geologic, human, or data-related influence on the given crater population. In this case, the anomaly is clearly visible in the differential and relative plots

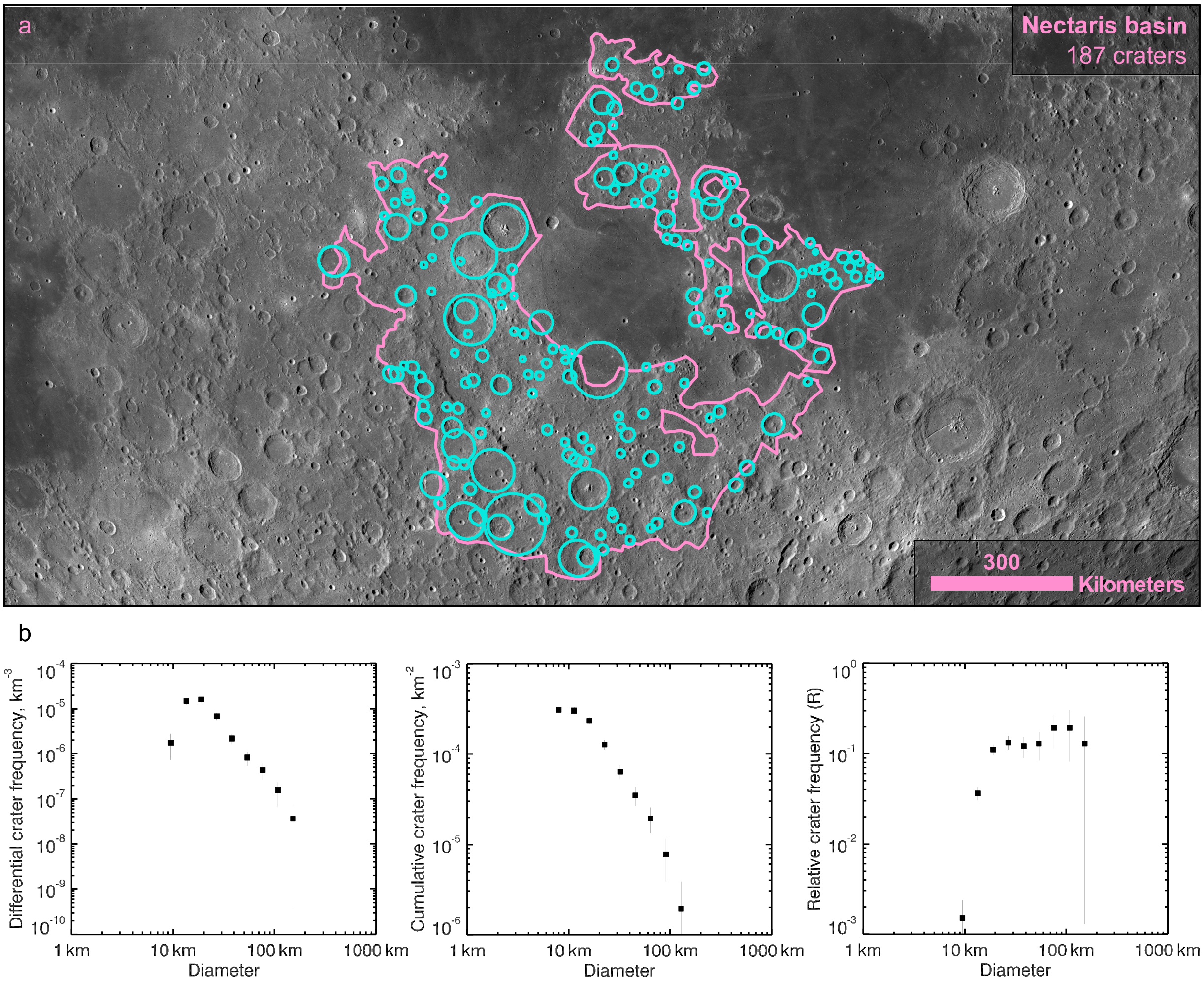

Figure 2.6: *Impact craters (cyan) measured on the remnants of the lunar Nectaris basin (pink) by Fassett et al. (2012) and Orgel et al. (2018) (a) and obtained CSFDs in differential, cumulative, and R-plots (b).*

but less easily identified in the cumulative representation. This shows that in the cumulative plot, size-dependent differences in the crater population may be more difficult to recognize due to the inherited weight from all larger impact craters, while size-dependent differences are strongly emphasized in the R-plot.

2.2.2. Analyzing Crater Populations

The obtained CSFDs of planetary surface units can reveal planetary chronologies (e.g., Öpik, 1960; Neukum, 1983; Melosh, 1989; Neukum & Invanov, 1994). If we assume that impact cratering is a spatially random process and that the cratering rate is fairly the same across a planetary body, then differences in crater densities can be used to measure surface age. For example, take a one-time geologic process on a planetary surface that locally erases all pre-existing craters, such as a lava flow. The young lava flow unit will start with no superposed impact craters. As the surface unit is exposed to impact cratering, it will accumulate craters over time. However, the accumulated crater population density on the lava flow unit will (in most cases) be lower than the surrounding terrain's crater density. Therefore, the basic hypothesis of using impact craters as a measure of surface age is that older terrains show higher crater densities than younger terrains.

Interpreting surface ages from measured CSFDs requires a model that describes how fast craters of a given size are produced. This includes (1) information about the impact-forming population (crater production) and (2) the rate of crater production over time (crater chronology). Accordingly, models that translate measured CSFDs to surface ages use two functions: the crater production function and the crater chronology function. If a planetary body's crater chronology is uncertain, relative surface ages can still be assessed from crater densities based on the above hypothesis. Since the crater population and chronology are best observed on the Moon, such models mainly use the lunar record as a reference for deriving surface ages.

2.2.2.1. Production Function

The production function approximates the relative crater formation rate on a planetary body as a function of diameter. It describes the inferred crater production population and can be used to investigate the evolution of crater populations on planetary surfaces. Production functions are often derived from measuring CSFDs on planetary surfaces (e.g., Neukum, 1983; Neukum & Invanov, 1994) but have also been determined from collision models (e.g., Marchi et al., 2009; Le Feuvre & Wieczorek, 2011). Here, the lunar production function is described based on the observations by Neukum (1983), who used CSFD measurements on the lunar surface to derive the lunar crater population.

The production function by Neukum (1983) describes the lunar crater population in the form of a polynomial function. Neukum (1983) argues that individual surface units on the Moon represent the sections of the lunar impact crater population at different accuracy. Younger units better represent the unmodified population of small craters, whereas older units better represent the population of large craters. Therefore, the production function was derived from CSFD measurements on different lunar surface units (Fig. 2.8a). The cumulative crater frequencies were normalized and fitted by a polynomial of 11th degree in the form

$$N_{\mathrm{Cum}}(D) = \log \frac{N(>D)}{\mathrm{km}^2} = a_0 + \sum_{j=1}^{11} a_j [\log D]^j ,$$

with coefficients given in Table 2.1. The production function by Neukum (1983) describes the relative rate of crater formation in a cumulative representation and is valid for impact craters ranging from 10 m to 300 km in diameter. Depending on the crater density (surface age), the production function can be shifted in the $\log \frac{N>D}{km^2}$ direction (Fig. 2.7a). Thus, coefficient a_0 is time-dependent and can be obtained by fitting an observed CSFD to the production function. In Table 2.1, a_0 is given for an arbitrary surface age of 1 Ga.

Coefficient	Value
a_0	-3.0768
a_1	-3.6269
a_2	0.4366
a_3	0.7935
a_4	0.0865
a_5	-0.2649
a_6	-0.0664
a_7	0.0379
a_8	0.0106
a_9	-0.0022
a_{10}	-0.000518
a_{11}	0.0000397

Table 2.1: *The coefficients for the lunar production function by Neukum (1983).*

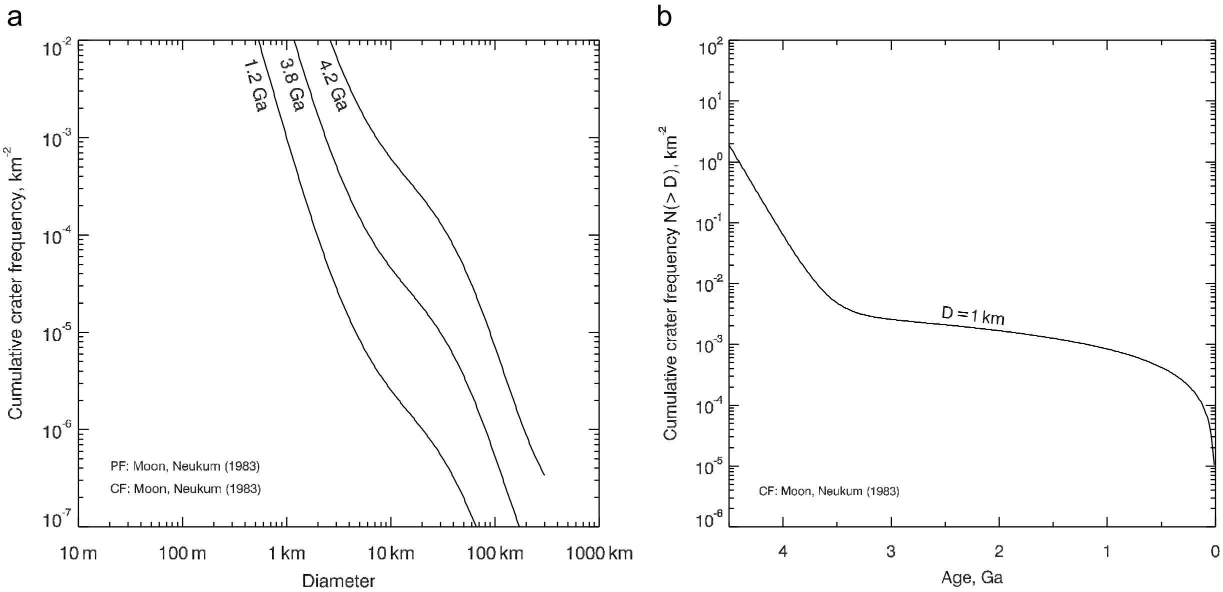

Figure 2.7: *Isochrones of the Neukum (1983) lunar production function (a) and chronology function (b). The lunar production function's isochrones show the expected size-frequency distribution of impact craters after a lunar surface unit has been exposed to impact cratering for 1.2, 3.8, and 4.2 Ga, according to the Neukum (1983) lunar chronology model. The chronology function shows the formation rate of craters with* $D > 1$ *km as a function of surface age.*

Fig. 2.7a shows isochrones of the lunar production function by Neukum (1983) for different crater densities (shifted along the y-axis). The lunar production function has a complex structure with several sections showing slopes in the form of $N_{\text{Cum}}(D) \propto D^b$ with b ranging from about -1 to -4 in the cumulative representation (Fig. 2.7a). The changes in slope occur as a function of diameter and show that, for example, small craters form more frequently than large craters on the lunar surface. By fitting the production function to an observed CSFD, it is possible to compare the frequencies of crater populations in different diameter ranges and calculate relative surface ages. To calculate absolute surface ages, the cumulative crater frequencies need to be referred to a function of crater chronology.

2.2.2.2. Chronology Function

The chronology function shows the rate of produced craters $N_{\text{Cum}}(D)$ as a function of surface age. It reflects the hypothesis that crater densities can be related to an absolute surface age. Its calibration is based on the radiometric ages of lunar rock samples collected by the Apollo and Luna missions in the 1960s and 1970s. Depending on the method, the ages derived from radioisotopic dating correspond to a rock's crystallization age, the timing of impact melt formation, or the time a rock has been exposed to cosmic rays (e.g., Stöffler, 2006; Kelley & Sherlock, 2012). In any case, it is assumed that the radiometric age corresponds to the time the underlying geologic unit was formed. Although the approach of correlating radiometric ages to crater densities comes with a certain ambiguity (e.g., Neukum, 1983 & Deutsch & Schärer, 1994), there is a general consistency between the obtained radiometric ages of lunar rocks and the density of craters they were deduced to have derived from (e.g., Neukum et al., 2001a; Stöffler, 2006; Fassett, 2016) (see. Fig. 2.8b).

This consistency between sample ages and crater densities allows constraining the lunar chronology function (e.g., Neukum, 1983). The

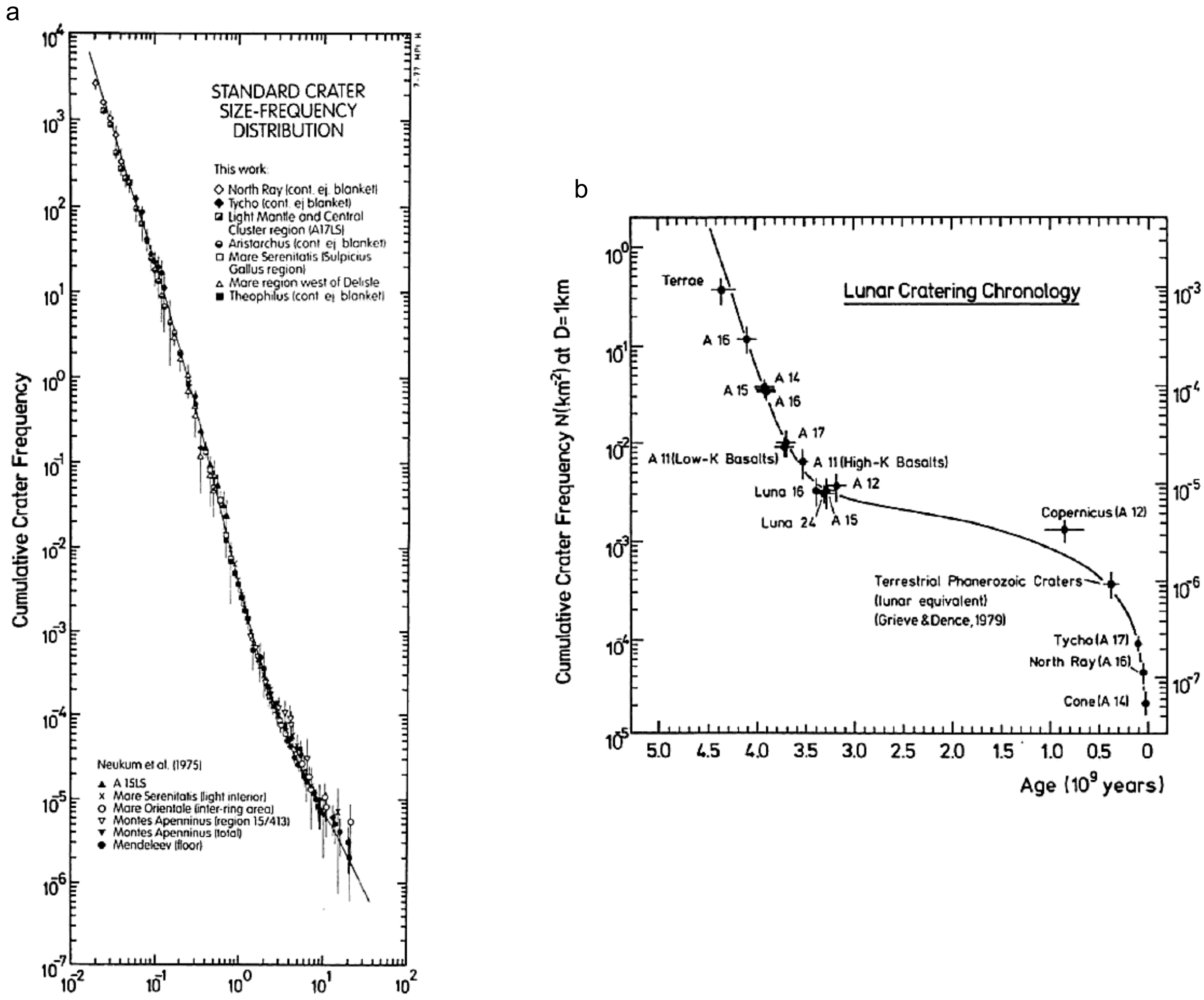

Figure 2.8: *Production function by Neukum (1975) showing normalized crater densities from various count areas to fit a polynomial function (a) (modified from König, 1977). The lunar chronology function (b) (taken from Neukum, 1983) shows calibration points where crater densities and radiometric ages were correlated.*

function refers to a reference diameter that correlates to the inferred crater production rate (the production function), where the cumulative frequency for craters with $D > 1$ km is often given as a reference (Fig. 2.7b). For a reference diameter of 1 km, the lunar chronology function by Neukum (1983) is described as

$$N(D \geq 1\text{km}) = 5.44 * 10^{-14}[e^{6.93T} - 1] + 8.38 * 10^{-4}T\,,$$

where T is the crater accumulation time.

This dependence allows for the determination of absolute model ages for any surface on the Moon based on crater densities from imaging data. Since the chronology function depends on crater densities from the crater production rate, the chronology function can be easily transferred to other planetary bodies (e.g., Neukum, 1983). Therefore, the crater production functions of other planetary bodies and the radiometric ages of lunar rock samples can be used to study the planetary surface evolution in the inner Solar System. Although additional anchor points in the chronology function would give further implications on whether lunar sample ages can be unambiguously related to crater densities, the analysis of crater densities is currently the only known approach to date planetary surfaces remotely. Recently, the Chang'E-5 mission (Zhao et al., 2017) returned rocks from young lunar mare units, which will soon give new insights on the refinement of the crater chronology curve.

2.2.2.3. Limitations

The determination of surface ages from production and chronology function is a straightforward approach. However, the technique comes with certain limitations. In general, the inferred size-frequency distribution of the primary crater population is theoretical since the production function neglects the influence of crater degradation processes. Although Neukum (1983) and other authors emphasize the importance of an unsaturated primary crater population to constrain a production population, the influence of crater saturation, crater erasure, and secondary impacts (Chapter 2.3) on the production function is debated (e.g., Xiao & Strom, 2012; Fassett, 2016; Xiao, 2018). Even when paying particular attention to possible contaminations, measured crater frequencies can be influenced by subjectivity and data-related factors (Robbins et al., 2014).

Furthermore, the radiometric ages of lunar samples may be difficult to interpret. There are various dating techniques available, each responding to individual sensitivity (e.g., Carlson, 2011). Approaches that rely on the rock's crystallization age or the cooling of impact melt measure the isotopic decay of naturally occurring elements (e.g., Kelley & Sherlock, 2012). This radiometric clock is typically reset when the heat that is induced to the rock passes a certain threshold. For example, the U-Pb system needs a higher temperature to be reset than the K-Ar system (e.g., Carlson, 2011). Consequently, applying different techniques to various rocks at the respective sampling sites naturally reveals several different radiometric ages (e.g., Stöffler, 2006; Snape et al., 2016a) and may therefore raise doubt about the precise event that reset the radiometric clock and whether that event is related to the formation of the underlying geologic unit. Effects such as material transport (Huang et al., 2017; Liu et al., 2020) or a sampling bias due to the overprint of subsequent impact events (Michael et al., 2018; Liu et al., 2020) accompany the scientific discussions. As a compromise, Neukum (1983) considered the sample age with the maximum number of occurrences to correspond to the underlying geologic unit's formation age. Although this solution may seem arbitrary, the correlation between crater densities and sample ages supports the hypothesis that crater densities increase with advancing surface age, making planetary surface dating from crater densities a convenient technique to study a planet's stratigraphy. Nevertheless, the lunar chronology curve needs further refinement and absolute model ages should be viewed cautiously. However, relative surface ages from crater densities can usually be obtained with less ambiguity

2.2.3. Bombardment Scenarios

For decades, the ambiguous conclusions from dating lunar rocks together with the limited number of samples allowed for numerous interpretations and passionate discussions about the rate and population of inner Solar System impactors. In general, investigations on crater densities and the ages of rock samples infer that the impact rate was significantly higher before ~4 Ga than today (e.g., Hartmann, 1972). However, several scenarios concerning variations in the impact flux are debated in the scientific community. Tera et al. (1974) concluded from the radiometric ages of lunar samples that most rocks

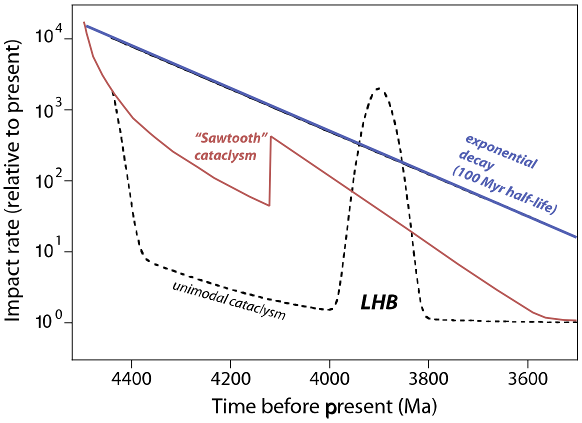

Figure 2.9: *Representation of various impact flux scenarios during the LHB period. The scenarios include an exponential decay in impact rate (e.g., Neukum, 1983), a spike in impact rate that describes the earliest LHB scenario (Tera et al., 1974; Ryder, 1990), and the Sawtooth Cataclysm model by Morbidelli et al. (2012). Figure modified after Hopkins and Mojzsis (2015).*

experienced recrystallization around 3.9 Ga. They attributed this signature to an effect by the Imbrium impact event or a spike in impactor rate during that time. The latter scenario became known as the Late Heavy Bombardment (LHB), during which the impact rate in the inner Solar System strongly increased over a short amount of time compared to the preceding cratering rate. This scenario was initially supported by radiometric evidence (e.g., Ryder, 1990) and later endorsed by modeling Solar System dynamics. For example, Gomes et al. (2005) proposed that the migration of Jupiter and Saturn in the early Solar System could induce the delivery of outer Solar System objects to the inner Solar System, which causes a spike in the impact rate. This model was termed the Nice model and has seen some modifications as the scenario of planetary instability due to gravitational changes in the early Solar System has experienced further extensions. For example, Bottke et al. (2012) suggested that Jupiter and Saturn's migration could also cause certain populations in the asteroid belt to become unstable, which would inject additional projectiles into the inner Solar System during the LHB. Another model that proposes a significant change in the impact rate during this period includes the Sawtooth Cataclysm model (Morbidelli et al., 2012), suggesting a less pronounced spike in impact rate than the LHB scenario and an overall decrease in impact flux (Fig. 2.9).

Regarding the population that dominates impacts in the inner Solar System, scientists generally presume that most projectiles origin from the Asteroid Belt between Mars and Jupiter (e.g., Neukum et al., 2001a). However, when dynamicists suggested different origins of impactor populations due to gravitational instability during the LHB, the size-frequency distribution of these projectiles was studied concerning the LHB scenario. Investigations by Strom et al. (2005, 2015) indicate that the CSFD of impact craters on the oldest terrains of Mars, Mercury, and the Moon deviate from younger units. Since the oldest surface units on these bodies formed before 3 Ga (e.g., Werner, 2014), Strom et al. (2005, 2015), Fassett et al. (2012), and Marchi et al. (2012) propose that the change in CSFDs could be associated with the LHB. Such a change would imply a transition in the size-frequency distribution of impacting projectiles during the LHB and therefore contradict a constant production function, as suggested by, e.g., Neukum (1983). Therefore, one could argue that the normalization of crater frequencies to infer a crater production population (e.g., Neukum, 1983; Neukum & Ivanov, 1994) is biased, as it a priori assumes a stable production function and, therefore, a constant size-frequency distribution of impactors (Strom et al., 1992).

Accordingly, it was debated whether the change in the CSFD on old terrains indicates a change in the crater production population or is related to geologic effects. For example, Kneissl et al. (2016) show that by considering the effects of geometric crater obliteration (sometimes referred to as cookie cutting – see Chapters 2.3 and 7), the obtained crater frequencies better represent a continuous crater production function. Since this obliteration effect becomes more pronounced with ongoing crater accumulation, they termed this effect to result from non-sparse cratering. Thus, the deviation of obtained CSFDs from a constant crater production function would occur as a natural result of impact cratering that becomes noticeable on old terrains with limited geologic activity. This could imply that no significant change in the impactor size-frequency distribution occurred during the LHB period. The observations by Kneissl et al. (2016) therefore question the hypothesis that different impactor populations were injected into the inner Solar System due to gravitational instability.

Similarly, the interpretation that the radiometric ages of lunar rocks indicate an impact spike around 3.9 Ga (e.g., Tera et al., 1974; Ryder, 1990) has been re-assessed. Since the earlier dating in the 1970s, sampling techniques have advanced and additional lunar rock samples were dated. Numerous authors suggested that a sample bias caused the apparent clustering of sample ages around 3.9 Ga. This bias is caused due to the 40Ar-39Ar technique, which is sensitive to reset by impact-induced events (McDougall & Harrison, 1999; Boehnke & Harrison, 2016), and the sample locations on the Moon, which are sensitive to modification by subsequent impact events (Michael et al., 2018; Hartmann, 2019). It was found that the spike in sample ages does not occur in lunar rocks that origin far from the Apollo landing sites (Cohen et al., 2000). Also, further radioisotopic dating using, for example, the U-Pb technique revealed that multiple large impacts occurred long before 3.9 Ga (e.g., Norman & Nemchin, 2014). Both findings suggest that early studies on lunar rock samples show the signature of a subsequent impact event instead of an atypical increase in impactor flux.

With advanced research on this topic, the term LHB adapted different meanings. While it was initially used to describe a short spike in impact rate (e.g., Tera et al., 1974; Ryder, 1990), it was later applied to characterize a prolonged change in impactor flux over several hundred million years (e.g., Bottke & Norman, 2017) and may also be used to outline the general decrease in impact rate in the inner Solar System before 3.8 Ga (e.g., Claeys & Morbidelli, 2015). Although most recent publications (summarized by Hartmann, 2019) on the topics of dating lunar rock samples and CSFD measurements argue in favor of a constant decrease in impact rate before 3 Ga and a constant crater production population, the scientific debate is ongoing. Several open questions remain as the impact flux is poorly constrained and interpretations of planetary chronology are subject to various contamination sources.

2.3. Contamination of the Primary Impactor Record

To correlate CSFDs with surface ages, the cratering record must reflect the impacting population as accurately as possible. However, as impact craters are erased by various processes, the connection from the cratering record to the impacting population is not necessarily direct. Endogenic geologic processes such as erosion and deposition can make the analysis of CSFDs challenging. On Mars, for example, various surface processes erased a substantial part of its impact crater record. On planetary bodies with no atmosphere, such as the Moon, Mercury, and Ceres, a substantial contribution to crater erasure comes from impact cratering itself. Here, fresh impact craters and their excavated material can

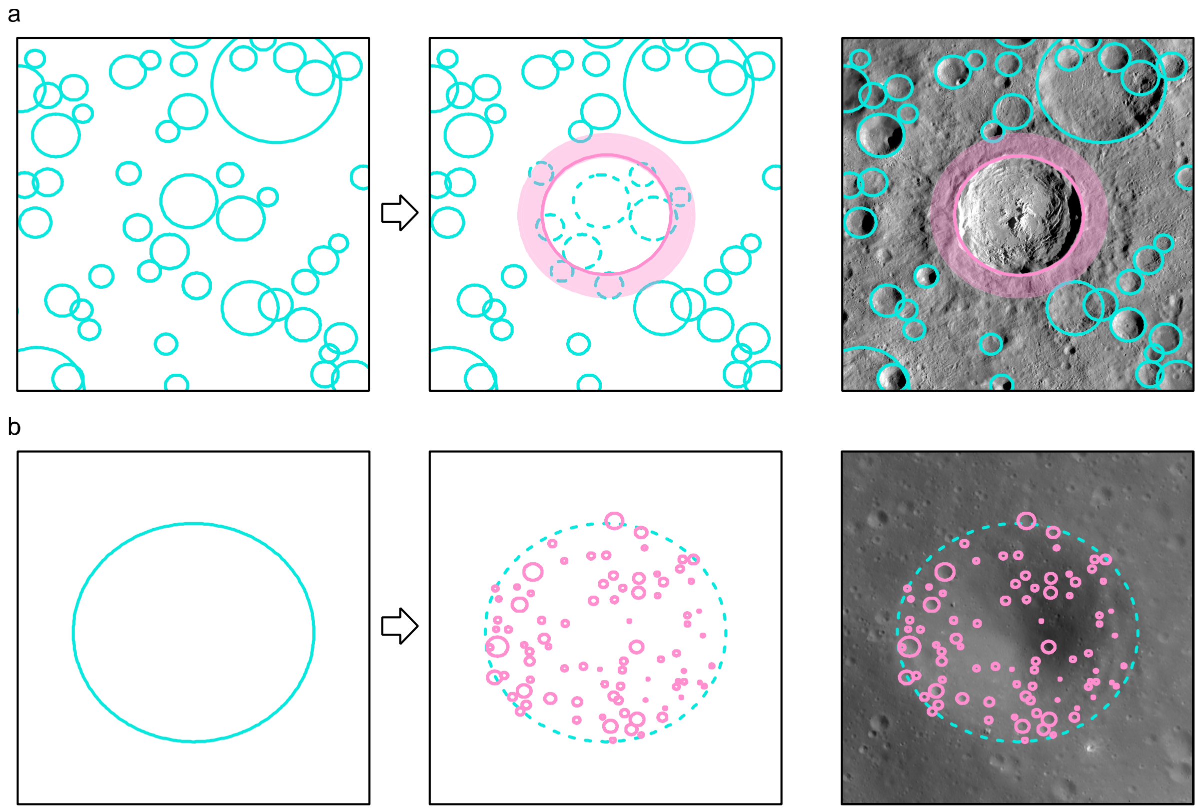

Figure 2.10: Schematic representation of crater degradation processes with fresh craters shown in pink and pre-existing craters shown in cyan. Crater obliteration by cookie cutting and proximal ejecta blanketing (a) buries pre-existing craters of smaller size. During sandblasting (b), smaller projectiles induce mass wasting on a larger craters' rim, which slowly degrades the crater's topography.

erase or degrade pre-existing craters. The excavated material of a primary impact may also contaminate the cratering record by adding secondary impacts. In contrast to contamination by primary impacts, the most noticeable contamination from secondary impacts is not due to crater erasure but the addition of craters to the observable cratering record.

2.3.1. Contamination by Primary and Secondary Impactors

Primary impacts contribute to crater erasure through degradation from downslope diffusion (also referred to as sandblasting), proximal ejecta blanketing, and geometric crater obliteration (also referred to as cookie cutting) (Fig. 2.10). Cookie cutting occurs when a large impact overlaps smaller pre-existing craters. The process erases pre-existing craters that fall completely inside the fresh crater's cavity and is thus entirely dependent on crater size. Cookie cutting is primarily a geometric process, where large craters erase smaller craters (e.g., Richardson, 2009; Minton et al., 2015).

Like cookie cutting, the proximal ejecta blanket (ejected at low velocity) covers pre-existing craters outside the fresh crater's rim. The magnitude to which proximal ejecta blankets degrade pre-existing craters depends on the pre-existing craters' size and distance to the fresh crater's rim. Since the thickness of proximal ejecta blankets decreases with increasing distance to the crater rim, proximal ejecta blanketing can contribute to crater erasure by the partial or complete burial of pre-existing craters (e.g., Fassett et al., 2011a; Hirabayashi et al., 2017).

Sandblasting describes the slope-dependent mass transport of surface material that slowly fills craters over time. The process is caused by small primary or secondary projectiles that induce material from the crater walls and infill the crater. In contrast to cookie cutting, sandblasting is primarily a three-dimensional effect in which small craters gradually erase large craters (diffusive degradation) (e.g., Soderblom, 1970; Minton et al., 2019).

Secondary impacts contribute to the cratering record's contamination by adding additional impact craters. Although most secondary craters occur in clusters or chains near the corresponding primary craters and exhibit shallow d/D ratios, they may be challenging to identify. Secondary projectiles that exceed a certain excavation velocity may also impact at great distances and form craters that show the morphology of primary impacts. In this case, identifying secondary craters is hardly possible. Thus, the influence of such background secondaries on crater populations and the determination of crater production functions have long been debated (e.g., Neukum & Ivanov, 1994; McEwen & Bierhaus, 2006; Hartmann, 2007; Xiao and Strom, 2012; Xie et al., 2017; Xiao, 2018).

2.3.2. Effects of Contamination on the CSFD

Since the CSFD only provides valid information about a geologic unit's bombardment history when it reflects the primary impactor population, knowledge about the contamination from impact cratering is crucial for analyzing crater populations. The contamination by cookie cutting, proximal ejecta blanketing, sandblasting, and secondary cratering affects the CSFD differently. With continuous bombardment, crater removal by cookie cutting, proximal ejecta blanketing, and sandblasting eventually leads to a state, in which on average, a fresh impact removes a pre-existing crater of the same size. This state is called crater equilibrium and has often been investigated for small, simple craters on the Moon with $D < 1$ km (e.g., Neukum & Ivanov, 1994; Xiao & Werner, 2015). Here, the density of craters smaller than a certain diameter (equilibrium onset) does not increase and the cumulative CSFD of small, simple craters in equilibrium follows a constant slope of $N_{\mathrm{Cum}}(D) \propto D^b$ with $b \sim -2$ (Fig. 2.11a). The information about the primary population are lost in this equilibrium scenario and with ongoing impact cratering, the equilibrium onset occurs at a constantly increasing diameter.

Since crater equilibrium is associated with a stable number of craters per unit area, it is often correlated to a distinct geometric configuration of impact craters. To that end, the spatial density of crater populations in equilibrium is often represented as a fraction of a maximum possible crater configuration, termed geometric saturation. The maximum possible configuration of impact craters (100 % geometric saturation) is a theoretical concept that describes a population in which crater geometries are aligned in a rim-to-rim configuration (Gault, 1970). Investigations of lunar crater populations suggest that crater equilibrium for small, simple craters occurs at 1-10 % of geometric saturation (e.g., Gault, 1970; Xiao & Werner, 2015). However, crater equilibrium wherein the CSFD follows a constant slope has only been observed for small, simple craters that are subject to diffusive degradation and, thus, strongly affected by sandblasting. It is not resolved whether the ancient crater populations on the lunar highlands have reached a state of equilibrium, too (e.g., Minton et al., 2019) The morphology of larger craters on the Moon, such as those on the densely cratered lunar highlands, do not show a strong

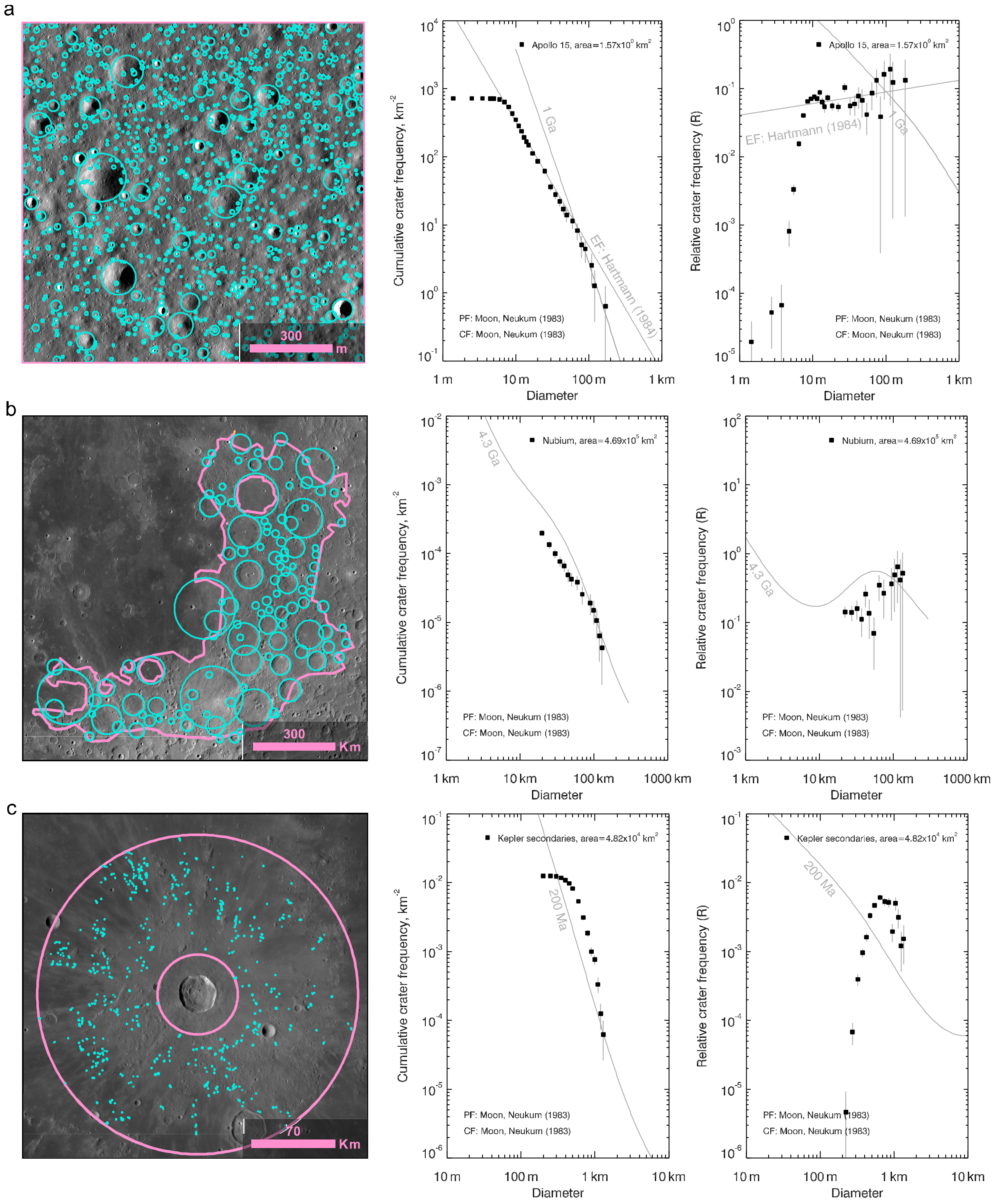

Figure 2.11: Contamination of the primary impactor population on the lunar surface. Binned CSFDs (pseudo-log) are shown in cumulative and R representations. The isochrones show the expected primary impactor populations from the Neukum (1983) chronology system using the largest craters as a reference. (a) shows Apollo 15 crater counts by Caleb Fassett in Robbins et al. (2014). Cumulative CSFDs for craters with $D < 70$ m follow a shallower slope than the expected production population, indicated by the Hartmann (1984) equilibrium function. (b) shows craters on the remnants of the Nubium basin counted by Fassett et al. (2012) and Orgel et al. (2018). Craters with $D < 90$ km are not consistent with the expected crater production population due to resurfacing by cookie cutting. (c) shows secondary craters within one to four radii around the Kepler crater identified by Singer et al. (2020). The CSFD steepens for craters with $D < 1$ km due to numerous secondary impacts.

modification from diffusive crater degradation and obtained CSFDs do not follow a constant slope. Instead, Kneissl et al. (2016) suggest that the CSFD of large lunar craters on ancient terrains are strongly affected by geometric crater obliteration. Here, obtained CSFDs reflect multiple surface ages due to a continuous resurfacing by large impact events. By applying a crater counting technique that accounts for the geometric crater obliteration from cookie cutting and proximal ejecta blanketing (Chapter 5), information about the buried primary population can be restored to some extent. Kneissl et al. (2016) suggest that the change in the CSFD shape from a continuous production function on heavily cratered surfaces in the inner Solar System, as observed by Strom et al. (2005, 2015), can be explained by geometric crater obliteration effects. However, it is unclear whether large lunar craters are in a cookie-cutting-induced equilibrium state that, in contrast to the equilibrium of small, simple craters, is not revealed by a CSFD that follows a constant slope or a crater configuration at less than 10 % geometric saturation.

Obvious secondary craters typically appear in clusters or rays of craters near a larger crater. Since secondary craters are smaller than the corresponding primary crater, they typically contaminate the CSFD of small craters in an investigated area. The contamination causes a steep rise in the CSFD due to the addition of impact craters that do not resemble the primary impactor population. In practice, secondary craters are often excluded from CSFD measurements by removing obvious secondary crater fields and their surrounding reference area by visual interpretation. However, since the visual identification of secondary crater clusters may be difficult and subjective, statistical approaches to identify non-randomly distributed crater populations have been developed (e.g., Michael et al., 2012; Chapter 4). Nevertheless, the identification of secondary craters is challenging when their spatial distribution and morphology resemble primary craters.

2.3.3. Contamination and Planetary Surface Evolution

The contamination of the primary impact population shows that the results from CSFD measurements should be carefully interpreted as the observed CSFD may not fully reflect the primary impactor population. Therefore, inaccurate conclusions due to contamination effects may lead to an inaccurate understanding of a planet's geologic and bombardment history. In an extreme case, the contamination may also question the validity of a previously obtained production function. For the Moon, this typically involves two scenarios: a change in the impactor size-frequency distribution and a contamination due to secondary cratering. Whereas previous interpretations that propose a change in the CSFD during the LHB period (e.g., Strom et al., 2005) may be attributed to contamination due to cookie cutting (e.g., Kneissl et al., 2016; Orgel et al., 2018; Orgel et al., 2020), the influence of secondary craters on the lunar cratering record is still debated (e.g., Neukum & Ivanov, 1994; McEwen & Bierhaus, 2006; Hartmann, 2007; Xiao and Strom, 2012; Xie et al., 2017; Xiao, 2018). This should be considered when measuring and interpreting CSFDs.

2.4. GIS-based CSFD Analysis

Investigations on the CSFD on planetary surfaces are typically conducted using geographic information systems (GIS) and statistics software. The procedure to derive and analyze CSFDs involves three steps: digitization of reference area

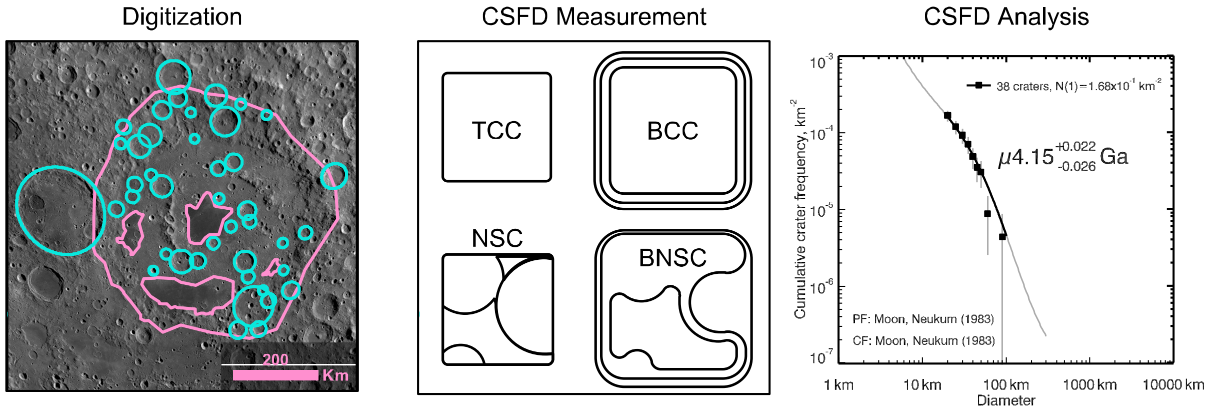

Figure 2.12: *Schematic process of a GIS-based CSFD analysis with the digitization of reference area and impact craters (Apollo basin, data from Fassett et al., 2012 and Orgel et al., 2018) (Fig. 1.12a), the application of CSFD measurement techniques that may modify the original reference area (Fig. 1.12b), and the visualization of the measured CSFD for further statistical analysis (Fig. 1.12c).*

and impact craters, measurement of the CSFD, and analysis of the CSFD (Fig. 2.12).

The first step to analyze crater populations includes digitizing the reference area and impact craters. The investigated craters should correspond to the formation of a homogeneous geologic unit that has seen no (or negligible) resurfacing after its emplacement. Digitized impact craters need to stratigraphically superpose the geologic unit and obvious secondary crater clusters together with the area they incorporate should be excluded from the investigation. Furthermore, the crater and area sizes need to be accurately calculated so that the influence of the planetary curvature on area and distance measurements is accounted for (Neukum & Ivanov 1994; Fassett, 2016).

In the second step, crater frequencies are obtained from the digitized data by applying crater counting techniques (see Chapter 5 and Fig. 2.12 for details). There are four crater counting techniques available to derive CSFDs:

- Traditional crater counting (TCC; used, e.g., by Neukum, 1983)
- Buffered crater counting (BCC; used, e.g., by Fassett et al., 2012)
- Non-sparseness correction (NSC; e.g., Kneissl et al., 2016)
- Buffered non-sparseness correction (BNSC; e.g., Kneissl et al., 2016)

TCC uses craters with their centroids inside the original reference area to obtain the CSFD. On the other hand, BCC is used to improve the statistics of the CSFD measurement by including craters that only partly superpose the reference area. The technique was developed to better measure CSFDs on linear features (Tanaka, 1982). NSC and BNSC were introduced to consider the effects of geometric crater obliteration during CSFD measurements. Here, the underlying area of all larger craters is excluded from the reference area for each crater. The excluded areas are considered resurfaced since they comprise regions in which the number of pre-existing smaller craters erased by a larger impact is unknown. Thus, the crater frequencies are increased compared to the TCC and BCC approaches, particularly for small craters. The NSC approach measures crater frequencies from craters with centroids inside the modified reference areas, whereas the modified areas are extended in the BNSC approach to increase further craters in the CSFD measurement and improve the statistics.

In the third step, the calculated crater frequencies are statistically analyzed. Here, the CSFD can be used to fit a production function in order to derive absolute model ages from a chronology system. The CSFD may also be used to determine relative surface ages or to identify geologic or impactor-related processes in the investigated area.

CHAPTER 3

TECHNICAL BACKGROUND

Since only a few crewed and robotic missions provide ground information from extraterrestrial surfaces, the analysis of geospatial data has been an essential method to study the evolution of planetary surfaces. Geospatial data involves vector and raster data that is referenced to a location on a planetary body. The data is commonly processed, modified and analyzed using geographic information systems (GIS). GIS techniques can be applied through Desktop GIS applications such as ESRI's proprietary ArcGIS software or the open-source GIS software QGIS. Desktop GIS applications provide a graphical user interface (GUI) in which a user can create, visualize, and analyze geospatial data using a set of pre-installed GIS algorithms. GIS techniques can also be applied through geospatial programming libraries, such as ESRI's proprietary ArcPy library or open-source libraries like GDAL, GeoPandas, or Shapely. Geospatial programming libraries allow for developing GIS algorithms that are not included in a Desktop GIS. Since many case studies of planetary surfaces require GIS techniques that are not provided in existing Desktop GIS software, such libraries are an important instrument for the scientific analysis of planetary spatial data. This chapter provides an overview of planetary spatial data and the development of GIS-based software tools for planetary applications.

3.1. Planetary Spatial Data

Geospatial data store information in the form of raster and vector data (e.g., Bill, 2016; Fig. 3.1). Vector data abstract information about geographic features using vector geometries and attribute information. The vector geometries involve point, line, and polygon elements, where assigned Cartesian coordinates determine their location on a planetary body. Point geometries with assigned coordinates are the basis of all vector geometry definitions. The shape of line features is determined by start, end, and intermediate points, termed vertices. The same applies to polygon features, where polygon edges are determined by start and endpoint, and intermediate vertices. For example, impact craters are often represented by polygon geometries, where attributes, such as crater name or diameter, can be stored to relate further information to each polygon geometry (e.g., Head et al., 2010).

Raster data store information about a geographic area in a grid of cells (pixels), in which a value represents the area covered by each cell. Although vector data can, in principle, be represented in raster form, too, raster datasets in planetary sciences typically involve the obtained and prepared data from planetary remote sensing systems and the raster-based products derived from it. This includes data from systems that record reflections of the electromagnetic spectra (e.g., Robinson et al., 2010; Green et al., 2011), radar-based images (e.g., Saunders et al., 1990), or derived products such as gravity information (e.g., Zuber et al., 2013) or digital terrain models (DTMs; e.g., Smith et al., 2010; Fig. 3.1b). In

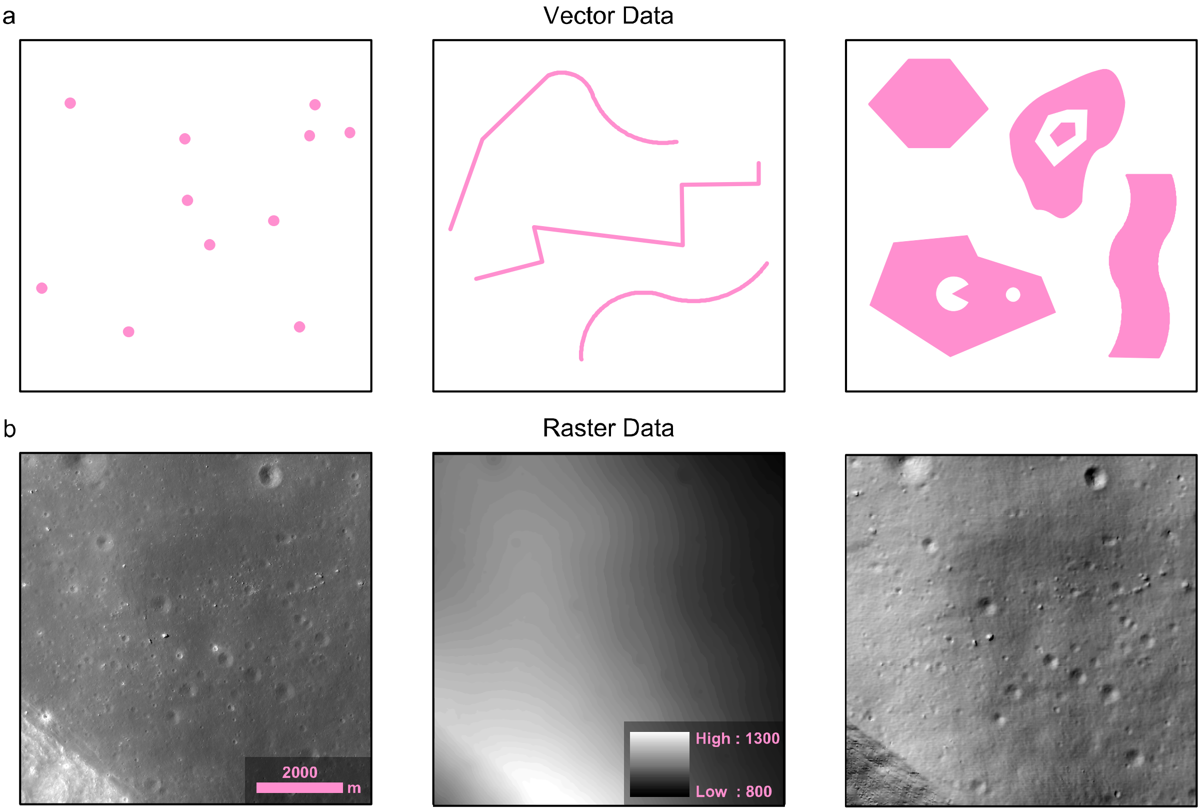

Figure 3.1: *Examples of geospatial data represented as vector (a) and raster data (b). Vector data show features as point (left), line (center), and polygon geometry types (right). Raster data display information in the form of pixels. (b) shows a raster image of the lunar surface, taken from the Lunar Reconnaissance Orbiter Camera (LROC) Narrow Angle Camera (NAC) (left) and products derived from NAC imagery. Derived raster products show a DTM (center) and a hillshade visualization (right).*

DTMs for example, the cell values correspond to the geographic location's altitude in relation to a reference body.

3.2. Map Projections

Geospatial raster and vector data are referenced to a coordinate system that determines the shape and position of a vector feature or raster cell. Coordinates use either a geographic or projected coordinate system to describe the position of a feature. In both systems, the locations are represented in relation to a three-dimensional reference body that approximates a planet's shape, mostly in the form of a sphere or a spheroid. Geographic coordinate systems use a superimposed grid to describe locations on the reference body in latitude and longitude. Latitude and longitude are given in angular units that describe the relation to horizontal and vertical planes that origin in the reference body's center. The longitude λ measures the east-west location along a central meridian and ranges from 0° at the prime meridian to ±180° at the Date Line. The (geocentric or geodetic) latitude φ measures the north-south location along the equatorial plane and ranges from 0° at the equator to ±90° at the poles.

Projected coordinate systems use a geographic coordinate system to map areas located on a three-dimensional curved body onto a two-dimensional plane. Since the projection of an area from a three-dimensional surface into a Cartesian system with X and Y coordinates introduces

Map projection	Equal area	Conformal	Equi-distant	True direction	Compro-mise
Mercator		●		○	
Cylindrical Equal-Area	●				
Equidistant Cylindrical			○		
Albers Equal-Area Conic	●				
Lambert Conformal Conic		●		○	
Equidistant Conic			○		
Orthographic				○	
Stereographic		●		○	
Lambert Azimuthal Equal-Area	●			○	
Azimuthal Equidistant			○	○	
Sinusoidal	●		○		
Mollweide	●				
Robinson					●

Table 3.1: *Selection of commonly used map projections and their projection properties (Snyder, 1987). Filled circles indicate a property that is completely satisfied. Unfilled circles indicate that the property is partly satisfied.*

distortions, mathematical techniques are applied in which certain geometric characteristics may be preserved. In a GIS environment, such techniques are summarized as map projections (for details, see, e.g., Snyder, 1987). A few selected map projections together with their projection properties are listed in Table 3.1.

Choosing a map projection to display and evaluate vector and raster data is a compromise that depends on the desired application since a single map projection preserves only certain geometric characteristics (Fig. 3.2). This includes information about the shape or the true area of a geometric feature. Map projections that distort a feature's shape but preserve its correct size are called equal-area projections. Map projections that distort an area's true size may preserve certain geometric characteristics. For example, conformal map projections correctly display relative angles and can be applied to represent characteristic directions. On the other hand, equidistant map projections are used to visualize the true distance as such projections partly preserve the geodesic distance between two points. Certain map projections, for example, azimuthal projections, preserve the correct direction between two points to a certain extent. Other map projections may not preserve any geometric characteristic or a feature's area but balance the individual disadvantages that arise due to distortions. Therefore, such projections can be used as a compromise to display geospatial data appropriately.

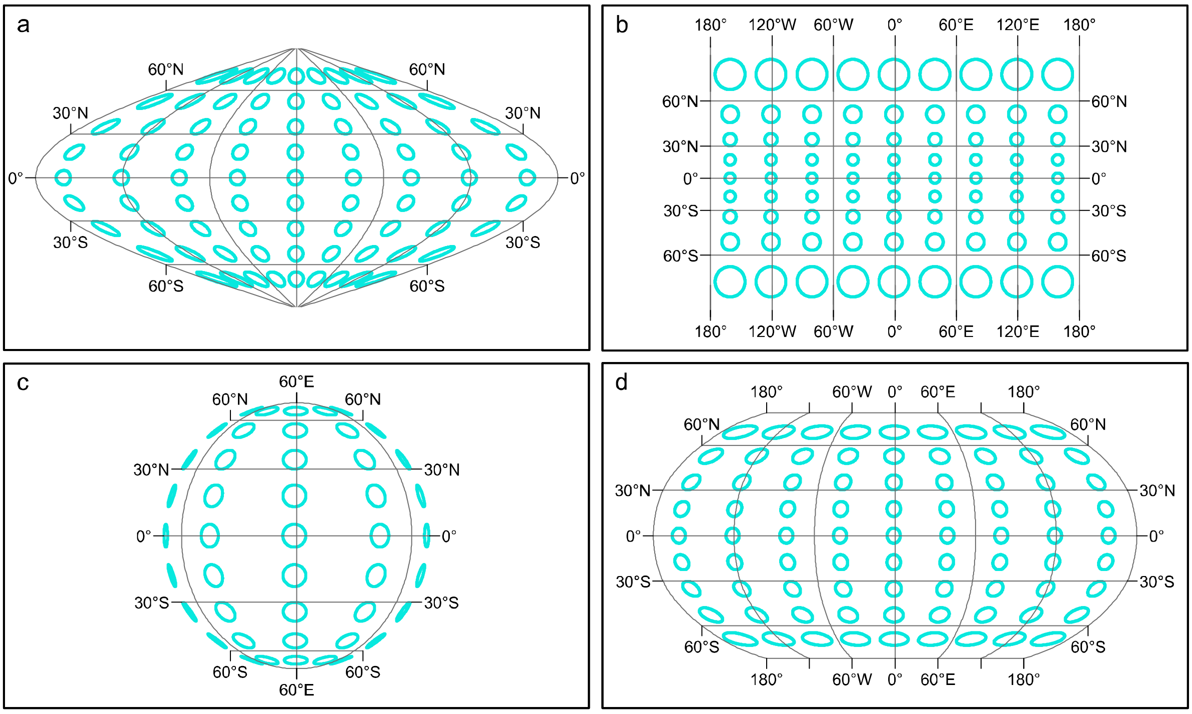

Figure 3.2: *Distortion of same-sized circular features (Tissot indicatrix) with* $D = 150$ *km on a sphere with lunar dimensions (1737.4 km in radius). In all map projections, the circular features appear distorted in shape. However, specific geometric characteristics can be preserved. For example, in the Sinusoidal equal-area projection (a), all features cover the same area despite changes in the features' shape. The conformal Mercator projection (b) distorts feature sizes but preserves relative angles. Thus, the presented features maintain their circular appearance. The orthographic projection (c) shows correct directions from the projection center but distorts shapes with increasing distance. The Robinson projection (d) does not preserve geometric characteristics but balances out the individual disadvantages that arise from map distortion effects and is typically used for visualization purposes.*

Since map projections involve a distorted portrayal of geospatial data, which represents features on a curved planetary surface, it is essential to consider the influence of map distortion effects when conducting spatial measurements, such as angle, distance, and area. The intensity to which data is distorted depends on the selected map projection and the distance to the projection center. Measurements may be further affected when inaccuracies due to imprecise shape models or uncertain coordinate systems are introduced (e.g., Kneissl et al., 2014). Therefore, considering map projections and their influence on spatial measurements is crucial when measuring CSFDs and developing GIS-based software tools to analyze geospatial data (e.g., Kneissl et al., 2011).

3.3. GIS Tools in Planetary Science

The analysis of geospatial data is an essential component in numerous investigations on planetary surface evolution. Therefore, the scientific community developed various customized software tools to process, modify, and analyze such data. For example, the ArcGIS extension CraterTools (Kneissl et al., 2011) and the Craterstats software (Michael & Neukum, 2010) are widely used to measure and analyze CSFDs on planetary surfaces based on geospatial data. CraterTools adds a toolbar to Esri's ArcMap software and provides tools to digitize reference areas and impact craters, and measure CSFDs. The tool uses Esri's ArcObjects and depends on a proprietary framework for the development and application. The dependence on proprietary software requires developers and users to buy a software license. This may create additional costs but can reduce the time needed for software development since the existing algorithms and frameworks are usually well tested and maintained.

On the other hand, many GIS-based software tools developed by the scientific community do not depend on proprietary software. Instead, these tools use open-source programming libraries that do not require any additional licensing expenses. Open-source libraries provide a framework that allows for the development of various customized features and algorithms and are therefore an essential instrument for building scientific software tools. However, building software may be challenging as open-source libraries for GIS applications are usually not as well tested and maintained and include fewer algorithms than, for example, Esri's programming framework. Thus, software development using open-source libraries requires a lot of testing, which may increase the workload for providing scientific tools. Nevertheless, such tools are widely developed by the scientific community. For example, open-source software such as JMARS (Christensen et al., 2009), a GIS with direct access to remote sensing data of various planetary missions, or the Integrated Software for Imagers and Spectrometers (ISIS; Edmundson et al., 2012), an image processing tool to process raw planetary remote sensing data, are commonly used by planetary scientists.

PART II

DEVELOPMENT OF GEOSPATIAL APPROACHES TO STUDY PLANETARY CRATER RECORDS

CHAPTER 4

STUDYING THE GLOBEL SPATIAL RANDOMNESS OF IMPACT CRATERS ON MERCURY, VENUS, AND THE MOON WITH GEODESIC NEIGHBORHOOD RELATIONSHIPS

by C. Riedel, G. G. Michael, C. Orgel, C. Baum, C. H. van der Bogert, and H. Hiesinger (2021), published in Journal of Geophysical Research: Planets, 126, e2020JE006693, https://doi.org/10.1029/2020JE006693.

Abstract: Impact crater records on planetary surfaces are often analyzed for their spatial randomness. Generalized approaches such as the mean second closest neighbor distance (M2CND) and standard deviation of adjacent area (SDAA) are available via a software tool but do not take the influence of the planetary curvature into account in the current implementation. As a result, the measurements are affected by map distortion effects and can lead to wrong interpretations. This is particularly critical for investigations of global data sets as the level of distortion typically increases with increasing distance from the map projection center. Therefore, we present geodesic solutions to the M2CND and SDAA statistics that can be implemented in future software tools. We apply the improved methods to conduct spatial randomness analyses on global crater data sets on Mercury, Venus, and the Moon and compare the results to known crater population variations and surface evolution scenarios. On Mercury, we find that the emplacement of smooth plain deposits strongly contributed to a global clustering of craters and that a random distribution of Mercury's basins is not rejected. On Venus, the randomness analyses show that craters are largely randomly distributed across all sizes but where local nonrandom distributions due to lower crater densities in regions of recent volcanic activity may appear. On the Moon, the global clustering of craters is more pronounced than on Mercury due to mare volcanism and the Orientale impact event. Furthermore, a random distribution of lunar basins is not rejected.

4.1 Introduction

Impact cratering on planetary bodies in the inner solar system occurs largely at spatially random locations. Accordingly, a significant nonrandom distribution of impact craters can indicate geologic processes that have modified the cratering record on a surface unit. Investigating whether a given crater population is either clustered, random, or in an ordered arrangement can thus provide information about the evolution of planetary surfaces. Such investigations have been used, for example, to identify possible contaminations of the primary impactor population (e.g., Iqbal et al., 2019; Michael et al., 2012), the presence of crater saturation (e.g., Kirchoff, 2017; Squyres et al., 1997), or the nature of impactor populations (e.g., Holo & Kite, 2020).

Often, the spatial randomness of crater populations is quantified by measuring the spatial relationships between craters. Since craters are located on a curved planetary surface, the determination of such relationships requires the consideration of the planetary curvature, particularly when investigating large or global surface units. This is typically considered in individual approaches that are developed for global applications (e.g., Turcotte et al., 1999). However, two commonly applied methods that are implemented in a software tool do not consider such effects. To overcome these limitations, we use geodesic measurements that determine distances and point coordinates on a great circle and include these measurements in the referred methods. We apply the improved approaches to investigate the global spatial randomness of crater populations on Mercury, Venus, and the Moon and use the results to draw parallels to previous investigations of the surface evolution on the respective planetary bodies.

4.2 Quantifying the Spatial Randomness of Impact Craters

The spatial randomness of impact craters is often analyzed using Monte Carlo approaches (e.g., Hirata et al., 2020; Kreslavsky, 2007; Kirchoff, 2017; Michael et al., 2012). In such approaches, a measure that describes the population of a given set of craters is compared to the same measure of n randomly distributed crater populations, each with the same number of craters. Depending on how much the measure of the examined population deviates from the measures of the randomly distributed populations, a statement on how strongly a given set of craters differs from a random distribution can be made. The deviation from a random distribution can be quantified using statistical measures such as percentile or Z-score (e.g., Kirchoff, 2017; Michael et al., 2012; Squyres et al., 1997). The crater populations itself can in turn be described by measurements that quantify the neighborhood relationships between the craters (e.g., Kreslavsky, 2007; Michael et al., 2012; Squyres et al., 1997). This can involve the distance or the area between neighboring craters, for example.

4.2.1 M2CND and SDAA Statistics in the Craterstats Software

Due to the widespread use of the Craterstats software (Michael & Neukum, 2010), the mean second closest neighbor distance (M2CND) and the standard deviation of adjacent area (SDAA) (Michael et al., 2012) are widely used neighborhood relationships (e.g., Adeli et al., 2016; Hao et al., 2020; Iqbal et al., 2019; Neesemann et al., 2019) that are used to quantify the spatial randomness of impact craters. In the M2CND approach, the distance to the second closest crater centroid is determined for each crater centroid. The M2CND value results from the mean of these values. The SDAA approach is based on a Voronoi diagram that is constructed from the crater centroids. The Voronoi diagram consists of polygons in which the distance of any point to the associated crater centroid is less or the same as to any other crater centroid. The SDAA value results from the standard deviation of the area of all Voronoi polygons. In order to assess the spatial randomness of a given crater data set, the obtained measures are compared to those of randomly distributed crater data sets.

The randomness analysis in Craterstats uses two statistical measures to quantify the deviation from a random population: Percentile and Z-score (the latter is termed n_σ in the Craterstats software). The percentile marks how many percent of the randomly distributed data sets yielded a lower randomness measure than the given population. The Z-score shows the deviation from the histogram in standard deviations from the mean. A low measure in the

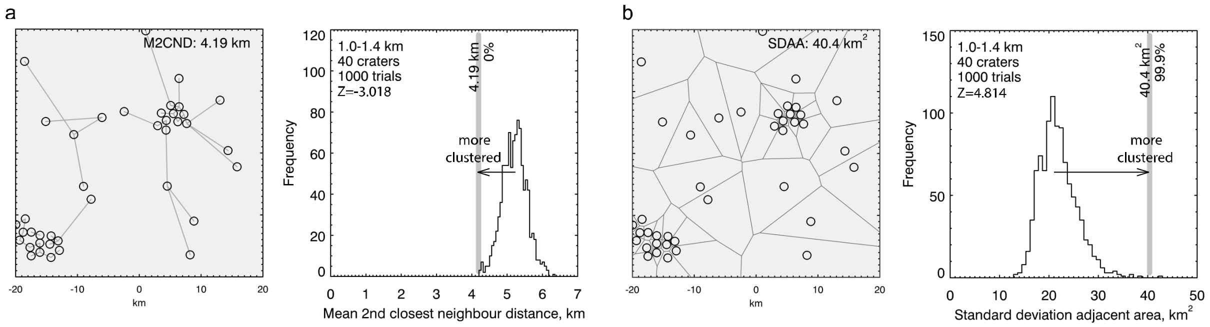

Figure 4.1: M2CND (a) and SDAA statistics (b) for a clustered set of craters. The map plots show the connecting lines between second closest neighbors that are used for the M2CND analysis (a) and the Voronoi polygons that are used for the SDAA analysis (b). M2CND, mean second closest neighbor distance; SDAA, standard deviation of adjacent area.

M2CND approach indicates a clustered population (because the mean distance of second closest neighbors is smaller than for randomly distributed populations); a high measure indicates an ordered population (because the mean distance of second closest neighbors is larger than for randomly distributed populations). In the SDAA statistics, this is reversed. Here, a low measure marks an ordered population (because there is less variance in the size of Voronoi polygons compared to randomly distributed population) and a high measure marks a clustered population (because the variation in Voronoi polygon sizes is larger than for randomly distributed populations).

To illustrate this, we generated a clustered set of 40 same-sized craters and calculated M2CND and SDAA statistics using Craterstats. In this example, the randomness measure of the data set is compared to the randomness measures of 1,000 sets of randomly distributed craters of the same quantity. The results are shown in Figure 4.1 In the M2CND statistics (Figure 4.1a), the M2CND value of the data set is located outside the lower end of the histogram; at the 0th percentile, with a Z-score of less than -3 (more than 3σ below the mean). In the SDAA statistics (Figure 4.1b), the SDAA value is located at the upper end of the histogram, with a Z-score of 4.814. 99.9% of the randomly distributed crater data sets yielded a lower SDAA value than our data set. The statistical measures in both the M2CND and the SDAA statistics strongly indicate the presence of crater clusters in the given data set.

4.2.2 M2CND and SDAA Statistics From Geodesic Measurements

In Craterstats, all measurements as well as the construction of the Voronoi diagram are carried out in a two-dimensional Cartesian coordinate system. Accordingly, the calculated distances and areas are susceptible to map distortion effects. This affects global measurements in particular, because the distortions typically intensify with increasing distance from the map projection center (e.g., Kneissl et al, 2011; Snyder, 1987). The randomness analysis in Craterstats for example, uses measurements in the Lambert Azimuthal Equal Area (LAEA) projection, which correctly maps area sizes on a sphere, but distorts distances and shapes with increasing distance from the projection center (Snyder, 1987). We therefore apply great circle measurements to account for the curvature of planetary surfaces directly and thus circumvent the limitations of projected measurements when determining M2CND and SDAA statistics. The measurements are applied in order to (1) measure distances between craters to identify second closest neighbors for the M2CND approach and (2) determine the geodesic boundaries of Voronoi polygons for the SDAA approach.

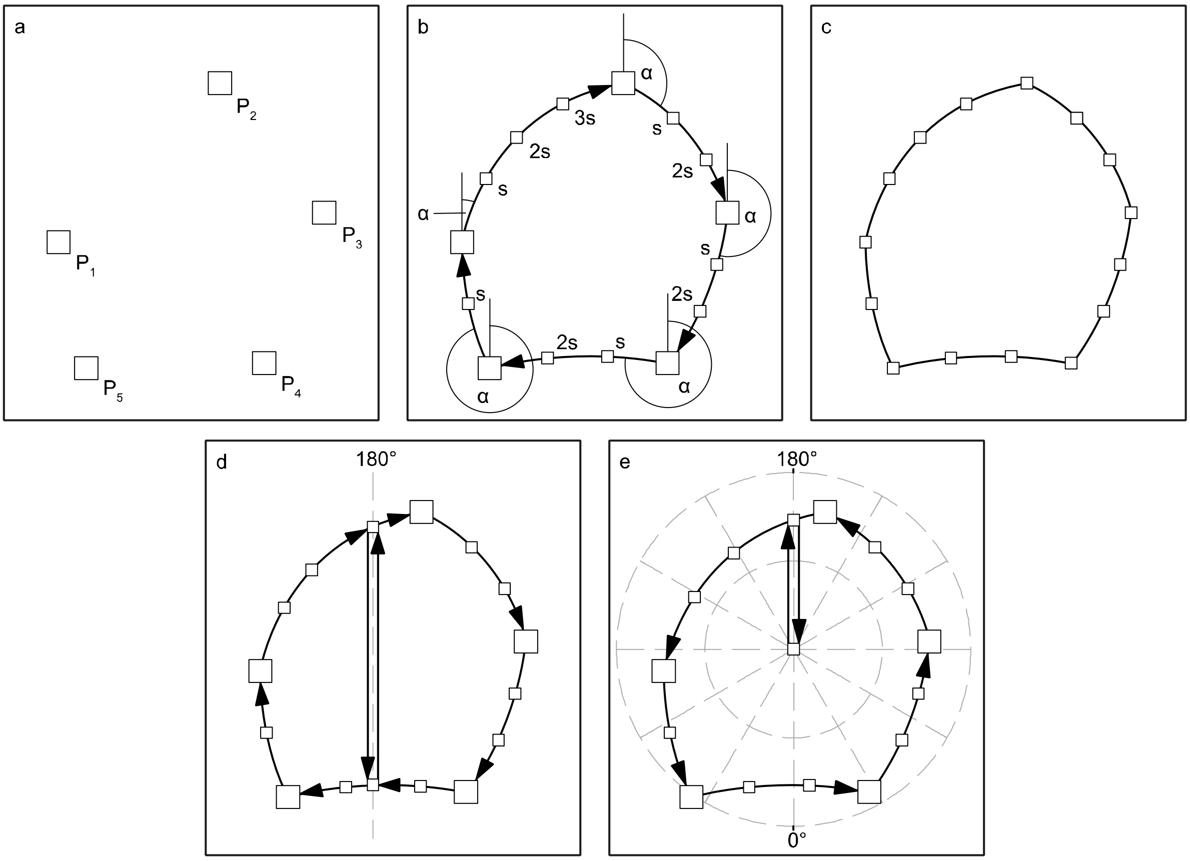

Figure 4.2: This figure illustrates the construction of geodesic Voronoi polygons from premliminary polygon vertices. Figure (a) shows an example of five preliminary polygon vertices P_1*–*P_5 *as the SphericalVoronoi algorithm generates them. To create geodesic polygon edges, we calculate the coordinates of additional vertices (shown as small squares) at* $s = 15\ km$ *intervals along geodesic lines (shown as black arrows) of azimuth* α *(b). The edges of the geodesic Voronoi polygon are determined from both preliminary and additional vertices (c). In the event of a date line intersection, the date line separates the geodesic Voronoi polygon into two parts, which are constructed individually (d). If a geodesic Voronoi polygon intersects a pole, the pole and the date line are included in the construction of the polygon (e).*

4.2.2.1 M2CND

We measure the geodesic distances to all other craters for each crater in the given population, determine the neighbor with the second lowest distance for each crater and determine the M2CND value. Because a crater must have at least two adjacent craters, a minimum of three craters is required in a data set for this measurement.

4.2.2.2 SDAA

The calculation of global SDAA statistics requires the generation of geodesic Voronoi diagrams. For this purpose, we use the SphericalVoronoi algorithm (version 0.18.0) which is implemented in Python's scipy library (version 1.2.1) (Virtanen et al., 2020). The algorithm returns the vertices of spherical Voronoi polygons but does not generate geodesic polygon edges in the given version. In order to produce geodesic polygon edges and to construct geodesic Voronoi polygons, we use the coordinates of the polygon vertices generated by the SphericalVoronoi algorithm (we refer to these vertices as preliminary polygon vertices) and add further polygon vertices between them along a geodesic line. This ensures that the planetary curvature is taken into account when constructing the edges of the geodesic Voronoi polygons. We calculate the geodesic distance s between two preliminary vertices P_n and P_{n+1}. If s is larger than 15 km, we calculate the coordinates of additional vertices at fixed intervals (we use intervals of 15km for our investigation) along a geodesic line between P_n and P_{n+1}. The geodesic Voronoi polygon is eventually constructed from both preliminary and additional vertices (see Figures 4.2a-c).

If a geodesic Voronoi polygon intersects the date line or one of the poles, the construction of the polygon is slightly modified to ensure that such polygons are correctly generated. If a Voronoi polygon intersects the date line, the intersection is used as an additional vertex. In such a case, the date line acts as a cutting line, which separates the polygon into two parts. Each part is constructed individually to avoid errors when creating geodesic Voronoi polygons that cross the date line (Figure 4.2d). In the case of a polar intersection, we use the intersection with the date line and the pole as additional vertices and modify the order of the vertices to generate the polygon. The pole and the date line intersection form the first two and the last two vertices of the polar Voronoi polygon. All intermediate vertices are added from west to east with increasing longitude values. The polygon with its first and last vertex at the pole is thus drawn in counter-clockwise direction around the pole (Figure 4.2e).

When a geodesic Voronoi polygon is constructed, it is projected to the LAEA projection (centered at the corresponding crater centroid) to measure its area. The areas of all geodesic Voronoi polygons allow the determination of the SDAA value. However, a current limitation in the SphericalVoronoi algorithm allows us to only apply the approach when there is a minimum of 20 craters in the data set. A smaller number of craters can lead to incorrectly calculated polygon vertices (see Supplementary Information S1 and S2 of the published article).

4.2.3 Projected Measurements Falsify the Results of M2CND and SDAA Statistics

To illustrate how projected measurements could falsify the results of the randomness analysis, we calculate geodesic as well as Cartesian M2CND and SDAA statistics for a global data set of 100 randomly arranged craters on a sphere with lunar dimensions and compare the results. We applied the traditional crater counting technique in CSFD Tools (Riedel et al., 2018) and conducted a randomness analysis in Craterstats (Michael and Neukum, 2010; Michael et al., 2012) using Cartesian M2CND and SDAA measurements. The results are shown in Figure 4.3.

Due to the influence of map distortion effects, the Cartesian M2CND and SDAA values (509 km and 196000 km^2 – see Figures 4.3a and 4.3b) are different from those obtained using geodesic measurements (472.54 km and 181000 km^2 – see Figures 4.3c and 4.3d). The same applies to the calculated Z-scores and percentiles. Of 100000 randomly distributed data sets, 88 % (Cartesian M2CND, Figure 4.3a) and 66.9 % (geodesic M2CND, Figure 4.3c) have lower M2CND values. This translates to Z-scores of 1.17 (Cartesian M2CND) and 0.45 (geodesic M2CND), respectively. In the SDAA analysis, 28.8 % (Cartesian SDAA, Figure 4.3b) and 22.9 % (geodesic SDAA, Figure 4.3d) of the randomly distributed data sets have lower SDAA values. The Z-scores are -0.59 in the Cartesian and -0.75 in the geodesic SDAA approach.

Although the differences between Cartesian and geodesic measurements in this example do not allow a reliable rejection of the random distribution, the results show that Cartesian measurements distort global M2CND and SDAA statistics. However, because it cannot be ruled out

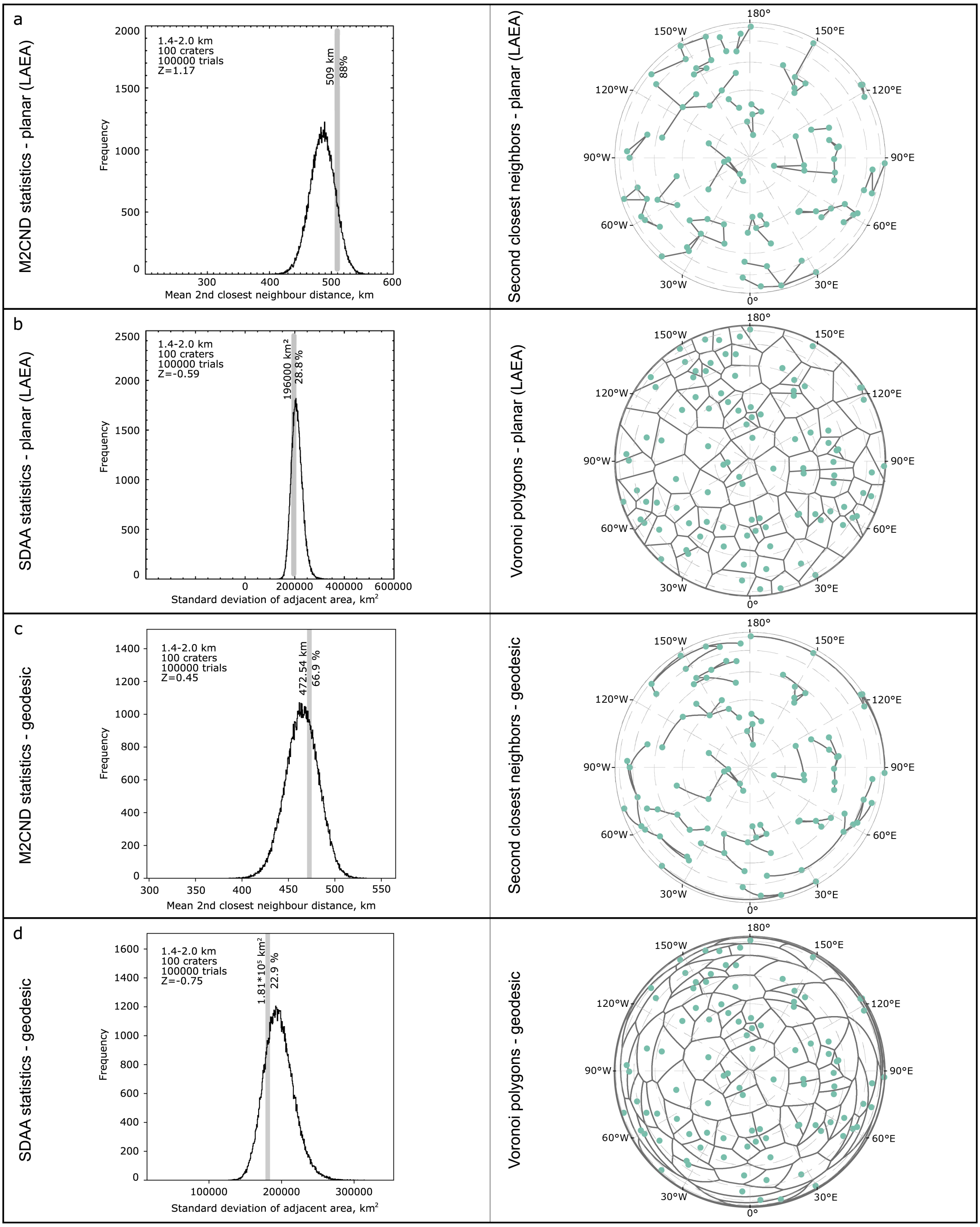

Figure 4.3: *Results from Cartesian (a and b) and geodesic M2CND (c) and SDAA (d) statistics. The histogram plots show the obtained M2CND and SDAA values of a randomly distributed set of 100 craters together with a histogram that summarizes the M2CND and SDAA values of 100000 sets of 100 randomly distributed craters. The map plots show the Cartesian (a) and geodesic (c) connecting lines between second closest neighbors that are used for the M2CND analysis as well as Cartesian (b) and geodesic Voronoi (d) polygons that are used for the SDAA analysis. Map plots are shown in LAEA projection.*

that Cartesian measurements can also lead to an incorrect assessment of the truly existing spatial randomness of impact craters, we apply geodesic measurements to calculate global M2CND and SDAA statistics for craters on Mercury, Venus, and the Moon. We apply both methods to consider the different sensitivities of the two approaches to particular crater distributions (e.g., Kreslavsky, 2007; Michael et al., 2012). In contrast to the Craterstats software, we do not apply a binning based on crater size but divide a given crater data set into overlapping bins with the same number of craters. This has several advantages: (1) the overlap allows randomness variations to be identified in a higher resolution, (2) the constant number of craters allows for a better comparison of crater populations on different planetary bodies, and (3) the constant number ensures that the randomness analysis is based on a sufficient number of craters. In our analysis, each bin contains 300 craters, with the 150 smallest craters in the next larger bin corresponding to the 150 largest craters in the next smaller bin. Due to the high number of histogram and map plots that show the results for each bin, we placed the detailed results to the published article's Supplementary Information (indicated by figure references that begin with an "S" in the following chapters). A few selected histogram and map plots are included in the respective chapters.

4.3 The Global Spatial Randomness of Impact Craters

4.3.1 Mercury

4.3.1.1 Background

Mercury has been tectonically and volcanically active for most of its evolution (e.g., Zuber et al., 2012; Watters et al., 2016) with volcanism in particular having a major impact on its surface evolution and observable cratering record (e.g., Head et al., 2008; Head et al., 2009). In its early history, the surface evolution of Mercury was dominantly shaped by effusive volcanism and global resurfacing (e.g., Fassett et al., 2011b; Marchi et al., 2013; Byrne et al., 2016). These processes formed Mercury's most ancient surfaces on which today's observable cratering record could accumulate – the most densely cratered terrains as well as the oldest basins (e.g., Strom et al., 1975; Neukum et al., 2001b; Fassett et al., 2012; Marchi et al., 2013; Orgel et al., 2020). These units were emplaced at around 4.0-4.1 Ga (e.g., Fassett et al., 2012; Marchi et al., 2013; Orgel et al., 2020) and are therefore a little younger than the most ancient terrains on the Moon (e.g., Orgel et al., 2018).

In the post-Late Heavy Bombardment era, volcanism continued to be an extensive process on Mercury (e.g., Head et al., 2011), but its large-scale activity declined over a relatively short period (e.g., Wilson and Head, 2008; Marchi et al., 2013; Byrne et al., 2016; Herrick et al., 2018) and ended at around 3.5 Ga (e.g., Byrne et al., 2016) due to interior cooling. The cooling led to a contraction of the planet and the appearance of tectonic features, such as thrust faults (e.g., Strom et al., 1975; Strom, 1977; Neukum et al., 2001b; Wilson and Head, 2008; Watters et al., 2009; Byrne et al., 2016, Giacomini et al., 2020). Subsequent tectonic and volcanic activity continued to shape the surface of Mercury. However, such activity was geographically isolated (e.g., Prockter et al., 2010; Marchi et al., 2013; Thomas et al., 2014; Byrne et al., 2016; Watters et al., 2016). Young volcanism, for example, took place primarily in the form of explosive vents (e.g., Head et al., 2009; Prockter et al., 2010; Thomas et al., 2014). Compared to the widespread flood volcanism, which dominated the surface modification of Mercury for a long

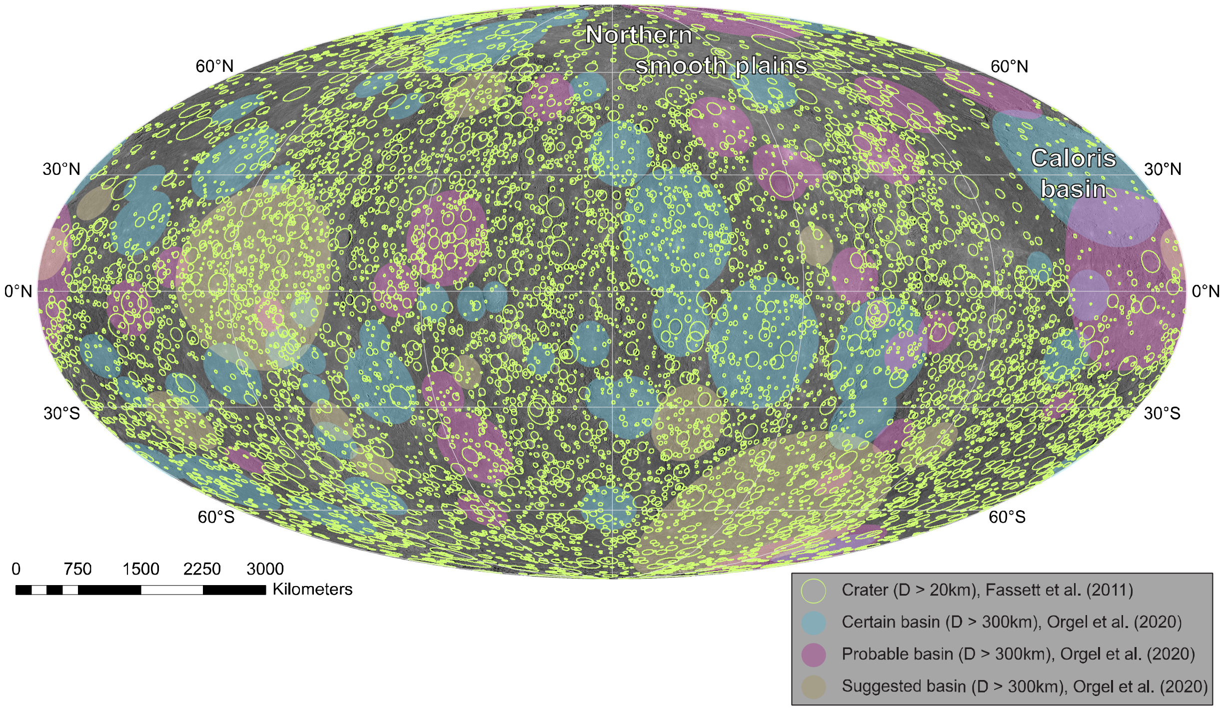

Figure 4.4: Map in Mollweide projection showing impact craters (D > 20 km) on Mercury from the data sets by Fassett et al. (2011b) and Orgel et al. (2020) on a MESSENGER MDIS mosaic.

time (e.g., Head et al., 2009; Fassett et al., 2012; Marchi et al., 2013), these volcanic events have little influence on the modification of Mercury's existing surface.

The geologic activities on Mercury led to the formation of two major geologic units – smooth plains and inter-crater plains. The inter-crater plains form the oldest terrains on Mercury and comprise areas of high crater density with interspersed smoother areas (e.g., Strom et al., 1975; Neukum et al., 2001b; Fassett et al., 2011b; Strom et al., 2011; Denevi et al., 2013; Kreslavsky et al., 2014). With an age of >4.0 Ga (e.g., Strom et al., 1975; Neukum et al., 2001b), they were emplaced at a time when Mercury was volcanically very active. Although a formation as ejecta material has been debated (e.g., Wilhelms, 1976), most recent papers favor a volcanic origin of the inter-crater plains (e.g., Strom, 1977; Strom et al., 2011; Denevi et al., 2013; Byrne et al., 2016). Its densely cratered landscape has a large number of secondary craters (e.g., Neukum et al., 2001b; Strom et al., 2011; Herrick et al., 2018). However, due to strong surface modification and efficient crater degradation (e.g., Neukum et al., 2001b; Fassett et al., 2011b; Fassett et al., 2012; Fassett et al., 2017), the crater densities here are lower than on the most heavily cratered terrains on the Moon (e.g., Neukum et al., 2001b; Ostrach et al., 2015; Fassett et al., 2017).

The smooth plains, on the other hand, are younger than the inter-crater plains and therefore have lower crater densities (e.g., Strom et al., 1975; Neukum et al., 2001b; Strom et al., 2011; Fassett et al., 2011b; Fassett et al., 2012; Denevi et al., 2013; Kreslavsky et al., 2014; Ostrach et al., 2015; Byrne et al., 2016). They are sharply demarcated from the surrounding terrain, are distributed asymmetrically, and cover roughly one third of Mercury's surface (e.g., Denevi et al., 2009; Denevi et al., 2013). Its largest coherent units cover broad areas on the northern polar region of Mercury and around the Caloris basin (161°E; 30°N) (e.g., Neukum et al., 2001b; Fassett et al., 2011b; Head et al., 2011; Fassett et al., 2012; Denevi et al., 2013; Ostrach et al., 2015) – Mercury's youngest large multi-ring structure (e.g., Neukum et al., 2001b; Fassett et al., 2009; Orgel et al., 2020). These northern units comprise more than half of all smooth plains (e.g., Deveni et al., 2013). Smaller smooth plain units are distributed irregularly across Mercury's surface (e.g., Neukum et al., 2001b; Denevi et al., 2013; Byrne et al., 2016).

The majority of Mercury's smooth plains were emplaced over a relatively short period at around 3.5-3.9 Ga (e.g., Strom et al., 1975; Denevi et al., 2013; Marchi et al., 2013; Ostrach et al., 2015; Byrne et al., 2016; Fassett et al., 2017). Although there are also smaller and younger units that may have been formed by fluidized ejecta (e.g., Wilhelms, 1976; Denevi et al., 2013; Ostrach et al., 2015; Byrne et al., 2016) due to a high level of impact melt production (e.g. Ostrach et al., 2012). Overall, it is assumed that a large part of the smooth plains originated from flood volcanism (e.g., Strom et al., 1975; Neukum et al., 2001b; Head et al., 2009; Watters et al., 2009; Head et al., 2011; Zuber et al., 2012; Denevi et al., 2013; Marchi et al., 2013; Kreslavsky et al., 2014; Ostrach et al., 2015; Byrne et al., 2016), that was emplaced at various episodes (e.g., Neukum et al., 2001b; Denevi et al., 2013; Ostrach et al., 2015; Byrne et al., 2016) and obliterated large parts of pre-existing crater and basin records (Head et al., 2009; Fassett et al., 2011b; Fassett et al., 2012; Ernst et al., 2015; Ostrach et al., 2015; Orgel et al., 2020). Such large-scale volcanic activity left most craters and basins on Mercury at least partly filled (e.g., Fassett et al., 2012; Herrick et al., 2018; Orgel et al., 2020) and strongly contributed to a lower density of craters and basins when compared to the Moon (Neukum et al., 2001b; Fassett et al., 2011b; Fassett et al., 2012; Orgel et al., 2020).

In this context, Fassett et al. (2012) and Orgel et al. (2020) analyzed the magnitude of basin asymmetry between Mercury's hemispheres. They found that the distribution of basins ($D \geq 300\,\mathrm{km}$) on Mercury's hemispheres is nonuniform and that the erasure of basins by resurfacing events may have contributed to it. However, the studies by Fassett et al. (2012) and Orgel et al. (2020) only considered the distribution of basins over longitude. To provide more detailed information about the basin spatial relationships, we re-investigate the global spatial randomness of impact craters and basins on Mercury by applying geodesic M2CND and SDAA analyses. To this end, we use two data sets. (1) The crater catalogue by Fassett et al. (2011b) (v19) to analyze the crater populations ($20.36\,\mathrm{km} \leq D < 300\,\mathrm{km}$) and (2) the basin data set by Orgel et al. (2020) to analyze Mercury's basin populations ($D \geq 300\,\mathrm{km}$) (Figure 4.4). The latter data set was created from recent investigations of Mercury's basin inventory and contains 94 basins that are labeled as "certain", "probable", and "tentative", based on their visual detectability.

4.3.1.2 Results

Figure 4.5. summarizes the results of the randomness analysis at normalized Z-scores for each bin of the crater data set by Fassett et al. (2011b). The results show that the number of bins where randomness is rejected at a two-sigma confidence level is higher in the SDAA than in the M2CND analysis. Out of 47 bins, randomness is rejected in 37 (SDAA) and 14 (M2CND) populations at the given confidence level. This indicates that both approaches have a different sensitivity for the crater configurations in the given bins. Crater populations where randomness cannot be rejected at a two-sigma confidence level are more numerous in the M2CND approach and appear across all

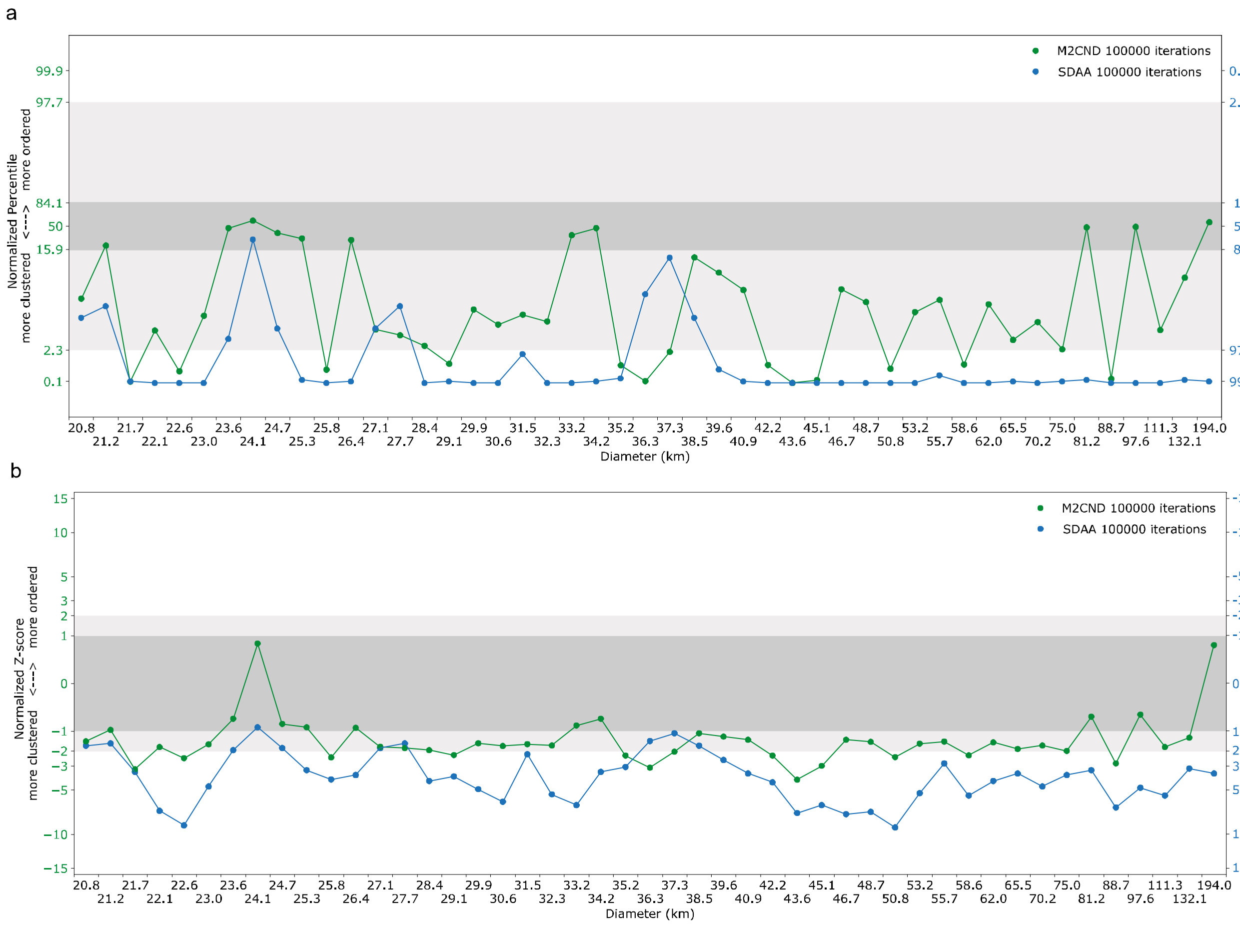

Figure 4.5: *Normalized percentiles (a) and Z-scores (b) for binned crater data by Fassett et al. (2011b), derived from geodesic M2CND and SDAA analyses. Grey bands show confidence levels at one- and two-sigma confidence levels. X-axis labels show the geometric mean of minimum and maximum crater diameter for each bin.*

diameters in both methods. There are eight bins where a non-random distribution of impact craters cannot be rejected from M2CND and SDAA analyses. They occur in bins with mean diameters of 20.8, 21.2, 23.6, 24.1, 24.7, 27.1, 27.7, and 38.5 km (Figure 4.5 and Figures S3-S5, S8). The most significant rejection of randomness according to the SDAA analysis occurs in crater populations with $21.7 \leq D_{\text{mean}} \leq 23$ km (Percentiles > 99.9 %, Z-scores between 3.4 and 8.9), $28.4 \leq D_{\text{mean}} \leq 35.2$ km (Percentiles > 98 %, Z-scores between 2.2 and 6.5), and $D_{\text{mean}} \geq 40.9$ km (Percentiles > 99.5 %, Z-scores between 2.8 and 9.1). Although the significance of randomness rejection is less strong in the M2CND approach, populations where randomness is rejected at a two-sigma confidence level can be found at various size ranges as well. Therefore, the results do not expose a clear correlation between crater size and significance of non-randomness.

The map plots (Figures S3-S12) visually indicate at which geographic locations the binned crater populations occur at different densities. This allows the identification of areas in which extensive crater erasure contributed to a global-scale clustering of crater populations. Often, crater populations appear in patchy groups with extended areas of lower crater densities in between. In some bins, such as those with $23.56\text{ km} \leq D \leq 24.64\text{ km}$ ($D_{\text{mean}} = 24.1$ km) or $37.37\text{ km} \leq D \leq 39.62\text{ km}$ ($D_{\text{mean}} =$ 38.5 km), the distribution of craters appears less

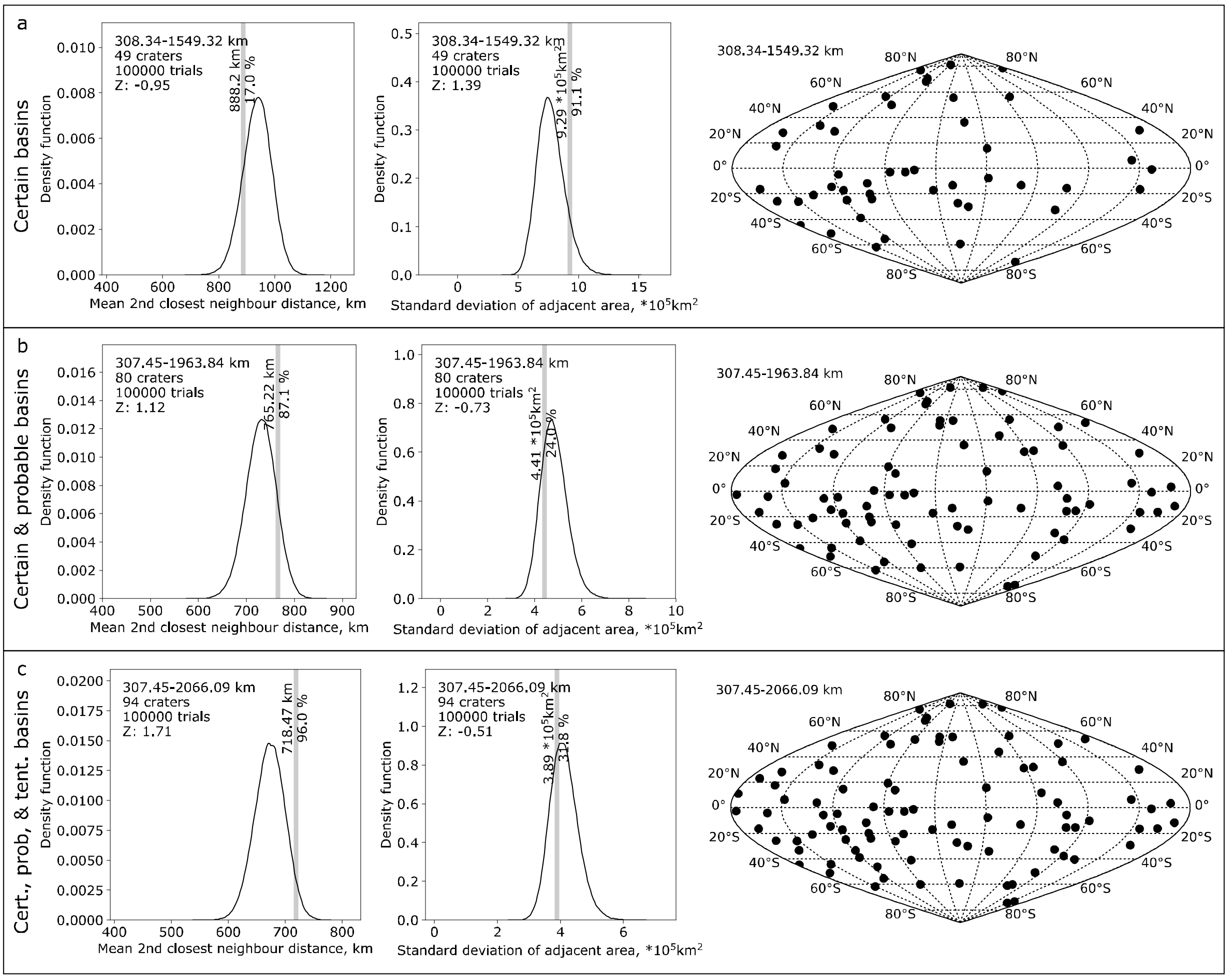

Figure 4.6: Histogram and map plots for certain (a), certain and probable (b), and certain, probable, and tentative basins (c) (Orgel et al., 2020). The distribution of basins is shown in sinusoidal projection.

grouped over the surface, which leads to a non-rejection of randomness at a two-sigma confidence level in the corresponding randomness analysis. However, because the results of the randomness analysis largely reject randomness and because crater size and the significance of randomness rejection does not correlate in our analysis, we consider this a stochastic effect rather than an indication that resurfacing did not affect the distribution of craters in the respective bins. The largest coherent areas where craters appear in a less dense configuration are located around Caloris basin and, to a lesser extent, in the northern polar region. These regions are dominated by extensive smooth plains deposits, which erased pre-existing crater records. In fact, many craters in this region that are included in the crater catalogue are covered by volcanic material. We therefore conclude that the emplacement of smooth plains had a significant influence on the global spatial randomness of Mercury's impact craters, where differences in surface age and crater densities cause the rejection of randomness at the given confidence level in various bins. Further small-scale resurfacing processes such as tectonics (e.g., Watters et al., 2016), the geometric overlap of pre-existing craters by a new impact (sometimes referred to as cookie cutting – e.g. Woronow, 1977; Richardson, 2009; Kneissl et al., 2016), degradation from downslope diffusion (sometimes referred to as sandblasting – e.g., Soderblom, 1970; Richardson, 2009; Minton et al., 2019), and the deposition of young smooth plains (e.g., Byrne et al., 2016) or volcanic material (e.g., Thomas et al., 2014; Herrick et al., 2018) likely contributed to the erasure of pre-existing craters and the appearance of clusters in certain regions on Mercury. However, such processes occurred at a regional scale and therefore had a much smaller impact on the global clustering of impact craters.

Figure 4.6 shows the results from the basin data set by Orgel et al. (2020). Orgel et al. (2020) grouped basins into categories of "certain", "certain and probable", and "certain, probable, and tentative" basins and analyzed whether there is a basin asymmetry between the hemispheres on Mercury. We adopt their classification to re-analyze the distribution of Mercury's basin population. Note however, that the number of basins is much lower than the number of craters that are used to analyze the cratering record with $D < 300\,\mathrm{km}$. Therefore, the results are not directly comparable to the spatial randomness of Mercury's cratering record.

In all basin categories, randomness is not rejected at two-sigma confidence by either approach, with percentiles ranging from 17 % to 96 % (M2CND) as well as from 24 % to 91.1 % (SDAA) along with Z-scores between -0.95 and 1.71 (M2CND) as well as -0.51 and 1.39 (SDAA). Although the map plots in Figure 4.6 indicate that the number of basins is larger in the western than in the eastern hemisphere, as pointed out by Fassett et al., (2012) and Orgel et al., (2020), the results do not imply that such an asymmetry corresponds to a strictly non-random distribution of basins. Thus, the large basin distribution on Mercury could nevertheless represent a random population.

4.3.2 Venus

4.3.2.1 Background

Compared to other planetary bodies in the inner Solar System, the number of craters on Venus is low (Figure 4.7) with most craters showing pristine topographic features (e.g., Phillips et al., 1992; Schaber et al., 1992; Strom et al., 1994; Kreslavsky et al. 2015). Despite the presence of various geologic units that are stratigraphically different (e.g., Phillips et al. 1992; Basilevsky et al.,1997; Basilevsky & Head, 1998; Basilevsky & Head, 2000; Basilevsky & Head; 2006; Ivanov & Head, 2011; Ivanov et al., 2015; Kreslavsky et al. 2015), crater size-frequency distribution analyses have shown that there is very little variation in the spatial densities of impact craters between them (e.g., Schaber et al., 1992; Strom et al. 1994; Kreslavsky et al., 2015). This indicates that the observable surface of Venus is very young and that the visible cratering record accumulated over a recent period of probably a few hundred million years (e.g., Phillips et al. 1992; Strom et al. 1994; Herrick & Rumpf, 2011; Kreslavsky et al., 2015). Accordingly, the geologic history of Venus has strongly been influenced by resurfacing events that erased pre-existing craters, mainly due to volcanic and tectonic events (e.g., Schaber et al. 1992).

There are two scenarios that describe the resurfacing history of Venus – equilibrium resurfacing and global resurfacing. In the equilibrium scenario (e.g., Phillips et al., 1992; Guest & Stofan 1999; Bjonnes et al., 2012), volcanic and tectonic resurfacing occurred at a somewhat constant rate throughout the geologic history of Venus. This implies that the observable cratering record is related to a global crater equilibrium, where craters accumulate at the same rate they are erased. In the global resurfacing scenario (e.g., Phillips et al. 1992;

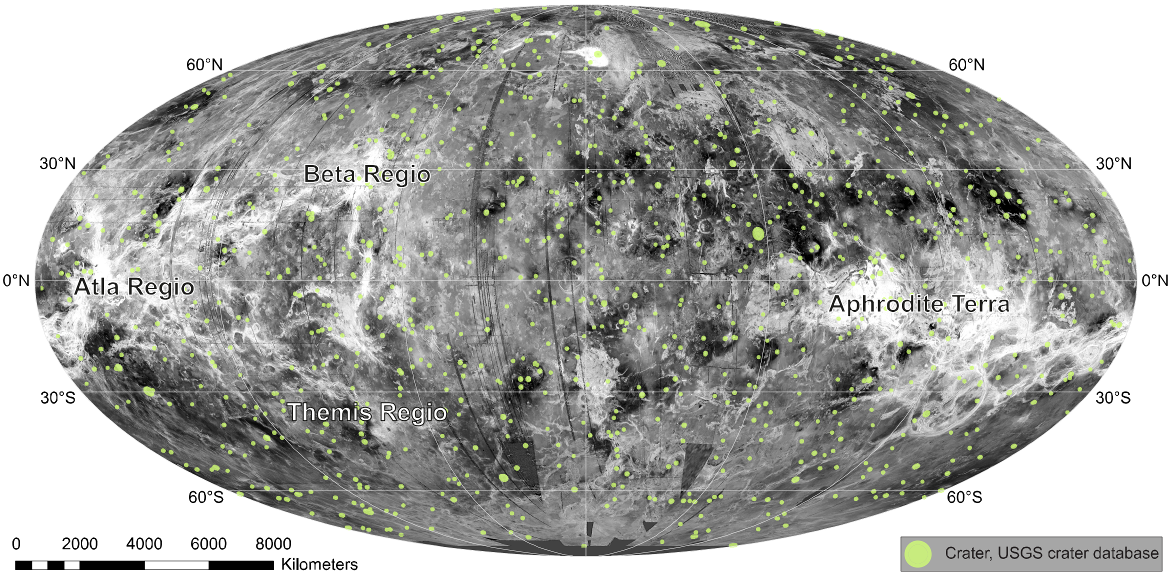

***Figure 4.7:** Map in Mollweide projection showing impact craters on Venus from the USGS Crater Database on a C3-MIDR Magellan radar mosaic.*

Schaber et al., 1992; Price and Suppe, 1995; Strom et al., 1994; Basilevsky et al., 1997; Basilevsky & Head, 2000; Basilevsky & Head, 2006; Ivanov & Head, 2011; Ivanov et al., 2015; Kreslavsky et al., 2015; Airey et al., 2017), an epoch of intensive volcanism and tectonic resurfacing eliminated all craters that pre-date the current surface units. This was followed by an epoch of decreasing and spatially limited resurfacing activity (see e.g., Ivanov & Head, 2011) during which the observable geologic record was formed, and impact craters accumulated. Accordingly, the observable crater record on Venus largely resembles the production population and has only experienced limited volcanic and tectonic modification (e.g., Schaber et al., 1992; Price & Suppe, 1995; Strom et al. 1994). Due to the presence of many well-preserved impact craters (e.g., Schaber et al., 1992; Strom et al. 1994), similar crater size-frequency distributions and crater retention ages on stratigraphically different units (e.g., Schaber et al., 1992; Strom et al. 1994; Kreslavsky et al., 2015), and investigations on rift evolutions (e.g., Airey et al., 2017), most recent publications favor the global resurfacing scenario in order to describe the resurfacing history of Venus. However, this scenario is still under investigation. For example, the observations by Hauck et al. (1998) and Bjonnes et al. (2012) suggest that the equilibrium scenario cannot be excluded and that, according to Grindrod et al. (2010), Herrick & Rumpf (2011), and O'Rourke et al. (2014), the influence of volcanic and tectonic activity on crater modification may be underestimated.

In this context, the spatial randomness of impact craters was also examined and it was found that the global cratering record on Venus is randomly distributed across all crater sizes (e.g., Phillips et al., 1992; Strom et al. 1994; Turcotte et al., 1999; Hauck et al., 1998; O'Rourke et al., 2014). While Strom et al. (1994) used a chi-squared test on the sine of latitude for this purpose, Phillips et al. (1992), Hauck et al. (1998), Turcotte et al. (1999), and O'Rourke et al. (2014) used a more sensitive approach based on the nearest neighbor relationships from angular distances. Here, we re-investigate the spatial randomness of Venus' observable impact crater record based on geodesic M2CND and SDAA measurements. To this end, we use the USGS Venus Crater Database

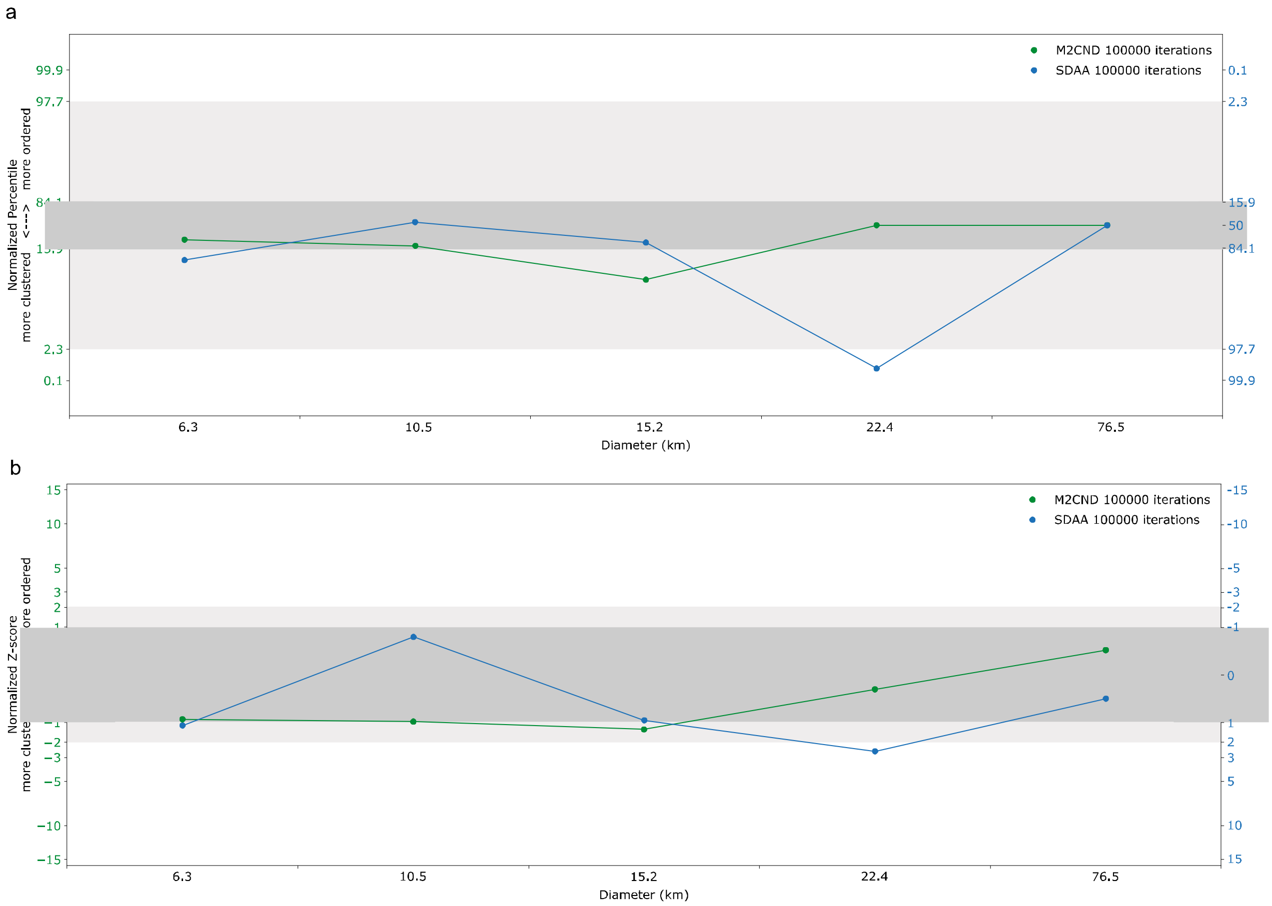

Figure 4.8: *Normalized Percentile (a) and Z-score (b) for binned crater data on Venus, derived from geodesic M2CND (green) and SDAA (blue) analyses. M2CND, mean second closest neighbor distance; SDAA, standard deviation of adjacent area.*

(see e.g., Schaber et al. 1992, Strom et al. 1994, Schaber et al. 1995) with a total of 967 craters from 1.3 to 270 km in diameter.

4.3.2.2 Results

Figure 4.8 summarizes the results from the geodesic M2CND and SDAA analyses for each bin of the crater data set (for details, see Figure S13). It shows that in most cases, the crater populations cannot be distinguished from a random population at two-sigma confidence. The crater population with $D_{\mathrm{mean}} = 22.4$ km however, is an exception. While the M2CND analysis does not reject randomness even at a one-sigma confidence level, randomness is rejected at two-sigma confidence in the SDAA analysis. Accordingly, the SDAA approach reacts more sensitively to the different densities of impact craters in this bin than the M2CND approach. The map plot in Figure 4.9 indicates that areas where craters with $15.19\ \mathrm{km} \leq D \leq 33.09\ \mathrm{km}$ are somewhat less abundant are irregularly distributed across the surface. Extended areas with lower crater densities occur for example along 140°W, between 60°N and 40°S and along 20°S, between 60°E and 180°E. Although not exclusively, these areas include Aphrodite Terra area, as well as the rift zones and lobate plains of eastern Aphrodite and the Beta-Atla-Themis region. While the overall low number of small craters on Venus may be related to atmospheric filtering (e.g., Schaber et al., 1992; Strom et al., 1994) and the rejection of randomness may have a stochastic origin, the

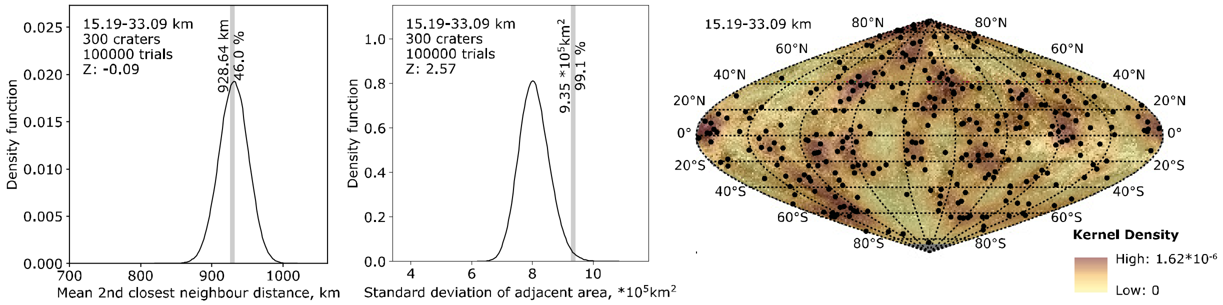

Figure 4.9: *Results from the randomness analyses of craters with* $D_{mean} = 22.4$ *km. The map shows the distribution of craters together with crater density based on a kernel density estimation.*

rejection of randomness in the SDAA analysis could as well be caused by local crater degradation from volcanic and tectonic events in those regions. Although recent volcanic activity on Venus is less pronounced than on Earth (e.g., Strom et al., 1994), the Beta-Atla-Themis region has been identified as an area of recent volcanic activity (e.g., Head et al., 1992; Schaber et al., 1992; Airey et al., 2017). It is therefore possible that craters have not only been modified, but also erased in these regions (e.g., Strom et al., 1994; Grindrod et al., 2010; Herrick & Rumpf, 2011), which in turn could result in a nonrandom distribution of craters with $15.19\,\text{km} \leq D \leq 33.09\,\text{km}$. However, given that randomness is not rejected at two-sigma confidence in the remaining bins, this effect would be very low compared to other planetary bodies in the inner Solar System. This implies that ever since the observable cratering record accumulated on Venus, no resurfacing event was strong enough to cause significant non-randomness of craters on a global scale. However, this does not exclude the possibility of local crater erasure by volcanic or tectonic events.

This alone however, would not necessarily reject the possibility of an equilibrium resurfacing scenario. In order to erase craters at a somewhat constant rate and to keep the global crater population spatially random, the local resurfacing events must have been efficient at degrading craters but weak at resurfacing on a global level. Still, such a scenario seems unlikely since the presence of extended areas of recent volcanic activity would contradict a random distribution of craters on Venus (e.g., Kreslavsky, 1996; Romeo & Turcotte, 2009; Romeo, 2013). Therefore, the results from the geodesic M2CND and SDAA analysis are most consistent with the global resurfacing scenario, where craters accumulated in an epoch of decreasing and spatially limited volcanic and tectonic activity (e.g., in the Beta-Atla-Themis region). In this scenario, we see a crater population that is spatially random for the most part, but where local variations in spatial crater densities due to volcanic and tectonic activity can cause a non-random cratering record to some extent.

4.3.3 Moon

4.3.3.1 Background

Due to the absence of an atmosphere and limited surface modification processes during its evolution, the Moon has the best preserved cratering record in the inner Solar System (Figure 4.10). The lunar cratering record has been used to understand the bombardment history and the planetary surface evolution on various other bodies in the Solar System (e.g. Neukum et al., 2001a; Strom et al., 2005; Stöffler et al., 2006; Fassett, 2016; Orgel et al. 2018).

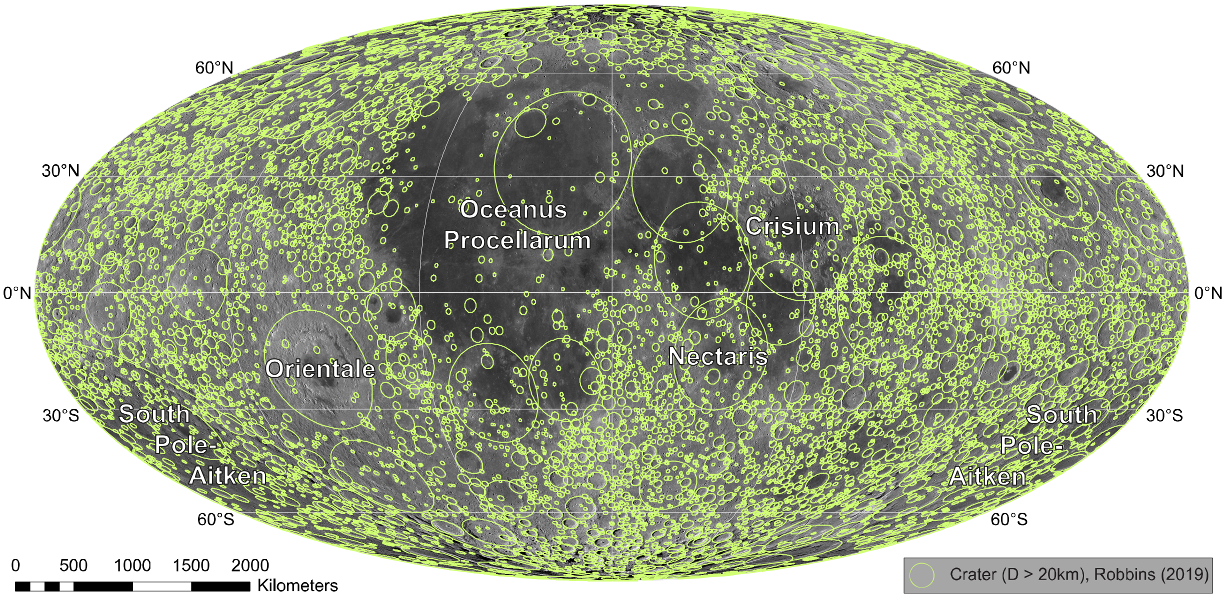

Figure 4.10: *Map in Mollweide projection showing impact craters ($D > 20$ km) on the Moon from the Robbins (2019) data set on an LROC WAC mosaic*

Intensive bombardment and accretion of basins and craters as well as lunar volcanism have led to the formation of two major geologic units—low albedo lunar maria with smooth terrain and high albedo lunar highlands with rough terrain (e.g., Wilhelms, 1987). The lunar highlands contain the oldest lunar surface units and cover large parts of the lunar surface. They are heavily cratered, with a high density of large craters. Crater retention ages show that some lunar highland units may have surface ages of >4.3 Ga (e.g., Neukum & Ivanov, 1994; Orgel et al., 2018). The lunar maria, on the other hand, are sparsely cratered with a lower density of large craters. They are a result of flood volcanism and consist of younger surface units, which formed in topographic lows, often within old basins (e.g., Head & Wilson, 1992; Wilhelms, 1987). Lunar maria cover roughly 17% of the lunar surface (e.g., Head & Wilson, 1992), the vast majority of which is located on the lunar nearside around the Procellarum KREEP terrane (PKT). On the farside, the lunar maria are sparsely distributed and cover much smaller areas, mostly within large craters and basins. The asymmetric distribution of lunar maria has been attributed to increased volcanic activity on the lunar nearside due to a thinner crust and a higher abundance of heat producing elements (e.g., Head & Wilson, 1992; Joliff et al., 2000; Miljković et al., 2013; Wieczorek et al., 2012; Zhu et al., 2019). This in turn, resulted in higher subsurface temperatures compared to the lunar farside and the formation of larger craters and basins due to differences in target properties (Miljković et al., 2013). Crater retention ages revealed that most nearside mare were emplaced at the late stage of lunar basin formation, during the late Imbrian period, around 3.3–3.7 Ga (Hiesinger et al., 2000, 2003, 2011). Volcanic activity decreased after the late Imbrian and came to an end around 1.2 Ga, when the youngest mare units in the center of the Procellarum KREEP terrane were emplaced (Hiesinger et al., 2003). Due to the decrease in cratering rate (e.g., Neukum & Ivanov, 1994), the lunar maria are in a much more sparsely cratered state than the lunar highlands, despite their relatively long exposure to impact cratering.

With the exception of mare emplacement, geologic resurfacing and crater erasure on the Moon has largely been controlled by impact cratering processes. Cratering-related effects that contribute to the erasure of the lunar cratering record include 'cookie cutting' which occurs when cratering becomes non-sparse (e.g., Woronow, 1977; Richardson, 2009; Kneissl et al., 2016; Povilaitis et al., 2018; Orgel et al., 2018; Riedel et al., 2018; Minton et al., 2019), sandblasting which contributes to topographic diffusion and simple crater equilibrium (e.g., Soderblom, 1970; Minton et al., 2019), and burial by proximal ejecta blankets (e.g., Richardson, 2009). The intensity to which the individual processes influence the modification of the topography likely depends on the size of the impact (Riedel et al., 2020). Accordingly, the lunar landscape and the visible cratering record is highly influenced by crater formation and erasure. Here, we apply geodesic M2CND and SDAA statistics to investigate the global spatial randomness of lunar impact craters with $D \geq 20.08$ km. To this end, we use the lunar crater catalogue by Robbins (2019) with a total of 6973 digitized craters larger than 20 km in diameter. Smaller craters, although included in the catalogue, are not taken into account in the investigation. Due to the low number of basins, we investigate the lunar cratering ($D < 300$ km) and basin record ($D \geq 300$ km) separately.

4.3.3.2 Results

The results from the geodesic M2CND and SDAA analyses are summarized in Figure 4.11 (for details, see Figures S14-S22). It shows that randomness is rejected at two-sigma confidence for nearly all binned crater populations. The significance at which randomness is rejected is stronger in the SDAA analysis, which implies that the approach reacts more sensitively to the given crater configurations than the M2CND. There are two of 45 bins where randomness is not rejected at two-sigma confidence. In bins with $D_{\text{mean}} = 29.5$ km and $D_{\text{mean}} = 87.0$ km, 13% and 2.75 % of randomly distributed data sets yield a lower M2CND value than the given population, resulting in Z-scores of -1.13 and -1.96, respectively. However, given that the remaining binned populations as well as the SDAA analysis reject randomness at two-sigma confidence, we consider this a stochastic effect rather than an indication for a randomly distributed population.

The results from the randomness analysis largely confirm previous investigations on lunar surface evolution and can therefore be used as an indicator that our geodesic modification of the M2CND and SDAA statistics deliver valid results. For example, the map plots (Figures S14-S22) indicate that throughout all sizes, there is a global clustering of impact craters in the binned crater populations due to differences in crater densities between ancient lunar highlands and younger surface units. These younger units involve the extended mare deposits on the lunar nearside as well as the area that surrounds Orientale basin, the youngest large basin on the Moon (e.g., Orgel et al., 2018). Accordingly, the lower density of impact craters together with a rejection of randomness confirms that a large part of pre-existing craters were erased by the Orientale impact event and mare volcanism (e.g., Fassett et al., 2011a; Whitten et al., 2011; Povilaitis et al., 2018).

Mare volcanism in the PKT occurred during the Imbrian, Eratosthenian, and Copernican periods, with the youngest volcanism occurring in the central PKT region (e.g., Hiesinger et al., 2003). In contrast, the mare units surrounding the center of the PKT as well as the mare areas east of it were emplaced during an earlier episode of mare volcanism, mainly during the late Imbrian period (e.g., Hiesinger et al., 2000; Hiesinger et al.,

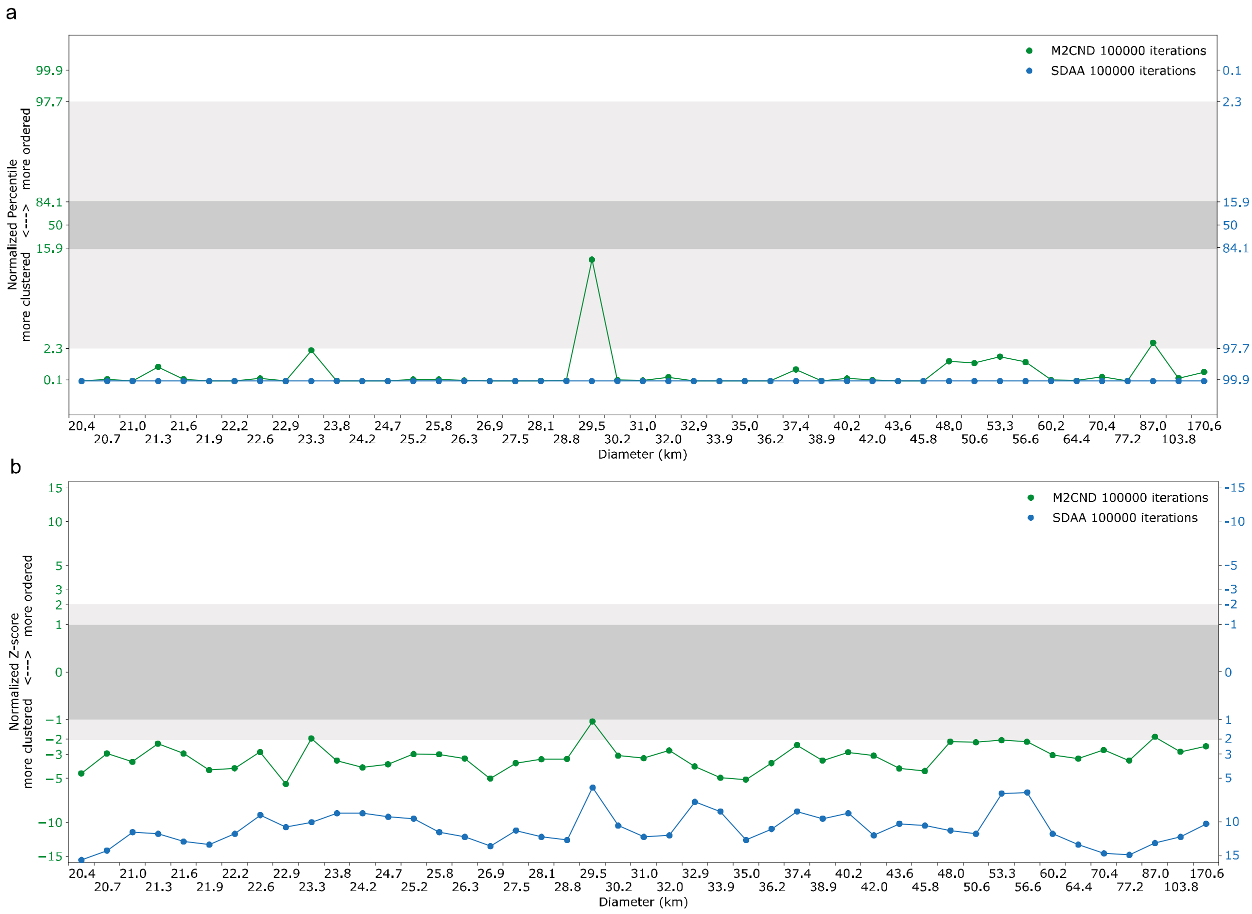

Figure 4.11: *Normalized Percentile (a) and Z-score (b) for binned lunar crater data, derived from geodesic M2CND (green) and SDAA (blue) analyses. M2CND, mean second closest neighbor distance; SDAA, standard deviation of adjacent area.*

2003; Hiesinger et al., 2006; Hiesinger et al., 2011). As a result of the different timing of mare emplacement, smaller craters with $D < 32$ km could largely accumulate in mare regions east of the PKT and around large basins, such as Crisium and Nectaris, where mare volcanism ended early, whereas ongoing mare volcanism in the central PKT contributed to a longer lasting erasure of craters, which can be seen in a low abundance of craters in all bins (Figures S14-S22). Furthermore, crater populations within the PKT are not necessarily affected by a superposing basin impact. This suggests that mare emplacement in this area could have caused the erasure of large pre-existing craters larger than 100 km in diameter. Buried craters of such size have been identified by Evans et al. (2016) and Sood et al. (2017) beneath lunar mare deposits. Accordingly, lunar mare deposits in this region would have to reach thicknesses of several kilometers in order to completely cover such craters. Although the depth of lunar mare deposits is poorly constrained, various studies found evidence for a similar thickness of lunar nearside maria (e.g., Williams & Zuber, 1998; Thomson et al., 2009; Gong et al., 2016).

In contrast to the cratering record ($D <$ 300 km), randomness is not rejected at two-sigma confidence for lunar basins with $D \geq$ 300 km (Figure 4.12). The obtained M2CND value is larger than in 87.6 % of the randomly distributed data sets ($Z = 1.14$) and the obtained SDAA value is larger than 29.4 % of the randomly

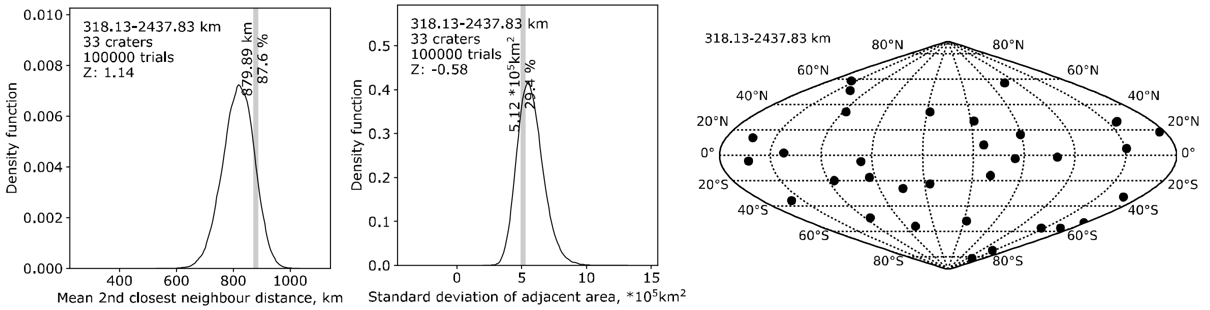

Figure 4.12: Histogram and map plots for lunar basins. The distribution of basins is shown in sinusoidal projection.

distributed data sets ($Z = -0.58$). However, since all basins are summarized in one bin, a detailed distinction between basin sizes is not possible. This implies that the non-rejection of randomness at two-sigma confidence does not necessarily contradict an asymmetry in target properties at the time of basin accretion, which influenced the final size of lunar near side and far side basins (Miljković et al., 2013). Such an investigation using M2CND and SDAA statistics would require a further subdivision of the basin population, which would involve fewer craters in the M2CND and SDAA analyses. Since involving fewer craters would yield in less representative results, M2CND and SDAA are not suitable in making such distinction from the lunar basin record. Furthermore, as the number of basins per bin is far less than 300, the results from the randomness analysis of lunar basins are not directly comparable to the spatial randomness of the lunar cratering record ($D < 300$ km).

4.4 Conclusions

In this paper, we presented improved techniques to quantify the global spatial randomness of impact craters with respect to planetary curvature. The methods are applicable on all planetary bodies that are well approximated by a sphere. As the presented approaches are sensitive to the number of input craters, the planetary cratering records are subdivided into populations of the same quantity. Thus, it is possible to identify size-dependent variations from spatial randomness and to directly compare the spatial randomness of cratering records on different planetary bodies. The size of the subdivisions is a balance between a minimum number of craters at which variations from spatial randomness due to resurfacing events are detected and a maximum number of craters at which size-dependent variations in spatial randomness can still be identified. In our investigation, we subdivided the cratering record of the investigated bodies into bins of 300 craters to compare the results of Mercury, the Moon, and the cratering record of Venus. This number can certainly be adjusted. However, we recommend using 300 as a minimum number to properly identify non-random populations and to minimize stochastic effects when quantifying the spatial randomness of impact craters. We also recommend using both (or further) approaches to identify deviations from non-random populations since different methods can react at specific sensitivities to certain non-random distributions. In general, the SDAA approach showed a higher sensitivity towards non-random distributions in the given crater populations.

On Mercury, we identified a global clustering of impact craters with $20.36\,\text{km} \leq D < 300\,\text{km}$ due to the emplacement of extensive smooth plains deposits and the Caloris impact event. However, since the timing between the emplacement of inter-crater plains and smooth plains is relatively close, the deviations from random populations are generally less significant than on the Moon. Particularly with the M2CND analysis, a random distribution of craters was not rejected at two-sigma confidence in various populations. This implies that, although major resurfacing events occurred on Mercury that cause the global cratering record with $20.36\ \mathrm{km} \leq D < 300\ \mathrm{km}$ to be in a clustered distribution, their influence on the global spatial randomness is less intense than on the Moon. Furthermore, the SDAA approach is more sensitive in recognizing such a resurfacing scenario. In contrast, a random distribution of basin-sized craters, was not rejected at two-sigma confidence, although previous studies indicated a basin asymmetry between Mercury's eastern and western hemisphere (Fassett et al., 2012; Orgel et al., 2020).

The randomness analyses show that craters on Venus are largely randomly distributed across all sizes. However, randomness was rejected at two-sigma confidence for the crater population with $D_{\mathrm{mean}} = 22.4\ \mathrm{km}$ using the SDAA approach. Although it is not clear whether the rejection of randomness is due to a stochastic effect, some of the areas where the crater density of this population is lower correspond to regions of recent volcanic activity. We therefore suggest that local volcanic activity on Venus may have contributed to crater erasure, which in turn can result in a certain non-random distribution of impact craters. Our results also confirm that the influence of recent volcanism on crater erasure was not strong enough to cause a significant clustering of impact craters on a global scale across all crater sizes. The given configuration could in principle be explained by an equilibrium resurfacing scenario in which the given crater configurations were caused by volcanic processes that are highly efficient at erasing craters at a local scale, but weak at resurfacing on a global level. However, such a scenario seems less likely since the geologic units in which recent volcanic modification occurred are too large to maintain a random distribution of craters (e.g., Kreslavsky, 1996; Romeo & Turcotte, 2009; Romeo, 2013). Therefore, our results are more consistent with a global resurfacing scenario, in which craters on Venus accumulated in an epoch of decreasing geologic activity and where local crater erasure in areas of recent volcanic and tectonic activity may cause the rejection of randomness in certain crater populations.

The investigation of the lunar cratering record with $20.08\ \mathrm{km} \leq D < 300\ \mathrm{km}$ shows that a random distribution of craters is rejected at two-sigma confidence in almost all populations, with normalized Z-scores that are clearly below the values of Mercury's crater populations in both approaches. Therefore, the global clustering of craters is more pronounced on the Moon than on Mercury. The stronger rejection of randomly distributed crater populations on the Moon is most likely caused by a greater difference in surface age between the oldest and the youngest geologic units, which leads to greater differences in crater densities. The results confirm that mare volcanism, as well as the Orientale impact event, had a major impact on the erasure of the pre-existing crater record. The results also suggest that mare emplacement in the central PKT likely caused the erasure of pre-existing craters larger than 100 km in diameter. This indicates that mare deposits in this region can reach a thickness of several kilometers. In the analysis of the lunar basin record, a random distribution was not rejected at two-sigma confidence by either approach. However, this does not contradict a possible asymmetry in target properties during the time of basin emplacement (e.g., Miljković et al., 2013).

In summary, our improved methods together with a binning of crater populations allow for an accurate randomness analysis of global crater populations. The results are consistent with known population variations on Mercury, Venus, and the Moon and can be used to support a number of surface evolution scenarios on the respective planetary bodies. Therefore, we consider the presented approach to be a robust improvement to measure the spatial randomness of impact craters with respect to the planetary curvature.

Acknowledgements

We thank Mikhail Kreslavsky and an anonymous reviewer for their helpful comments to improve this manuscript. We also thank Caleb Fassett for making his latest crater catalog of Mercury available to us, as well as the contributors to scipy's spherical voronoi algorithm. C. Riedel and C. Orgel were supported by German Research Foundation SFB-TRR 170, Subproject A03-126. G. G. Michael was supported by the German Aerospace Center (DLR), Grant 50QM1702. H. Hiesinger and C. H. van der Bogert were supported by DLR Project 50OW1504. The associated data are available via Mendeley Data: Riedel et al. (2020). Studying the global spatial randomness of impact craters on Mercury, Venus, and the Moon with geodesic neighborhood relationships [Data set]. Mendeley. https://doi.org/10.17632/MN2B542K5R.2.

CHAPTER 5

A NEW TOOL TO ACCOUNT FOR CRATER OBLITERATION EFFECTS IN CRATER SIZE-FREQUENCY DISTRIBUTION MEASUREMENTS

by C. Riedel, G. G. Michael, T. Kneissl, C. Orgel, H. Hiesinger, and C. H. van der Bogert (2018), published in Earth and Space Science, 5, 258-267, https://doi.org/10.1002/2018EA000383.

Abstract: The analysis of crater size-frequency distributions (CSFDs) is a widely used technique to date and investigate planetary surface processes. There are two well-established crater measurement techniques, traditional crater counting and buffered crater counting, and two new geometric corrections, nonsparseness correction and buffered nonsparseness correction. The new techniques consider the effects of crater obliteration and subsequent recratering while measuring CSFDs in areas of high crater density. Currently, the ArcGIS add-in CraterTools can be used to apply the well-established techniques. The tool relies on Esri's ArcGIS environment and is restricted to 32 bit and single-core computing. These limitations make the implementation of the new geometric corrections in CraterTools inefficient, as the new techniques are computationally more intensive than the well-established ones. To this end, we developed CSFD Tools, an application to conduct CSFD measurements from shapefiles. It supports 64 bit and multicore data processing and uses existing open geospatial libraries. Open libraries, however, conduct spatial measurements on a Cartesian plane and do not take a curved planetary surface into account. Therefore, we implemented methods for geodesic measurements and workarounds for the geodesic modification of polygon data to minimize map distortion effects during CSFD measurements. As a result, the new nonsparseness correction and buffered nonsparseness correction techniques can be applied through a software tool.

5.1 Introduction

Absolute and relative ages of planetary surfaces have long been determined by statistical analyses of crater size-frequency distributions (CSFDs; e.g., Baldwin, 1964; Hartmann, 1965; Shoemaker et al., 1962). The procedure combines information from crater formation rates and radiometric ages of lunar rock samples to define relative and absolute chronology models for planetary bodies in the solar system (Neukum, 1983; Neukum et al., 2001a; Stöffler et al., 2006; Stöffler & Ryder, 2001). When investigating a planetary surface, the CSFD of an area of interest can be compared to chronology models. This allows the investigation and dating of planetary surface processes from remotely sensed data.

The CSFD of a given surface unit is obtained by the application of crater measurement techniques. Such techniques describe which craters are included in the process and which reference area is assigned to each crater. There are four techniques available. Traditional crater counting (TCC; used, e.g., by Neukum, 1983 and Hiesinger et al., 2012a) and buffered crater counting (BCC; Fassett et al., 2012; Fassett & Head, 2008; Kneissl et al., 2015; Tanaka, 1982) are well-established techniques and already implemented in a software tool. The nonsparseness correction (NSC) and buffered nonsparseness correction (BNSC; Kneissl et al., 2016; Orgel et al., 2018) are new geometric corrections that have not been implemented in a software tool yet.

5.2 Methods Requiring Implementation

5.2.1 Crater Obliteration and Subsequent Recratering

Crater obliteration and subsequent recratering can affect the shape of the CSFD and lead to variations when compared to observed crater formation rates. It is anticipated that larger craters plus their surrounding ejecta blanket eliminate smaller craters on impact, leading to crater equilibrium (Gault, 1970; Woronow, 1977) or nonsparseness effects (Hartmann, 1995; Kneissl et al., 2016). Due to such effects, the number of craters as seen in remote sensing data may not be consistent with the total number of impact craters which formed over time, particularly on densely cratered surfaces. The new NSC and BNSC techniques perform a geometric correction to consider the underrepresentation of small impact craters on surfaces, which are affected by nonsparseness. Craters that intersect the reference area are enlarged to represent an approximated area in which smaller craters were eliminated by the ejecta blanket of the larger impact. If the centroid of a smaller diameter crater is located inside this area, it is excluded from the analysis. For all remaining craters, all larger diameter craters plus their modeled ejecta zones are removed from the original reference area. In the BNSC approach, the modified reference area is buffered according to the radius of the currently investigated crater. If the centroid of the crater is located inside the modified reference area, it is considered for the CSFD. The new geometric corrections lead to greater consistencies with observed crater formation rates and, hence, improve the quality of CSFD measurements on nonsparsely cratered surfaces. The benefits of BNSC are described in details by Kneissl et al. (2016) and Orgel et al. (2018).

Currently, the Esri ArcGIS add-in CraterTools (Kneissl et al., 2011, available at http://www.geo.fu-berlin.de/en/geol/fachrichtungen/planet/software/index.html) can be used to conduct CSFD measurements. Together with ArcGIS, the add-in provides an environment for the manual identification of impact craters from remote sensing data and the application of the well-established CSFD measurement techniques. The new NSC and BNSC techniques are not implemented. Compared to TCC, BCC, and NSC, the BNSC technique requires more computational resources due to more complex modification of the given reference area (Figure 5.1). CraterTools, however, relies on Esri's ArcObjects environment, which limits data processing to 32 bit and single-core computations. This makes the implementation of BNSC in CraterTools impractical. To overcome the given limitations and to efficiently implement NSC and BNSC in a software tool, we developed a new application to derive CSFD information from shapefiles. The new software tool supports multicore and 64 bit computations and uses the open GDAL and Shapely libraries for the handling of geospatial data. However, geospatial measurements with GDAL and Shapely are not performed on a sphere or spheroid but within a Cartesian map projection. Neglecting the

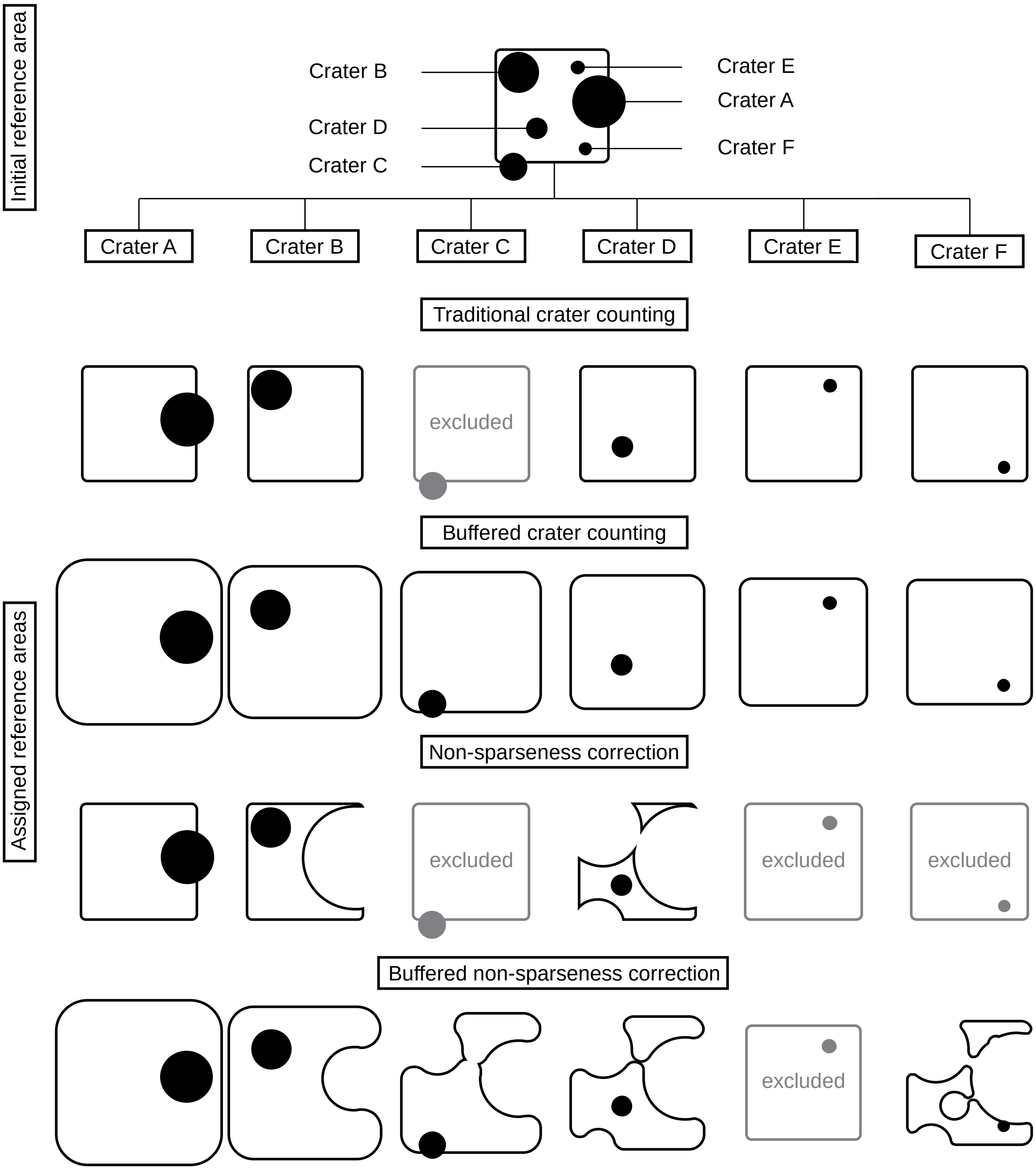

Figure 5.1: *Assignment of reference areas for four crater measurement techniques. This schematic example uses a rectangular reference area and six impact craters A–F, with crater A being the largest and crater F being the smallest. In TCC, all impact craters, which have their centroids inside the initial reference area, are included. Crater C is excluded. When using BCC, the initial reference area is extended by one crater radius. All craters are included. During NSC, craters C, E, and F are excluded. Crater C is located outside the initial reference area, and craters E and F are located on top of crater A's ejecta blanket. The ejecta blanket is defined by one crater radius in width. During BNSC, crater E is excluded since it is located entirely on top of crater A's ejecta blanket. However, crater E's ejecta blanket still affects the assigned reference area of crater F.*

influence of a curved planetary body would lead to the derived CSFD information being affected by map distortion errors. Hence, in order to give accurate results, we implemented methods for geodesic measurements and developed workarounds for the modification of polygon data with respect to a curved planetary surface. This allows the use of open geospatial libraries for accurate and consistent generation of CSFDs.

5.2.2 Point, Distance, and Area Measurements on Planetary Surfaces

Position measurements on planetary surfaces are conducted on a three dimensional curved reference body with angular latitude and longitude coordinates. This is commonly represented by a two dimensional Cartesian plane with numerical x and y coordinates. The Cartesian plain is a transformed representation of a planetary surface and is affected by map distortion effects. The distortion effects can influence the true representation of angles, distances and areas (Snyder, 1987). If one map projection is used for all measurements during CSFD measurements, it may lead to imprecise results (Kneissl et al., 2011). However, certain features can be measured in two dimensional map projections without distortion. True areas of polygons for example can be determined from measurements in equal-area map projections. When planetary data is transformed according to such projections, shapes become distorted but areas are preserved with respect to a spherical reference body (Snyder, 1987; Kneissl et al., 2011).

Geodesic measurements, on the other hand, take the effect of a curved planetary body, i.e. a sphere or biaxial ellipsoid, into account and allow the determination of true relationships between two points on a reference body. There are essentially two classes of calculations known as the direct problem and the inverse problem (for details, see Rapp, 1993).

Direct problem: Given are the geographic coordinates λ_1, φ_1 of a point P_1, the geodesic azimuth α_1 and the geodesic distance s to a second point P_2. The geographic coordinates of the second point λ_2, φ_2 and the azimuth of the geodesic line α_2 at P_2 are to be determined:

Given: $\lambda_1, \varphi_1, \alpha_1, s$ Find: $\lambda_2, \varphi_2, \alpha_2$

Inverse problem: Given are the geographic coordinates of two points. The azimuth of the geodesic line at P_1 and P_2 as well as the geodesic distance between both points are to be determined:

Given: $\lambda_1, \varphi_1, \varphi_2, \lambda_2$ Find: α_1, α_2, s

Vincenty's formulae (Vincenty, 1975) are widely used for conducting geodesic measurements between points on a sphere or biaxial ellipsoid. The approach uses great circle calculations on a sphere to determine the final parameters. When a biaxial ellipsoid is used, the given variables are iteratively projected to an auxiliary sphere for computation. The spherical results are eventually projected back to represent the respective values on the given ellipsoid.

5.3 Implementation

5.3.1 Geodesic Polygon Buffer

The application of BCC, NSC, and BNSC requires the use of polygon buffers with respect to a curved planetary surface. Since GDAL's buffer function measures the polygon offset in a two dimensional map projection, we applied the geodesic measurements by Vincenty (1975) to develop an approach for the generation of geodesic polygon buffers. The approach is displayed in Figure 5.2. The outer vertices (P_n) of a polygon are used to determine the coordinates of the buffered

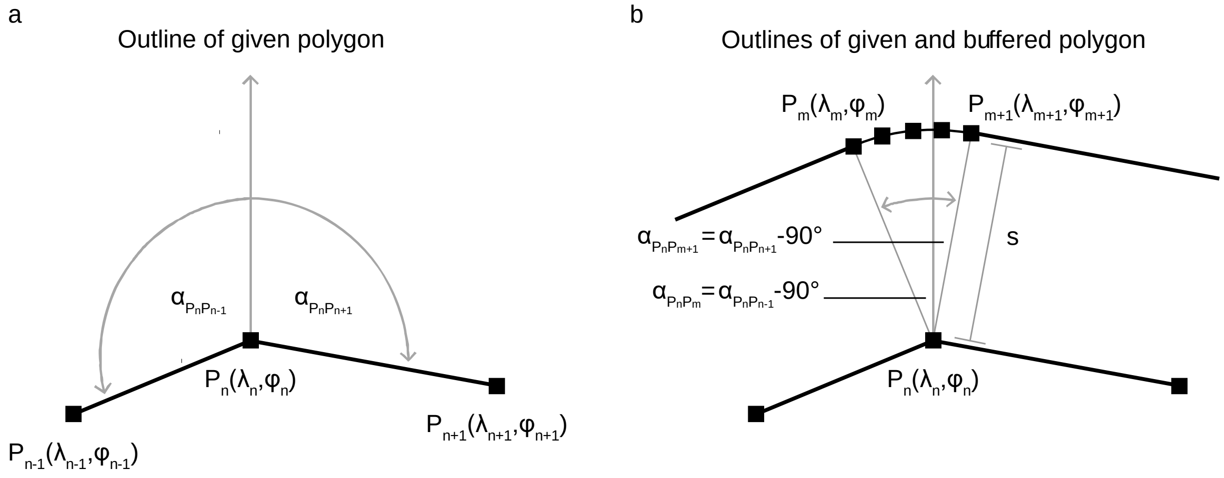

Figure 5.2: *Application of geodesic polygon buffer by using geodesic measurements. Polygon outlines and vertices are shown in black.*

polygon's outer vertices (P_m). For every vertex on a given polygon's outer boundary, the azimuth α between the current and its two neighboring vertices is calculated from their geographic coordinates (λ_n, φ_n) according to Vincenty's inverse formula (Figure 5.2a). Both values are subtracted by 90° to indicate a perpendicular azimuth. The perpendicular azimuth indicates the direction from a vertex to which the vertices of the buffered polygon are created. To generate round edges, further intermediate azimuth values are added. With the geographic coordinates of a given vertex (λ_n, φ_n), the azimuth values to describe the direction of the buffered polygon's vertices ($\alpha_{P_nP_m}$) and the distance of the geodesic buffer (s), the coordinates of the buffered polygon's vertices (λ_m, φ_m) are derived from Vincenty's direct formula (Figure 5.2b).

The connection of individual vertices to shape the buffered polygon may lead to self-intersecting outlines. In such cases, the outermost boundary of the self-intersecting polygon defines the correct outline while the spaces within the self-intersections lead to the formation of holes in the buffered polygon. To avoid this problem, a planar buffer of zero distance as implemented in the GDAL library is applied to the self-intersecting polygon. In doing so, holes from self-intersections are filled and the outer boundary of the geodesically buffered polygon is correctly determined.

This workaround is suitable for a geodesic buffer outlining a polygon. When a given reference area is represented by a polygon with holes, the polygon is split vertically at each of the holes' central meridians. In doing so, a polygon with one hole is described by the outlines of two polygons. The outlines of the polygons are buffered according to the methodology described above and merged. Thus, the geodesic buffer approach can be applied to polygons with holes by only considering the outlines of a polygon..

5.3.2 Measurement of Crater Diameters and Areas

To measure areas and crater diameters in CraterTools, spatial data is projected to the equal-area sinusoidal projection (Kneissl et al., 2011). The projection preserves area sizes and maintains true distances along the central meridian. During digitization of impact craters with CraterTools, the crater diameter is determined by using a sinusoidal projection, which is centered to a crater's centroid. The north-south diameter along the central meridian corresponds to the undistorted metric diameter of the crater. This value is written to the attribute table of the shapefile. However, this process is conducted during digitization and requires the reprojection of the data with every crater. Since CSFD Tools works independently from the digitization environment and the content of the attribute table, a different approach is used. The given shapefile data is projected to Lambert azimuthal equal area (LAEA) projection to measure area sizes of impact craters and reference areas. The central coordinates of the given reference areas is used to define the LAEA projection center. This projection remains unchanged during all measurements. The diameter of a crater is measured from its area size by $D = 2\sqrt{\frac{Area}{\pi}}$. By using one projection for all Cartesian measurements, the number of reprojection processes is reduced and, thus, the computational effort is minimized.

5.3.3 Development

CSFD Tools is available as an executable Windows application. Programming was done in Python 2.7, and the executable file was compiled using PyInstaller. The graphical user interface was developed using PyQt4 bindings and Matplotlib Basemap. GDAL and Shapely libraries are used for the handling of spatial data.

5.3.4 Workflow

CSFD measurements with CSFD Tools are conducted by processing two polygon shapefiles. One shapefile contains circular impact craters and the other shapefile contains reference areas. Any spatial reference can be assigned to the data. Nevertheless, the same spatial reference has to be applied for the crater and the area shapefiles to avoid inconsistencies from map distortion effects between the two data sets.

There are two parameters, buffer factor and obliteration factor, which regulate the modification of the initial reference area during BCC, NSC, and BNSC. The buffer factor (BCC and BNSC) is used to define the buffer distance of the reference area (Kneissl et al., 2015). By multiplying the radius of a crater with the buffer factor, craters, which only partly intersect the reference area, are included in the analysis. The obliteration factor (NSC and BNSC) is used to define the extent of impact craters plus their surrounding ejecta blanket and, thus, the area in which smaller craters have been removed (Kneissl et al., 2016). An obliteration factor of 1 describes the impact crater without ejecta blanket; an obliteration factor of 2 describes an impact crater plus a surrounding ejecta blanket of one crater radius in width.

The workflow to conduct CSFD measurements is shown in Figure 5.3. After measuring crater diameters from LAEA projected data, two major processes are executed. The first process is to identify impact craters that are relevant for the selected measurement technique. The size of the given reference area is measured, and Vincenty's formulae are applied to determine the distance between the centroid of each crater and the reference area. If a crater is located inside the reference area (all techniques) and if the distance between crater center and reference area is smaller than a crater's radius plus ejecta (determined by obliteration factor [NSC] or buffer factor [BCC and BNSC]), a crater is considered for further data processing. During NSC and BNSC, all considered craters are reinvestigated regarding the distance of every crater to all larger craters. If the distance of a crater to any larger crater is smaller than the larger crater's radius plus its ejecta blanket (determined by obliteration factor [NSC and BNSC] and buffer factor [BNSC]), it is excluded

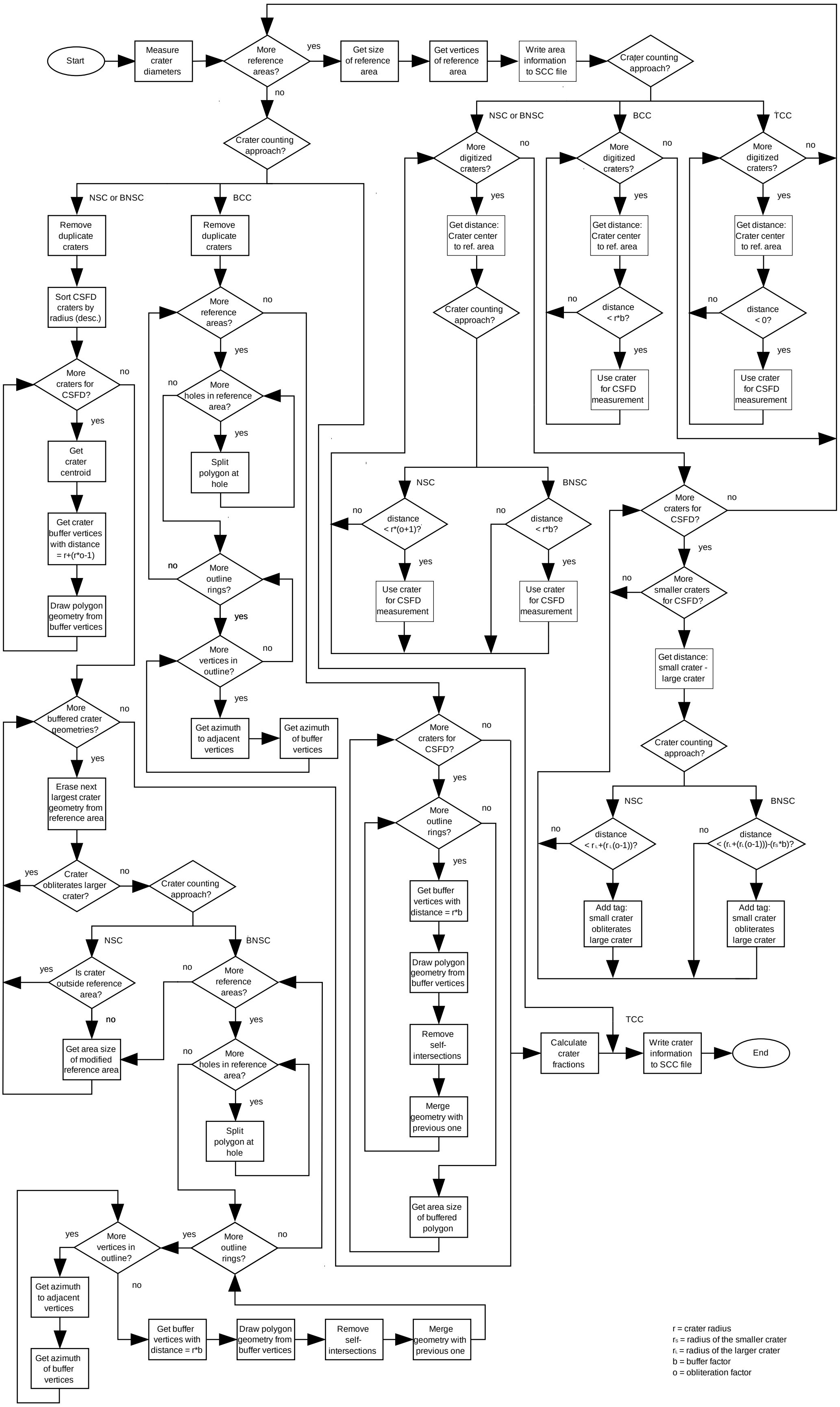

r = crater radius
r_S = radius of the smaller crater
r_L = radius of the larger crater
b = buffer factor
o = obliteration factor

Figure 5.3: Flow chart of CSFD measurements with CSFD Tools.

from the CSFD measurement. The second process is to modify the initial reference area (BCC, NSC, and BNSC). Here the individual reference area that is assigned to each crater is determined. During BCC, the original reference area is buffered for every crater that is included in the CSFD measurement. The buffer distance is determined by a crater's radius and the buffer factor. During NSC and BNSC, all craters are extended to represent the size of craters plus their ejecta blankets. The extent is defined by the radius of a crater and the obliteration factor. The buffering of craters also includes craters that were previously excluded from the analysis. For every crater that is included in the CSFD measurement, all larger buffered craters, that is, craters with their ejecta blankets, are removed from the original reference area. During BNSC, this modified reference area is buffered according to a crater's radius and the buffer factor.

When an individual reference area is generated, the size of the modified reference area is determined. By dividing the size of the original reference area by the size of the modified reference area, a fractional density value is calculated and assigned to each crater. This acts as a coefficient to describe how a crater's density on the original reference area is weighted to correspond to its density on the modified reference area. During NSC and BNSC, for example, the modified reference area decreases in size with decreasing crater diameter. This indicates that small diameter craters are counted on a smaller surface unit that was not affected by crater obliteration. On such a surface, the density of small diameter craters is higher than it would appear on the entire original surface. Accordingly, the weight of small diameter craters on the original reference area is increased by their respective fraction values to correspond to the measured crater densities on the modified areas.

The resulting CSFDs are saved in an SCC or DIAM text file for further statistical CSFD analyses with the Craterstats software (Michael & Neukum, 2010, available at http://www.geo.fu-berlin.de/en/geol/fachrichtungen/planet/software/index.html).

5.4 Discussion

5.4.1 Cartesian and Geodesic CSFD Measurements

CSFD measurements are conducted with respect to the surface of a planetary body. To demonstrate the differences in the CSFD when measurements are conducted in a given map projection, we applied TCC on a densely cratered region on the lunar surface and obtained results from geodesic and Cartesian measurements. Cartesian measurements were conducted in equirectangular and Mercator map projections, centered at 0°N, 0°E. The results are shown in a cumulative size-frequency plot in Figure 5.4.

The application of geodesic and Cartesian measurements leads to changes in crater diameter sizes and varying CSFD shapes. While the shape of the CSFD that was derived from geodesic measurements is largely consistent with the lunar production function, the CSFDs, which were derived from Cartesian measurements, show different shapes. This affects the quality of the production function fit. In the Mercator example, the CSFD is hardly suitable for precisely fitting the production function. The CSFD from equirectangular projection measurements shows a larger consistency with the lunar production function, and results may be similar to the results from the geodesic measurements. However, the difference in the shape of the CSFDs is significant. Due to the influence of map distortion effects, Cartesian measurements are too imprecise to be used for CSFD measurements.

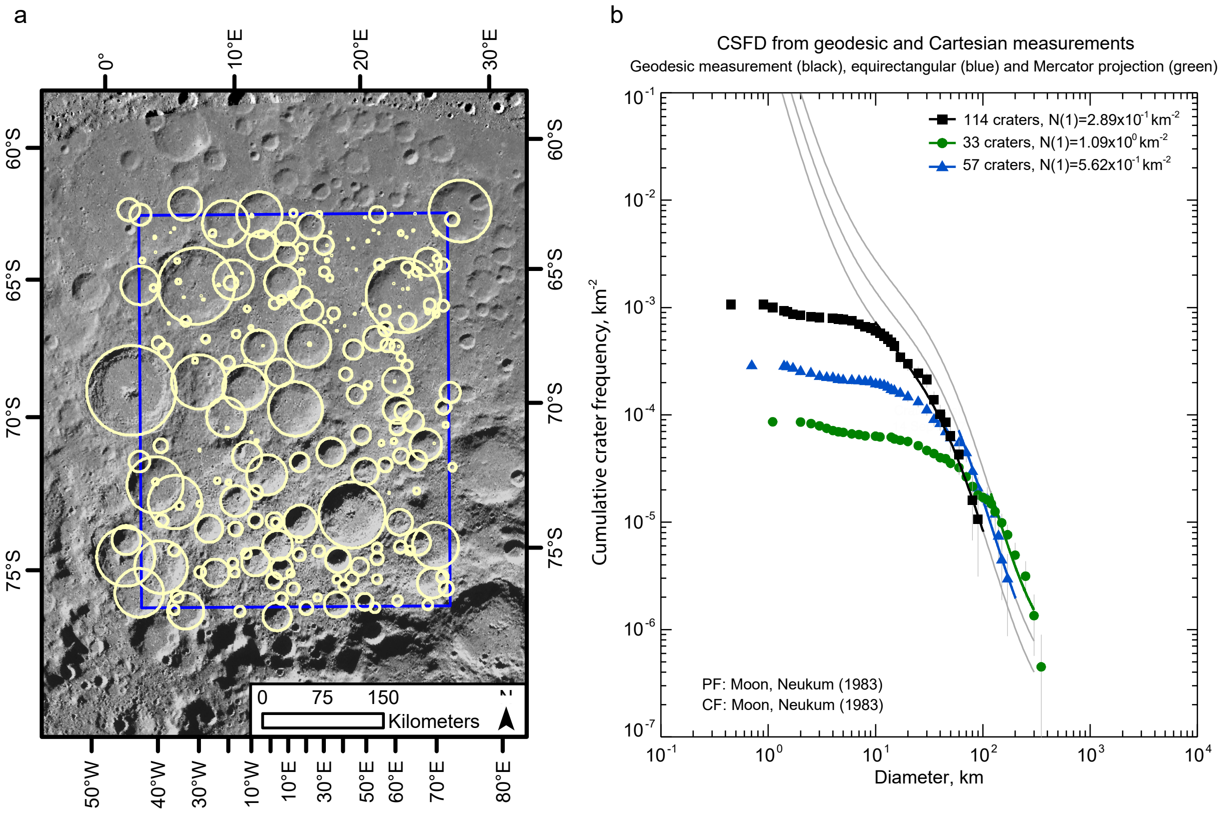

Figure 5.4: Densely cratered reference area (blue) north of Malapert Massif on the lunar nearside at ~15°E, 70°S. The map shows the impact craters (yellow) within this area from the LU78287GT crater catalogue by Salamunićcar et al. (2013) on an LROC-WAC mosaic and is projected in Lambert azimuthal equal area projection (centered at 15°E, 70°S) (a). Resulting CSFDs when data is processed with geodesic (black) and Cartesian equirectangular (blue) and Mercator (green) projection measurements (b).

The accuracy of Vincenty's geodesic measurements depends on the iterative evaluation of geodesic parameters. When using the same iteration criteria as in the original approach, Vincenty's formulae are accurate within 4.2 × 10−9° on the reference body that is used (Vincenty, 1975). Since the approach was implemented without further modification, we evaluate the accuracy as sufficient for geodesic measurements with our application.

5.4.2 Accuracy of Area Measurements

Area sizes with LAEA are preserved on a sphere but distort with growing eccentricity of the reference body. To investigate LAEA area scale errors with biaxial ellipsoidal reference bodies, we used Tissot's indicatrices (for details, see Snyder, 1987). In the approach, circular polygons of constant size are projected from an ellipsoidal reference body to a map projection. The resulting ellipses are used to measure map distortion effects. Here circular polygons with a fixed size of 20 km in diameter were generated using the geodesic buffer approach described in section 5.3.1 and projected to LAEA. We compared the expected size of geodesic circles with measured area sizes in LAEA projection and calculated the aerial distortion in percent. A reference body with a semimajor axis of 1,737.4 km was used, and three different flattening values of 0.175, 0.25, and 0.3 were applied. Circular polygons were generated in a 5° interval between 0 N, 0°E, and 0°N, 180°E along both the ellipsoid's central meridian and the

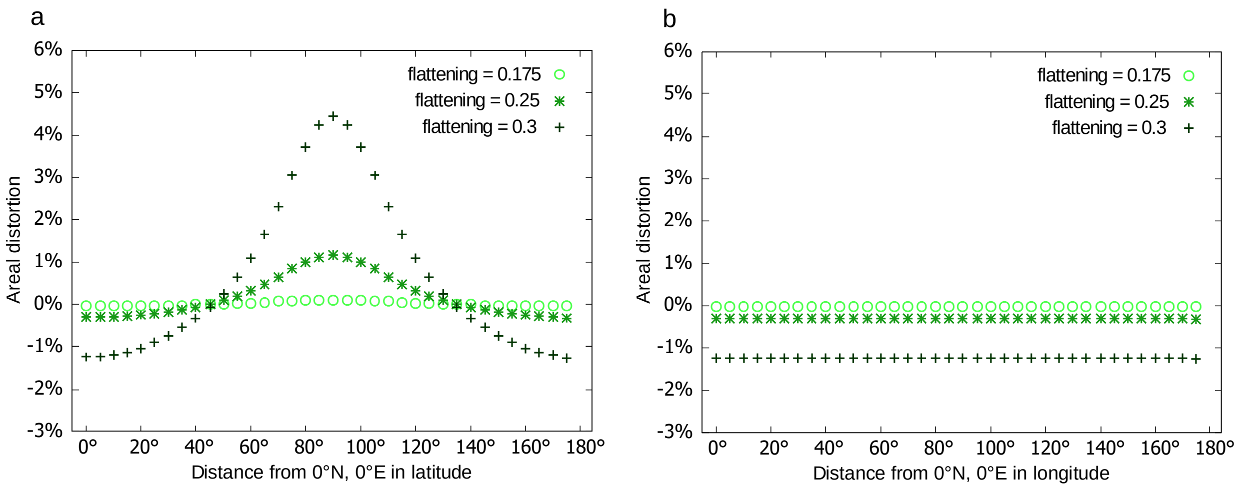

Figure 5.5: *Distortion of area measurements in Lambert azimuthal equal area projection with growing eccentricity of the reference body. Measurements were conducted along the central meridian (where 0°, 90°, and 180° indicate circular polygons at 0°N, 0°E; 90°N, 0°E, and 0°N, 180°E) (a) and the equator (where 0°, 90°, and 180° indicate circular polygons at 0°N; 0°E, 0°N; 90°E and 0°N; 180°E) (b). Differences between geodesic sizes and sizes in LAEA projection are given in percent.*

ellipsoid's equator. The results are visualized in Figure 5.5.

The results show that there is a correlation between area distortion, eccentricity of the reference body, and the location of the data. While the distortion remains constant with changing longitude values (Figure 5.5b), the areal distortion varies notably latitudinally toward the poles (Figure 5.5a). This effect is independent from the LAEA projection center and increases with growing eccentricity of the ellipsoid. However, this effect is only significant on biaxial ellipsoids with a flattening of >0.3 when the maximum area distortions become >5%. Planetary bodies with similar eccentricities as the ones that we investigated have an irregular shape due to their rough topography and are only roughly approximated by a biaxial ellipsoid. On such planetary bodies, variations in measured sizes can occur not only from LAEA distortions but also from the influence of their terrain, that is, when a rough three-dimensional terrain is inconsistent with the shape of the planetary reference body. In these cases, we recommend the application of further topography correction methods (e.g., Kneissl et al., 2014).

However, severe distortions occur with antipodal polygons. In our investigation, circles with a distance of 180° from the projection center were measured to be larger than the surface of the respective ellipsoid. For scaling reasons, they are not displayed in Figure 5. The antipodal distortion in LAEA is related to the antipode of the LAEA projection center. To minimize this effect during CSFD measurements, the LAEA projection center is defined by the center of the reference area. Thus, a modified reference area would have to cover the whole reference body to be affected by antipodal distortion. This can be avoided by selecting reference areas that do not exceed 180° in extent when modified with BCC or BNSC.

5.5 Conclusions

We developed an application to execute CSFD measurements from shapefiles generated on planetary surfaces. The necessary information are obtained from polygon geometries and shapefile metadata and do not depend on values from the attribute table. Accordingly, any desktop geographic information system can be used to digitize the data. The tool uses GDAL and Shapely libraries to avoid the performance limitations of the ArcGIS environment. However, spatial operations with GDAL and Shapely are conducted on a two-dimensional Cartesian plane. We developed workarounds for the processing of spatial data with respect to a curved planetary surface. The implemented methods are valid for CSFD measurements on planetary bodies that can be approximated by a biaxial ellipsoid with a flattening of 0.3 or lower with a precision of better than 5%. Data processing was parallelized for multicore support to increase performance. This is mandatory for the implementation of the new NSC and BNSC techniques and will allow further analyses on the geologic history of planetary bodies in the Solar System. However, since existing production functions were derived using TCC, we recommend further investigations on production function consistencies with obtained CSFDs from NSC and BNSC.

Acknowledgements

We thank two anonymous reviewers for their helpful comments to improve this manuscript. C. R. and C. O. were supported by German Research Foundation SFB-TRR 170, subproject A03-46. G. M. was supported by the German Aerospace Center (DLR), grant 50QM1702. H. H. and C. H. vdB were supported by DLR project 50OW1504. CSFD Tools is available via http://www.geo.fu-berlin.de/en/geol/fachrichtungen/planet/software/index.html. The source code of the application is accessible via https://github.com/ch-riedel/CSFD_Tools.

PART III

PLANETARY SURFACE EVOLUTION

CHAPTER 6

ANCIENT BOMBARDMENT OF THE INNER SOLAR SYSTEM: REINVESTIGATION OF THE FINGERPRINTS OF DIFFERENT IMPACTOR POPULATIONS ON THE LUNAR SURFACE

by C. Orgel, G. G. Michael, C. I. Fassett, C. H. van der Bogert, C. Riedel, T. Kneissl, and H. Hiesinger (2020), published in Journal of Geophysical Research: Planets, 123(3), 748-762, https://doi.org/10.1002/2017JE005451.

Abstract: The lunar cratering record provides valuable information about the late accretion history of the inner solar system. However, our understanding of the origin, rate, and timing of the impacting projectiles is far from complete. To learn more about these projectiles, we can examine crater size-frequency distributions (CSFDs) on the Moon. Here we reinvestigate the crater populations of 30 lunar basins (≥ 300 km) using the buffered nonsparseness correction technique, which takes crater obliteration into account, thus providing more accurate measurements for the frequencies of smaller crater sizes. Moreover, we revisit the stratigraphic relationships of basins based on N(20) crater frequencies, absolute model ages, and observation data. The buffered nonsparseness correction-corrected CSFDs of individual basins, particularly at smaller crater diameters are shifted upward. Contrary to previous studies, the shapes of the summed CSFDs of Pre-Nectarian (excluding South Pole-Aitken Basin), Nectarian (including Nectaris), and Imbrian (including Imbrium) basins show no statistically significant differences and thus provide no evidence for a change of impactor population.

6.1 Introduction

The Moon has the best preserved impact record in the inner solar system due to the absence of an atmosphere and the extremely low rates of surface modification. The lunar cratering record has long been used by the planetary community to determine relative and absolute surface ages (Baldwin, 1964; Neukum, 1983; Öpik, 1960) and provides valuable information about the late accretion history of the inner solar system. Crater size-frequency distributions (CSFDs) have been used to define the lunar "production function" (PF) (Neukum, 1983), which describes the population of craters forming on the Moon's surface. The PF can be used to extrapolate the measured CSFD from a particular surface unit to a reference diameter (1 km) whose frequency will give an absolute model age from the lunar "chronology function" (CF) (Neukum, 1983). Neukum's approach assumes that the PF has remained unchanged, but this is debated (Bottke et al., 2007; Fassett et al., 2012; Head et al., 2010; Marchi et al., 2012; Morbidelli et al., 2012; Strom et al., 2005). Neukum (1983) and Hartmann (1995) argued it is possible to use one PF to analyze CSFDs from surfaces of all ages, but if this is not correct, it would systematically affect the derived age results. If the PF has been unchanged, this could suggest the Moon had only one impactor population, or that multiple populations that contributed to its impact record had the same size-frequency distribution. For example, collisional evolution tends to cause all impactor populations to evolve to the same size-frequency distribution (Bottke et al., 2005). However, if it can be shown that the PF changed over time, it would also indicate that more than one impactor population may have contributed to the lunar cratering record (O'Brien & Greenberg, 2003). Therefore, constraining whether the PF shape changed over time is crucial for improving this widely used method of crater-based age determination on the Moon and other planetary bodies.

Many potential projectile families for the Moon exist, such as main-belt asteroids, asteroids from the hypothesized E-belt a proposed inner extension of the asteroid belt that is now mostly extinct, comets, or even remnant ejecta fragments from the giant impact that formed the Moon (Bottke et al., 2012, 2015; Gomes et al., 2005; Morbidelli et al., 2010; Strom et al., 2005). These objects are characterized by specific projectile size-frequency distributions that can be scaled to crater sizes using crater scaling laws (Housen & Holsapple, 2011; Ivanov, 2001). Since the shape of the CSFD in the absence of modifying processes is directly connected to the size-frequency distribution of the impacting projectiles, this shape can be used to identify the projectile source(s). Determining the source region(s) of the impacting projectiles is of particular importance for understanding the timing of lunar basin (D ≥ 300 km) formation.

The timing and sequence of impact basin formation are an important part of lunar geologic history. There are two major views about the origin of lunar basins. First, the basins result from the exponentially declining number of planetesimals from planetary accretion (Hartmann, 1995; Neukum, 1983; Neukum & Ivanov, 1994). Second, the basins formed in an impact spike, called Late Heavy Bombardment (LHB) or the terminal lunar cataclysm originally based on the radiometric ages of lunar samples, which concentrated around 3.9 Gyr (Stöffler & Ryder, 2001; Tera et al., 1974). However, the timing and nature of the cataclysm are both debated. It was proposed based on the Nice model (Gomes et al., 2005; Morbidelli et al., 2005, 2012; Tsiganis et al., 2005) that the migration of the giant planets could have destabilized the Main Asteroid Belt and the hypothesized E-belt and injected projectiles into the inner solar system. Furthermore, numerical models (Bottke et al., 2012; Marchi et al., 2012; Morbidelli et al., 2012) and crater counting results from Fassett et al. (2012) show an uptick in the impact flux near 4.1 Gyr, which could be consistent with the Nectaris basin-forming event; however, this is not fully consistent with the radiometric ages of the lunar samples, which show a peak in impact melt age of 3.9 Gyr at all landing sites.

Several authors have suggested that the shape of the PF changed over time and suggested that different impactor populations may have played a role during the formation of the lunar basins (Bottke et al., 2012; Fassett et al., 2012; Head et al., 2010; Marchi et al., 2012; Morbidelli et al., 2012; Strom et al., 2005). However, different authors proposed different transition times for when the shape of the PF changed, as well as different characteristics for the older and younger populations. Strom et al. (2005) proposed two different impactor populations (Population 1 and Population 2), which formed the oldest lunar basins and bombarded the younger mare terrains, respectively. They argued from the CSFDs that a transition in impactor populations occurred

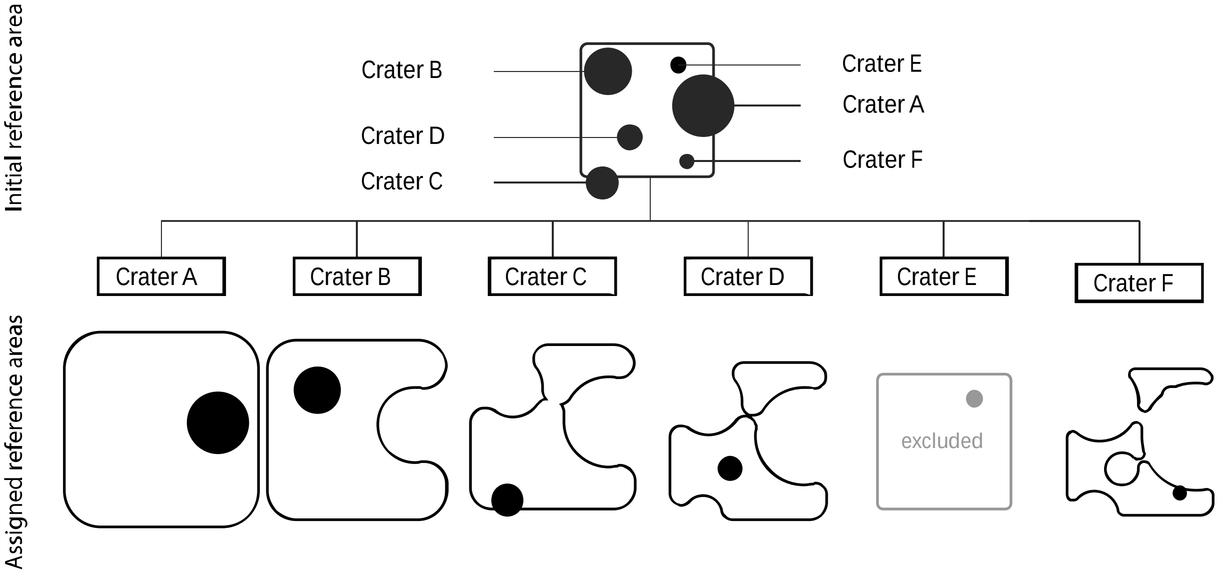

Figure 6.1: Assignment of individual reference areas during buffered nonsparseness correction. In this example, there is a rectangular reference area with six intersecting craters A–F, with crater A being the largest and crater F being the smallest crater. We assume a surrounding ejecta blanket of one crater radius in width for every crater. Accordingly, the area that is affected by crater obliteration is 2 times a crater's radius (crater rim plus ejecta blanket). For every crater, all larger craters plus their surrounding ejecta blankets are removed from the initial reference area. The remaining area is buffered by one crater radius of the crater that is currently under investigation. If the centroid of the crater is located inside the modified reference area, the investigated crater is considered for the crater size-frequency distribution measurement. In this example, crater E is excluded since it is located entirely on top of crater A's ejecta blanket.

between 3.9 and 3.8 Gyr. These results are supported by a later CSFD study by Head et al. (2010). Head et al. (2010) identified two different populations with a transition during the Imbrian period at less than 3.9 Ga, close to the time of the Orientale basin event. Their findings were mainly based on the Nectaris, Imbrium, and Orientale cratering records. In contrast to the analysis by Head et al. (2010), Fassett et al. (2012) normalized and combined the CSFDs of all basins assigned to the same period, then compared these summed CSFDs to each other. They found that the transition between the two populations occurred earlier than mid-Nectarian and that there was no change in the shape of the CSFDs between the Nectarian basins and the Imbrian basins.

In addition to the findings described above, Marchi et al. (2012) identified a third population of impactors, distinct from the "early" population on the lunar highlands and the "late" population on the lunar maria. According to their findings, the transition from the early population to an intermediate population, which they assign to the impactors that produced the LHB, occurred near the time of the Nectaris basin event. Marchi et al. (2012) interpreted their impactor population changes from the "early" population to an intermediate population to be caused by impactor velocities twice as fast as the "early" population, but without change in the impactor SFD. This is consistent with the model that the LHB projectiles came from an ancient E-belt at the inner margin of the asteroid belt (Bottke et al., 2012; Morbidelli et al., 2012). Head et al. (2010) and Fassett et al. (2012), however, stated that their observed CSFDs agree with findings from Strom et al. (2005), who concluded that the LHB projectiles came from the Main Asteroid Belt, not just a specific region at its inner margin.

However, Cuk et al. (2010) argued that the source of lunar cataclysm impactors could not be the Main Asteroid Belt.

These observations and findings on varying CSFDs on the lunar surface are at variance with one another and highly depend on the interpretation of asteroid belt evolution models and subsequent geological processes. Thus, to address the question of whether the PF has changed with time and when the potential transition occurred to produce differently shaped CSFDs, we reinvestigated the crater frequencies of the key lunar basins as listed by Fassett et al. (2012) using their crater measurements, but applying a new CSFD technique. The buffered non-sparseness correction (BNSC) (Kneissl et al., 2016) more rigorously accounts for crater obliteration on densely cratered surfaces. Then, we examined the basin stratigraphy based on both N(20) value, that is, the crater frequencies ≥ 20 km and the derived absolute model ages. We also used image and topographical data sets to explore the basin relationships, as well as previous studies (Fassett et al., 2012; Hiesinger et al., 2012b; Wilhelms et al., 1987). Finally, we studied the shape of the summed CSFDs of Pre-Nectarian-, Nectarian-, and Imbrian-aged basins and inferred potential projectile populations.

6.2 Data and Methods

For the direct comparison of our corrected CSFDs with Fassett et al. (2012), we use their crater measurements along with their geologic mapping. The mapping covers the remnants of each investigated basin and attempts to exclude the resurfaced areas (e.g., mare deposits or ejecta material from larger impacts). The crater measurements are based on the lunar crater catalog (Head et al., 2010), which was compiled using Lunar Reconnaissance Orbiter Lunar Orbiter Laser Altimeter data (Smith et al., 2010, 2017) and contains all impact craters with diameters ≥ 20 km. Additional craters beyond that database were included from younger surfaces (Fassett et al., 2012). First, we reloaded all the CSFD measurements into new shapefiles and recalculated the area and crater sizes in an updated CraterTools extension (Kneissl et al., 2011, 2016) in Environmental Systems Research Institute ArcGIS 10.3.

Then, we used the new CSFD method, the BNSC (Kneissl et al., 2016), which was implemented in CraterTools in ArcGIS, but not yet released to the public. A stand-alone tool will be soon available (Riedel et al., 2017). The motivation for the new technique comes from the fact that smaller craters on highly cratered surfaces were previously undercounted with respect to their accumulation due to their obliteration by larger craters and their ejecta blankets. Thus, this technique takes nonsparseness into account (see in Kneissl et al., 2016, Figure 1, and this study Figure 6.1). It is important to mention that each crater is referenced to an area excluding regions in the study area that have been resurfaced by larger craters; thus, the reference area becomes smaller for correspondingly smaller crater sizes. The other part of the new method makes use of buffered crater counting (BCC), which includes all craters overlapping the counting area with a buffer, but whose center is located outside of the region of interest (Kneissl et al., 2016; Fassett & Head, 2008; Fassett et al., 2012). The use of the buffer allows us to increase the number of craters included in the measurements, giving better statistics. The width of the buffer depends on the estimated range of the ejecta blanket (Kneissl et al., 2016). In this study we took the region affected by ejecta to be 1 crater radius radial from the crater rim. This removes the region obliterated by the craters and the thickest part of

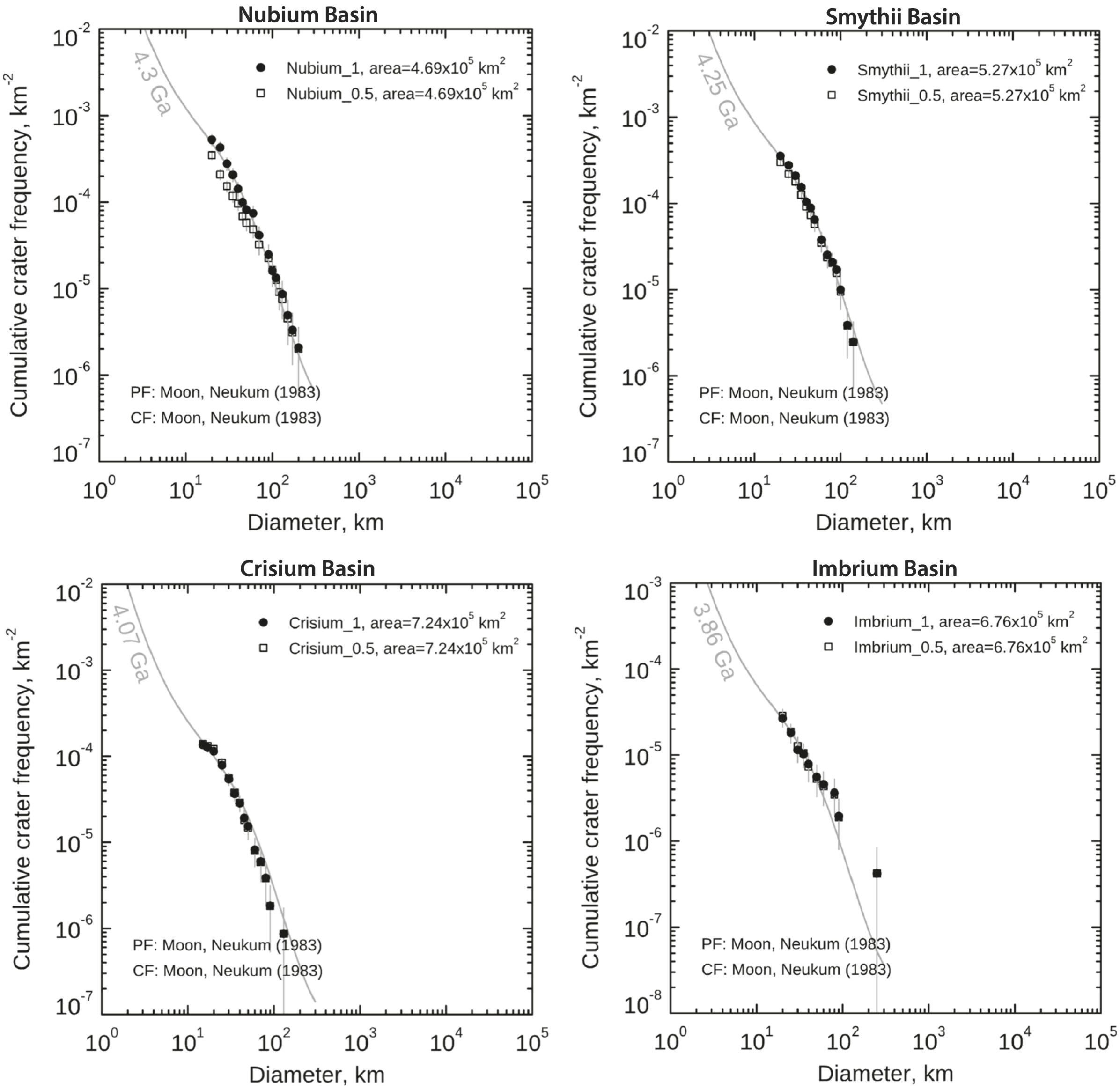

Figure 6.2: *The figure compares the effect of different exclusion radius: 1 (black filled circle) and 0.5 (black empty square) from the crater rim. We can say that the different exclusion radii do not significantly change the results. Although, the Pre-Nectarian-aged Nubium and Smythii basins represent slightly larger difference than Nectarian-aged Crisium and Imbrian-aged Imbrium basin.*

the ejecta. We could increase the area removed to be more certain, but at the cost of further decreasing the counting statistics. We compiled a figure to show different exclusion radius, namely, 1 and 0.5 crater radius from the crater rim. We can say that the different exclusion radii do not significantly change the results. It has a larger effect in the case of older basins (Nubium and Smythii) (Figure 6.2). Thus, if a nearby, smaller crater's center falls into this 1 crater radius, the smaller crater will be excluded unless a portion of this crater still overlaps the counting area. In this case, the smaller crater will be taken into consideration with the buffer, because the crater has age information about the area under consideration. The included and excluded craters for each basins can be seen in supporting information S1 and S2 of the published manuscript and also in Figure 6.3. We represent the CSFDs using two different approaches: (1)

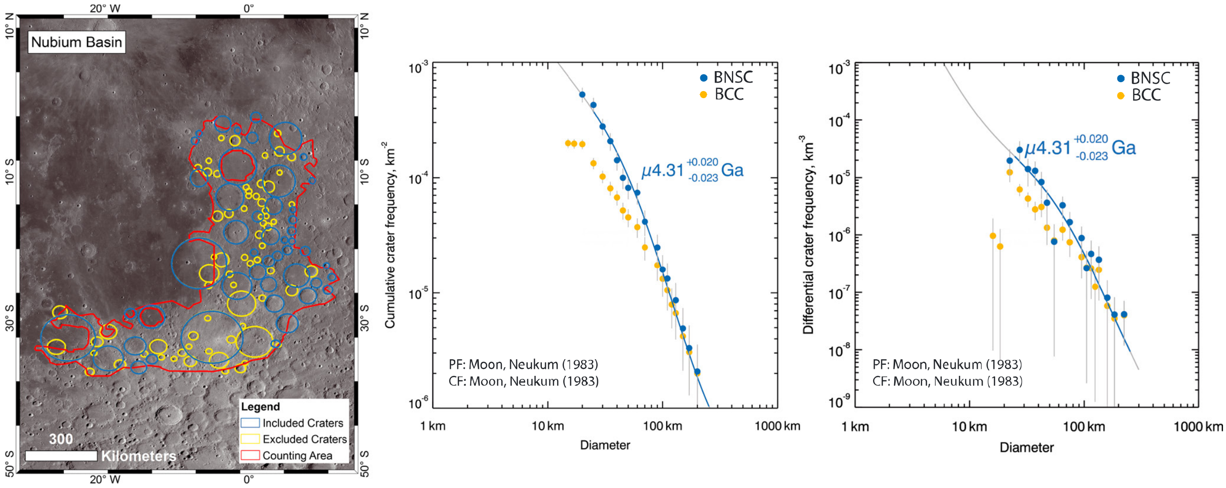

Figure 6.3: Crater measurement map and derived crater size-frequency distribution with absolute model age of Nubium Basin after Neukum (1983). Counting area over Lunar Reconnaissance Orbiter Camera Wide Angle Camera 100 m/pixel mosaic basemap. Craters marked with blue circle were counted during calculation; craters marked in yellow were excluded. Crater size-frequency distribution cumulative and differential plots of Nubium Basin using two different crater counting techniques: BCC (yellow filled circle) and BNSC (blue filled circle). The BNSC data show that the smallest crater bins are corrected to higher crater frequencies when accounting for crater nonsparseness. Absolute model age was derived from Neukum (1983) and included the μ notation, which shows the uncertainty of calibration of the chronology model.

BCC, as done by Fassett et al. (2012), and the new approach (2) BNSC. To understand how crater obliteration affects the CSFDs, we investigated the general influence of BNSC techniques on CSFD curves (Kneissl et al., 2016) (see in Figure 6.3) by comparing the results of different techniques applied systematically to different key regions used in the previous study (Fassett et al., 2012).

We derived the N(20) and N(64) values, that is, the frequency of craters ≥ 20 km and ≥ 64 km, as was done by Fassett et al. (2012), and normalized these to an area of 106 km2. Using N(20) allows the comparison of the crater densities over a larger diameter range than N(64). The error was calculated as follows: N(X) crater frequency divided by the square root of the number of craters. The basins were listed in two tables: (1) based on N(20) as presented in Fassett et al. (2012) (see in Table 6.1) and (2) the determined absolute model age (Table 6.2) values. Table 6.1 shows the comparison of N(20)* from Fassett et al. (2012) and N(20) as well as N(64) from this study. The factor in Table 6.1 shows the difference in N(20) as a percentage for the individual basins. The changes in Table 6.1 refer to the differences in the ranking of the basins compared to Fassett et al. (2012). Additionally, we studied the relationships of the crater frequencies and absolute model ages to stratigraphical observations from previous studies (Fassett et al., 2012; Wilhelms et al., 1987).

We determined the absolute model ages of lunar basins (Table 6.2) making use of the CraterStats software (Michael & Neukum, 2010; Michael, 2013) and applied the lunar PF and CF from Neukum (1983). To derive the absolute model ages, we used the cumulative fit and the μ notation, which represents the compounded uncertainties of the particular chronology model (Michael et al., 2016). Here we applied the cumulative and differential plots with pseudolog crater binning (Neukum, 1983). All CSFD plots with corresponding counting areas are available in the published article's appendix. Finally, to compare the nature of the impactor population(s) to Fassett et al. (2012), we derived the shape of the summed CSFDs of Pre-Nectarian-, Nectarian-, and Imbrian-aged basins using an R-plot with 10/decade binning (Figure 6.4). Note that the only change in data analysis between Fassett et al. (2012) and this study is the distinct CSFD analysis technique, because we aggregated the same basins from each time period as Fassett et al. (2012). The bins were fitted to the lunar PF (Neukum, 1983) in the crater diameter range of 20–200 km (Pre-Nectarian basins), 20–130 km (Nectarian basins) to get compared to Fassett et al. (2012), and 8–70 km (Imbrian basins) to show the shape of the CSFD curve.

6.3 Results and Interpretation

6.3.1 Crater Frequencies With BNSC

Due to their old ages, the lunar basins are non-sparsely cratered surfaces where craters overlap each other at various sizes. We derived the crater densities of key lunar basins (Fassett et al., 2012) using two different CSFD techniques: BCC and BNSC (Figure 6.3). The crater frequencies given by the BNSC technique reflect an increase in the measured frequencies of smaller craters (Table 6.1), seen as upward shifted crater bins in the CSFD with respect to the crater frequencies derived from the BCC technique alone (Figure 6.3). Our results show that crater frequencies increase by a factor of 24% (Table 6.1/Factor) compared to Fassett et al. (2012). The shift is due to the corrected reference areas, namely, that the density of smaller craters become higher in the correspondingly smaller reference areas when areas resurfaced by larger subsequent craters have been removed. This difference in the CSFDs grows systematically larger for older surfaces, such as Pre-Nectarian and Nectarian basins. However, there is little to no effect of the BSNC technique on Imbrian basins, because craters are sparse on these younger surfaces. In fact, almost no craters were excluded from the analysis because of their sparse distribution. Furthermore, the results of all individual basins correspond better to the lunar PF (Neukum, 1983) over a larger diameter range, than those CSFDs derived with BCC, as shown in Figure 6.3.

6.3.2 Refined Basin Sequence

As a result of the improved CSFDs, our derived N(20) crater frequencies for the individual lunar basins are different than Fassett et al. (2012), which changes the basin sequence significantly. The differences increase on surfaces with higher crater densities, since these surfaces are where the largest corrections in CSFDs were made using the BNSC technique. Consequently, the changes in basin sequence are more noticeable on older (Pre-Nectarian-aged and Nectarian-aged) than younger (Imbrian-aged) surfaces (Table 6.1/Changes). Nubium basin has the highest N(20) crater frequency (526 ± 77) with a high N(64) (61 ± 14) as well. The difference (169%) compared to Fassett et al. (2012) is the largest. The higher crater frequency can be explained by the exclusion of area that had been resurfaced by subsequent craters and their ejecta. Furthermore, Amundsen-Ganswindt basin with a factor of 77% includes Schrödinger basin, which in turn causes the exclusion of a large portion of relatively smaller craters from the counting area and increases the density of the rest of the craters in the area of interest. The discrepancy between N(20)* (Fassett et al., 2012) and our N(20) is lowest in Coulomb-Sarton (+3%) and Fitzgerald-Jackson (+5%) basins. Hertzsprung basin shows a negative factor, namely, a decreased crater frequency compared to Fassett et al. (2012). This

Basin	Period	N(20)*	N(20)	N(64)	Factor**	Change***	Model age
SPA	PN	156 ±7	254 ±21	39±5	+62	0	$4.31^{+0.019}_{-0.021}$ Ga
Nubium	PN	195 ±18	526 ±77	61 ±14	+169	↑ 6	$4.31^{+0.020}_{-0.023}$ Ga
Cruger-Sirsalis	PN	262 ±46	365 ±86	43 ±19	+39	↑ 1	$4.26^{+0.032}_{-0.041}$ Ga
Amundsen-Ganswindt	PN	202 ±37	359 ±108	56 ±25	+77	↑ 3	$4.26^{+0.038}_{-0.052}$ Ga
Smythii	PN	225 ±19	355 ±39	32 ±8	+57	0	$4.26^{+0.016}_{-0.018}$ Ga
Dirichlet-Jackson	PN	266 ±36	346 ±60	28 ±11	+30	↓ 3	$4.23^{+0.022}_{-0.026}$ Ga
Serenitatis	PN	298 ±60	334 ±73	6 ±6	+12	↑ 7	$4.22^{+0.027}_{-0.033}$ Ga
Poincare	PN	194 ±44	286 ±61	38 ±16	+47	↑ 1	$4.23^{+0.031}_{-0.040}$ Ga
Coulomb-Sarton	PN	271 ±54	281 ±63	26 ±13	+3	↓ 8	$4.23^{+0.025}_{-0.030}$ Ga
Lorentz	PN	179 ±31	275 ±60	37 ±14	+53	0	$4.20^{+0.029}_{-0.036}$ Ga
Schiller-Zucchius	PN	211 ±47	234 ±65	29 ±15	+10	↓ 5	$4.24^{+0.038}_{-0.052}$ Ga
Birkhoff	PN	170 ±33	223 ±58	49 ±19	+31	0	$4.29^{+0.035}_{-0.047}$ Ga
Ingenii	PN	167 ±33	198 ±53	63 ±22	+18	0	$4.28^{+0.035}_{-0.047}$ Ga
Fitzgerald-Jackson	PN	175 ±34	184 ±70	80 ±36	+5	↓ 3	$4.26^{+0.044}_{-0.063}$ Ga
Freundlich-Sharanov	PN/N	140 ±18	173 ±25	17 ±6	+23	↑ 1	$4.14^{+0.019}_{-0.023}$ Ga
Nectaris	N	135 ±14	172 ±20	15 ±4	+27	0	$4.17^{+0.012}_{-0.014}$ Ga
Grimaldi	N	126 ±28	165 ±43	28 ±13	+30	↑ 3	$4.14^{+0.033}_{-0.044}$ Ga
Mendel-Rydberg	N	125 ±17	158 ±26	14 ±5	+26	↑ 3	$4.13^{+0.022}_{-0.026}$ Ga
Apollo	N	151 ±23	158 ±29	12 ±6	+4	↓ 5	$4.14^{+0.024}_{-0.029}$ Ga
Planck	N	118 ±36	135 ±48	17 ±12	+14	↑ 2	$4.13^{+0.038}_{-0.053}$ Ga
Moscoviense	N	120 ±17	128 ±19	10 ±4	+6	↑ 2	$4.09^{+0.020}_{-0.024}$ Ga
Korolev	N	127 ±22	128 ±24	8 ±5	+0.7	↓ 5	$4.11^{+0.021}_{-0.025}$ Ga
Mendeleev	N	129 ±36	125 ±40	14 ±10	−3.2	↓ 5	$4.13^{+0.044}_{-0.064}$ Ga
Humorum	N	108 ±21	121 ±25	9 ±5	+12	↑ 1	$4.09^{+0.023}_{-0.023}$ Ga
Hertzsprung	N	129 ±22	116 ±26	17 ±7	−22.5	↓ 6	$4.09^{+0.030}_{-0.037}$ Ga
Crisium	N	113 ±11	114 ±13	7 ±3	+0.8	↓ 2	$4.07^{+0.016}_{-0.018}$ Ga
Humboldtianum	N	93 ±14	109 ±19	9 ±4	+17	↓ 1	$4.08^{+0.026}_{-0.032}$ Ga
Imbrium	I	30 ±5	26 ±5	4 ±2	−13.4	0	$3.87^{+0.035}_{-0.046}$ Ga
Schrödinger	I	19 ±7	19 ±7	4 ±3	0	0	$3.86^{+0.025}_{-0.030}$ Ga
Orientale	I	21 ±4	20 ±4	1 ±1	−5	0	$3.81^{+0.081}_{-0.085}$ Ga

Table 6.1: *Derived Absolute Model Ages of Lunar Basins Using the Buffered Non-Sparseness Correction, Ranked by N(20) Frequency. *: Data from Fassett et al. (2012); **: Difference in crater frequencies between N(20)* and N(20) in percent; ***: Change in sequence compared to Fassett et al. (2012). The model ages quoted for each basin with the respected μ notation do not include the systematic uncertainties in the chronology model.*

effect of the technique could be interpreted with the distribution of larger craters that are separated from each other and relatively large craters are excluded from the calculation due to obliteration. The derived Imbrian crater frequencies are slightly lower or the same as Fassett et al. (2012) reported. As mentioned above, the BNSC technique plays only a minor role for sparsely cratered surfaces (Kneissl et al., 2016). In the case of the Schrödinger basin, there is no difference between the crater frequencies. The outcome is due to the relatively large (318,076 km2) counting area and the widely distributed craters, which means that crater obliteration is negligible in the investigated crater size range. The same can be concluded for Imbrium and Orientale basins as for Hertzsprung basin.

The absolute model ages are dependent on the chronology model and the crater diameter range that can be fitted to the PF (Neukum, 1983); thus, we highlight the basin sequence based on the model ages in a separate Table 6.2. Birkhoff, Ingenii, and Fitzgerald-Jackson basins represent relatively older ages and high N(64) values (49 ±19, 63 ±22, and 80 ±36, respectively), although very low N(20) crater frequencies (223 ±58, 198 ±53, and 184 ±70, respectively). This means that the larger craters were preserved better on the surface than smaller craters as also observed by Povilaitis et al. (2017). These old basins, however, contain many large superposed craters that have destroyed craters in the 20 km range, thus resulting in low N(20) values. Thus, these basins are shown in the lower section of the basin sequence based on N(20). This is due to the fact that the PF (Neukum, 1983) appears more consistent with the larger crater sizes in the CSFD and the smaller craters <30 km fall off from that PF suggesting there has been some loss at this scale and the low N(20) could be explained by resurfacing.

We note the following differences between the stratigraphical observations and derived basin sequences. In the current study, to compare N(20) with basin stratigraphy, Freundlich-Sharanov was placed as a Nectarian basin, instead of Pre-Nectarian (Fassett et al., 2012; Wilhelms et al., 1987). It has been debated whether Apollo basin belongs to the Pre-Nectarian period (Fassett et al., 2012; Hiesinger et al., 2012b; Wilhelms et al., 1987), but according to our absolute model age, it is clearly younger than the Nectaris basin-forming event, although the error bars overlap in N(20). Coulomb-Sarton and Lorentz predate Birkhoff basin in the stratigraphy (Wilhelms et al., 1987), and the N(20) reflects the same relationship in Fassett et al. (2012) and our work as well. However, the absolute model ages do not conform with this stratigraphy, because the N(64) value for Birkhoff basin places it much higher in the sequence. Mendeleev basin is younger than Moscoviense basin (Wilhelms et al., 1987), in good agreement with our N(20) result, but contradicts Fassett et al. (2012). On the other hand the absolute model age shows the opposite stratigraphic relationship, due to the high N(64) for Mendeleev basin, in agreement with Fassett et al. (2012). It should be pointed out that the stratigraphic sequence is debated in the case of the Humboldtianum and Crisium basins. The observation from Fassett et al. (2012) is consistent with both of our N(20) results, namely, that Crisium is older than Humboldtianum basin, although the error bars in the N(20) overlap, as well as the absolute model ages. The younger, Imbrian basin sequence retains the same stratigraphic position in our analysis as in Fassett et al. (2012).

Basin	Period	Model age	Stratigraphy*	Stratigaphy **	Sample ages	Ref
SPA	PN	$4.31^{+0.019}_{-0.021}$ Ga	Oldest lunar basin			
Nubium	PN	$4.31^{+0.020}_{-0.023}$ Ga	> Humorum	> Imbrium, Humorum	Modified	
Birkhoff	PN	$4.29^{+0.035}_{-0.047}$ Ga		> Imbrium, Hertzsprung	After	
Ingenii	PN	$4.28^{+0.035}_{-0.047}$ Ga			Orgel et al.	
Amundsen-Ganswindt	PN	$4.26^{+0.038}_{-0.052}$ Ga	> Schrödinger	> Schrödinger	Modified	
Cruger-Sirsalis	PN	$4.26^{+0.032}_{-0.041}$ Ga				
Smythii	PN	$4.26^{+0.016}_{-0.018}$ Ga	> Crisium	> Crisium		
Fitzgerald-Jackson	PN	$4.26^{+0.044}_{-0.063}$ Ga	> Freundlich-Sharanov			
Schiller-Zucchius	PN	$4.24^{+0.038}_{-0.052}$ Ga		> Orientale, Humorum		
Dirichlet-Jackson	PN	$4.23^{+0.022}_{-0.026}$ Ga	> Korolev			
Coulomb-Sarton	PN	$4.23^{+0.025}_{-0.030}$ Ga	> Birkhoff	> Orientale, Imbrium, Hertzsprung, Lorentz, Birkhoff		
Poincare	PN	$4.23^{+0.031}_{-0.040}$ Ga		> Schrödinger, Planck		
Serenitatis	PN	$4.22^{+0.027}_{-0.033}$ Ga	> Nectaris	> Imbrium	$3.98^{+0.05}_{-0.05}$, $3.89^{+0.01}_{-0.01}$, $3.87^{+0.03}_{-0.03}$	1
Lorentz	PN	$4.20^{+0.029}_{-0.036}$ Ga		> Orientale, Imbrium, Birkhoff		
Nectaris	N	$4.17^{+0.012}_{-0.014}$ Ga		> Imbrium	$4.10^{+0.10}_{-0.10}$, $3.92^{+0.03}_{-0.03}$, $3.85^{+0.05}_{-0.05}$, $4.22^{+0.01}_{-0.01}$, 3.75-9.96	1, 2, 3
Grimaldi	N	$4.14^{+0.033}_{-0.044}$ Ga	> Mendel-Rydberg	> Orientale		
Freundlich-Sharanov	N	$4.14^{+0.019}_{-0.023}$ Ga	> Moscoviense	> Moscoviense, Mendeleev, Korolev		
Apollo	N	$4.14^{+0.024}_{-0.029}$ Ga	> Korolev, Hertzsprung	> Orientale, Hertzsprung, Korolev		
Mendeleev	N	$4.13^{+0.044}_{-0.064}$ Ga				
Planck	N	$4.13^{+0.038}_{-0.053}$ Ga	> Schrödinger	> Schrödinger		
Mendel-Rydberg	N	$4.13^{+0.022}_{-0.026}$ Ga		> Orientale		
Korolev	N	$4.11^{+0.021}_{-0.025}$ Ga	> Hertzsprung	> Orientale, Hertzsprung		
Humorum	N	$4.09^{+0.023}_{-0.023}$ Ga		> Orientale, Imbrium		
Hertzsprung	N	$4.09^{+0.030}_{-0.037}$ Ga		> Orientale		
Moscoviense	N	$4.09^{+0.020}_{-0.024}$ Ga		> Mendeleev, Humboldtianum		
Humboldtianum	N	$4.08^{+0.026}_{-0.032}$ Ga				
Crisium	N	$4.07^{+0.016}_{-0.018}$ Ga	> Humboldtianum	> Imbrium, Serenetatis	$3.895^{+0.017}_{-0.017}$, $3.89^{+0.02}_{-0.02}$, $3.84^{+0.04}_{-0.04}$, 3.89-3.93	1, 4, 5
Imbrium	I	$3.87^{+0.035}_{-0.046}$ Ga			$3.91^{+0.01}_{-0.01}$, $3.85^{+0.02}_{-0.02}$, $3.77^{+0.02}_{-0.02}$, $3.866^{+0.09}_{-0.09}$, $3.926^{+0.02}_{-0.02}$	1, 6, 7
Schrödinger	I	$3.86^{+0.025}_{-0.030}$ Ga		> Orientale		
Orientale	I	$3.81^{+0.081}_{-0.085}$ Ga				

Table 6.2: *Derived Absolute Model Ages of Lunar Basins Using the Buffered Nonsparseness Correction, Ranked by Model Age. The model ages quoted for each basin with the respected μ notation do not include the systematic uncertainties in the chronology model. Data listed in "Stratigraphy" from Fassett et al. (2012) (*) and Wilhelms et al. (1987) (**). The sample ages are from the review of Stöffler et al. (2006, and references therein). (1) Stöffler et al. (2006), (2) Norman et al. (2006), (3) Norman and Nemchin (2014), (4) Swindle et al. (1991), (5) Schmitt et al. (2017), (6) Norman et al. (2010), and (7) Snape et al. (2016b).*

6.3.3 Impactor Population

To investigate the nature of the impactor population(s), we plotted the summed CSFDs of the Pre-Nectarian-aged basins (excluding South Pole-Aitken Basin (SPA)), Nectarian-aged basins (including Nectaris), and Imbrian-aged basins (including Imbrium) on an R-plot as was done by Fassett et al. (2012). Figure 6.4 displays a comparison between the study by Fassett et al. (2012) (Figure 6.4a) and the current study (Figure 6.4b), where the summed CSFDs were produced by two different CSFD techniques: (1) BCC and (2) BNSC, respectively. Figure 6.4a (Fassett et al., 2012) shows a distinct difference in the CSFD of the Pre-Nectarian distribution, in comparison to the Nectarian and Imbrian distributions, expressed as a steep slope in the CSFD below 100 km size range, that does not conform to the lunar PF (gray isochrons). This observation led to the conclusion that different impactor populations could explain the change in the CSFD from the Pre-Nectarian to the Nectarian period (Fassett et al., 2012). However, our results show that the shape of the CSFD is in fact unchanged (Figure 6.4). The above mentioned steep slope does not appear in our Pre-Nectarian CSFD. The proper accounting of smaller craters corrects the crater bins in the CSFD upward; thus, the slope is removed by using the nonsparseness correction. Moreover, the CSFDs correspond better to the PF (Neukum, 1983) over almost the entire crater diameter range. Nevertheless, a few crater bins in the larger end of Pre-Nectarian (150–170 km) and Nectarian (110–120 km) basins fall off from that PF, when applying the nonsparseness correction.

6.4 Discussion

6.4.1 Impactor Populations and the LHB

During the formation periods of the Pre-Nectarian and Nectarian basins, crater obliteration was an important process that affected the crater population on the surface (Kneissl et al., 2016). Applying the BNSC to the CSFDs for the lunar basins, we found N(20) densities that were on average 24% higher than in Fassett et al. (2012), who already reported 50% higher crater densities in comparison to Wilhelms et al. (1987). This may be explained in part by the global data coverage both from the Wide Angle Camera and Lunar Reconnaissance Orbiter Lunar Orbiter Laser Altimeter instruments on the Lunar Reconnaissance Orbiter, but the improvements are primarily due to the improved CSFD technique. The observed shift in the CSFDs come from the correct accounting of the smaller crater population on highly cratered surfaces by excluding those areas where obliteration has occurred. Thus, we can much more accurately measure crater production on a given surface.

A changing CSFD would indicate more than one impacting population. Tera et al. (1974) found an age of 3.9 Ga for the lunar rock samples and suggested the existence of the LHB. Based on CSFD measurements from the lunar surface, a changing impactor population between 4.1 and 3.8 Ga was suggested by numerous authors (Head et al., 2010; Fassett et al., 2012; Marchi et al., 2012; Strom et al., 2005). One possible scenario for a changing population could be an event in the solar system that caused an impact rate spike or cataclysm on the Moon. For example, a migration of the giant planets might eject projectiles with an increased flux from the Main Asteroid Belt into the inner solar system causing a higher impact rate on the Moon (Gomes et al., 2005; Morbidelli

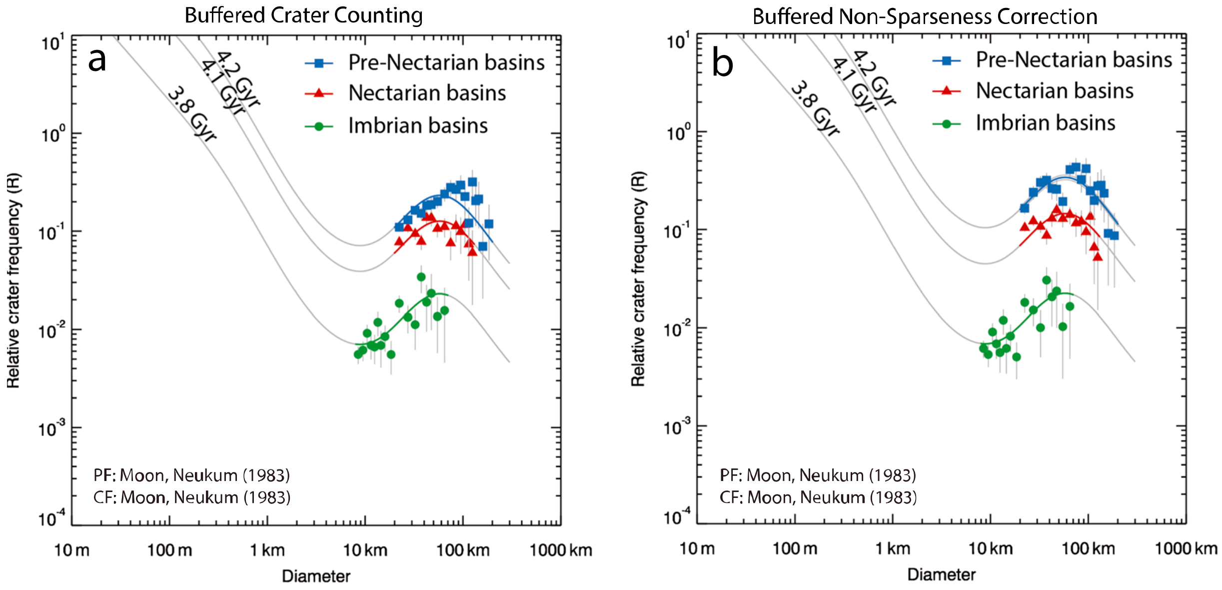

***Figure 6.4**: Summed crater size-frequency distribution (CSFDs) of the Pre-Nectarian-aged basins (excluding South Pole-Aitken Basin, blue filled square), Nectarian-aged basins (including Nectaris, red filled triangle), and Imbrian-aged basins (including Imbrium, green filled circle) to study the impactor population(s) using an R-plot representation. (a) Fassett et al. (2012) found a change in the shape of CSFDs using the BCC method (Fassett & Head, 2008) and suggested different impactor populations with a transition occurred from Pre-Nectarian to Nectarian periods (blue filled square versus red filled triangle), but earlier than mid-Nectarian. Note that the shape of Pre-Nectarian CSFD shows a steep slope in the diameter range from 20 km to 100 km. (b) In contrast, our study shows similarities in the shape of the summed CSFDs derived using the BNSC technique for each period. The steep slope in the summed CSFD of the Pre-Nectarian basins is no longer present in our study.*

et al., 2005, 2012; Tsiganis et al., 2005). Fassett et al. (2012) saw a steep slope in the diameter range from 20 km to 100 km in the summed CSFD of the Pre-Nectarian basins and concluded a changing impactor population earlier than the mid-Nectarian period. In contrast, our results indicate that the steep slope is due to the undercounting of smaller crater densities in nonsparsely cratered terrain. We find a CSFD consistent with those from later periods without a steep slope in the distribution. Nevertheless, an unchanging population of the impacting projectiles likewise gives no timing information and does not exclude the impact spike scenario. It does, however, constrain the spike scenario—if it occurred—to bombardment of the Moon with a similar SFD impactor population: this could be by excitement of the same source population, or alternatively a collisionally evolved population with similar SFD.

6.4.2 Basin Sequence and Sample Ages

The Apollo and Luna missions provided the samples to derive radiometric ages of mare basalts and impact events. The uncertainty of the provenance of impact melt breccias on the lunar surface makes the age dating of the lunar basins highly challenging. Because of the clustered locations and limited number of Apollo landing sites, the contamination of impact melt breccias from different impact events is highly possible (Stöffler et al., 2006). Nevertheless, these rock samples are the only direct age information from the lunar impact basins.

6.4.2.1 Serenitatis Basin

In earlier studies, Serenitatis was classified as a Pre-Nectarian basin (Baldwin, 1974; Fassett et al., 2012; Head, 1974; Stuart-Alexander & Howard, 1970; Wilhelms & McCauley, 1971), although Wilhelms et al. (1987) thought Serenitatis was younger than the nearby Crisium basin based on stratigraphy. Dating of the Serenitatis basin was attempted by analyzing impact melt from the Apollo 17 mission, which landed in the Taurus-Littrow region, on the eastern rim of Serenitatis basin. Unfortunately, most of the impact melt breccias collected there have an uncertain provenance due to subsequent impact events, such as those forming the Imbrium and Crisium basins, or Tycho Crater. The radiometric ages of the impact melt breccias vary between 3.87 and 3.98 Ga (Stöffler et al., 2006) and recalculated ^{40}Ar-^{39}Ar analysis of samples shows ages between 3.89 and 3.93 Ga (Schmitt et al., 2017), which are not consistent with the CSFD results from Fassett et al. (2012) or our study ($4.22^{+0.027}_{-0.033}$ Ga) (Table 6.2). Nevertheless, a recent study from Spudis et al. (2011) also placed Serenitatis stratigraphically in the middle of the Pre-Nectarian period and they explained the absence of older sample ages by the fact that impact melt from Serenitatis was not collected. They interpret the young radiometric ages as samples originating mostly from Imbrium. Furthermore, Fassett et al. (2012) provided observational evidence that Serenitatis predates Crisium: (1) sculptured ejecta from Nectaris and Crisium basins overlapping, (2) large and degraded craters that are filled with Imbrium ejecta material, and (3) crater densities on Serenitatis that are twice those on Crisium. The old age of Serenitatis from our study is consistent with the crater density and observational evidence from Fassett et al. (2012). We agree that Serenitatis must be a Pre-Nectarian basin.

6.4.2.2 Nectaris Basin

Apollo 16 landed on the highlands of Nectaris basin. The earlier studies (Stöffler et al., 2006) indicated that the most reliable age constraints for the age of Nectaris basin might come from analysis of the Descartes Formation. The samples show a range of ages between 3.85 and 4.1 Ga, the youngest of which represents the basement of North Ray Crater and was proposed as the age of Nectaris basin-forming event (Stöffler et al., 1985). Recent ^{40}Ar-^{39}Ar analysis of impact melt breccias by Norman et al. (2006) indicated a radiometric age in the range from 3.75 Ga to 3.96 Ga. Only one sample (63525) from North Ray Crater gave an outlying result of 4.19 Ga. Moreover, Norman and Nemchin (2014) analyzed the zirconolite and apatite in another sample (67955) with the U-Pb system and derived an absolute age of $4.22^{+0.01}_{-0.01}$ Ga indicating a basin-scale impact melting event. Additionally, Norman et al. (2010) determined a radiometric age of $3.866^{+0.09}_{-0.09}$ Ga from the trace element composition of lunar breccias (67016 and 67455) from the Descartes region. Based on geochemistry, the provenance for the impact melt breccia might be the Procellarum-potassium, rare earth element, and phosphorus terrane, thus most likely indicate the Imbrium impact, rather than Nectaris. In this study an age of $4.17^{+0.012}_{-0.014}$ Ga has been proposed for the Nectaris basin, which corresponds well with the older age results from Norman et al. (2006, 2010) and Norman & Nemchin (2014) but exceeds the ages proposed in Stöffler et al. (1985, 2006) (Table 6.2).

6.4.2.3 Crisium Basin

The robotic Luna 20 exploration mission visited the southern rim of Crisium basin and brought

30 g of samples back to Earth. The majority of the sample represented anorthositic highland material; however, one fragment may represent Crisium (Swindle et al., 1991). In the review from Stöffler et al. (2006), the radiometric age is in the range from 3.84 Ga to 3.89 Ga, which might date the formation of the Crisium basin (see in Table 6.2), although it remains uncertain whether the samples represent Crisium or different impact event. The recent study from Schmitt et al. (2017) corrected radiometric ages of samples between 3.89 and 3.93 Ga, while traditional CSFD measurements on proposed impact melt exposures in Crisium give an absolute model age of $\geq 3.94^{+0.05}_{-0.05}$ Ga (van der Bogert et al., 2018). Crater statistics from this study yield $4.07^{+0.016}_{-0.018}$ Ga which is slightly older than the radiometric ages of samples. Both the proposed radiometric and absolute model ages of Serenitatis are still older than Crisium; thus, Crisium must be younger in age as our study also suggested.

6.4.2.4 Imbrium Basin

The extent of the lunar surface affected by the Imbrium impact event and the consequences for the sample collection is still debated. The Apollo 15 mission landed on the rim of Imbrium basin, but rock samples from Apollo 14, 16, and 17 landing sites might also contain ejecta material from Imbrium. The ages of impact melts from Apollo 15 vary between 3.77 Ga and 3.92 Ga (Norman et al., 2010; Snape et al., 2016b; Stöffler et al., 2006) (see Table 6.2). Impact melt rocks at Apollo 15 landing site were collected from the Apennine Front and have a radiometric age of $3.85^{+0.02}_{-0.02}$ Ga (Stöffler et al., 2006). The Fra Mauro Formation at Cone Crater near Apollo 14 is interpreted to be the continuous ejecta blanket of Imbrium, which has been dated as $3.85^{+0.02}_{-0.02}$ Ga (Stöffler et al., 2006). Apollo 16 polymict breccias and impact melt rocks of the Cayley Formation might also represent Imbrium discontinuous ejecta material, with an age of 3.86 Ga (Stöffler et al., 2006). Recent studies show slightly older ages such as 3.92–3.99 Ga based on U-Pb and Lu-Hf radiometric measurements (Haber et al., 2017; Snape et al., 2016b). These radiometric ages are in reasonably good agreement with our CSFD measurements, which gives an absolute model age of $3.87^{+0.035}_{-0.046}$ Ga for the formation of Imbrium basin.

The differences between the absolute model ages and crater frequencies derived in our study (Tables 6.1 and 6.2) are generally related to the relatively high N(64) with respect to the N(20) values in the cases of the older aged basins, which also tend to have more variable N(20) values. The N(20) provides point-like information about the crater frequency of craters ≥ 20 km. This position in the CSFD could be located off from the major trend of the CSFD and therefore may not represent the entire CSFD. The absolute model ages give a better approach to establishing the basin sequence, because they reflect the formation age of the basins by using a wide range of crater diameter or so-called "population density" to fit a trend to CSFD. We argue that measuring the population density from the CSFD is a more robust approach than any specific point such as N(20). Such a value may be represented either by an extrapolated N(1) value, or as we do here, by a model age found through a CF. Even if one disagrees with the choice of CF, we note that the CF preserves the sequence as ranked by population density, so that the relative age sequence is maintained. On the other hand, we show that in some cases the absolute model age does not correspond to the stratigraphical observations from Wilhelms et al. (1987). It is noteworthy to mention that the image quality and the geographic coverage of data was limited in the 1980s. We may expect that we are able to make

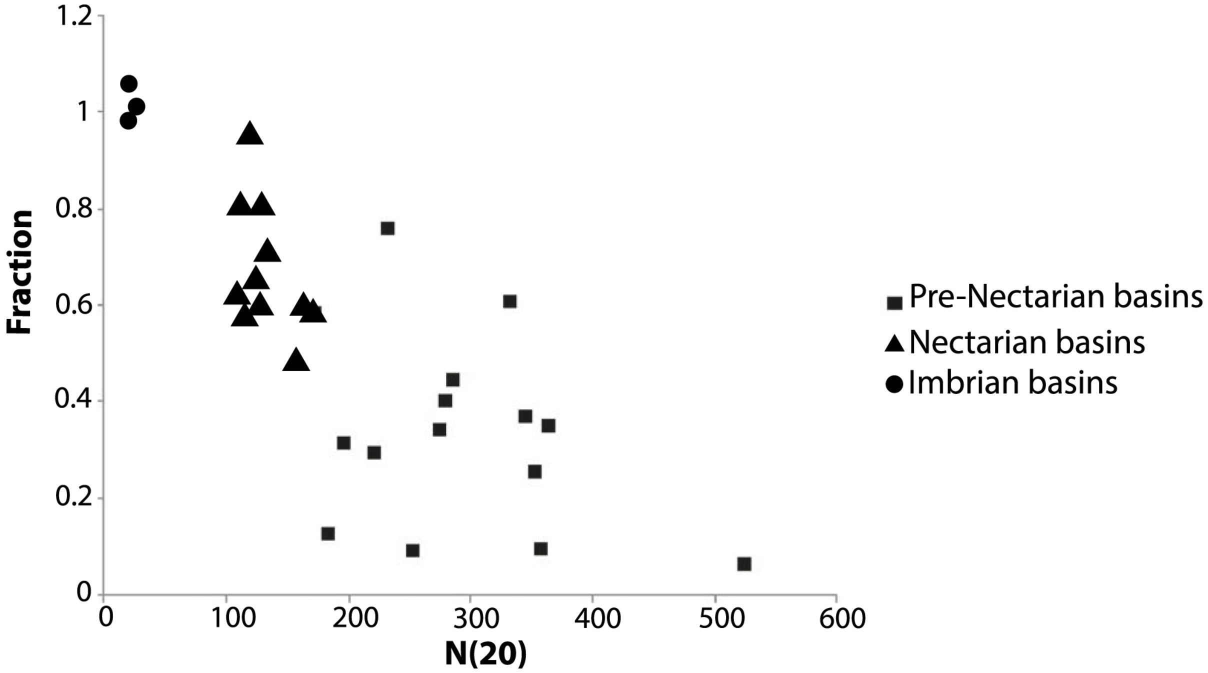

Figure 6.5: *N(20) versus fraction of original count area used to measure N(20) crater density. The diagram shows the decrease of the remaining area after the correction ("fraction") and the increase of the N(20) value toward older surfaces. The black box indicates the Fitzgerald-Jackson, South Pole-Aitken, Amundsen-Ganswindt, and Nubium basins. These basins might be in saturation equilibrium. The N(20) value of the corresponding basins is listed in Table 6.1.*

more comprehensive measurements of the crater populations and thus derive more accurate results. Our new analysis, on the basis of recent global lunar data sets provides an updated and more complete view of the basin sequence. Therefore, we believe that the basin sequence based on model age is more accurate than the use of N(20), alone.

6.4.3 Saturation Equilibrium

Some areas of the lunar highlands exhibit crater densities for craters ≥ 20 km that may be close to saturation equilibrium (Fassett et al., 2012; Head et al., 2010; Povilaitis et al., 2017; Xiao & Werner, 2015). Saturation equilibrium occurs when the formation of new craters destroy equal numbers of old craters, resulting in a steady state population density (Gault, 1970; Shoemaker, 1965; Woronow, 1977). Essentially, saturation equilibrium represents the highest level of nonsparseness that a count area can reach before that count area no longer provides absolute age information. Some heavily cratered areas, such as on the central farside, have CSFDs that cannot be fit with a PF, which might indicate a role of equilibrium processes at the small crater diameter bins, but these distributions can also not be fit with any existing equilibrium function (Povilaitis et al., 2017). These CSFDs likely exhibit a suppression of the smaller crater diameter frequencies due to the nonsparseness of the craters (Neukum, 1983) and would also benefit from the BNSC. After applying the BSNC, could the corrected CSFDs tell us something new about saturation equilibrium on the Moon?

To investigate this possibility, we compared the corrected count area extents for the small crater diameter bins in our study to their respective N(20) crater frequencies for each basin (Figure 6.5). As expected, we see a linear decrease in the used counting area with increasing N(20) value toward older surfaces, because the level of nonsparseness increases with basin age. For example, for Imbrian basins N(20) values are determined using around 100% of the original area. N(20) values for Nectarian basins are based on 40–90% of the defined count area, while most N(20)s for Pre-Nectarian basins were derived from 20 to 40% of the original areas. Four Pre-Nectarian basins (Fitzgerald-Jackson, South Pole-Aitken, Amundsen-Ganswindt, and Nubium) have less than 20% of their original count area remaining after the BNSC for determination of an N(20) (Figure 6.5). This might suggest that these basins have almost reached saturation equilibrium at crater diameters of 20 km, because the remaining count area for craters of this diameter is approaching zero, where no pristine surface remains and almost 100% of the surface has been resurfaced by craters or their ejecta. However, the relatively small number of basins in this position on the graph, suggests that few basins are saturated with craters that have diameters of 20 km, a conclusion consistent with the findings of Povilaitis et al. (2017). The BNSC method may thus be a new approach to study equilibrium condition for various crater diameters on planetary surfaces.

6.5 Conclusion

We applied a BNSC (Kneissl et al., 2016) to a crater size-frequency analysis of 30 key lunar basins. The shift in smaller crater density in the CSFD compared to the BCC technique (Figure 6.3) (Fassett et al., 2012; Fassett & Head, 2008) represents the effect and scale of crater obliteration, and once corrected allows a larger range of the CSFD to be used to analyze the relative ages of the lunar basins, as well as shed light on the characteristics of the impactor population. This correction effect is greater on surfaces with higher crater frequencies. The corrected CSFDs better correspond to the PF from Neukum (1983) over a broader crater size range. The BNSC technique proved to make a significant difference in accounting crater densities on highly cratered surfaces.

In this study, we refined the basin sequence based on both N(20) and absolute model ages. The difference in our results compared to Fassett et al. (2012) comes from the fact that some basins such as Birkhoff, Ingenii, and Fitzgerald-Jackson have relatively high N(64) with respect to N(20). The low N(20) values placed these basins in the lower section of the Pre-Nectarian basin sequence, whereas our absolute model age results, using the full size-frequency range available in each case for the fit, provides an improved stratigraphy. Even though the relative stratigraphies from previous studies (Fassett et al., 2012; Hiesinger et al., 2012b; Wilhelms et al., 1987) disagree in a few cases with our basin sequence based on absolute model ages, we still consider that those measurements made from a broader crater size range to be more robust than establishing basin sequence based on N(20) value alone.

In contrast to previous studies (Fassett et al., 2012; Head et al., 2010), which show a change in the shape of the CSFDs for the lunar periods, our results indicate no change in the shapes and thus, no evidence for a change in impactor population between the Pre-Nectarian and Nectarian periods.

In the future, the BNSC technique can be extended to heavily cratered surfaces of other planets in the inner solar system, such as Mercury and Mars, because these planets have been bombarded by the same impacting projectile populations as the Moon and the lunar cratering chronology has been adapted for surface age dating on these other bodies (Ivanov et al., 2002; Neukum et al., 2001a; Strom et al., 2005). Using recently obtained MErcury Surface, Space ENvironment, GEochemistry, and Ranging; Mars Express; and Mars Reconnaissance Orbiter data, reanalyzing the cratering record of these planets and applying appropriate crater analysis techniques will provide further information about the history of different impactor populations in the inner solar system.

As the oldest (our study: $4.31^{+0.019}_{-0.021}$ and Hiesinger et al. (2012b): $4.26^{+0.03}_{-0.03}$) and deepest impact structure on the Moon, the South Pole-Aitken Basin on the lunar farside remains a high-priority candidate for exploration and sample return mission for National Aeronautics and Space Administration's third New Frontiers program, called MoonRise (National Research Council, 2011). Additionally, the Chinese Chang'e-4 mission proposed to visit the Apollo basin inside SPA by the end of 2018 (Wang & Liu, 2016). The question of the existence of the LHB and the relative and absolute stratigraphy of major lunar basins are still active questions. Sample return missions from various well preserved key locations from different time periods, such as Nubium, Smythii, Nectaris, Crisium, Humboldtianum, Orientale, and basins inside SPA (Cohen et al., 2018; Kring & Durda, 2012; Potts et al., 2015; Steenstra et al., 2016; Orgel et al., 2017) should be visited by robotic and human exploration missions, to help further constrain the lunar cratering chronology.

Acknowledgments

We would like to thank David Minton, Simone Marchi, and an anonymous reviewer for their helpful comments that improved this manuscript. C. O. and C. R. were funded by the Deutsche Forschungsgemeinschaft (SFB-TRR 170, subproject A3-37). G. M. was supported by the German Space Agency (DLR Bonn), grant 50QM1702 (HRSC on Mars Express), on behalf of the German Federal Ministry of Economics and Technology. C. H. vdB and H. H. were funded by German Aerospace Center (DLR) project 50OW1504, and H. H. was also funded by the SFB-TRR 170, subproject A2. All the raw data for this work are available in the PDS. The original data are from Fassett et al. (2012). The derived data products are available at university data repository (http://www.planet.geo.fu-berlin.de/Orgel_etal_2017_Lunar_basins.zip) and as supporting information.

CHAPTER 7

DEGRADATION OF SMALL SIMPLE AND LARGE COMPLEX LUNAR CRATERS: NOT A SIMPLE SCALE DEPENDENCE

by C. Riedel, D. A. Minton, G. G. Michael, C. Orgel, C. H. van der Bogert, and H. Hiesinger (2020), published in Journal of Geophysical Research: Planets, 125, e2019JE006273, https://doi.org/10.1029/2019JE006273.

Abstract: The crater record of a planetary surface unit is often analyzed by its cumulative size-frequency distribution (CSFD). Measuring CSFDs involves traditional approaches, such as traditional crater counting (TCC) and buffered crater counting (BCC), as well as geometric corrections, such as nonsparseness correction (NSC) and buffered nonsparseness correction (BNSC). NSC and BNSC consider the effects of geometric crater obliteration on the CSFD. On the Moon, crater obliteration leads to two distinct states in which obtained CSFDs do not match the production CSFD—crater equilibrium and nonsparseness. Crater equilibrium occurs when each new impact erases a preexisting crater of the same size. It is clearly observed on lunar terrains dominated by small simple craters with steep-sloped production CSFDs, such as Imbrian to Eratosthenian-era mare units. Nonsparseness, on the other hand, is caused by the geometric overlap of preexisting craters by a new impact, which is also known as "cookie cutting." Cookie cutting is most clearly observed on lunar terrains dominated by large craters with shallow-sloped production CSFDs, such as the pre-Nectarian lunar highlands. We use the Cratered Terrain Evolution Model (CTEM) to simulate the evolution of a pre-Nectarian surface unit. The model was previously used to simulate the diffusion-induced equilibrium for small craters of the lunar maria. We find that relative to their size, large craters contribute less to the diffusion of the surrounding landscape than small craters. Thus, a simple scale dependence cannot account for the per-crater contribution to degradation by small simple and large complex craters.

7.1 Introduction: The Evolution of Lunar Surface Units

The surface evolution of the Moon is largely controlled by impact cratering. Its surface provides a well-preserved cratering record that has long been used to also understand the surface evolution of planetary bodies in the inner solar system (e.g., Baldwin, 1964; Hiesinger et al., 2012a; Neukum, 1983; Neukum et al., 2001a; Öpik, 1960; Stöffler et al., 2006; Stöffler & Ryder, 2001). One big challenge, however, is that the impact record of the most ancient lunar terrains is incomplete due to crater degradation and erasure processes. This circumstance has led to a long debate about the bombardment history of the Moon, particularly during the Nectarian and pre-Nectarian periods. Investigations on such ancient lunar surface units showed a change in the cumulative size-frequency distribution (CSFD) slope, which has been attributed to the presence of multiple impactor populations that hit the lunar surface (e.g., Fassett et al., 2012; Marchi et al., 2012; Strom et al., 2005; Strom et al., 2015).

Strom et al. (2005), Marchi et al. (2012), and Strom et al. (2015) proposed that the crater populations prior to the Eratosthenian were distinct from those more recent and were part of a putative lunar cataclysm (Tera et al., 1974). During this cataclysm, projectiles with different impactor characteristics hit the lunar surface during a period of intense bombardment. Thus, the ancient lunar highland was postulated to have been bombarded by an impactor population different from the one that shapes the lunar surface since the emplacement of the maria. However, the hypothesis that there was a distinct impactor population in the cataclysm is disputed. Neukum and Ivanov (1994), Hartmann (1995), and Neukum et al. (2001a) argued that a single-production population can entirely explain the lunar cratering record. The CSFD slope on ancient lunar terrain is therefore not due to different impactor populations but to geologic resurfacing effects.

Marchi et al. (2012) proposed that an observed change in the CSFD of craters from the pre-Nectarian onward could be explained by an increase in the average impactor velocity over time. They attributed this change to the dynamical evolution of objects destabilized from the main asteroid belt or an inner extension of the main asteroid belt during the Nice model giant planet instability (Bottke et al., 2012; Gomes et al., 2005). However, investigations by Orgel et al. (2018) suggest that the change in the observed crater size-frequency distribution noted by Marchi et al. (2012) and in earlier work could instead be a natural consequence of the cratering process. Because each new crater causes a geologic resurfacing of the preexisting surface, as craters accumulate, the geometric obliteration of preexisting small craters by larger ones causes a size-dependent change in the number of observed craters relative to the production population. This effect would be more pronounced for more heavily cratered terrains, thus would only appear to be a change in the CSFD through time.

A number of recent studies (summarized by Hartmann, 2019) have led to the revision of the lunar cataclysm theory. Michael et al. (2018) and Liu et al. (2019) argue that the radioisotopic dating of lunar rock samples, on which the theory of the lunar cataclysm is based, is affected by a sample bias caused by the transport of Imbrian impact melt. Biases in samples dated by the ^{40}Ar-^{39}Ar method may also give the appearance of a cataclysm when none occurred (Boehnke & Harrison, 2016). Therefore, it is possible that the change in the CSFD slope on ancient lunar surface units was not influenced by a cataclysm but by crater degradation processes. Thus, to properly interpret ancient crater populations, we must better quantify how craters have been degraded and erased over time.

Except in the limited regions affected by mare volcanism, the primary contribution to crater erasure on the Moon has been from impact cratering itself (e.g., Öpik, 1960; Ross, 1968). As cratering progresses on a surface unit, the cratering record typically reaches a state where on average every new impact erases a preexisting crater of the same size. In this condition, the crater density of craters smaller than a certain size does not increase anymore despite ongoing cratering. This condition is called crater equilibrium (e.g., Gault, 1970; Melosh, 1989; Woronow, 1977). The largest crater diameter that is affected by this condition is called equilibrium onset Deq. When the CSFD of crater populations in equilibrium is compared to a function of crater production (e.g., Neukum, 1983; Neukum et al., 2001a), the obtained cumulative crater frequencies (Crater Analysis Techniques Working Group, 1979) typically do not follow a

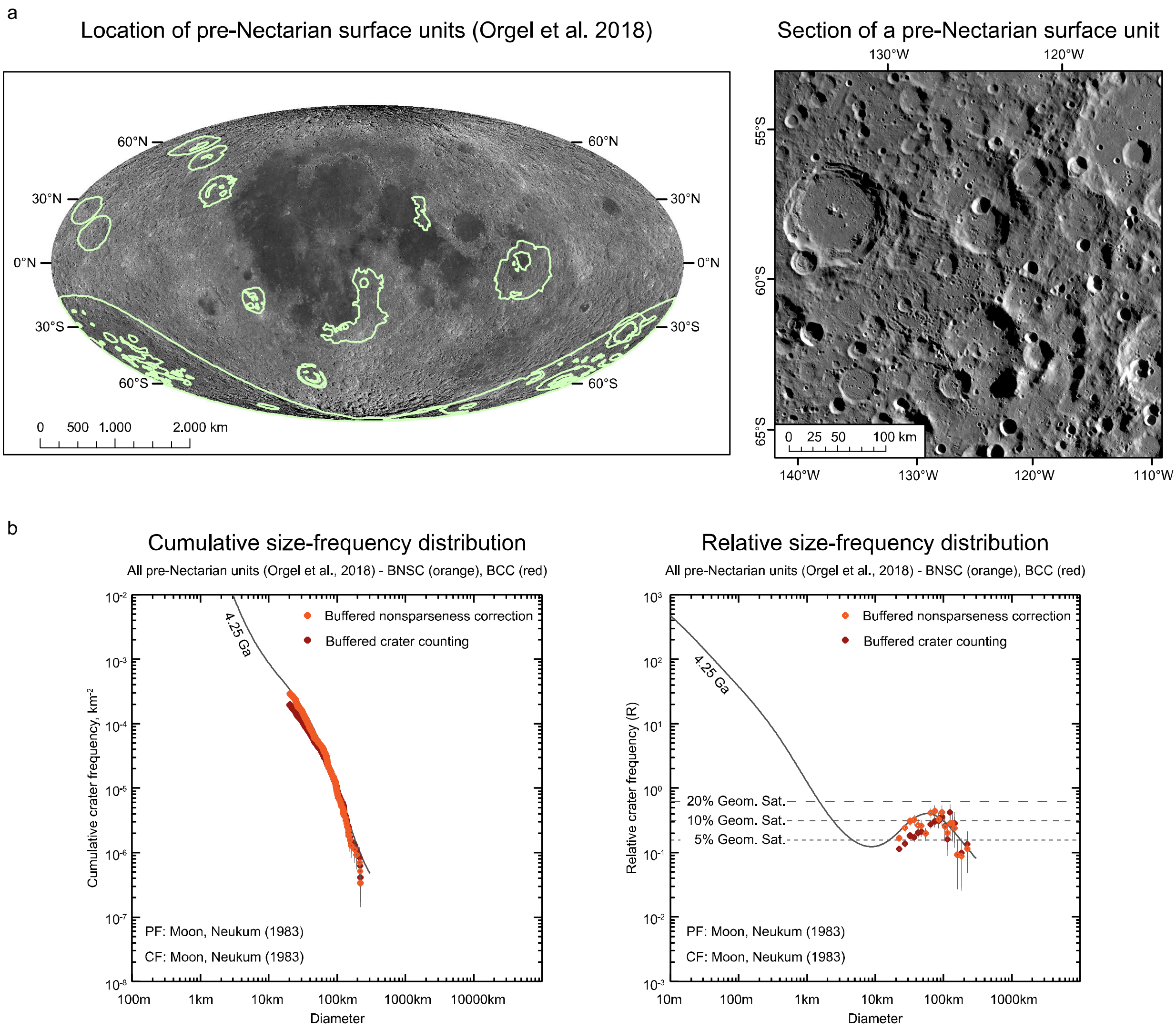

Figure 7.1: *Pre-Nectarian surface observations by Orgel et al. (2018). The authors conducted crater size-frequency distribution measurements of craters with a diameter of 20-200 km, which are located on the remnants of lunar basins. Those units in which the absolute model age is older than the Nectaris unit (4.17 Ga) were considered pre-Nectarian. Figure (a) shows the location of the pre-Nectarian surface units as identified by Orgel et al. (2018) and a section of such surface unit. Figure (b) shows the obtained crater size-frequency distributions from BCC (red) and BNSC (orange) measurements on pre-Nectarian surface units. The crater size-frequency distribution obtained with BNSC is in a better agreement with the lunar production function by Neukum (1983) (grey) than the crater size-frequency distribution obtained with the BCC technique.*

function of crater production but a power law of the form

$$N_{\mathrm{eq}}(D) = aD^b, \qquad (1)$$

where a is a coefficient constant and b is the equilibrium slope. Lunar surface investigations suggest that the slope for populations of small simple craters ($D < 1$ km) in equilibrium is relatively constant at $b \sim -2$ (e.g., Gault, 1970; Hartmann, 1984; Hirabayashi et al., 2017; Minton et al., 2019; van der Bogert et al., 2017; Xiao & Werner, 2015).

Crater populations in equilibrium, wherein the CSFD follows a power law in the form of equation 1, originate from a steep-sloped ($b < -2$) crater production CSFD in which degradation is dominated by small craters (e.g., Hirabayashi et al., 2017; Melosh, 1989;

Richardson, 2009; Xiao & Werner, 2015). Hirabayashi et al. (2017) found that in such an environment, the slope for crater populations in equilibrium is independent of the slope of the crater production CSFD and that degradation processes on the surface determine the equilibrium state. For shallow production CSFDs ($b > -2$), in which degradation is dominated by large craters, it is expected that the slope of the production population would be maintained in equilibrium (Hirabayashi et al., 2017; Melosh, 1989). As a result, both the evolution of the equilibrium state and the CSFD of crater populations in equilibrium are expected to differ from a small crater-induced equilibrium.

It has been suggested that the slope of the production CSFD would also be maintained in equilibrium for production CSFDs that have both steep and shallow branches, such as is seen in the $D > 20$ km population of craters of the ancient lunar highlands (Chapman & McKinnon 1986; Richardson, 2009). However, Minton et al. (2019) showed that even in the case of the steep sloped $D < 100$ m crater population of the mare, the equilibrium parameters a and b have a complicated dependence on how new craters of different sizes contribute to the degradation of old craters via process like distal secondary formation, and also on and how the visibility of craters to a human crater counter depends on size and accumulated degradation. These processes are poorly constrained for $D > 20$ km scale craters, and thus whether or not the lunar highlands are in a state of equilibrium and what an equilibrium CSFD looks like for the highlands remain open questions. The equilibrium onset occurs when the spatial number density of craters of a particular size reaches that of equilibrium. It is typical to specify the spatial number density of craters in equilibrium relative to that of geometric saturation (Melosh, 1989). Geometric saturation describes a theoretical case of maximum crater density at which circular features are arranged in a rim-to-rim configuration (Gault, 1970). The CSFD of a geometrically saturated crater population is represented by a power law with $a = 1.54$ and $b = -2$ (Gault, 1970; Xiao & Werner, 2015). It is common to represent the density levels of craters in equilibrium as a fraction of the maximum possible crater configuration. On the lunar surface, CSFD observations suggest that equilibrium for small simple craters occurs at 1–10% of geometric saturation (e.g., Gault, 1970; Xiao & Werner, 2015). However, Povilaitis et al. (2018) investigated lunar surface units where the configuration of large craters $D > 40$ km reaches more than 10% geometric saturation, without being in an equilibrium state. Thus, it has been suggested that an arbitrary saturation level alone cannot evaluate the presence of crater equilibrium (Povilaitis et al., 2018; Xiao & Werner, 2015), because crater degradation is likely a size-dependent process (e.g., Fassett & Thomson, 2014; Hirabayashi et al., 2017; Povilaitis et al., 2018; Minton et al., 2019).

Modeling and CSFD observations suggest that crater degradation for small simple craters is dominated by the topographic diffusion of impact craters (e.g., Craddock & Howard, 2000; Fassett & Thomson, 2014; Hartmann & Gaskell, 1997; Minton et al., 2019; Soderblom, 1970). In a diffusion-dominated degradation environment, impact craters become shallower over time until they can no longer be distinguished from the surrounding terrain. This process is mainly caused by continuous diffusive topographic degradation, also known as soil creep. In this form of degradation, the crater rims are slowly eroded, and the inner bowls filled in as surface material accumulate due to the preferred downslope transport of the loose material (e.g., Ross, 1968; Soderblom, 1970). This mechanism, where small craters erode larger ones, is also referred to as sandblasting (e.g., Hartmann & Gaskell, 1997; Hirabayashi et al., 2017; Minton et al., 2019; Richardson, 2009). Minton et al. (2019) concluded that sandblasting by primary impactors alone is not effective enough to induce the equilibrium CSFD to be <5% of geometric saturation as observed for simple, postmare craters. Instead, they concluded that the cumulative effects of energetic distal ejecta deposition, which includes the formation of secondary craters, dominate diffusive crater degradation on the lunar maria.

The diffusion-dominated equilibrium that characterizes the populations of $D < {\sim}100$ m postmare craters results in a very sparse spatial distribution of similar-sized craters. On the other hand, craters with $D > 20$ km on the oldest lunar surface units reveal an effect of nonsparse cratering (Kneissl et al., 2016; Orgel et al., 2018; Riedel et al., 2018), where the number of visible craters is lower than the number of produced craters as well. In contrast to a diffusion-dominated crater equilibrium, the number of visible craters continues to increase with ongoing cratering and CSFDs do not follow an equilibrium power law (e.g., Fassett et al., 2012; Orgel et al., 2018). Furthermore, crater density rates on the lunar highlands can reach geometric saturation levels of 10% or more (Povilaitis et al., 2018), which is higher than the geometric saturation rates at which crater equilibrium (wherein the CSFD follows an equilibrium power law) typically occurs for smaller craters (Xiao & Werner, 2015). The nonsparseness effect is caused by the geometric overlap of existing craters by a larger impact. This process is also referred to as cookie cutting (e.g., Hirabayashi et al., 2017; Minton et al., 2019; Richardson, 2009; Woronow, 1977). Due to the erasure of the previously existing crater record, the new impact contributes to a partial resurfacing of the smaller craters on the surface unit. Thus, the observed crater densities are lower than the total number of produced craters. Orgel et al. (2018) investigated this effect for craters with $D > 20$ km on the remnants of lunar basins. They found that by excluding areas of crater obliteration from the crater count area via nonsparseness correction (NSC) or buffered nonsparseness correction (BNSC) methods (Kneissl et al., 2016; Riedel et al., 2018), the mismatch between the CSFD and crater production function on the heavily cratered Nectarian and pre-Nectarian surface units can be corrected (Figure 7.1b). Traditional CSFD measurement techniques like traditional crater counting (TCC; used, e.g., by Neukum, 1983, and Hiesinger et al., 2012a) or buffered crater counting (BCC; used, e.g., by Tanaka, 1982, and Fassett et al., 2012) do not correct this effect.

Investigations on diffusive crater degradation and nonsparse cratering suggest that crater degradation affects the evolution of sparsely and heavily cratered surfaces on the Moon differently. In this work, we use a three-dimensional surface evolution model to investigate how the most ancient lunar terrain evolved under the influence of both topographic diffusion arising from distal energetic ejecta as well as cookie cutting. To this end, we apply diffusion models that were previously constrained from simulations of the evolution of a terrain dominated by small simple craters that reach a state of equilibrium (Minton et al., 2019). We model the evolution of a pre-Nectarian surface unit to investigate whether the per-crater contribution to topographic diffusion scales in an environment in which the nonsparseness effect occurs.

7.2 Modeling Surface Evolution With CTEM

7.2.1 Modeling Crater Degradation

We use the Cratered Terrain Evolution Model (CTEM) (Minton et al., 2015; Minton et al., 2019; Richardson, 2009) to simulate the evolution of a cratered surface on the Moon. CTEM uses a user-defined impactor population to form craters on a planetary surface unit over time. Unlike other codes to study surface evolution (e.g., Hartmann & Gaskell, 1997; Marchi et al., 2012; Woronow, 1985), CTEM generates a three-dimensional surface model with human-calibrated crater counts (Minton et al., 2015; Minton et al., 2019). CTEM simulations have been used to study cratering-related processes on the Moon such as the crater equilibrium of large highland craters (Richardson, 2009), the flux of ancient lunar impactors (Minton et al., 2015), and the effects of distal ejecta on both surface mixing (Huang et al., 2017) and small crater equilibrium (Minton et al., 2019). In this context, the surface evolution models in CTEM have undergone some modifications over time. For our study, we use the surface evolution models that Minton et al. (2019) implemented into the CTEM code. In this model, four processes contribute to the erasure of existing craters by new impacts: cookie cutting, low-velocity proximal ejecta blanketing, sandblasting by primary impacts, and sandblasting by high-velocity distal ejecta (secondary impacts parameterized with a topographic diffusion model). When describing the degradation models, we differentiate between existing craters with radius r that experience degradation and a new impact with radius ř that contributes to the degradation of the preexisting landscape.

7.2.2 Cookie Cutting

Cookie cutting describes a geometric crater obliteration process, where a new crater superposes smaller craters during impact. All craters whose rims are located within the rim of the new, larger crater are erased. Cookie cutting can cause large-scale resurfacing of the preexisting terrain.

7.2.3 Proximal Ejecta Blanketing (Low-Energy Ejecta Deposition) and Sandblasting

When a new impact forms on the CTEM-generated surface, the excavated material forms a continuous blanket around the crater rim. The ejecta thickness h is approximated by a function of distance d from the rim of a fresh crater with radius ř

$$h = h_{\text{rim}}\left(\frac{d}{\check{r}}\right)^{-3}. \quad (2)$$

h_{rim} describes the ejecta thickness at the rim and is determined by $h_{\text{rim}} = 0.14 * \check{r}^{0.74}$ (McGetchin et al., 1973; Fassett et al., 2011a). The proximal ejecta blanket is geometrically similar for craters of all sizes and therefore represented in a simplified manner.

When a fresh crater forms on a slope, the proximal ejecta deposits preferably move in downslope direction (e.g., Ross, 1968; Soderblom, 1970). This leads to a crater obliteration process called sandblasting, where small craters degrade the slopes of larger craters and slowly fill the large crater with proximal ejecta. Proximal ejecta also degrades craters by burying them (e.g., Fassett et al. 2011a). The efficiency with which ejecta of a given thickness buries craters of a given depth is determined using a topographic diffusion model (see section 7.2.5).

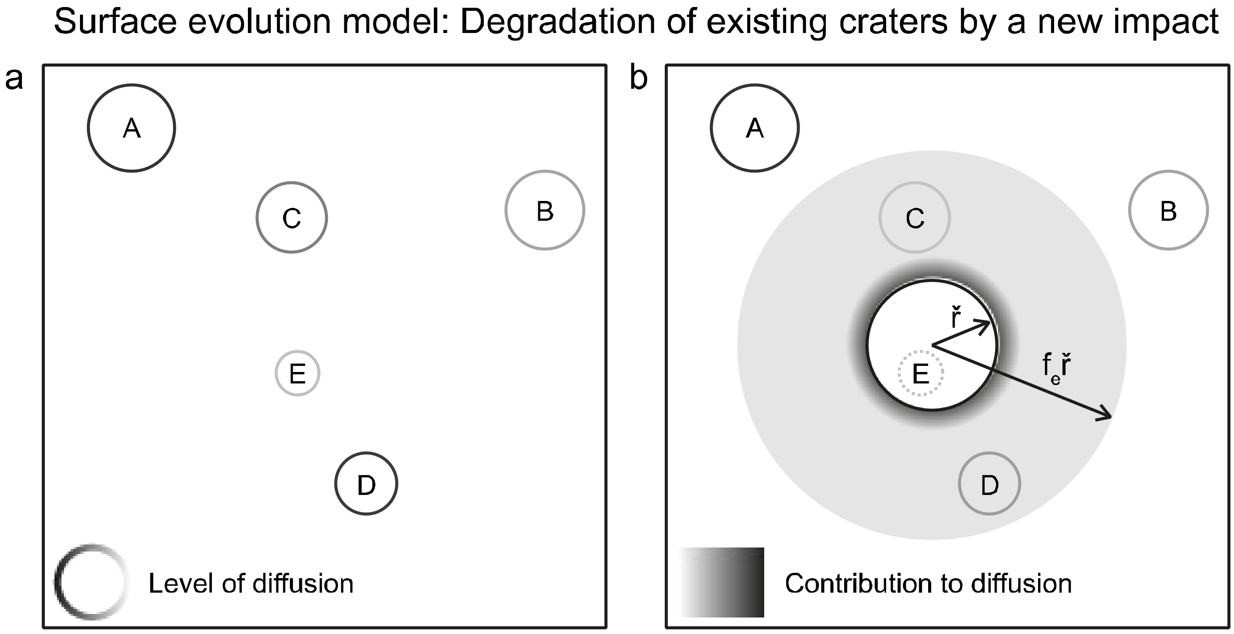

Figure 7.2: *This image shows how crater degradation from cookie cutting, proximal ejecta blanketing and distal ejecta blanketing is modeled in the simulations. In this example, there are five craters A-E with various degradation states on the modeled surface (a). Black indicates that a crater is fresh, light grey means that a crater is highly degraded from diffusive degradation processes. After a new impact of radius ř occurs, some of the pre-existing craters are subject to crater degradation (b). Here, crater E is erased due to cookie cutting. The impact craters within the circular degradation region of radius* f_e*ř, C and D, experience diffusive degradation from proximal (*$K_{d,ej}$*) and distal (*K_d*(ř)) ejecta. Dark areas represent a higher contribution to topographic diffusion than bright areas.* K_d*(ř) is uniformly distributed over the degradation region. The influence of proximal ejecta blanketing on topographic diffusion decreases rapidly with growing distance from the fresh crater. In this example, the new impact does not contribute to the degradation of craters A and B.*

7.2.4 Distal Ejecta Blanketing (High-Energy Ejecta Deposition)

In addition to the low-energy proximal ejecta, an impact excavates high-energy secondary projectiles that are deposited at a great distance from the crater rim (e.g., Speyerer et al., 2016). The secondary projectiles hit the surface and contribute to proximal ejecta blanketing and sandblasting in the same way as the primary impactors. Minton et al. (2019) concluded that this distal energetic ejecta deposition dominated the degradation of simple craters. For simplicity reasons in this work, we ignore the spatial complexity of distal ejecta rays (e.g., Elliott et al., 2018; Huang et al., 2017; Minton et al., 2019) in the simulations. Instead, we assume that the distal ejecta is deposited uniformly over a circular region. Although Minton et al. (2019) placed constraints on the strength of energetic distal ejecta degradation needed to produce the observed equilibrium of postmare craters, we allow the strength to vary as a parameter in our simulations for the ancient lunar terrains.

7.2.5 Modeling Topographic Diffusion With CTEM

In the CTEM models by Minton et al. (2019), topographic diffusion from new impacts is modeled as a linear accumulation of a degradation state K. Under a classical diffusion model in which the diffusivity, κ, is constant over time, t, the degradation state is given by $K = \kappa t$. In a diffusion-dominated degradation mode, the more K a crater accumulates the shallower it appears. There are two functions to quantify the degradation state of a crater: a visibility function $K_v(r)$, and a degradation function $K_d(\check{r})$. The visibility function quantifies how much degradation is required to fully degrade a crater.

The degradation function, on the other hand, determines how much a single impact event contributes to the degradation of the surrounding surface. Here, each new crater of a radius ř contributes a certain amount to the degradation state K of the existing landscape. Geometric crater obliteration, or cookie cutting, can also be described using the degradation state framework. When a large crater completely overlaps a smaller crater, it produces $K_d(\check{r}) = K_v(r)$.

The area around a new impact that is affected by topographic diffusion from high-energy ejecta deposits from the formation of a new crater is finite. In the simulations, we model this in a simplified way using a circular region of radius $f_e\check{r}$, where the extent is controlled by the size of a new crater and the scale factor f_e. Here, the per-crater contribution to topographic diffusion is spatially averaged and uniformly distributed across the degradation region (Figure 7.2). The intensity with which each new impact contributes to the diffusive degradation of the pre-existing landscape is determined by the degradation function

$$K_d(\check{r}) = K_{d,1}\check{r}^{\psi}. \qquad (3)$$

The coefficient $K_{d,1}$ regulates the strength of diffusive degradation and the slope ψ controls how the per-crater contribution to topographic diffusion scales with crater size. In this work we set $\psi = 2$ for all the simulations. Because K_d has units of m^2, $\psi = 2$ represents a case where $K_{d,1}$ contains no information about scale. This implies that there is a simple scale dependence in the per-crater contribution to topographic diffusion. In other words, a tenfold increase in diameter increases a crater's contribution to topographic diffusion by a hundredfold. In such an environment, impact craters exhibit geometric similarity. Accordingly, the relative contribution to topographic diffusion of small craters equals that of large craters.

The amount that low energy ejecta deposition contributes to diffusive crater degradation depends on the ejecta thickness h, given by equation (2). Compared to the contribution of diffusive degradation by distal ejecta, proximal ejecta blanketing has little influence on diffusive crater degradation.

$$K_{d,\mathrm{ej}} = 1.5h^2 \qquad (4)$$

When a new impact forms on the modeled terrain, the pre-existing craters of radius r within the degradation region accumulate an amount of K according to equations (3) and (4). A crater can accumulate a certain amount of K before it is considered too degraded to be observed and thus, not countable anymore. The maximum amount of K that a crater can accumulate is determined by the visibility function

$$K_v(r) = K_{v,1}r^{\gamma}. \qquad (5)$$

The visibility function is calibrated by investigating the depth-to-diameter (d/D) ratio of simple craters on a CTEM generated surface unit. Minton et al. (2019) used human crater counts to determine a minimum d/D ratio at which diffusively degraded craters are typically not recognized by visual interpretation anymore. By normalizing the minimum d/D ratio with respect to K, they determined a visibility function with the coefficient $K_{v,1} = 0.17$ and a slope $\gamma = 2$ that describes the maximum amount of K that craters can assemble before they are fully degraded. As in the $\psi = 2$ case mentioned above, $\gamma = 2$ represents a condition where craters exhibit geometric similarity, since K_v has units of m^2. This indicates that a tenfold increase in diameter requires a hundredfold increase in K to fully degrade it.

7.3 Modeling Pre-Nectarian Lunar Surface Evolution

Minton et al. (2019) applied the diffusion models to investigate the influence of distal ejecta from small simple craters on crater equilibrium. The simulations were conducted under the assumption that craters exhibit geometric similarity. However, because large complex craters are morphologically different from small simple ones (e.g., Pike, 1977; Williams & Zuber, 1998; Kalynn et al., 2013), it is not clear how well geometric similarity approximates both the per-crater contribution to topographic diffusion as well as the required amount of diffusive degradation to erase a crater.

In order to investigate how topographic diffusion contributes to lunar surface evolution, we model the evolution of a pre-Nectarian surface unit that contains larger craters than those investigated by Minton et al. (2019) – with diameters between 15.4 and 905 km. However, the diffusive effects of craters at all scales down to 12 μm in diameter are taken into account during surface evolution (Minton et al., 2019). The model impactor population reproduces the Neukum et al. (2001a) crater production function.

For the simple mare craters, Minton et al. (2019) used a "cutoff" value of $d/D = 0.05$ as a proxy for a fully degraded simple crater. However, the d/D of fresh complex craters is shallower than that of small simple craters, such that fresh craters with $D > {\sim}80$ km would have $d/D < 0.05$ (Pike 1977). Clearly, a constant d/D cutoff value is an imperfect proxy for degradation state. Also, currently CTEM does not model the full morphological complexity of complex craters, such as terraced walls and central peaks/peak rings. Thus, it is more difficult to calibrate the crater counting algorithm in a realistic way for complex craters relative to their simple counterparts.

Qualitatively, the shallower initial d/D and morphological complexity suggest that it would require relatively less accumulated degradation K to render a complex crater uncountable compared to a simple crater. However, for simplicity, in this study we assume instead that the visibility function parameters are the same for complex craters as simple ones ($K_{v,1} = 0.17$ and a slope $\gamma = 2$) and compute the resulting d/D cutoff value for complex craters as a function of crater size. This should result in somewhat higher observed crater number densities in our simulations compared to a more realistic treatment, though our results are much more strongly influenced by the degradation function than the visibility function (see supplementary information of the published article).

We assume geometric similarity for the degradation function ($\psi = 2$) and apply three different values for $K_{d,1}$ to vary the strength of the per-crater contribution to topographic diffusion. For simplicity, the diffusion from high velocity ejecta occurs over a circular degradation region with $f_e = 10$. The modeled surfaces have a square dimension of 2000x2000 pixels, with 6160 km on each side and a resolution of 3.08 km/pixel. Craters smaller than the resolution limit ($D <$ 15.4 km) are not modeled as individual craters, but still contribute to diffusive degradation. For each pixel, their contribution to topographic diffusion is determined and scaled to the pixel area (Minton et al., 2019). We analyze the crater densities on the modeled surface units and compare the results to observations on pre-Nectarian surface units in section 7.4.

7.3.1 Simulation 1: Strength of $K_{d,1}$ Corresponds to Mare Observations

Minton et al. (2019) used $K_{d,1} = 0.003$, $f_e = 10$, and $\psi = 2$ to model a surface unit that reproduces the crater equilibrium of the Apollo 15 landing site. In this simulation, we investigate, how well the parameterization of the diffusion model scales with increasing crater size and surface age.

7.3.2 Simulation 2: Strength of $K_{d,1}$ is Reduced to 1/30th of the Mare Intensity

In the second simulation, we reduced the strength of the degradation function by a factor of 30 to $K_{d,1} = 0.0001$. Here, we investigate how precisely CTEM models a pre-Nectarian surface unit when the effect of topographic diffusion from secondary impacts is reduced. In this simulation, the relative contribution of cookie cutting and proximal ejecta blanketing to surface evolution is higher than in Simulation 1.

7.3.3 Simulation 3: No Extra Diffusion From High-Energy Ejecta Deposits

We apply $K_{d,1} = 0$ to investigate the evolution of a pre-Nectarian surface unit when no topographic diffusion from secondary craters contributes to crater erasure. In this simulation, only the accumulation of proximal ejecta is modelled as a diffusive process. Hence, cookie cutting and proximal ejecta blanketing dominate crater erasure in the third simulation.

7.4 Results

We simulate the surface evolution of a pre-Nectarian surface unit in order to constrain how distal topographic diffusion influences the evolution of large craters on the most ancient lunar terrain. To this end, we conduct CSFD measurements on the modeled surfaces and compare the obtained results to lunar surface observations. Because we constrain the production CSFD to be that of the Neukum production function (Neukum et al. 2001a), any deviations in the observable CSFD of simulated craters must be the result of size-dependent crater degradation processes. We consider a modeled surface to be similar to that of a pre-Nectarian surface unit when (1) the obtained CSFDs do not follow an equilibrium power law, (2) a notable non-sparseness effect is present, and (3) the crater spatial number density is at about 10% geometric saturation (Fassett et al., 2012; Xiao and Werner, 2015; Kneissl et al., 2016; Povilaitis et al., 2018; Orgel et al., 2018).

We use a modified version of CSFD Tools (Riedel et al., 2018) to allow CSFD measurements on the CTEM-generated Cartesian plane with a repeating boundary condition. The CSFDs of visible craters are measured using the TCC and NSC techniques (Kneissl et al., 2016; Riedel et al., 2018). We consider the non-sparseness effect to be significant when there is a prominent difference between obtained CSFDs from the TCC and NSC approaches. In the NSC approach, we consider only the area within the crater rim as relevant for crater erasure. We do not consider any proximal ejecta blanket in the geometric overlap of pre-existing craters.

We use Craterstats (Michael et al., 2010) to analyze the obtained CSFDs in terms of non-sparseness effects, crater equilibrium conditions, and geometric saturation levels. A population is considered to be in equilibrium when the small crater CSFD largely does not follow the CSFD of the produced craters, but a power law function of the form of equation (1). When a population is in equilibrium, we use a least squares fit to determine the parameters a and b of the equilibrium power law. Geometric saturation rates are derived by comparing the CSFDs and equilibrium functions to a power law with $a =$

1.54 and $b = -2$, which describes a geometrically saturated crater population (Gault, 1970; Xiao and Werner, 2015).

7.4.1 Simulation 1: Strength of $K_{d,1}$ Corresponds to Mare Observations

In this simulation, we investigate how the degradation parameters that successfully reproduced the surface evolution for the Apollo 15 landing site (Minton et al., 2019) scales with size. Because we assume geometric similarity, craters of all sizes share the same relative contribution to surface degradation and also share the same relative relationship between accumulated degradation and visibility.

Figure 7.3a shows how the lunar surface would look if large complex craters on the lunar highlands shared the same relative contribution to topographic diffusion as small simple craters on the lunar maria. The modeled terrain appears very smooth with various highly degraded craters. This implies that topographic diffusion has a strong influence on the surface evolution. This is also evident in the obtained CSFDs. Because there is hardly any difference between the SFDs from the TCC and NSC approaches, the non-sparseness effect is negligible. Accordingly, the influence of cookie cutting on crater erasure is low, compared to diffusive processes.

The strong influence of topographic diffusion in combination with the variable sloped CSFD of the production population also causes the observed CSFD to reach an equilibrium state that is quite different from what is observed on the lunar surface. For craters smaller than 600 km in diameter, the CSFD follows an equilibrium power law with $a = 2.45 * 10^{-3}$ and a slope of $b = -1.09$. This is much shallower than the crater equilibrium for small simple craters on the lunar maria (e.g., Gault, 1970; Hartmann, 1984; Xiao and Werner, 2015). The equilibrium onset $D_{\mathrm{eq}} =$ 600 km occurs at 5.4 % geometric saturation. Craters with $D = 15$ km only exhibit 0.2 % geometric saturation.

Overall, both the crater spatial density and the morphology of the modeled surface differs from that on pre-Nectarian surface units. Figure 7.4 shows the geometric saturation rates on both the modeled surfaces and the pre-Nectarian units that Orgel et al. (2018) investigated. In the dataset that Orgel et al. (2018) used, craters appear in the densest configuration at diameters of 55-70 km. Here, the crater configuration exceeds 8% geometric saturation (BCC) and 10% geometric saturation (BNSC), respectively. On the modeled terrain, such dense crater configurations do not occur. The crater spatial distribution is densest at $D_{\mathrm{eq}} = 600$ km and becomes less dense with decreasing crater diameter. When we compare the results from this simulation to CSFD analyses on the lunar surface (Fassett et al., 2012; Orgel et al., 2018; Povaltitis et al. 2018), it becomes evident that the influence of topographic diffusion on the evolution of a pre-Nectarian surface unit is strongly overestimated in this simulation. Accordingly, when normalized by crater size, the relative contribution to topographic diffusion from secondary impacts must be lower for larger crater diameters than it is for the small simple craters that Minton et al. (2019) investigated.

7.4.2 Simulation 2: Strength of $K_{d,1}$ is Reduced to 1/30th of the Mare Intensity

Because the per-crater contribution to topographic diffusion was overestimated in Simulation 1, we next investigate a scenario in which we reduce the strength of the contribution of distal degradation. In a first study, we reduced the degradation function coefficient by one order of magnitude to make the scaling more intuitive. However, we found that the surface evolution

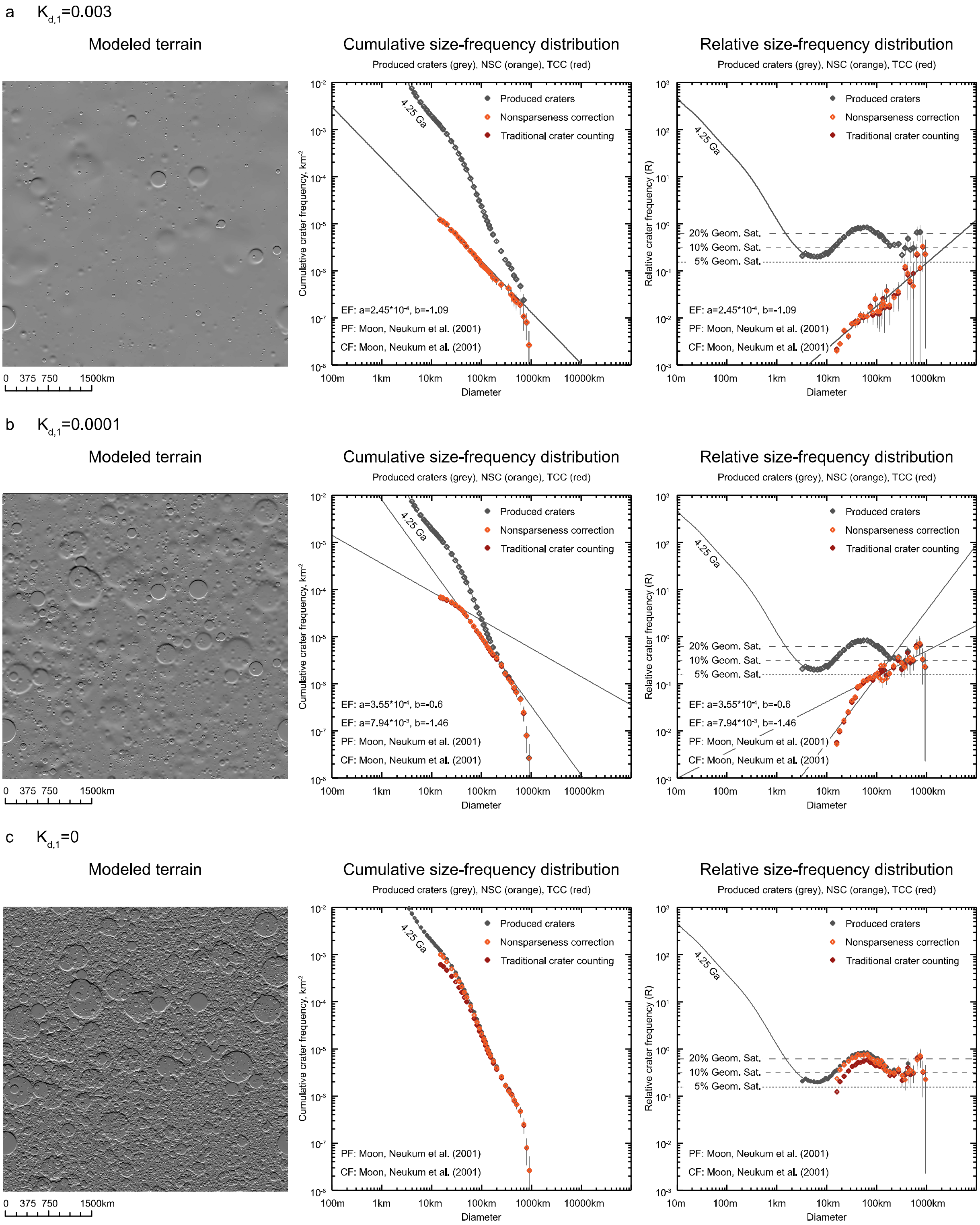

Figure 7.3: Modeled terrains with obtained cumulative and relative size-frequency distributions. Each row represents the results of one simulation. The results of a) Simulation 1, $K_{d,1} = 0.003$, b) Simulation 2: $K_{d,1} = 0.0001$, and c) Simulation 3: $K_{d,1} = 0$. The CSFDs are illustrated in a log binning. SFDs of produced craters (grey) follow an isochron of the Neukum et al. (2001a) production function that corresponds to a model age of 4.25 Ga. Note that the scale of the modeled terrain is different than in Fig. 1a.

models were still strongly dominated by topographic diffusion. For this reason, we further reduced $K_{d,1}$ by 1/30th of the value of Simulation 1.

Figure 7.3b shows that the modeled terrain of Simulation 2 has a rougher surface than that of Simulation 1. However, the obtained SFDs from NSC and TCC continue to coincide. This indicates that the non-sparseness effect is still negligible and that the effects of topographic diffusion continue to dominate crater erasure. For craters with $D < 150$ km, the obtained SFDs transition into an equilibrium state where the SFDs follow a function with a discontinuous slope.

The CSFDs of large craters follow a steeper equilibrium power law than the CSFDs of smaller craters. We approximate the equilibrium condition by fitting two power law functions to the CSFD. One function approximates the steeper part of the CSFD for craters between 40 and 150 km in diameter. A second function approximates the shallower part of the CSFD for craters with 15 to 40 km in diameter. We determined a power law function with $a = 7.94 * 10^{-3}$ and $b = -1.46$, which describes the steep part and a function with $a = 3.55 * 10^{-4}$ and $b = -0.6$, which describes the shallow part of the CSFD in equilibrium. Both slopes are much shallower than those observed for crater equilibrium on the lunar maria (e.g., Hartmann, 1984; Xiao and Werner, 2015). The equilibrium onset $D_{\text{eq}} = 150$ km occurs at 7.7% geometric saturation. The transition to the shallower equilibrium power law at $D_{\text{eq}} = 40$ km occurs at 4% geometric saturation. Craters with a diameter of 15 km appear in a configuration of 1% geometric saturation. Here, craters occur at a denser configuration than in Simulation 1. However, the crater saturation levels on the modeled terrain are different from the pre-Nectarian surface units that Orgel et al. (2018) investigated (see Fig. 7.4). In this simulation, craters larger than 100 km in diameter are in a much denser configuration than those observed on pre-Nectarian units. Craters of 15-100 km in diameter, on the other hand, are in a less dense configuration. This indicates that the topographic diffusion by distal ejecta continues to dominate crater erasure. Therefore, the relative contribution to topographic diffusion for craters larger than 15 km in diameter must be less than 1/30th of that of small simple craters.

7.4.3 Simulation 3: No Extra Diffusion From High-Energy Ejecta Deposits

$K_{d,1} = 0$ represents a scenario in which no topographic diffusion from distal ejecta contributes to the evolution of a pre-Nectarian surface unit. Hence, cookie cutting and proximal ejecta blanketing are the only processes that lead to crater erasure. Since there is only little smoothening from diffusive processes through proximal ejecta blanketing, the modeled terrain appears very rugged (Fig. 7.3c). This indicates that cookie cutting dominates crater erasure in this simulation.

The strong influence of cookie cutting is also apparent in the obtained SFDs. Here, the application of NSC leads to an increase in crater frequencies and to a better representation of crater production over the TCC approach. This is consistent with the observations by Orgel et al. (2018) and shows that a cookie cutting-dominated crater degradation environment causes the non-sparseness effect. In this regime, the number of visible craters is lower than the number of produced craters. In contrast to crater equilibrium, however, the crater densities continue to increase as the bombardment progresses. For this reason, craters on the simulated terrain are in a much denser configuration compared to simulations 1 and 2

(Fig. 7.4). Craters of 15-200 km in diameter are at a spatial number density of 9.1-16.4% (TCC) and 9.6-21.8% (NSC) geometric saturation, respectively. The crater configuration is densest for craters around 40 km (TCC) and 30 km in diameter (NSC). This roughly corresponds to the diameter range in which the crater density in the areas studied by Orgel et al. (2018) is highest. However, the crater density on pre-Nectarian surface units is lower than in this simulation (Orgel et al., 2018; Povilaitis, 2018). Accordingly, craters on the modeled surface unit persist much longer than on the Moon. This implies that although we can simulate a surface evolution that reproduces the non-sparseness effect and no crater equilibrium, we clearly underestimate the intensity of crater degradation when we ignore the diffusive effects of high velocity ejecta on lunar surface evolution.

7.5 Interpretations

The simulations in this work, together with lunar surface investigations reveal that there are two different crater degradation environments on the Moon. In one regime, topographic diffusion dominates the degradation of existing craters; in another regime, cookie cutting dominates the erasure of pre-existing craters. The former causes the CSFDs to follow an equilibrium power law, the latter leads to the non-sparseness effect, where the application of NSC results in a better recovery of the production function. Crater equilibrium, wherein the CSFD follows an equilibrium power law with $b \sim -2$, has been observed for small simple craters (e.g., Gault, 1970; Hartmann, 1984; Xiao and Werner, 2015; van der Bogert et al., 2018). Non-sparseness, on the other hand, affects large craters on pre-Nectarian surface units (Kneissl et al., 2016; Orgel et al., 2018; Riedel et al., 2018). This indicates that the different crater degradation environments depend on both crater size and surface age. When Minton et al. (2019) concluded that the high-energy deposition of distal ejecta is the primary process that causes crater equilibrium, they modeled the surface evolution for craters with $D \leq 200$ m. Craters in this size range are morphologically similar (Pike, 1977) and may be expressed by a simple scale dependence where craters exhibit geometric similarity. When we applied the same parameterization to craters with $D > 15$ km in Simulation 1, we did not generate a surface that is consistent with a pre-Nectarian surface unit with non-sparseness. Instead, we generated a surface unit in which the CSFD follows an equilibrium power law. The same happened when we reduced the per-crater contribution to topographic diffusion to 1/30th compared to the first simulation.

Only when we ignored the effects of distal ejecta on topographic diffusion were we able to simulate a pre-Nectarian surface unit that is to some extent consistent with the observations by Orgel et al. (2018). This illustrates that the simple scale dependence that controls diffusive crater degradation, indicated by $\psi = 2$, cannot account for lunar surface evolution of both small and large craters alike. In other words, relative to their size, large complex craters are less destructive to the surrounding terrain than small simple craters, as postulated by Povilaitis et al. (2018). Minton et al. (2019) used $\psi = 2$ to model the per-crater contribution to the degradation state K for craters with $D \leq 200$ m. The investigations by Xie et al. (2017) and Fassett et al. (2018) suggest that the size-dependent diffusivity κ that mare craters with diameters $800 \text{ m} \leq D \leq 2 \text{ km}$ experienced over time goes as $\kappa \propto D^{\sim 0.9}$. In an environment where the production and degradation function can be approximated by a power law with a constant slope, this corresponds to a scenario in which the average per-crater

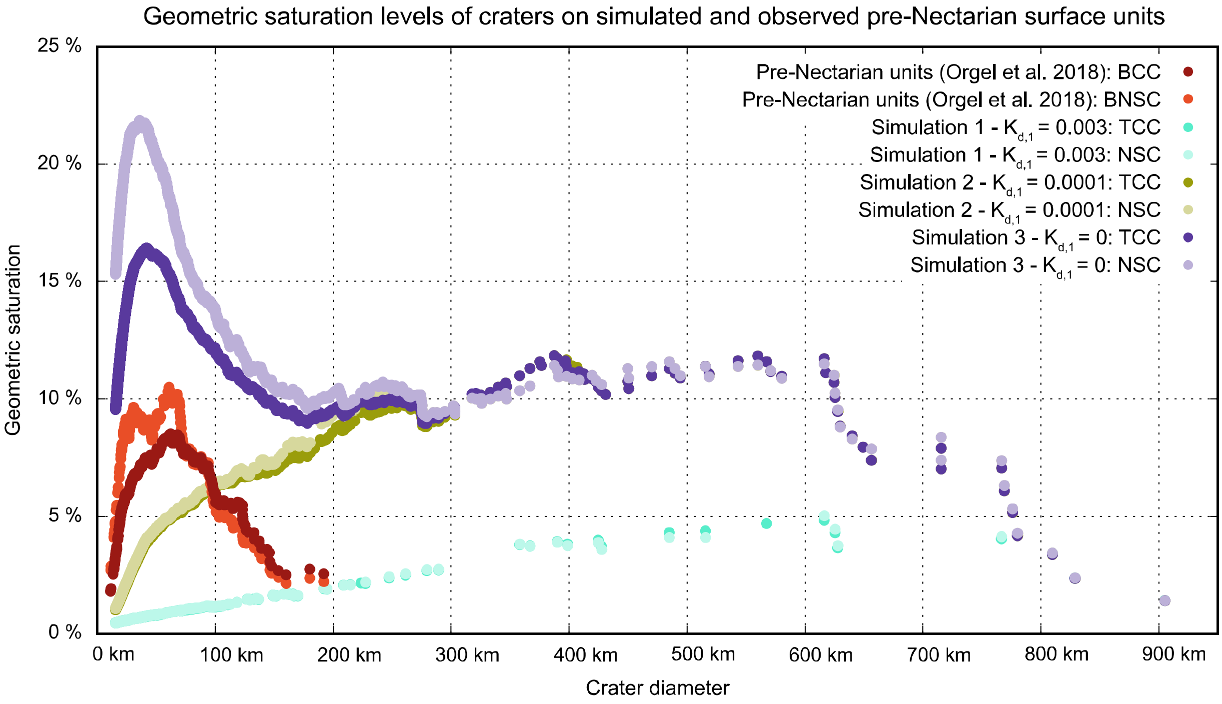

Figure 7.4: Geometric saturation levels of craters on simulated and observed pre-Nectarian surface units. Crater densities determined using traditional CSFD measurement techniques (TCC and BCC) are represented in a darker hue than their comparative populations, which were determined using geometric corrections (NSC and BNSC).

contribution to the degradation state K can also be approximated by $\psi = 2$ (see supplementary information of the published article).

The simulations presented in this paper, in turn, show that the surface evolution of craters with $D > 15$ km correspond most closely to a pre-Nectarian surface unit when the extra diffusion caused by distal ejecta is significantly reduced. This scenario is equivalent to a diffusivity exponent of $\psi < 2$. Thus, as the relative per crater contribution to diffusive degradation decreases with increasing crater size, the exponent ψ must be scale-dependent. In order to determine a scale-dependent ψ that is equally valid for small and large craters, further studies of the lunar surface, particularly on the transition between the cookie cutting and the diffusion-dominated crater degradation environments, are required. The same applies to the slope of the visibility function γ. In the $\gamma = 2$ case, the relative amount of accumulated K that is needed to fully degrade a crater is the same for craters of any size. Such simple scale dependence does not take into account the morphologic differences of simple and complex craters, such as d/D ratios (Pike 1977). It can be expected that the size-dependent morphological properties influence the amount of K that is needed in order to completely degrade a crater. As the visibility of a crater depends on its d/D ratio, it is very likely that γ is scale-dependent as well. However, this requires further studies on the d/D related crater visibility of complex craters.

7.6 Conclusions

In this work, we simulated the surface evolution of a pre-Nectarian surface unit to investigate how topographic diffusion affects the evolution of the earliest lunar terrains. We used a simple scale dependence to describe both the per-crater contribution to diffusion and the per-crater requirement for erasure by diffusion. We conclude that such simple scale dependence cannot account for crater erasure of small simple and large complex craters alike, and that relative to their size, large craters are less destructive to their environment than small craters. This circumstance leads to a diffusion-dominated degradation regime for small craters and a cookie cutting-dominated degradation regime for large craters. Thus, the exponent, which controls diffusion in our simulations, must be scale-dependent. A simple scale dependence in the per-crater contribution to topographic diffusion (indicated by $\psi = 2$) can only account for the evolution of a diffusion-dominated crater equilibrium, which typically affects small simple craters. Thus, we assume that the diffusion exponent must decrease with increasing crater diameter. However, in order to determine a realistic model that accounts for the surface evolution of small simple and large complex craters alike, further investigations on the transition between a cookie cutting and a diffusion-dominated crater degradation regime on the lunar surface need to be conducted.

Acknowledgements

We thank Brad Thomson and an anonymous reviewer for their helpful comments to improve this manuscript. We also thank Alicia Neesemann and Caleb Fassett for the helpful discussions. C. R. and C. O. were supported by German Research Foundation SFB-TRR 170, Subproject A03-95. G. M. was supported by the German Aerospace Center (DLR), Grant 50QM1702. H. H. and C. H. vdB were supported by DLR Project 50OW1504. The associated data are available via Mendeley Data (doi: 10.17632/xphn7c7scs.1).

PART IV

CONCLUSIONS

CHAPTER 8

CONCLUSIONS

This thesis contains four peer-reviewed publications that are presented in parts II and III. The publications presented in part II (Chapters 4 and 5) comprise two papers that describe the development of geospatial methods to investigate crater populations on planetary surfaces. In part III, Chapters 6 and 7 include two publications investigating the lunar cratered surface evolution based on geospatial techniques. Each chapter contains distinctive conclusions that refer to the respective study. In this chapter, the individual results of the presented studies are summarized and related to the research questions that were introduced in Chapter 1.2.

8.1 Summary of Results

The studies that are presented in this thesis cover technical and scientific topics. The technical aspects in part II involve considering planetary curvature when modifying and analyzing geospatial data. In Chapter 4, two existing techniques (M2CND and SDAA) to quantify the spatial randomness of impact craters are improved by implementing geodesic measurements and polygon modifications. This improvement allows for the investigation of areas where planetary curvature would lead to incorrect results using previous implementations of the M2CND and SDAA techniques. To demonstrate the improvements' effectiveness, the global spatial randomness of impact craters on Mercury, Venus, and the Moon is investigated. The obtained results support individual crater population variations and surface evolution scenarios previously examined on the respective planetary bodies.

For example, it was shown that the global crater records ($20 < D < 300$ km) on Mercury and the Moon are in a clustered arrangement due to extended resurfacing of ancient terrains by younger geologic units. On Mercury, the emplacement of smooth plains and the Caloris impact event erased a substantial part of the pre-existing crater record. The interval between these events and the formation of Mercury's oldest terrains, the inter-crater plains, is relatively short. On the Moon, where mare volcanism and the Orientale impact event had a strong influence on pre-existing craters' erasure, the interval between the emplacement of young and ancient surfaces (the lunar highlands) is greater. Therefore, the global clustering of impact craters is more significant on the Moon than on Mercury. On Venus, craters are mostly randomly distributed across all sizes due to its young surface and the insignificant influence of recent volcanism on crater erasure. The study suggests that a global decline in volcanic activity influenced the recent surface evolution of Venus.

The study results are summarized in Figure 8.1, where the relative fraction of binned crater populations ($D < 300$ km) on Mercury, Venus, and the Moon that fall into Z-Score categories of $|Z| < 2$, $2 \leq |Z| < 5$, $5 \leq |Z| < 10$, and $|Z| \geq 10$ is presented. Crater sizes in binned populations are determined by D_{mean} and represented by brightness gradations. The results show that the amount of binned crater populations that are indistinguishable from a random population is highest on Venus and significantly lower on Mercury and the Moon. Figure 8.1 also illustrates that the SDAA technique reacts more sensitive to non-random crater configurations on planetary surfaces than the M2CND approach.

Chapter 5 presents the implementation of CSFD measurement techniques to consider the effects of geometric crater obliteration in a new software tool. The NSC and BNSC techniques are applied to better represent the lunar production function in areas where crater erasure by cookie cutting strongly affects the visible crater record (Fig. 8.2). For each crater considered in the CSFD measurement, a strongly modified outline of the initial reference area is assigned to determine the crater frequency (Fig. 8.2b). The implemented techniques require geospatial data modification on a curved planetary surface and therefore rely on geodesic measurements to avoid map-distortion effects. To that end, geodesic measurements and polygon calculations are implemented. The software tool supports 64 bit and multicore data processing and was developed using open software libraries. Therefore, the source code of the tool and the CSFD measurement techniques are provided to the scientific community for application and potential further development.

The scientific studies presented in part III investigate the effects of cratering-induced crater obliteration on the lunar surface evolution. Chapter 6 presents the application of the BNSC technique to consider the influence of geometric crater obliteration (Chapter 5) onto the lunar crater record. The study shows that an apparent time-dependent change in CSFD shape can be

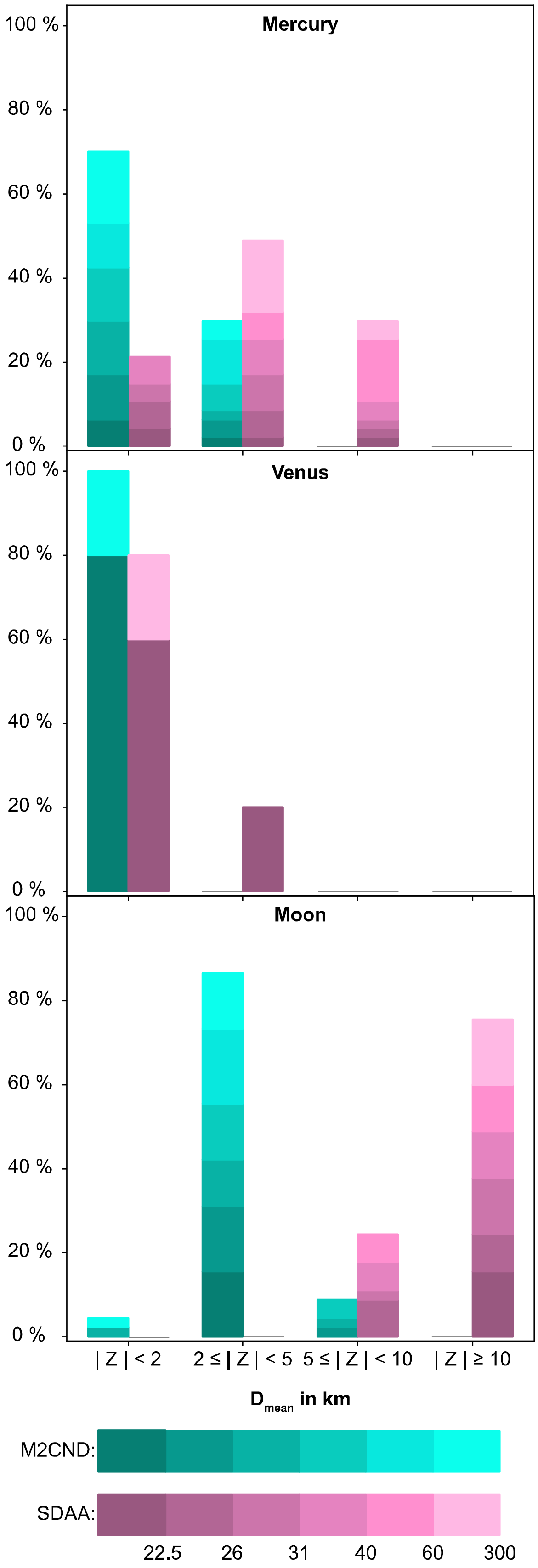

Figure 8.1: Z-Scores of binned crater populations from geodesic M2CND and SDAA measurements.

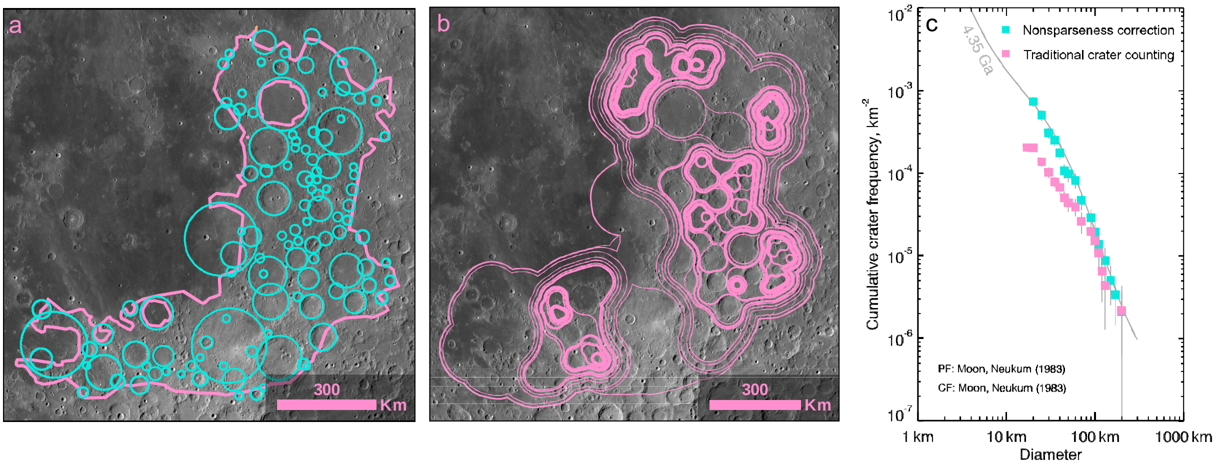

Figure 8.2: Results from applying BNSC to craters on the remnants of the lunar Nubium basin, with spatial data defining reference area and impact craters (a) (data from Fassett et al. (2012) and Orgel et al. (2018)), assigned reference areas generated for the BNSC measurement (b), and obtained CSFDs from TCC and BNSC techniques (c).

caused by the effects of geometric crater obliteration. This implies that the change in CSFD on ancient lunar terrains postulated by Strom et al. (2005), Fassett et al. (2012), and Strom et al. (2015) is not necessarily caused by a change in the size-frequency distribution of impacting projectiles but by crater erasure from subsequent impacts. This effect becomes more pronounced the more craters accumulate. Therefore, the change in CSFD occurs as a natural effect of impact cratering, which implies that a continuous production function well approximates the lunar cratering record. However, the intensity to which the cratering flux during the LHB period may have deviated from an exponentially declining cratering rate remains subject to further investigation.

The study in Chapter 7 simulates the evolution of a cratered lunar surface to investigate the influence of cratering-induced degradation on the pre-existing cratered landscape. The model uses an impactor population that resembles the continuous lunar production function by Neukum et al. (2001a) and relies on various scaling laws and scientific investigations to determine crater formation and visibility. One parameter that determines the per-crater contribution to topographic diffusion from sandblasting is modified in the investigation. The study demonstrates that crater obliteration processes lead to two distinct states – crater equilibrium and non-sparseness (Fig. 8.3). Craters in equilibrium are subject to diffusive crater degradation, which is primarily controlled by the cumulative effects of distal ejecta fragments. The process is well-investigated for small, simple craters on the Moon. However, the investigation in Chapter 6 demonstrates that large lunar craters are subject to non-sparseness, which is controlled by the geometric obliteration of pre-existing craters by a fresh impact.

The study in Chapter 7 shows that to create a cratered lunar landscape, in which cratering-induced crater degradation leads to crater equilibrium for small and non-sparseness for large craters, the per-crater contribution to topographic diffusion of the pre-existing landscape must be size-dependent. Therefore, relative to their size, small lunar craters are more destructive to the pre-existing lunar terrain than large craters due to their immense contribution to topographic diffusion by high-velocity distal ejecta. The study also shows that the NSC and BNSC techniques (Chapters 5 and 6) are

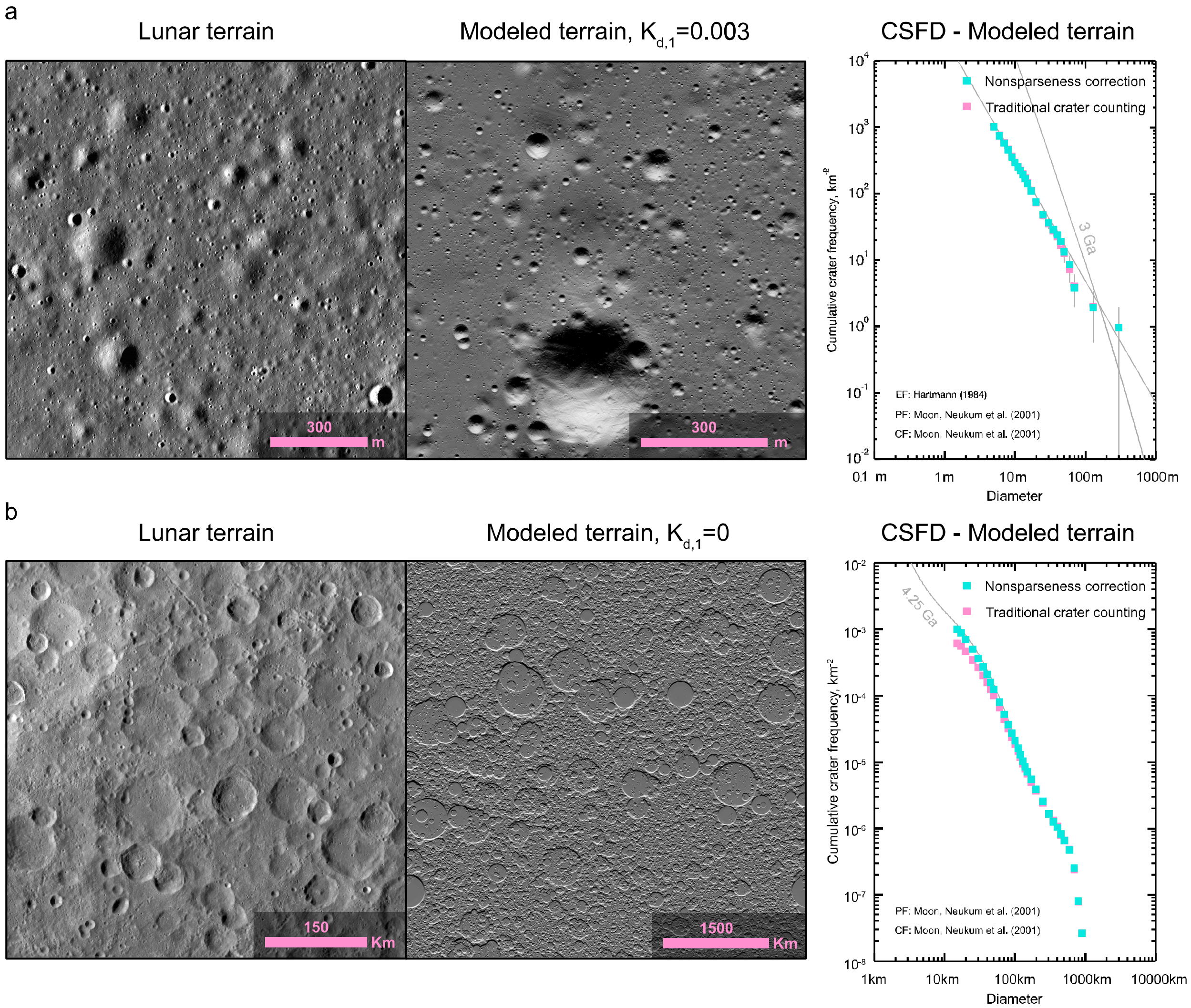

Figure 8.3: Lunar surface units, modeled lunar surface units, and obtained CSFDs from CTEM models. The lunar surface in (a) shows small simple craters of various degradation states near the Apollo 15 landing site. The presented crater population is in a diffusion-induced crater equilibrium (Robbins et al., 2014; Minton et al., 2019). A surface unit with a similar appearance and CSFD was modeled by Minton et al. (2019) using $K_{d,1} = 0.003$ *to simulate the per-crater contribution to topographic diffusion by high-velocity ejecta. In this case, information about the production population cannot be inferred by applying NSC. The lunar surface in (b) shows an area of high crater density north of Tsiolkovskiy crater, where crater topographies show less intense degradation from downslope diffusion. To model a surface unit with a similar appearance and CSFD, fresh impact craters in the CTEM model do not contribute to the topographic diffusion of the pre-existing terrain by its distal ejecta (*$K_{d,1} = 0$*), as shown in Chapter 7. Here, only cookie cutting and proximal ejecta blanketing contribute to crater erasure. In such a scenario, cratering-induced crater erasure leads to a state of non-sparse cratering and information about the impactor population can be inferred by applying the NSC and BNSC techniques.*

appropriate methods to restore information about the crater production population on surfaces where the geometric obliteration of pre-existing craters by a fresh impact is the dominant crater degradation process.

8.2 Research Questions

This thesis contains four general research questions introduced in Chapter 1.2. They are addressed using the conclusions from the studies presented in parts II and III of this thesis.

1. How do surface processes affect the global spatial distribution of impact craters?

Since impact cratering is a spatially random process with an impact flux that is reasonably uniform over a planetary body, any geologic process that causes a considerable erasure of the crater record leads to a non-random distribution of impact craters. Such large-scale resurfacing processes can be endogenic (e.g., a lava flow) or exogenic (e.g., impact-induced). The study presented in Chapter 4 shows that the emplacement of extended volcanic units and the formation of young basins led to a substantial erasure of the pre-existing crater record on Mercury and the Moon. On Venus, the absence of extended volcanism and the low number of impacts ever since its cratering record started accumulating developed a crater population, which is indistinguishable from a random population. Therefore, extended surface processes and continuous cosmic bombardment lead to a global non-random distribution of impact craters on planetary surfaces.

2. How do fresh impacts contribute to the degradation of the pre-existing cratered landscape?

Fresh impacts contribute to the erasure of pre-existing craters through geometric obliteration, ejecta blanketing, and downslope diffusion. The study presented in Chapter 7 shows that geometric crater obliteration and ejecta blanketing lead to a state of non-sparse cratering, in which the measured CSFD does not resemble the production population but where crater densities continue to increase with ongoing cratering. Downslope diffusion, particularly from high-velocity ejected material, leads to a crater equilibrium state, where crater densities do not increase despite ongoing impact cratering and wherein the CSFD does not follow the size-frequency distribution of the production population, but a power law with a constant slope. On the Moon, the per-crater contribution to the degradation of the pre-existing landscape is size-dependent. Here, relative to their size, small craters are more destructive to the pre-existing landscape due to the higher contribution to topographic diffusion from high-velocity ejected material.

3. How does the cratering-induced degradation of impact craters affect planetary surface evolution interpretations?

Cratering-induced crater erasure leads to a difference between the size-frequency distribution of visible impact craters and the size-frequency distribution of the impactor population. Therefore, simple conclusions about the impactor population from cratering records may be subject to observation biases. Such deviations also affect planetary surface dating. In cases where the fit of the crater production function to the measured CSFD is ambiguous or misleading, a remote-sensing-based surface dating is not practicable. The studies presented in Chapters 6 and 7 show that measured CSFDs can strongly differ from the size-frequency distribution of the impactor population. While there is currently no method to retain information on the impactor size-frequency distribution of craters in equilibrium, the NSC and BNSC techniques presented in Chapter 5 allow for an acceptable reconstruction of the crater production population in an environment, where cookie cutting is the major cause for the cratering-induced erasure of pre-existing impact craters.

4. Does the change in the CSFD on ancient lunar surface units reflect a change in the impactor population?

The cumulative effects of geometric crater obliteration lead to a non-sparse cratered landscape, in which the CSFD of the visible crater population does not correspond to the crater production population. This effect occurs as a natural effect of impact cratering, and the deviation between both populations increases as bombardment in a cookie cutting dominated degradation regime continues. The application of the BNSC technique to the lunar crater record, presented in Chapter 6, shows that the observed change in the CSFD on ancient lunar surface units can be compensated allowing the recovery of the original production function when the effects of geometric crater obliteration on the visible crater record are considered. Furthermore, the study presented in Chapter 7 shows that this effect of non-sparse cratering can be simulated in a cratered surface evolution model. Therefore, a continuous production function approximates the observable lunar production population to an adequate degree and the change in the CSFD on ancient lunar surface units can be corrected by applying the NSC and BNSC CSFD measurement techniques.

BIBLIOGRAPHY

Adeli, S., Hauber, E., Kleinhans, M., Le Deit, L., Platz, T., Fawdon, P., & Jaumann, R(2016). Amazonian-aged fluvial system and associated ice-related features in Terra Cimmeria, Mars. Icarus, 277, 286–299. https://doi.org/10.1016/j.icarus.2016.05.020

Airey, M. W., Mather, T. A., Pyle, D. M., & Ghail, R. C. (2017). The distribution of volcanism in the Beta-Atla-Themis region of Venus: Its relationship to rifting and implications for global tectonic regimes. Journal of Geophysical Research: Planets, 122(8), 1626–1649. https://doi.org/10.1002/2016je005205

Baldwin, R. B. (1964). Lunar crater counts. The Astronomical Journal, 69(5), 377–392. https://doi.org/10.1086/109289

Baldwin, R. B. (1974). On the accretion of the Earth and Moon. Icarus, 23, 97–107. https://doi.org/10.1016/0019-1035(74)90107-9

Basilevsky, A. T., Head, J. W., Schaber, G. G., & Strom, R. G. (1997). The resurfacing history of Venus. In W. Bougher, D. M. Hunten, & R. J. Phillips (Eds.), Venus II (pp. 1047). Tucson: University of Arizona Press.

Basilevsky, A. T., & Head, J. W., III. (1998). The geologic history of Venus: A stratigraphic view. Journal of Geophysical Research, 103(E4), 8531–8544. https://doi.org/10.1029/98je00487

Basilevsky, A. T., & Head, J. W. (2000). Geologic units on Venus: Evidence for their global correlation. Planetary and Space Science, 48(1), 75–111. https://doi.org/10.1016/s0032-0633(99)00083-5

Basilevsky, A. T., & Head, J. W. (2006). Impact craters on regional plains on Venus: Age relations with wrinkle ridges and implications for the geological evolution of Venus. Journal of Geophysical Research, 111(E3). https://doi.org/10.1029/2005je002473

Bill, R. (2016). Grundlagen der Geo-Informationssysteme. Heidelberg: Wichmann.

Bjonnes, E. E., Hansen, V. L., James, B., & Swenson, J. B. (2012). Equilibrium resurfacing of Venus: Results from new Monte Carlo modeling and implications for Venus surface histories. Icarus, 217(2), 451–461. https://doi.org/10.1016/j.icarus.2011.03.033

Boehnke, P., & Harrison, T. M. (2016). Illusory late heavy bombardments. Proceedings of the National Academy of Science, 113(39), 10802–10806. https://doi.org/10.1073/pnas.1611535113

Bottke, W. F., Durda, D. D., Nesvorny, D., Jedicke, R., Morbidelli, A., Vokrouhlicky, D., & Levison, H. F. (2005). Linking the collisional history of the main asteroid belt to its dynamical excitation and depletion. Icarus, 179, 63–94. https://doi.org/10.1016/j.icarus.2005.05.017

Bottke, W. F., Levison, H. F., Nesvorny, D., & Dones, L. (2007). Can planetesimals left over from terrestrial planet formation produce the lunar Late Heavy Bombardment? Icarus, 190, 203–223. https://doi.org/10.1016/j.icarus.2007.02.010

Bottke, W. F., Vokrouhlický, D., Minton, D., Nesvorný, D., Morbidelli, A., Brasser, R., et al. (2012). An Archaean heavy bombardment from a destabilized extension of the asteroid belt. Nature, 485(7396), 78–81. https://doi.org/10.1038/nature10967

Bottke, W. F., Vokrouhlicky, D., Marchi, S., Jackson, A., Levison, H. F., & Swindle, T. (2015). The earliest lunar bombardment produced by Moon-forming impact ejecta (pp. 3012). Houston, TX: LPI Contributions 1826.

Bottke, W. F., & Norman, M. D. (2017). The Late Heavy Bombardment. Annual Review of Earth and Planetary Sciences, 45(1), 619–647. https://doi.org/10.1146/annurev-earth-063016-020131

Byrne, P. K., Ostrach, L. R., Fassett, C. I., Chapman, C. R., Denevi, B. W., Evans, A. J., et al. (2016). Widespread effusive volcanism on Mercury likely ended by about 3.5 Ga. Geophysical Research Letters, 43(14), 7408–7416. https://doi.org/10.1002/2016gl069412

Carlson, R. W. (2011). Absolute Age Determinations: Radiometric. In H. K. Gupta, (Ed.), Encyclopedia of Solid Earth Geophysics (pp. 1–8). Dordrecht: Springer Netherlands. https://doi.org/10.1007/978-90-481-8702-7_69

Chao, E. C. T., Shoemaker, E. M., & Madsen, B. M. (1960). First Natural Occurrence of Coesite. Science, 132(3421), 220–222. https://doi.org/10.1126/science.132.3421.220

Claeys, P., & Morbidelli, A. (2015). Late Heavy Bombardment. In Encyclopedia of Astrobiology (pp. 1365–1369). Springer Berlin Heidelberg. https://doi.org/10.1007/978-3-662-44185-5_869

Cohen, B. A. (2000). Support for the Lunar Cataclysm Hypothesis from Lunar Meteorite Impact Melt Ages. Science, 290(5497), 1754–1756. https://doi.org/10.1126/science.290.5497.1754

Cohen, B. A., Petro, N. E., Lawrence, S. J., Clegg, S. M., Denevi, B. W., Dya, M. E., … Wiens, R. C. (2018). Curie: Constraining Solar System Bombardment using in situ radiometric dating. In 49th Lunar and planetary science conference (1029 pp.). Houston, TX.

Crater Analysis Techniques Working Group (1979). Standard techniques for presentation and analysis of crater size-frequency data. Icarus, 37(2), 467–474. https://doi.org/10.1016/0019-1035(79)90009-5

Christensen, P. R., E. Engle, S. Anwar, S. Dickenshied, D. Noss, N. Gorelick, & Weiss-Malik, M. (2009), JMARS – A planetary GIS, Paper Presented at AGU Fall Meeting, San Francisco, CA.

Craddock, R. A., & Howard, A. D. (2000). Simulated degradation of lunar impact craters and a new method for age dating farside mare deposits. Journal of Geophysical Research, 105, 20,387–20,402. https://doi.org/10.1029/1999JE001099

Cuk, M., Gladman, B. J., & Stewart, S. T. (2010). Constraints on the source of lunar cataclysm impactors. Icarus, 207, 590–594. https://doi.org/10.1016/j.icarus.2009.12.013

Denevi, B. W., Robinson, M., Solomon, S. C., Murchie, S. L., Blewett, D. T., Domingue, D. L., et al. (2009). The evolution of Mercury's crust: A global perspective from MESSENGER. Science, 324(5927), 613–618. https://doi.org/10.1126/science.1172226

Denevi, B. W., Ernst, C. M., Meyer, H. M., Robinson, M. S., Murchie, S. L., Whitten, J. L., et al. (2013). The distribution and origin of smooth plains on Mercury. Journal of Geophysical Research: Planets, 118(5), 891–907. https://doi.org/10.1002/jgre.20075

Deutsch, A. & Schärer, U. (1994). Dating terrestrial impact events. Meteoritics, 29, 301-322. 10.1111/j.1945-5100.1994.tb00595.x

Edmundson, K. L., Cook, D. A., Thomas, O. H., Archinal, B. A., & Kirk, R. L. (2012). Jigsaw: The ISIS3 Bundle Adjustment for Extraterrestrial Photogrammetry. ISPRS Annals of Photogrammetry, Remote Sensing and Spatial Information Sciences, I–4, 203–208. https://doi.org/10.5194/isprsannals-i-4-203-2012

Elliott, J. R., Huang, Y.-H., Minton, D. A., & Freed, A. M. (2018). The length of lunar crater rays explained using secondary crater scaling. Icarus, 312, 231–246. https://doi.org/10.1016/j.icarus.2018.04.015

Ernst, C. M., Denevi, B. W., Barnouin, O. S., Klimczak, C., Chabot, N. L., Head, J. W., et al. (2015). Stratigraphy of the Caloris basin, Mercury: Implications for volcanic history and basin impact melt. Icarus, 250, 413–429. https://doi.org/10.1016/j.icarus.2014.11.003

Evans, A. J., Soderblom, J. M., Andrews-Hanna, J. C., Solomon, S. C., & Zuber, M. T. (2016). Identification of buried lunar impact craters from GRAIL data and implications for the nearside maria. Geophysical Research Letters, 43(6), 2445–2455. https://doi.org/10.1002/2015gl067394

Fassett, C. I., & Head, J. W. (2008). The timing of Martian valley network activity: Constraints from buffered crater counting. Icarus, 195(1), 61–89. https://doi.org/10.1016/j.icarus.2007.12.009

Fassett, C. I., Head, J. W., Blewett, D. T., Chapman, C. R., Dickson, J. L., Murchie, S. L., et al. (2009). Caloris impact basin: Exterior geomorphology, stratigraphy, morphometry, radial sculpture, and smooth plains deposits. Earth and Planetary Science Letters, 285, 297–308. https://doi.org/10.1016/j.epsl.2009.05.022

Fassett, C. I., Head, J. W., Smith, D. E., Zuber, M. T., & Neumann, G. A. (2011a). Thickness of proximal ejecta from the Orientale Basin from lunar Orbiter laser altimeter (LOLA) data: Implications for multi-ring basin formation. Geophysical Research Letters, 38, L17201. https://doi.org/10.1029/2011gl048502

Fassett, C. I., Kadish, S. J., Head, J. W., Solomon, S. C., & Strom, R. G. (2011b). The global population of large craters on Mercury and comparison with the Moon. Geophysical Research Letters, 38(10). https://doi.org/10.1029/2011gl047294

Fassett, C. I., Head, J. W., Kadish, S. J., Mazarico, E., Neumann, G. A., Smith, D. E., & Zuber, M. T. (2012). Lunar impact basins: Stratigraphy, sequence and ages from superposed impact crater populations measured from Lunar Orbiter Laser Altimeter (LOLA) data. Journal of Geophysical Research, 117, E00H06. https://doi.org/10.1029/2011JE003951

Fassett, C. I., & Thomson, B. J. (2014). Crater degradation on the lunar maria: Topographic diffusion and the rate of erosion on the Moon. Journal of Geophysical Research: Planets, 119, 2255–2271. https://doi.org/10.1002/2014JE004698

Fassett, C. I. (2016). Analysis of impact crater populations and the geochronology of planetary surfaces in the inner solar system. Journal of Geophysical Research: Planets, 121(10), 1900–1926. https://doi.org/10.1002/2016je005094

Fassett, C. I., Crowley, M. C., Leight, C., Dyar, M. D., Minton, D. A., Hirabayashi, M., et al. (2017). Evidence for rapid topographic evolution and crater degradation on Mercury from simple crater morphometry. Geophysical Research Letters, 44(11), 5326–5335. https://doi.org/10.1002/2017gl073769

Fassett, C. I., Minton, D. A., Thomson, B. J., Hirabayashi, M., & Watters, W. A. (2018). Re-analysis of observations of crater degradation on the lunar maria accounting for anomalous diffusion. In Paper presented at 49th Lunar and Planetary Science Conference (LPI Contrib. No. 2083). The Woodlands: TX.

French, B. M. (1998). Traces of catastrophe: a handbook of shock-metamorphic effects in terrestrial meteorite impact structures. Houston: Lunar and Planetary Institute, LPI Contribution No. 954.

Gault, D. E., (1968). Impact cratering mechanics and structures. In French, B.M. & N.M. Short, (Eds.), Shock Metamorphism of Natural Materials (pp. 87-99). Baltimore: Mono Book Corp.

Gault, D. E. (1970). Saturation and equilibrium conditions for impact cratering on the lunar surface: Criteria and implications. Radio Science, 5(2), 273–291. https://doi.org/10.1029/rs005i002p00273

Giacomini, L., Massironi, M., Galluzzi, V., Ferrari, S., & Palumbo, P. (2020). Dating long thrust systems on Mercury: New clues on the thermal evolution of the planet. Geoscience Frontiers, 11(3), 855–870. https://doi.org/10.1016/j.gsf.2019.09.005

Gomes, R., Levison, H. F., Tsiganis, K., & Morbidelli, A. (2005). Origin of the cataclysmic late heavy bombardment period of the terrestrial planets. Nature, 435(7041), 466–469. https://doi.org/10.1038/nature03676

Gong, S., Wieczorek, M. A., Nimmo, F., Kiefer, W. S., Head, J. W., Huang, C., et al. (2016). Thicknesses of mare basalts on the Moon from gravity and topography. Journal of Geophysical Research: Planets, 121(5), 854–870. https://doi.org/10.1002/2016je005008

Green, R. O., et al. (2011), The Moon Mineralogy Mapper (M3) imaging spectrometer for lunar science: Instrument description, calibration, on-orbit measurements, science data calibration and on-orbit validation, J. Geophys. Res., 116, E00G19, doi:10.1029/2011JE003797

Grindrod, P. M., Stofan, E. R., & Guest, J. E. (2010). Volcanism and resurfacing on Venus at the full resolution of Magellan SAR data. Geophysical Research Letters, 37(15). https://doi.org/10.1029/2010gl043424

Guest, J. E., & Stofan, E. R. (1999). A new view of the stratigraphic history of Venus. Icarus, 139(1), 55–66. https://doi.org/10.1006/icar.1999.6091

Haber, T., Scherer, E. E., Bast, R., & Sprung, P. (2017). 176Lu–176Hf Isochron Dating of Strongly Cosmic ray exposed samples—A case study on Apollo 14 Impact Melt Rock 14310. In 48th Lunar and planetary science conference XLVIII (2911 pp.). Houston, TX.

Hamann, C. (2018). Projectile-target interaction and rapid, high-temperature geochemical processes in impact melts, (Dissertation thesis). Berlin, Germany. Freie Universität Berlin. https://doi.org/10.17169/REFUBIUM-1238

Hao, J., Michael, G. G., Adeli, S., Jaumann, R., Portyankina, G., Hauber, E., et al. (2020). Variability of spider spatial configuration at the Martian south pole. Planetary and Space Science, 185, 104848. https://doi.org/10.1016/j.pss.2020.104848

Hartmann, W. K. (1965). Secular changes in meteoritic flux through the history of the solar system. Icarus, 4(2), 207–213. https://doi.org/10.1016/0019-1035(65)90062-X

Hartmann, W. K. (1972). Paleocratering of the Moon: Review of post-Apollo data. Astrophysics and Space Science, 17(1), 48–64. https://doi.org/10.1007/bf00642541

Hartmann, W. K. (1984). Does crater "saturation equilibrium" occur in the solar system? Icarus, 60, 56–74. https://doi.org/10.1016/0019-1035(84)90138-6

Hartmann, W. K. (1995). Planetary cratering 1. The question of multiple impactor populations: Lunar evidence. Meteoritics, 30(4), 451–467. https://doi.org/10.1111/j.1945-5100.1995.tb01152.x

Hartmann, W. K., & Gaskell, R. W. (1997). Planetary cratering 2: Studies of saturation equilibrium. Meteoritics, 32, 109–121. https://doi.org/10.1111/j.1945-5100.1997.tb01246.x

Hartmann, W. K. (2007). Martian cratering 9: Toward resolution of the controversy about small craters. Icarus, 189(1), 274–278. https://doi.org/10.1016/j.icarus.2007.02.011

Hartmann, W. K. (2019). History of the Terminal Cataclysm Paradigm: Epistemology of a Planetary Bombardment That Never (?) Happened. Geosciences, 9(7), 285. https://doi.org/10.3390/geosciences9070285

Hauck, S. A., II, Phillips, R. J., & Price, M. H. (1998). Venus: Crater distribution and plains resurfacing models. Journal of Geophysical Research, 103(E6), 13635–13642. https://doi.org/10.1029/98je00400

Head, J. W. (1974). Morphology and structure of the Taurus-Littrow Highlands (Apollo 559 17): Evidence for their origin and evolution. Moon, 9, 355–395. https://doi.org/10.1007/BF00562579

Head, J. W., Crumpler, L. S., Aubele, J. C., Guest, J. E., & Saunders, R. S. (1992). Venus volcanism: Classification of volcanic features and structures, associations, and global distribution from Magellan data. Journal of Geophysical Research, 97(E8), 13153. https://doi.org/10.1029/92je01273

Head, J. W., Murchie, S. L., Prockter, L. M., Robinson, M. S., Solomon, S. C., Strom, R. G., et al. (2008). Volcanism on Mercury: Evidence from the first MESSENGER flyby. Science, 321(5885), 69–72. https://doi.org/10.1126/science.1159256

Head, J. W., Murchie, S. L., Prockter, L. M., Solomon, S. C., Chapman, C. R., Strom, R. G., et al. (2009). Volcanism on Mercury: Evidence from the first MESSENGER flyby for extrusive and explosive activity and the volcanic origin of plains. Earth and Planetary Science Letters, 285(3–4), 227–242. https://doi.org/10.1016/j.epsl.2009.03.007

Head, J. W., Fassett, C. I., Kadish, S. J., Smith, D. E., Zuber, M. T., Neumann, G. A., & Mazarico, E. (2010). Global Distribution of Large Lunar Craters: Implications for Resurfacing and Impactor Populations. Science, 329(5998), 1504–1507. https://doi.org/10.1126/science.1195050

Head, J. W., Chapman, C. R., Strom, R. G., Fassett, C. I., Denevi, B. W., Blewett, D. T., et al. (2011). Flood Volcanism in the Northern High Latitudes of Mercury Revealed by MESSENGER. Science, 333(6051), 1853–1856. https://doi.org/10.1126/science.1211997

Herrick, R. R., & Rumpf, M. E. (2011). Postimpact modification by volcanic or tectonic processes as the rule, not the exception, for Venusian craters. Journal of Geophysical Research, 116(E2). https://doi.org/10.1029/2010je003722

Herrick, R. R., Bateman, E. M., Crumpacker, W. G., & Bates, D. (2018). Observations from a global database of impact craters on Mercury with diameters greater than 5 km. Journal of Geophysical Research: Planets, 123(8), 2089–2109. https://doi.org/10.1029/2017je005516

Hiesinger, H., Jaumann, R., Neukum, G., & Head, J. W., III. (2000). Ages of mare basalts on the lunar nearside. Journal of Geophysical Research, 105(E12), 29239–29275. https://doi.org/10.1029/2000je001244

Hiesinger, H., Head, J. W., Wolf, U., Jaumann, R., & Neukum, G. (2003). Ages and stratigraphy of mare basalts in Oceanus Procellarum, Mare Nubium, Mare Cognitum, and Mare Insularum. Journal of Geophysical Research, 108(E7), 5065. https://doi.org/10.1029/2002JE001985

Hiesinger, H., Head, J. W., III, Wolf, U., Jaumann, R., & Neukum, G. (2006). New ages for basalts in Mare Fecunditatis based on crater size-frequency measurements. Paper presented at 37th Lunar and Planetary Science Conference, Lunar and Planetary Institute, The Woodlands, Texas, abstract #1151.

Hiesinger, H., Head, J. W., III, Wolf, U., Jaumann, R., & Neukum, G. (2011). Ages and stratigraphy of lunar mare basalts: A synthesis. In W. A. Ambrose& D. A. Williams, (Eds.), Research Issues in Lunar Stratigraphy (pp. 1–51). Geological Society of America. https://doi.org/10.1130/2011.2477(01)

Hiesinger, H., van der Bogert, C. H., Pasckert, J. H., Funcke, L., Giacomini, L., Ostrach, L. R., & Robinson, M. S. (2012a). How old are young lunar craters? Journal of Geophysical Research, 117, E00H10. https://doi.org/10.1029/2011JE003935

Hiesinger, H., van der Bogert, C. H., Pasckert, J. H., Schmedemann, N., Robinson, M. S., Jolliff, B., & Petro, N. (2012b). New crater size-frequency distribution measurements of the South Pole-Aitken Basin. In Proceedings of the 43rd lunar and planetary science conference (pp. 2863). The Woodlands, TX: LPI Contribution 1659.

Hirabayashi, M., Minton, D. A., & Fassett, C. I. (2017). An analytical model of crater count equilibrium. Icarus, 289, 134– 143. https://doi.org/10.1016/j.icarus.2016.12.032

Hirata, N., Morota, T., Cho, Y., Kanamaru, M., Watanabe, S., Sugita, S., et al. (2020). The spatial distribution of impact craters on Ryugu. Icarus, 338, 113527. https://doi.org/10.1016/j.icarus.2019.113527

Holo, S., & Kite, E. (2020). The spatial signature of a changing ancient impactor population for Mars. Icarus, 337, 113447. https://doi.org/10.1016/j.icarus.2019.113447

Hopkins, M. D., & Mojzsis, S. J. (2015). A protracted timeline for lunar bombardment from mineral chemistry, Ti thermometry and U–Pb geochronology of Apollo 14 melt breccia zircons. Contributions to Mineralogy and Petrology, 169(3). https://doi.org/10.1007/s00410-015-1123-x

Housen, K. R., & Holsapple, K. A. (2011). Ejecta from impact craters. Icarus, 211, 856–875. https://doi.org/10.1016/j.icarus.2010.09.017

Huang, Y.-H., Minton, D. A., Hirabayashi, M., Elliott, J. R., Richardson, J. E., Fassett, C. I., & Zellner, N. E. B. (2017). Heterogeneous impact transport on the Moon. Journal of Geophysical Research: Planets, 122(6), 1158–1180. https://doi.org/10.1002/2016je005160

Iqbal, W., Hiesinger, H., & van der Bogert, C. H. (2019). Geological mapping and chronology of lunar landing sites: Apollo 11. Icarus, 333, 528–547. https://doi.org/10.1016/j.icarus.2019.06.020

Ivanov, B. A. (2001). Mars/Moon cratering rate ratio estimates. Space Science Reviews, 96, 87–104. https://doi.org/10.1023/A:1011941121102

Ivanov, B. A., Neukum, G., Bottke, W. F., & Hartmann, W. K. (2002). The comparison of size-frequency distributions of impact craters and asteroids and the planetary cratering rate. Asteroids, 3, 89–101.

Ivanov, M. A., Head, J. W., & Basilevsky, A. T. (2015). History of the long-wavelength topography of Venus. Solar System Research, 49(1), 1–11. https://doi.org/10.1134/s0038094615010025

Jolliff, B. L., Gillis, J. J., Haskin, L. A., Korotev, R. L., & Wieczorek, M. A. (2000). Major lunar crustal terranes: Surface expressions and crust-mantle origins. Journal of Geophysical Research, 105(E2), 4197–4216. https://doi.org/10.1029/1999je001103

Kalynn, J., Johnson, C. L., Osinski, G. R., & Barnouin, O. (2013). Topographic characterization of lunar complex craters. Geophysical Research Letters, 40, 38–42. https://doi.org/10.1029/2012GL053608

Kenkmann, T., Collins, G. S., & Wünnemann, K. (2012). The Modification Stage of Crater Formation. In G.R. Osinski & E. Pierazzo, (Eds.), Impact Cratering (pp. 60–75). Hoboken: John Wiley & Sons, Ltd. https://doi.org/10.1002/9781118447307.ch5

Kelley, S. P., & Sherlock, S. C. (2012). The Geochronology of Impact Craters. In G.R. Osinski & E. Pierazzo, (Eds.), Impact Cratering (pp. 240–253). Hoboken: John Wiley & Sons, Ltd. https://doi.org/10.1002/978111844307.ch16

Kirchoff, M. R. (2017). Can spatial statistics help decipher impact crater saturation? Meteoritics & Planetary Sciences, 53(4), 874–890. https://doi.org/10.1111/maps.13014

Kneissl, T., van Gasselt, S., & Neukum, G. (2011). Map-projection-independent crater size-frequency determination in GIS environments—New software tool for ArcGIS. Planetary and Space Science, 59(11-12), 1243–1254. https://doi.org/10.1016/j.pss.2010.03.015

Kneissl, T., Schmedemann, N., Neesemann, A., Raymond, C. A., & Russel, C. T. (2014). Crater counting on small bodies—The influence of topography-related distortions. Paper Presented at 45th Lunar and Planetary Science Conference, The Woodlands, TX.

Kneissl, T., Michael, G. G., Platz, T., & Walter, S. H. G. (2015). Age determination of linear surface features using the buffered crater counting approach – Case studies of the Sirenum and Fortuna Fossae graben systems on Mars. Icarus, 250, 384–394. https://doi.org/10.1016/j.icarus.2014.12.008

Kneissl, T., Michael, G. G., & Schmedemann, N. (2016). Treatment of non-sparse cratering in planetary surface dating. Icarus, 277, 187–195. https://doi.org/10.1016/j.icarus.2016.05.015

König, B. (1977). Untersuchung von primären und sekundären Einschlagsstrukturen auf dem Mond und Laborexperimente zum Studium des Auswurfs von Sekundärteilchen, (Ph.D. thesis). Heidelberg, Germany: University of Heidelberg.

Kreslavsky, M. A. (1996). Venus cratering record: Constraints on resurfacing history (pp. 18–22). Twenty-Seventh Lunar and Planetary Science Conference, Houston, TX.

Kreslavsky, M. A. (2007). Statistical characterization of spatial distribution of impact craters: Implications to present-day cratering rate on Mars. Seventh International Conference on Mars, Pasadena, CA.

Kreslavsky, M. A., Head, J. W., Neumann, G. A., Zuber, M. T., & Smith, D. E. (2014). Kilometer-scale topographic roughness of Mercury: Correlation with geologic features and units. Geophysical Research Letters, 41(23), 8245–8251. https://doi.org/10.1002/2014gl062162

Kreslavsky, M. A., Ivanov, M. A., & Head, J. W. (2015). The resurfacing history of Venus: Constraints from buffered crater densities. Icarus, 250, 438–450. https://doi.org/10.1016/j.icarus.2014.12.024

Kring, D. A., & Durda, D. D. (2012). A global lunar landing site study to provide the scientific context for exploration of the Moon. In Lunar and Planetary Institute (688 pp.). Houston, TX: LPI Contribution 1694.

Le Feuvre, M., & Wieczorek, M. A. (2011). Nonuniform cratering of the Moon and a revised crater chronology of the inner Solar System. Icarus, 214(1), 1–20. https://doi.org/10.1016/j.icarus.2011.03.010

Liu, T., Michael, G. G., Engelmann, J., Wünnemann, K., & Oberst, J. (2019). Regolith mixing by impacts: Lateral diffusion of basin melt. Icarus, 321, 691–704. https://doi.org/10.1016/j.icarus.2018.12.026

Liu, T., Michael, G., Wünnemann, K., Becker, H., & Oberst, J. (2020). Lunar megaregolith mixing by impacts: Spatial diffusion of basin melt and its implications for sample interpretation. Icarus, 339, 113609. https://doi.org/10.1016/j.icarus.2019.113609

Marchi, S., Morbidelli, A., & Cremonese, G. (2005). Flux of meteoroid impacts on Mercury. Astronomy & Astrophysics, 431(3), 1123–1127. https://doi.org/10.1051/0004-6361:20041800

Marchi, S., Mottola, S., Cremonese, G., Massironi, M., & Martellato, E. (2009). A new Chronology for the Moon and Mercury. The Astronomical Journal, 137(6), 4936–4948. https://doi.org/10.1088/0004-6256/137/6/4936

Marchi, S., Bottke, W. F., Kring, D. A., & Morbidelli, A. (2012). The onset of the lunar cataclysm as recorded in its ancient crater populations. Earth and Planetary Science Letters, 325-326, 27– 38. https://doi.org/10.1016/j.epsl.2012.01.021

Marchi, S., Chapman, C. R., Fassett, C. I., Head, J. W., Bottke, W. F., & Strom, R. G. (2013). Global resurfacing of Mercury 4.0–4.1 billion years ago by heavy bombardment and volcanism. Nature, 499(7456), 59–61. https://doi.org/10.1038/nature12280

Martelli, G., Ryan, E. V., Nakamura, A. M., & Giblin, I. (1994). Catastrophic disruption experiments: recent results. Planetary and Space Science, 42(12), 1013–1026. https://doi.org/10.1016/0032-0633(94)90002-7

McDougall, I. & Harrison, T. M. (1999). Geochronology and Thermochronology by the 40Ar/39Ar Method. Oxford: Oxford University Press.

McEwen, A. S., & Bierhaus, E. B. (2006). The importance of secondary cratering to age constraints on planetary surfaces. Annual Review of Earth and Planetary Sciences, 34(1), 535–567. https://doi.org/10.1146/annurev.earth.34.031405.125018

McGetchin, T. R., Settle, M., & Head, J. W. (1973). Radial thickness variation in impact crater ejecta: Implications for lunar basin deposits. Earth and Planetary Science Letters, 20(2), 226– 236. https://doi.org/10.1016/0012-821X(73)90162-3

Melosh, H. J. (1989). Impact Cratering: A Geologic Process. New York: Oxford University Press.

Melosh, H. J., & Ivanov, B. A. (1999). Impact crater collapse. Annual Review of Earth and Planetary Sciences, 27(1), 385–415. https://doi.org/10.1146/annurev.earth.27.1.385

Melosh, H. J. (2012). The Contact and Compression Stage of Impact Cratering. In G.R. Osinski & E. Pierazzo (Eds.), Impact Cratering (pp. 32–42). Hoboken: John Wiley & Sons, Ltd. https://doi.org/10.1002/9781118447307.ch3

Michael, G. G., & Neukum, G. (2010). Planetary surface dating from crater size-frequency distribution measurements: Partial resurfacing events and statistical age uncertainty. Earth and Planetary Science Letters, 294(3–4), 223–229. https://doi.org/10.1016/j.epsl.2009.12.041

Michael, G. G., Platz, T., Kneissl, T., & Schmedemann, N. (2012). Planetary surface dating from 828 crater size–frequency distribution measurements: Spatial randomness and clustering. Icarus, 829 218(1), 169–177. https://doi.org/10.1016/j.icarus.2011.11.033

Michael, G. G. (2013). Planetary surface dating from crater size–frequency distribution measurements: Multiple resurfacing episodes and differential isochron fitting, Icarus, 226, 885–890, doi:10.1016/j.icarus.2013.07.004

Michael, G. G., Kneissl, T., & Neesemann, A. (2016). Planetary surface dating from crater size-frequency distribution measurements: Poisson timing analysis. Icarus, 277, 279–285. https://doi.org/10.1016/j.icarus.2016.05.019

Michael, G. G., Basilevsky, A., & Neukum, G. (2018). On the history of the early meteoritic bombardment of the Moon: Was there a terminal lunar cataclysm? Icarus, 302, 80–103. https://doi.org/10.1016/j.icarus.2017.10.046

Miljkovic, K., Wieczorek, M. A., Collins, G. S., Laneuville, M., Neumann, G. A., Melosh, H. J., et al. (2013). Asymmetric distribution of lunar impact basins caused by variations in target properties. Science, 342(6159), 724–726. https://doi.org/10.1126/science.1243224

Minton, D. A., Richardson, J. E., & Fassett, C. I. (2015). Re-examining the main asteroid belt as the primary source of ancient lunar craters. Icarus, 247, 172–190. https://doi.org/10.1016/j.icarus.2014.10.018

Minton, D. A., Fassett, C. I., Hirabayashi, M., Howl, B. A., & Richardson, J. E. (2019). The equilibrium size-frequency distribution of small craters reveals the effects of distal ejecta on lunar landscape morphology. Icarus, 326, 63– 87. https://doi.org/10.1016/j.icarus.2019.02.021

Morbidelli, A., Levison, H. F., Tsiganis, K., & Gomes, R. (2005). Chaotic capture of Jupiter's Trojan asteroids in the early solar system. Nature, 435, 462–465. https://doi.org/10.1038/nature03540

Morbidelli, A., Brasser, R., Gomes, R., Levison, H. F., & Tsiganis, K. (2010). Evidence from the asteroid belt for a violent past evolution of Jupiter's orbit. The Astronomical Journal, 140, 1391–1401. https://doi.org/10.1088/0004-6256/140/5/1391

Morbidelli, A., Marchi, S., Bottke, W. F., & Kring, D. A. (2012). A sawtooth-like timeline for the first billion years of lunar bombardment. Earth and Planetary Science Letters, 355–356, 144–151. https://doi.org/10.1016/j.epsl.2012.07.037

Neesemann, A., van Gasselt, S., Schmedemann, N., Marchi, S., Walter, S. H. G., Preusker, F., et al. (2019). The various ages of Occator crater, Ceres: Results of a comprehensive synthesis approach. Icarus, 320, 60–82. https://doi.org/10.1016/j.icarus.2018.09.006

Neukum, G., König, B., & Arkani-Hamed, J. (1975). A study of lunar impact crater size-distributions. The Moon, 12(2), 201–229. https://doi.org/10.1007/bf00577878

Neukum, G. (1983). Meteoritenbombardement und Datierung planetarer Oberflächen, (Habilitation thesis). Munich, Germany: Ludwig-Maximilians-Universität München.

Neukum, G., & Ivanov, B. A. (1994). Crater size distributions and impact probabilities on Earth from lunar, terrestrial-planet, and asteroid cratering data. In T. Gehrels, M. S. Matthews, & A.

Schumann (Eds.), Hazards due to comets and asteroids (pp. 359–416). Tuscon, AZ: University of Arizona Press.

Neukum, G., Ivanov, B. A., & Hartmann, W. K. (2001a). Cratering Records in the Inner Solar System in Relation to the Lunar Reference System. In Space Sciences Series of ISSI (pp. 55–86). Springer Netherlands. https://doi.org/10.1007/978-94-017-1035-0_3

Neukum, G., Oberst, J., Hoffmann, H., Wagner, R., & Ivanov, B. A. (2001b). Geologic evolution and cratering history of Mercury. Planetary and Space Science, 49(14–15), 1507–1521. https://doi.org/10.1016/s0032-0633(01)00089-7

Norman, M., Duncan, R. A., & Huard, J. J. (2006). Identifying impact events within the lunar cataclysm from 40Ar–39Ar ages and compositions of Apollo 16 impact melt rocks. Geochimica et Cosmochimica Acta, 70, 6032–6049. https://doi.org/10.1016/j.gca.2006.05.021

Norman, M., Duncan, R. A., & Huard, J. J. (2010). Imbrium provenance for the Apollo 16 Descartes terrain: Argon ages and geochemistry of lunar breccias 67016 and 67455. Geochimica et Cosmochimica Acta, 74, 763–783. https://doi.org/10.1016/j.gca.2009.10.024

Norman, M. D., & Nemchin, A. A. (2014). A 4.2 billion year old impact basin on the Moon: U–Pb dating of zirconolite and apatite in lunar melt rock 67955. Earth and Planetary Science Letters, 388, 387–398. https://doi.org/10.1016/j.epsl.2013.11.040

O'Brien, D. P., & Greenberg, R. (2003). Steady-state size distributions for collisional populations: Analytical solution with size-dependent strength. Icarus, 164, 334–345. https://doi.org/10.1016/S0019-1035(03)00145-3

Orgel, C., Allender, E. J., Almeida, N. V., Cook, J., Ende, J. J., Kamps, O., … Kring, D. A. (2017). Landing site assessment for Phase-2 of eDSH-enabled Lunar missions being examined as an ISECG's GER mission scenario. In 5th European Lunar Symposium (pp. 167–168). München, Germany.

Orgel, C., Michael, G. G., Fassett, C. I., van der Bogert, C. H., Riedel, C., Kneissl, T., & Hiesinger, H. (2018). Ancient bombardment of the inner solar system—Reinvestigation of the ‘fingerprints’ of different impactor populations on the lunar surface. Journal of Geophysical Research: Planets, 123, 748– 762. https://doi.org/10.1002/2017JE005451

Orgel, C., Fassett, C. I., Michael, G., Riedel, C., van der Bogert, C. H., & Hiesinger, H. (2020). Re-examination of the population, stratigraphy, and sequence of Mercurian basins: Implications for Mercury's early impact history and comparison with the Moon. Journal of Geophysical Research: Planets, 125, e2019JE006212. https://doi.org/10.1029/2019JE006212

Osinski, G. R., Grieve, R. A. F., & Tornabene, L. L. (2012). Excavation and Impact Ejecta Emplacement. In G.R. Osinski & E. Pierazzo, (Eds.), Impact Cratering (pp. 43–59). Hoboken: John Wiley & Sons, Ltd. https://doi.org/10.1002/9781118447307.ch4

Osinski, G. R., & Pierazzo, E. (2012). Impact Cratering: Processes and Products. In G.R. Osinski & E. Pierazzo, (Eds.), Impact Cratering (pp. 1–20). Hoboken: John Wiley & Sons, Ltd. https://doi.org/10.1002/9781118447307.ch1

Ostrach, L. R., Robinson, M. S., & Denevi, B. W. (2012). Distribution of impact melt on Mercury and the Moon. 43th Lunar and Planetary Science Conference, The Woodlands, TX, #1113.

Ostrach, L. R., Robinson, M. S., Whitten, J. L., Fassett, C. I., Strom, R. G., Head, J. W., & Solomon, S. C. (2015). Extent, age, and resurfacing history of the northern smooth plains on Mercury from MESSENGER observations. Icarus, 250, 602–622. https://doi.org/10.1016/j.icarus.2014.11.010

O'Rourke, J. G., Wolf, A. S., & Ehlmann, B. L. (2014). Venus: Interpreting the spatial distribution of volcanically modified craters. Geophysical Research Letters, 41(23), 8252–8260. https://doi.org/10.1002/2014gl062121

Öpik, E. J. (1960). The lunar surface as an impact counter. Monthly Notices of the Royal Astronomical Society, 120(5), 404– 411. https://doi.org/10.1093/mnras/120.5.404

Phillips, R. J., Raubertas, R. F., Arvidson, R. E., Sarkar, I. C., Herrick, R. R., Izenberg, N., & Grimm, R. E. (1992). Impact craters and Venus resurfacing history. Journal of Geophysical Research, 97(E10), 15923. https://doi.org/10.1029/92je01696

Pierazzo, E., & Melosh, H. J. (2012). Environmental Effects of Impact Events. In G.R. Osinski & E. Pierazzo, (Eds.), Impact Cratering (pp. 146–156). Hoboken: John Wiley & Sons, Ltd. https://doi.org/10.1002/9781118447307.ch10

Pike, R. J. (1977). Apparent depth/diameter relations for lunar crater. In Paper presented at 8th Lunar Science Conference (pp. 427–3436). Houston: TX.

Price, M., & Suppe, J. (1995). Constraints on the resurfacing history of Venus from the hypsometry and distribution of volcanism, tectonism, and impact craters. Earth, Moon, and Planets, 71(1–2), 99–145. https://doi.org/10.1007/bf00612873

Prockter, L. M., Ernst, C. M., Denevi, B. W., Chapman, C. R., Head, J. W., Fassett, C. I., et al. (2010). Evidence for young volcanism on Mercury from the third MESSENGER flyby. Science, 329(5992), 668–671. https://doi.org/10.1126/science.1188186

Potter, R. W. K. (2015). Investigating the onset of multi-ring impact basin formation. Icarus, 261, 91–99. https://doi.org/10.1016/j.icarus.2015.08.009

Potts, N. J., Gullikson, A. L., Curran, N. M., Dhaliwal, J. K., Leader, M. K., Rege, R. N., & Kring, D. A (2015). Robotic traverse and sample return strategies for a lunar farside mission to the Schrödinger basin. Advances in Space Research, 55, 1241–1254. https://doi.org/10.1016/j.asr.2014.11.028

Povilaitis, R. Z., Robinson, M. S., van der Bogert, C. H., Hiesinger, H., Meyer, H. M., & Ostrach, L. R. (2018). Crater density differences: Exploring regional resurfacing, secondary crater populations, and crater saturation equilibrium on the Moon. Planetary and Space Science, 162, 41–51. https://doi.org/10.1016/j.pss.2017.05.006

Rapp, R. H. (1993). Geometric geodesy part 2. Columbus, OH: Ohio State University, Department of Geodetic Science and Surveying.

Richardson, J. E. (2009). Cratering saturation and equilibrium: A new model looks at an old problem. Icarus, 204(2), 697– 715. https://doi.org/10.1016/j.icarus.2009.07.029

Riedel, C., Michael, G. G., & Kneissl, T. (2017). Crater counting on heavily cratered surfaces: Implementing non-sparseness correction in an ArcGIS independent tool for planetary surface dating. In 3rd Planetary Data Workshop 2017 (7017 pp.). Flagstaff, AZ: LPI Contribution 1986.

Riedel, C., Michael, G., Kneissl, T., Orgel, C., Hiesinger, H., & van der Bogert, C. H. (2018). A new tool to account for crater obliteration effects in crater size-frequency distribution measurements. Earth and Space Science, 5, 258– 267. https://doi.org/10.1002/2018EA000383

Riedel, C., Minton, D. A., Michael, G., Orgel, C., van der Bogert, C. H., & Hiesinger, H. (2020). Degradation of small simple and large complex lunar craters: Not a simple scale dependence. Journal of Geophysical Research: Planets, 125, e2019JE006273. https://doi.org/10.1029/2019JE006273

Riedel, C., Michael, G. G., Orgel, C., Baum, C., van der Bogert, C. H., & Hiesinger, H. (2021). Studying the global spatial randomness of impact craters on Mercury, Venus, and the Moon with geodesic neighborhood relationships. Journal of Geophysical Research: Planets, 126, e2020JE006693. https://doi.org/10.1029/2020JE006693

Robbins, S. J., Antonenko, I., Kirchoff, M. R., Chapman, C. R., Fassett, C. I., Herrick, R. R., et al. (2014). The variability of crater identification among expert and community crater analysts. Icarus, 234, 109–131. https://doi.org/10.1016/j.icarus.2014.02.022

Robbins, S. J. (2019). A new global database of lunar impact craters >1–2 km: 1. Crater locations and sizes, comparisons with published databases, and global analysis. Journal of Geophysical Research: Planets, 124(4), 871–892. https://doi.org/10.1029/2018je005592

Robinson, M. S., Brylow, S. M., Tschimmel, M., Humm, D., Lawrence, S. J., Thomas, P. C., et al. (2010). Lunar Reconnaissance Orbiter Camera (LROC) Instrument Overview. Space Science Reviews, 150(1–4), 81–124. https://doi.org/10.1007/s11214-010-9634-2

Romeo, I., & Turcotte, D. L. (2009). The frequency-area distribution of volcanic units on Venus: Implications for planetary resurfacing. Icarus, 203(1), 13–19. https://doi.org/10.1016/j.icarus.2009.03.036

Romeo, I. (2013). Monte Carlo models of the interaction between impact cratering and volcanic resurfacing on Venus: The effect of the Beta-Atla-Themis anomaly. Planetary and Space Science, 87, 157–172. https://doi.org/10.1016/j.pss.2013.07.010

Ross, H. P. (1968). A simplified mathematical model for lunar crater erosion. Journal of Geophysical Research, 73, 1343–1354. https://doi.org/10.1029/JB073i004p01343

Ryder, G. (1990). Lunar samples, lunar accretion and the early bombardment of the Moon. Eos, Transactions American Geophysical Union, 71(10), 313. https://doi.org/10.1029/90eo00086

Salamunićcar, G., Lončarić, S., Grumpe, A., & Wöhler, C. (2013). Hybrid method for crater detection based on topography reconstruction from optical images and the new LU78287GT catalogue of lunar impact craters. Advances in Space Research, 53(12), 1783–1797. https://doi.org/10.1016/j.asr.2013.06.024

Saunders, R. S., Pettengill, G. H., Arvidson, R. E., Sjogren, W. L., Johnson, W. T. K., & Pieri, L. (1990). The Magellan Venus Radar Mapping Mission. Journal of Geophysical Research, 95(B6), 8339. https://doi.org/10.1029/jb095ib06p08339

Schaber, G. G., Strom, R. G., Moore, H. J., Soderblom, L. A., Kirk, R. L., Chadwick, D. J., et al. (1992). Geology and distribution of impact craters on Venus: What are they telling us? Journal of Geophysical Research, 97(E8), 13257. https://doi.org/10.1029/92je01246

Schaber, G. G., Strom, R. G., & Kirk, R. L. (1995). Update on the USGS crater database for Venus, LPSC XXVI, part 3 (pp. 1227–1228). Houston: Lunar and Planetary Institute.

Schmitt, H. H., Petro, N. E., Wells, R. A., Robinson, M. S., Weiss, B. P., & Mercer, C. M. (2017). Revisiting the field geology of Taurus–Littrow. Icarus, 1–32. https://doi.org/10.1016/j.icarus.2016.11.042

Shoemaker, E. M., Hackman, R. J., & Eggleton, R. E. (1962). Interplanetary correlation of geologic time. Advances in the Astronautical Sciences, 8, 70–89.

Shoemaker, E. M. (1965). Preliminary analysis of the fine structure of the lunar surface in Mare Cognitum. International Astronomical Union Colloquium, 5, 23–77.

Singer, K. N., Jolliff, B. L., & McKinnon, W. B. (2020). Lunar secondary craters and estimated ejecta block sizes reveal a scale-dependent fragmentation trend. Journal of Geophysical Research: Planets, 125, e2019JE006313. https://doi.org/10.1029/2019JE006313

Smith, D. E., Zuber, M. T., Jackson, G. B., Cavanaugh, J. F., Neumann, G. A., Riris, H., et al. (2009). The Lunar Orbiter Laser Altimeter Investigation on the Lunar Reconnaissance Orbiter Mission. Space Science Reviews, 150(1–4), 209–241. https://doi.org/10.1007/s11214-009-9512-y

Smith, D. E., Zuber, M. T., Neumann, G. A., Lemoine, F. G., Mazarico, E., Torrence, M. H., et al. (2010). Initial observations from the Lunar Orbiter Laser Altimeter (LOLA). Geophysical Research Letters, 37(18), L18204. https://doi.org/10.1029/2010gl043751

Smith, D. E., Zuber, M. T., Neumann, G. A., Mazarico, E., Lemoine, F. G., Head III, J. W., et al. (2017). Summary of the results from the lunar orbiter laser altimeter after seven years in lunar orbit. Icarus, 283, 70–91. https://doi.org/10.1016/j.icarus.2016.06.006

Snape, J. F., Nemchin, A. A., Bellucci, J. J., Whitehouse, M. J., Tartèse, R., Barnes, J. J., et al. (2016a). Lunar basalt chronology, mantle differentiation and implications for determining the age of the Moon. Earth and Planetary Science Letters, 451, 149–158. https://doi.org/10.1016/j.epsl.2016.07.026

Snape, J. F., Nemchin, A. A., Grange, M. L., Bellucci, J. J., Thiessen, F., & Whitehouse, M. J. (2016b). Phosphate ages in Apollo 14 breccias: Resolving multiple impact events with high precision U–Pb SIMS analyses. Geochimica et Cosmochimica Acta, 174, 13–29. https://doi.org/10.1016/j.gca.2015.11.005

Snyder, J. P. (1987). Map projections – A working manual. U.S. Geological Survey Professional Paper 1395. Washington, DC: U.S. Government Printing Office.

Soderblom, L. A. (1970). A model for small-impact erosion applied to the lunar surface. Journal of Geophysical Research, 75(14), 2655– 2661. https://doi.org/10.1029/JB075i014p02655

Sood, R., Chappaz, L., Melosh, H. J., Howell, K. C., Milbury, C., Blair, D. M., & Zuber, M. T. (2017). Detection and characterization of buried lunar craters with GRAIL data. Icarus, 289, 157–172. https://doi.org/10.1016/j.icarus.2017.02.013

Speyerer, E. J., Povilaitis, R. Z., Robinson, M. S., Thomas, P. C., & Wagner, R. V. (2016). Quantifying crater production and regolith overturn on the Moon with temporal imaging. Nature, 538(7624), 215–218. https://doi.org/10.1038/nature19829

Spudis, P. D. (1993). The Geology of Multi-Ring Impact Basins. Cambridge: Cambridge University Press. https://doi.org/10.1017/cbo9780511564581

Spudis, P. D., Wilhelms, D. E., & Robinson, M. S. (2011). The Sculptured Hills of the Taurus Highlands: Implications for the relative age of Serenitatis basin chronologies and the cratering history of the Moon. Journal of Geophysical Research, 116, E00H03. https://doi.org/10.1029/2011JE003903

Squyres, S., Howell, C., Liu, M., & Lissauer, J. (1997). Investigation of crater “saturation” using spatial statistics. Icarus, 125(1), 67–82. https://doi.org/10.1006/icar.1996.5560

Steenstra, E. S., Martin, D. J. P., McDonald, F. E., Paisarnsombat, S., Venturino, C., O’Hara, S., et al. (2016). Analyses of robotic traverses and sample sites in the Schrödinger basin for the HERACLES human-assisted sample return mission concept. Advances in Space Research, 58(6), 1050–1065. https://doi.org/10.1016/j.asr.2016.05.041

Stöffler, D., Gault, D. E., Wedekind, J., & Polkowski, G. (1975). Experimental hypervelocity impact into quartz sand: Distribution and shock metamorphism of ejecta. Journal of Geophysical Research, 80(29), 4062–4077. https://doi.org/10.1029/jb080i029p04062

Stöffler, D., et al. (1985), Composition and evolution of the lunar crust in the Descartes Highlands, Apollo 16, J. Geophys. Res., 90(S02), C449– C506, doi:10.1029/JB090iS02p0C449.

Stöffler, D., & Ryder, G. (2001). Stratigraphy and isotope ages of lunar geologic units: Chronological standard for the inner solar system. Space Science Reviews, 96(1/4), 9–54. https://doi.org/10.1023/A:1011937020193

Stöffler, D., Ryder, G., Ivanov, B. A., Artemieva, N. A., Cintala, M. J., & Grieve, R. A. F. (2006). Cratering history and lunar chronology. In B. L. Jolliff, M. A. Wieczorek, C. K. Shearer, & C. R. Neal (Eds.), New Views of the Moon: Reviews in Mineralogy and Geochemistry (Vol. 60, pp. 519–596). Washington, DC: Mineralogical Society of America. https://doi.org/10.2138/rmg.2006.60.05

Strom, R. G., Trask, N. J., & Guest, J. E. (1975). Tectonism and volcanism on Mercury. Journal of Geophysical Research, 80(17), 2478–2507. https://doi.org/10.1029/jb080i017p02478

Strom, R. G. (1977). Origin and relative age of lunar and Mercurian intercrater plains. Physics of the Earth and Planetary Interiors, 15(2–3), 156–172. https://doi.org/10.1016/0031-9201(77)90028-0

Strom, R.G.,Croft ,S.K., & Barlow, N.G. (1992). The martian impact cratering record. In H.H. Kieffer, B.M. Jakosky, C.W. Snyder, & M.S. Matthews (Eds.), Mars (pp 383–423), Tuscon: University of Arizona Press.

Strom, R. G., Schaber, G. G., & Dawson, D. D. (1994). The global resurfacing of Venus. Journal of Geophysical Research, 99(E5), 10899. https://doi.org/10.1029/94je00388

Strom, R. G., Malhotra, R., Ito, T., Yoshida, F., & Kring, D. A. (2005). The Origin of Planetary Impactors in the Inner Solar System. Science, 309(5742), 1847–1850. https://doi.org/10.1126/science.1113544

Strom, R. G., Banks, M. E., Chapman, C. R., Fassett, C. I., Forde, J. A., Head, J. W., III, et al. (2011). Mercury crater statistics from MESSENGER flybys: Implications for stratigraphy and resurfacing history. Planetary and Space Science, 59(15), 1960–1967. https://doi.org/10.1016/j.pss.2011.03.018

Strom, R. G., Malhotra, R., Xiao, Z.-Y., Ito, T., Yoshida, F., & Ostrach, L. R. (2015). The inner solar system cratering record and the evolution of impactor populations. Research in Astronomy and Astrophysics, 15(3), 407–434. https://doi.org/10.1088/1674-4527/15/3/009

Stuart-Alexander, D. E., & Howard, K. A. (1970). Geologic map of the central far side of the Moon. Washington: U.S. Geological Survey Map I–1047. https://doi.org/10.3133/i1047

Swindle, T. D., Spudis, P. D., Taylor, G. J., Korotev, R. L., Nichols Jr., R. H., & Olinger, C. T. (1991). Searching for Crisium basin ejecta: Chemistry and ages of Luna 20 impact melts. In Proceedings of the 21st lunar and planetary science conference (pp. 167–181). Houston, TX: Lunar and Planetary Institute.

Tanaka, K. L. (1982). A new time-saving crater-count technique with application to narrow features. In Reports of Planetary Geology Program – 1982, NASA Technical Memorandum 85127 (pp. 123–125). Washington, DC: NASA.

Tera, F., Papanastassiou, D. A., & Wasserburg, G. J. (1974). Isotopic evidence for a terminal lunar cataclysm. Earth and Planetary Science Letters, 22, 1– 21. https://doi.org/10.1016/0012-821X(74)90059-4

Thomas, R. J., Rothery, D. A., Conway, S. J., & Anand, M. (2014). Long-lived explosive volcanism on Mercury. Geophysical Research Letters, 41(17), 6084–6092. https://doi.org/10.1002/2014gl061224

Tsiganis, K., Gomes, R., Morbidelli, A., & Levison, H. F. (2005). Origin of the orbital architecture of the giant planets of the solar system. Nature, 435, 459–461. https://doi.org/10.1038/nature03539

Turcotte, D. L., Morein, G., Roberts, D., & Malamud, B. D. (1999). Catastrophic resurfacing and episodic subduction on Venus. Icarus, 139(1), 49–54. https://doi.org/10.1006/icar.1999.6084

van der Bogert, C. H., Hiesinger, H., Dundas, C. M., Krüger, T., McEwen, A. S., Zanetti, M., & Robinson, M. S. (2017). Origin of discrepancies between crater size-frequency distributions of coeval lunar geologic units via target property contrasts. Icarus, 298, 49–63. https://doi.org/10.1016/j.icarus.2016.11.040

van der Bogert, C. H., Hiesinger, H., Spudis, P., Runyon, K. D., & Denevi, B. W. (2018). The age of the Crisium impact basin. In 49th Lunar and planetary science conference (1028 pp.). Houston, TX.

Vincenty, T. (1975). Direct and inverse solutions of geodesics on the ellipsoid with application of nested equations. Survey Review, 23(176), 88–93. https://doi.org/10.1179/sre.1975.23.176.88

Virtanen, P., Gommers, R., Oliphant, T. E., Haberland, M., Reddy, T., Cournapeau, D., et al. (2020). SciPy 1.0: Fundamental algorithms for scientific computing in Python. Nature Methods, 17(3), 261–272. https://doi.org/10.1038/s41592-019-0686-2

Wang, Q., & Liu, J. (2016). A Chang'e-4 mission concept and vision of future Chinese lunar exploration activities. Acta Astronautica, 127, 678–683. https://doi.org/10.1016/j.actaastro.2016.06.024

Watters, T. R., Head, J. W., Solomon, S. C., Robinson, M., Chapman, C. R., Denevi, B. W., et al. (2009). Evolution of the rembrandt impact basin on Mercury. Science, 324(5927), 618–621. https://doi.org/10.1126/science.1172109

Watters, T. R., Daud, K., Banks, M. E., Selvans, M. M., Chapman, C. R., & Ernst, C. M. (2016). Recent tectonic activity on Mercury revealed by small thrust fault scarps. Nature Geoscience, 9(10), 743–747. https://doi.org/10.1038/ngeo2814

Weidenschilling, S. J. (2000). Formation of Planetesimals and Accretion of the Terrestrial Planets. Space Science Reviews, 92(1/2), 295–310. https://doi.org/10.1023/a:1005259615299

Werner, S. C. (2014). Moon, Mars, Mercury: Basin formation ages and implications for the maximum surface age and the migration of gaseous planets. Earth and Planetary Science Letters, 400, 54–65. https://doi.org/10.1016/j.epsl.2014.05.019

Whitten, J., Head, J. W., Staid, M., Pieters, C. M., Mustard, J., Clark, R., et al. (2011). Lunar mare deposits associated with the Orientale impact basin: New insights into mineralogy, history, mode of emplacement, and relation to Orientale Basin evolution from Moon Mineralogy Mapper (M3) data from Chandrayaan-1. Journal of Geophysical Research, 116. https://doi.org/10.1029/2010je003736

Wieczorek, M. A., Neumann, G. A., Nimmo, F., Kiefer, W. S., Taylor, G. J., Melosh, H. J., et al. (2012). The crust of the Moon as seen by GRAIL. Science, 339(6120), 671–675. https://doi.org/10.1126/science.1231530

Wilhelms, D. E., & McCauley, J. F. (1971). Geologic map of the nearside of the Moon. Washington, DC: U.S. Geological Survey Map, I–703. https://doi.org/10.3133/i703

Wilhelms, D. E. (1976). Mercurian volcanism questioned. Icarus, 28(4), 551–558. https://doi.org/10.1016/0019-1035(76)90128-7

Wilhelms, D. E. (1987). The geologic history of the Moon. Professional Paper. US Geological Survey. https://doi.org/10.3133/pp1348

Williams, K. K., & Zuber, M. T. (1998). Measurement and analysis of lunar basin depths from clementine altimetry. Icarus, 131, 107–122. https://doi.org/10.1006/icar.1997.5856

Wilson, L., & Head, J. W. (2008). Volcanism on Mercury: A new model for the history of magma ascent and eruption. Geophysical Research Letters, 35(23). https://doi.org/10.1029/2008gl035620

Wood, C. A., Head, J. W., & Cintala, M. J. (1977). Apparent depth/diameter relations for lunar crater. Paper presented at 8th Lunar Science Conference (pp. 3503–3520). Houston: TX.

Woronow, A. (1977). Crater saturation and equilibrium—A Monte Carlo simulation. Journal of Geophysical Research, 82(17), 2447–2456. https://doi.org/10.1029/JB082i017p02447

Woronow, A. (1985). A Monte Carlo study of parameters affecting computer simulations of crater saturation density. Journal of Geophysical Research: Solid Earth, 90, 817–824. https://doi.org/10.1029/JB090iS02p0C817

Xiao, Z., & Strom, R. G. (2012). Problems determining relative and absolute ages using the small crater population. Icarus, 220(1), 254–267. https://doi.org/10.1016/j.icarus.2012.05.012

Xiao, Z., & Werner, S. C. (2015). Size-frequency distribution of crater populations in equilibrium on the Moon. Journal of Geophysical Research: Planets, 120, 2277–2292. https://doi.org/10.1002/2015JE004860

Xiao, Z. (2018). On the importance of self-secondaries. Geoscience Letters, 5(1). https://doi.org/10.1186/s40562-018-0116-9

Xie, M., Zhu, M.-H., Xiao, Z., Wu, Y., & Xu, A. (2017). Effect of Topography Degradation on Crater Size-Frequency Distributions: Implications for Populations of Small Craters and Age Dating. Geophysical Research Letters, 44(20), 10,171-10,179. https://doi.org/10.1002/2017gl075298

Zhao, J., Xiao, L., Qiao, L., Glotch, T. D., and Huang, Q. (2017). The Mons Rümker volcanic complex of the Moon: A candidate landing site for the Chang'E-5 mission, Journal of Geophysical Research: Planets, 122, 1419– 1442, https://doi.org/10.1002/2016JE005247

Zhu, M., Wünnemann, K., Potter, R. W. K., Kleine, T., & Morbidelli, A. (2019). Are the Moon's nearside-farside asymmetries the result of a giant impact? Journal of Geophysical Research: Planets, 124(8), 2117–2140. https://doi.org/10.1029/2018je005826

Zuber, M. T., Smith, D. E., Phillips, R. J., Solomon, S. C., Neumann, G. A., Hauck, S. A., et al. (2012). Topography of the northern hemisphere of Mercury from MESSENGER laser altimetry. Science, 336(6078), 217–220. https://doi.org/10.1126/science.1218805

Zuber, M. T., Smith, D. E., Watkins, M. M., Asmar, S. W., Konopliv, A. S., Lemoine, F. G., et al. (2013). Gravity Field of the Moon from the Gravity Recovery and Interior Laboratory (GRAIL) Mission. Science, 339(6120), 668–671. https://doi.org/10.1126/science.1231507